PHYSICS

A STUDY OF THE FINAL STATES $\pi^-\pi^-p\bar{K}^o$, $\pi^-\pi^-p\bar{K}^o\pi^o$ AND $\pi^-\pi^-\pi^+\bar{K}^o n$ PRODUCED IN K^-n INTERACTIONS AT 4.91 GeV/c

RONALD RHOADS PRICE

Dissertation under the direction of Professor Alfred Weinberg

Resonance production in the reactions containing a proton in the final state was characterized primarily by the production of $K^{*-}(890)$. The events with a final state neutron were characterized by the production of either $K^{*-}(890)$ or $N^{*-}(1236)$, but very little double resonance production. Cross-sections are presented. Exponential slopes for the momentum-transfer distributions of the $K^{*-}(890)$ and $N^{*-}(1236)$ were determined. For the four-constraint events the spin density matrix elements for the decay of the $K^{*-}(890)$ in the Jackson frame implied alignment. These data from all three reactions were compared with the predictions of the multiperipheral model of Chan, Loskiewicz, and Allison (CLA) as modified to include resonance production by Bassompierre, et al. The data from the four-constraint events are also compared with the multiperipheral model of Plahte and Roberts. Evidence for the possible production of an isospin 5/2, strangeness zero baryon enhancement is presented.

Approved _____ Date _____
Adviser

A STUDY OF THE FINAL STATES

$\pi^-\pi^-p\bar{K}^0$, $\pi^-\pi^-p\bar{K}^0\pi^0$ AND $\pi^-\pi^-\pi^+\bar{K}^0n$

PRODUCED IN K^-n INTERACTIONS

AT 4.91 GeV/c

By

Ronald Rhoads Price

Dissertation

Submitted to the Faculty of the

Graduate School of Vanderbilt University

in partial fulfillment of the requirements

for the degree of

DOCTOR OF PHILOSOPHY

in

PHYSICS

August, 1971

Nashville, Tennessee

Approved:	Date:
Alfred Weinberg	May 20, 1971
James R. Wilson	May 20, 1971
Charles E. Roos	May 20, 1971
Robert J. Baylor	May 20, 1971
Horace W. Crater	May 20, 1971
E. V. Salant	May 21, 1971

To The Memory of My Father

ACKNOWLEDGMENTS

This work would not have been possible without the cooperation and assistance of many people. In this regard I would like to acknowledge the staff of the Vanderbilt University Bubble Chamber Group. This group consisted of the following people: Dr. F. Bomse, Dr. E. J. Moses, Dr. E. O. Salant, Dr. J. W. Waters, Dr. M. S. Webster and Dr. A. Weinberg. I am particularly indebted to Dr. Weinberg for encouragement, direction and innumerable discussions during the course of this work. I will always appreciate having had the opportunity of working with Dr. Weinberg.

I would like to thank Professor E. O. Salant, in particular, for his support and encouragement during the course of this work.

I would also like to acknowledge my fellow graduate students. Working with them has been both pleasant and profitable. They were: R. Berg, T. B. Borak, W. R. Burdett, J. H. Hanlon and J. Mandzy. In particular I would like to thank Ron Berg. His cooperation and assistance were greatly appreciated.

The successful completion of this work was made possible by the efforts of a large number of scanners. In particular I am indebted to the following: Mr. Erol Sayen, Mrs. Gulsen Buyukbayli, Mrs. Georgia Grivetti, Mrs. Sylvia Maia, Mrs. Krishna Akanuri, Mrs. Indira Kodali and Mrs. Anastasia Koshakji. Mrs. Koshakji was chief supervisor and was responsible for coordinating all scanning and measuring activities. Her efforts are gratefully acknowledged.

I would like to acknowledge the services of the A.E.C. Computing Center, Courant Institute of Mathematical Sciences, New York University, New York, New York. At this facility Mr. R. Malchie has provided invaluable assistance. I would also like to acknowledge the services of the staff of the Vanderbilt University Computing Center.

I am indebted to Mr. and Mrs. Wallace Rice, Jr. for their invaluable assistance in the typing and preparation of this manuscript. Their efforts were greatly appreciated.

My graduate work at Vanderbilt was made possible by the support of an A.E.C. Health Physics Fellowship and an N.S.F. Traineeship. These are gratefully acknowledged.

I would like to take this opportunity to thank my wife, Donna, for her understanding and continued encouragement throughout my graduate work. I would also like to thank her for her assistance in the preparation of this manuscript.

TABLE OF CONTENTS

DEDICATION ii

ACKNOWLEDGMENT iii

LIST OF TABLES vii

LIST OF FIGURES viii

Chapter

I. INTRODUCTION 1

II. EXPERIMENTAL SETUP AND DATA PROCESSING 3

A. Bubble Chamber Exposure 3

B. Data Collection and Reduction 3

1. Scanning 3

2. Measuring 8

3. Event reconstruction and kinematic fitting 8

4. Data retrieval 12

5. Event type selection 13

C. Beam Momentum 14

D. Cross-Section Per Event 18

III. SEARCH FOR BIASES AND DETERMINATION OF SMALL CORRECTIONS 23

A. Missing Mass 23

B. Spectator Proton 29

C. Chi-Square Probabilities 38

D. Stretch Variable Distributions 41

Chapter Page

E. Magnetic Field 41

F. Corrections for Loss of Vees 46

IV. PHENOMENOLOGICAL CONSIDERATIONS 54

A. Multiperipheral Models 54

1. The CLA model 58

2. Plahte and Roberts' modified CLA model 67

B. Decay Angular Correlations 71

V. EXPERIMENTAL RESULTS AND MODEL COMPARISONS 74

A. $K^-n \rightarrow \pi^-\pi^-p\overline{K}^o$ 74

1. Data and CLA model calculation 76

2. Comparison of the data with the model of Plahte and Roberts 117

B. $K^-n \rightarrow \pi^-\pi^- pK^o\pi^o$ 130

C. $K^-n \rightarrow \pi^-\pi^-\pi^+\overline{K}^o n$ 156

VI. BARYON ENHANCEMENT IN THE $n\pi^-\pi^-$ INVARIANT MASS DISTRIBUTION 212

VII. RESULTS AND CONCLUSIONS 235

LIST OF REFERENCES 242

LIST OF TABLES

Table		Page
1.	Cross-Section Corrections	21
2.	Model Parameter Values	61
3.	Trajectory Properties Used	62
4.	Cross-Sections	236
5.	Exponential Slope of $\lvert t - t_{min} \rvert$ Distribution	238
6.	Production Cos θ Chi-Square Probabilities	238
7.	Average Value of Single Particle Transverse and Longitudinal Momentum	239
8.	Fractions of Baryons Produced in the Forward Hemisphere	241

LIST OF FIGURES

Figure		Page
1.	Sketch of BNL 80-Inch Bubble Chamber and Camera Positions	4
2.	Sketch of a Typical Frame in View One Showing Fiducial Volumes	6
3.	Distribution of Missing Energy for Events Fitting Reaction II-5	16
4.	Distribution of Square of Missing Mass for $K^-d \rightarrow P_s\pi^-\pi^-p\overline{K}^o(MM)$	24
5.	(a) Distribution of Square of Missing Mass for $K^-d \rightarrow P_s\pi^-\pi^-\pi^+\overline{K}^o(MM)$. (b) Same Distribution with Events Having Unambiguous Fits to Reaction II-6 Shaded	27
6.	The Distribution in the Quantity $F = \frac{(MM)^2 - (M_p)^2}{\Delta(MM^2)}$ for Reactions (a) II-7 and (b) II-6	30
7.	Measured Spectator Proton Momentum Distribution	33
8.	Momentum Distributions for (a) Proton Produced in Reaction II-5, (b) Proton Produced in Reaction II-6, and (c) Neutron from Reaction II-7	36
9.	Chi-Square Probability Distributions for (a) $\overline{K}^o$ Vee and the Production Vertices of (b) Reaction II-5, (c) Reaction II-6, and (d) Reaction II-7	39
10.	Typical Stretch Variable Distributions. Distributions for π^- from Reaction II-5; (a) Stretch ϕ, (b) Stretch tan λ, and (c) Stretch 1/p	42
11.	Distribution of Measured $\pi^+\pi^-$ Invariant Mass for $\overline{K}^o \rightarrow \pi^+\pi^-$	44
12.	(a) Distribution of Lifetime of $\overline{K}^o$ in Units of t/τ. Distributions of the Probability the Vee Would Decay in the Distance It Traveled for Reactions (b) II-7, (c) II-6, and (d) II-5	47

Figure | Page

13. Distributions of the Cosine of the $\overline{K}^{o}$ Decay Angle for Reactions (a) II-7, (b) II-6, and (c) II-5 50

14. Sketch of Geometry Used in Vee-Loss Correction Calculation 53

15. Feynman Diagram Describing Meson-Baryon Scattering 54

16. Feynman Diagram Describing Meson-Baryon Scattering at Lower Vertex 55

17. Diagram Representing the Full Amplitude of a Three Vertex Meson-Baryon Interaction 56

18. Typical n^{th} Order Multiperipheral Diagram 57

19. Typical n^{th} Order Multiperipheral Diagram Showing the Variables t_i and s_i 59

20. One of the Multiperipheral Diagrams Used in the CLA Calculation for Reaction II-5 65

21. A Multiperipheral Diagram Modified to Incorporate Resonance Production 66

22. (a) Multiperipheral Diagram Used in Plahte and Roberts Model Calculation. (b) Diagrams Showing Incorporation of Isospin Clebsch-Gordon Coefficients 70

23. (a) The $\overline{K}^{o}\pi^{-}$ Invariant Mass Plot for Reaction II-5. (b) Corresponding Production Angular Distribution 76

24. (a) The $|t - t_{min}|$ distribution for $K^{*-}(890)$ Produced in Reaction II-5. (b) The $|t - t_{min}|$ Distribution for $K^{*-}(890)$ Produced in Reaction II-6 81

25. Distributions for the Reaction $K^{-}n \rightarrow K^{*-}(890)\pi_2 p \rightarrow \overline{K}^{o}\pi_1^{-}\pi_2^{-}p$; (a) $K^{*-}(890)p$ Invariant Mass, (b) $K^{*-}\pi_2^{-}$ Invariant Mass, (c) $p\pi_2^{-}$ Invariant Mass, Cosine of Production Angle for (d) π_1^{-}, and (e) π_2^{-} 85

26. Feynman Diagram for $K^{*-}(890)$ Production by Nucleon Charge-Exchange Scattering in Reaction II-5 84

Figure | Page

27. Feynman Diagram for Simultaneous $K^{*-}N^{*\circ}$ Production in Reaction II-5 88

28. The Single Particle Production Angular Distribution for Reaction II-5; (a) π^-, (b) $\bar{K}^\circ$, and (c) Proton 90

29. Jackson Frame of Reference for the Decay of $K^*(890) \rightarrow \bar{K}^\circ\pi^-$ 92

30. Jackson Frame Distributions for Decay of $K^{*-}(890)$ for (a) Cos θ and (b) ϕ 93

31. Histogram of the Quantity R as a Function of the Jackson ϕ for the Decay of $K^{*-}(890)$ in Reaction II-5 99

32. The Invariant Mass Distribution for $p\pi^-$ Produced in Reaction II-5 103

33. Invariant Mass Plots for (a) $\bar{K}^\circ\pi^-p$ and (b) $\bar{K}^\circ\pi^-\pi^-$ 107

34. The Dependence of Single Particle Production Angle on CLA b_i for (a) π^-, (b) $\bar{K}^\circ$, and (c) Proton 110

35. A Sketch Defining Production Angle 109

36. The Longitudinal Momentum Distributions for the Single Particles (a) π^-, (b) $\bar{K}^\circ$, and (c) Proton Produced in Reaction II-5 115

37. The Transverse Momentum Distributions for the Single Particles (a) π^-, (b) $\bar{K}^\circ$, and (c) Proton Produced in Reaction II-5 118

38. A Comparison of $\bar{K}^\circ\pi^-$ Invariant Mass Distribution with Plahte and Roberts Model 120

39. A Comparison of $p\pi^-$ Invariant Mass Distribution with Plahte and Roberts Model 122

40. Dependence of Single Particle Production Angle on Exchanged Trajectories for Plahte and Roberts Model Calculation 125

41. A Multiperipheral Diagram for $K^-n \rightarrow \bar{K}^\circ\pi^-\pi^-p$ 124

42. (a) The $N^{*\circ}(1236)$ Production Angular Distribution Compared to Plahte and Roberts Model Restricted to I = 0 Exchange. (b) Corresponding Plot for Control Region $1.390 \leq M^*(p\pi^-) \leq 1.590$ GeV/c^2 128

Figure | Page

43. The Production Angular Distribution for $K^{*-}(890)$ Compared to Plahte and Roberts Model Calculation Requiring I = 0 Exchange only 131

44. (a) The $\overline{K}^{o}\pi^{-}$ Effective Mass Distribution for Reaction II-6. (b) Corresponding Production Angular Distribution 134

45. Jackson Frame Distributions for $K^{*-}(890)$ Produced in Reaction II-6; (a) Cos θ, and (b) ϕ 138

46. Invariant Mass Distribution for $\overline{K}^{o}\pi^{-}\pi^{o}$ Produced in Reaction II-6 141

47. Invariant Mass Distribution for $\overline{K}^{o}\pi^{-}\pi^{-}\pi^{o}$ Produced in Reaction II-6 144

48. The Dependence of Single Particle Production Angles on CLA b_i for (a) $\overline{K}^{o}$ and (b) Proton Produced in Reaction II-6 147

49. The Dependence of Single Particle Production Angles on CLA b_i for (a) π^{o} and (b) π^{-} 149

50. Single Particle Longitudinal Momentum Distribution for (a) $\overline{K}^{o}$ and (b) p Produced in Reaction II-6 152

51. Longitudinal Momentum Distribution for (a) π^{o} and (b) π^{-} 154

52. Transverse Momentum Distribution for (a) Proton and (b) $\overline{K}^{o}$ 157

53. Transverse Momentum Distribution for (a) π^{o} and (b) π^{-} 159

54. (a) The Invariant Mass Distribution for the $\overline{K}^{o}\pi^{-}$ Produced in Reaction II-7. (b) Corresponding Production Angular Distribution 162

55. The $|t - t_{min}|$ Distribution for $K^{*-}(890)$ Produced in Reaction II-7, Corrected for Background 166

56. Jackson Frame Distributions for $K^{*-}(890)$; (a) Cos θ and (b) ϕ 169

Figure | Page

57. The Invariant Mass Distribution of the $n\pi_2^-$ Produced in $K^-n \to K^{*-}(890)n\pi_2^- \to \bar{K}^0\pi_1^-n\pi_2^-$ 172

58. (a) The Invariant Mass Distribution for $n\pi^-$ Produced in Reaction II-7. (b) Corresponding Production Angular Distribution 174

59. The $|t - t_{min}|$ Distribution for N*(1236) Produced in Reaction II-7 178

60. A Sketch of the Jackson Frame of Reference for the N*(1236) Decay 181

61. Jackson Frame Distributions for N*(1236); (a) ϕ and (b) Cos θ 183

62. The $\pi^+\pi^-$ Invariant Mass Histogram with Momentum Transfer Cuts of .2 and 1.0 $(GeV/c)^2$ 186

63. (a) The $\pi^+\pi^-$ Invariant Mass Histogram with CLA Model Modified by Clayton's Ratio Factor. (b) Curve from Claytons' paper Showing Deviations of $\pi\pi$ Invariant Mass Distributions from Phase Space 188

64. The Invariant Mass Distribution of $\bar{K}^0n\pi^+\pi^-$ Produced in Reaction II-7 191

65. (a) Sketch of Jackson Frame of Reference in $\bar{K}^0n\pi^+\pi^-$ Rest Frame for $\bar{K}^0$ Distribution. (b) Jackson Frame of Reference for Observing Distribution of Neutron 193

66. Production Angular Distributions for (a) $\bar{K}^0$ and (b) Neutron 194

67. Production Angular Distributions for Neutron. The Curve Is CLA Calculation Where All Pomeron Exchange Was Replaced by Intercept 0.5 Meson Exchange 198

68. Single Particle Production Angular Distributions for (a) π^+ and (b) π^- 200

69. Longitudinal Momentum Distributions for (a) $\bar{K}^0$ and (b) Neutron 205

Figure | Page

70. Longitudinal Momentum Distributions for (a) π^+ and (b) π^- 205

71. Transverse Momentum Distributions for (a) Neutron and (b) $\overline{K}^o$ 207

72. Transverse Momentum Distributions for (a) π^- and (b) π^+ 209

73. (a) Invariant Mass Distribution for $n\pi^-\pi^-$ from Reaction II-7 and (b) Corresponding χ^2 Probability Distribution 213

74. Ideogram for $n\pi^-\pi^-$ Invariant Mass Distribution 216

75. (a) Invariant Mass Distribution of the $n\pi^-$ from the $n\pi^-\pi^-$ Enhancement Region. (b) Corresponding Dalitz Plot 219

76. (a) Invariant Mass Distribution of the $\overline{K}^o\pi^-$ from the $n\pi^-\pi^-$ Enhancement Region. (b) Production Angular Distribution of $n\pi^-\pi^-$ Enhancement Region 222

77. (a) The $n\pi^+$ Invariant Mass Distribution from Reaction II-7 and (b) Invariant Mass Distribution of the $n\pi^+$ from $n\pi^-\pi^-$ Enhancement Region 225

78. (a) The $\overline{K}^o n$ Invariant Mass Distribution from Reaction II-7 and (b) Invariant Mass Distribution of the $\overline{K}^o n$ from $n\pi^-\pi^-$ Enhancement Region 228

79. (a) The $\pi^+\pi^-$ Invariant Mass Distribution from Reaction II-7 and (b) Invariant Mass Distribution of the $\pi^+\pi^-$ Enhancement Region 230

CHAPTER I

INTRODUCTION

In order to understand the nature of the strong interaction, much effort has gone into studying reactions produced by the bombardment of nucleons with pions, K-mesons, nucleons, and anti-nucleons. When the bombarding energy is sufficiently high, two general characteristics have emerged. These are peripherality and resonance production. [Reference: J. D. Jackson, Rev. Mod. Phys. 37, 484 (1963); this review article contains many references.] Observed peripherality has led to the development of the single-particle-exchange models. These peripheral models deal with two-particle and quasi-two-particle final states. As the energy of the bombarding particle is raised, the average number of particles in the final state increases. The success of the single-particle-exchange models generated interest in multiperipheral models as a possible description for the multi-particle final states.

In this work we have investigated several interactions having multi-particle final states and have compared these data with multiperipheral models. The interactions studied in this work were produced by the bombardment of deuterium nuclei with K^- mesons having a momentum of 4.9 GeV/c. These were

$$K^-d \rightarrow \pi^-\pi^- p\overline{K}^0 \ (P_s), \qquad (1\text{-}1)$$

$$\rightarrow \pi^-\pi^- p\overline{K}^0 \pi^0 \ (P_s), \qquad (1\text{-}2)$$

and

$$\rightarrow \pi^-\pi^-\pi^+ \overline{K}^0 n \ (P_s). \qquad (1\text{-}3)$$

The quantity P_s refers to a spectator proton, which does not take part in the interaction. Therefore, the reactions can be thought of as initiated by a K^- incident on a neutron.

Chapter II briefly describes the data collection and reduction. Chapter III is an investigation of possible biases present in the experiment. All were found to be small. Chapter IV is devoted to a brief description of the multiperipheral models compared with these data. Chapter V is a presentation of the data and the related model calculations. Chapter VI reports evidence suggesting the possible existence of a non-strange baryon enhancement of isotopic spin 5/2. A short conclusion is presented in Chapter VII.

CHAPTER II

EXPERIMENTAL SETUP AND DATA PROCESSING

A. Bubble Chamber Exposure

The initial phase of this experiment took place at Brookhaven National Laboratory (BNL) making use of the Alternating Gradient Synchrotron (AGS) and the BNL 80-inch deuterium-filled bubble chamber operating in an electrostatically separated K^- beam from the AGS. The beam momentum was determined to be 4.910 ± .007 GeV/c. The beam momentum is discussed further in Section C of this chapter. The AGS and the 80-inch BNL bubble chamber have been discussed extensively in the literature.[1,2,3] A rough sketch of the bubble chamber and the camera locations are shown in Figure 1.

The exposure consisted of approximately 100,000 pictures. The chamber was simultaneously viewed by three separate cameras. The film quality of this exposure was good.

B. Data Collection and Reduction

1. Scanning

Essentially all of the film was scanned and measured simultaneously. Image-plane digitizing tables were used for this. The scanners were instructed to scan all frames in all three views. They were told to do both an area scan and an along-the-track scan. They area-scanned for all two-pronged beam track interactions. They sighted along the beam tracks to detect partially obscured interactions and vee vertices. All

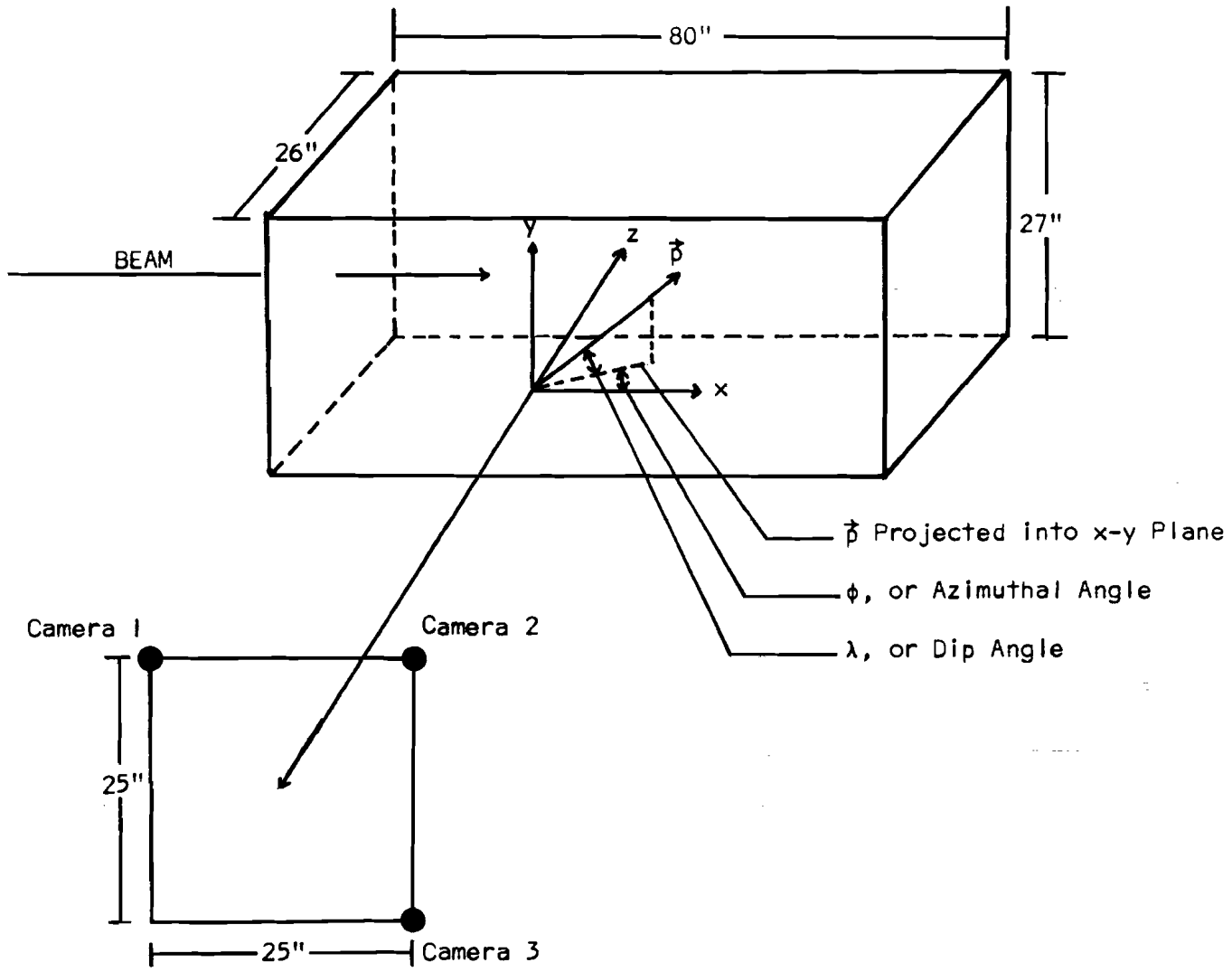

Figure 1.--Sketch of BNL 80-inch bubble chamber and camera positions.

events having one or more vees associated with a main vertex which had three or more prongs leaving it were recorded. The research work reported in this thesis only used the three-pronged events and four-pronged events with a visible stopping proton. A vee was called associated unless three-momentum conservation implied it did not result from the decay of a neutral particle produced at the beam track interaction. To determine association, a straight edge was placed with one end on the primary vertex and the other on the vee vertex. If the straight edge then passed between the vee prongs in all three views, the vee was taken as associated, provided the scanner could not rule it out on the basis of obvious failure to conserve momentum.

A fiducial volume is set so that the momenta of prongs belonging to vertices within this volume can be measured. Somewhat arbitrarily, two fiducial volumes were defined separately for the primary interaction vertex and the vee decay vertex. Figure 2 is a sketch showing how the ends of the fiducial volume were determined by using the view of camera number one. The average length of the primary interaction fiducial volume was 146 cm. The vee fiducial volume was 7.5 cm longer on the average. Conservation of energy and momentum imply that high momentum prongs are in the beam direction. Also, the beam is approximately centered in the bubble chamber. Therefore the side boundaries of the fiducial volumes were chosen as the limits of the illuminated liquid.

If a scanned event was determined to be out of the specified fiducial volumes, the instruction was to neither record nor measure the event. Likewise, if the beam particle which initiated the interaction was clearly not parallel to the other beam tracks in the frame, the

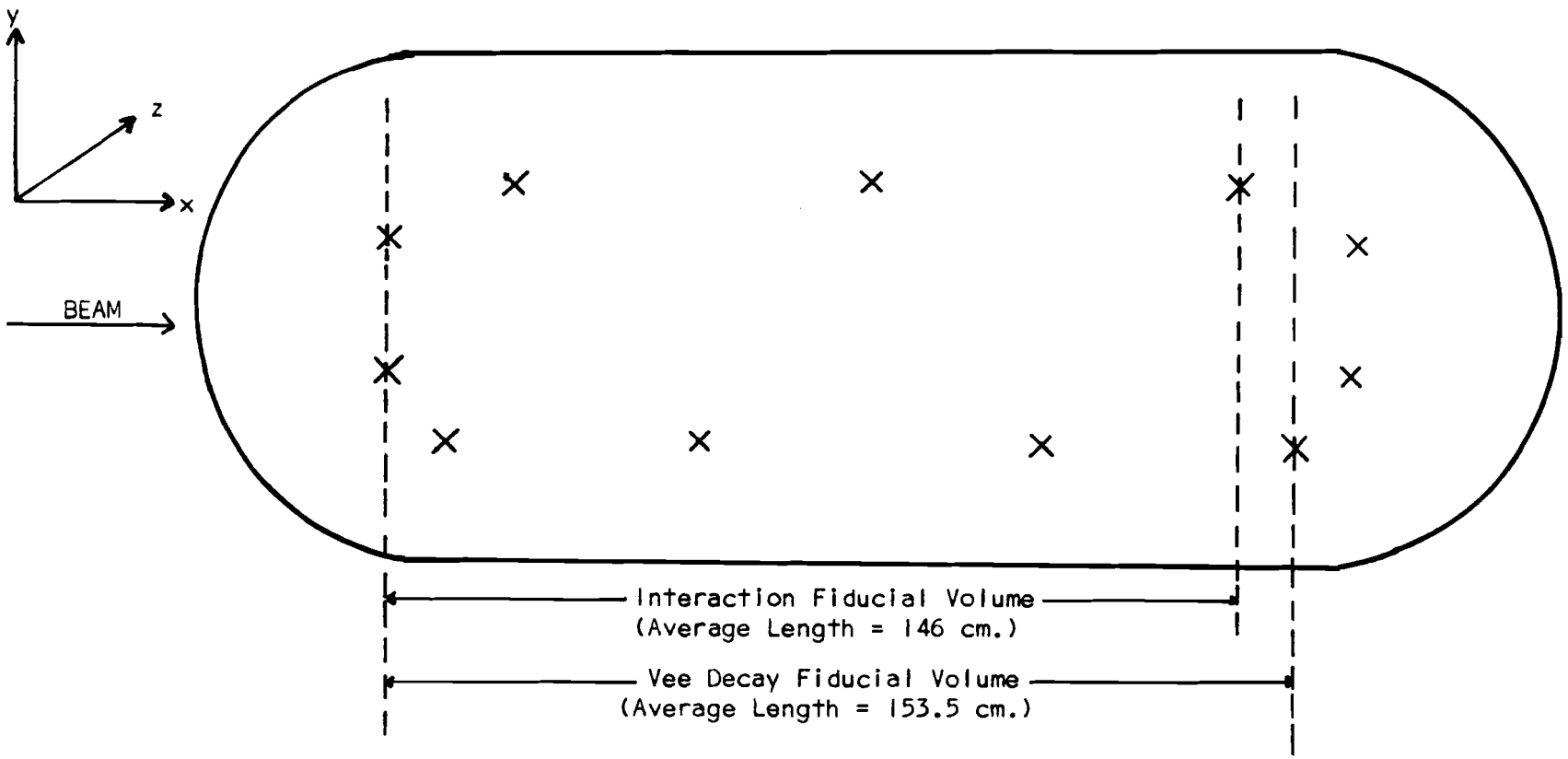

Figure 2.--Sketch of a typical frame in view one showing fiducial volumes.

event was dropped.

When all of the scanning criteria were met, the scanner recorded the appropriate information on a scanning record sheet. The scan sheet contained such information as roll, frame and event numbers, the beam track count, event type, area codes for both main vertex and vee vertex, ionization information for each track, stopping information, and comment codes that might help in identification at some later date. The format and codes of the scan sheet are discussed in detail by Mandzy.[4]

The efficiency of the scan was determined by a rescan of every fifth picture by a very good scanner. Disagreements in the two different scans were refereed by an excellent scanner. From this, the scanning efficiency E was calculated for the roll of film.

$$E = \frac{N}{N_T} \qquad \text{(II-1)}$$

where E is the scanning efficiency,

N is the number of events found in every fifth picture of the first scan,

and N_T is the best estimate of the true number of events in every fifth frame.

Rolls with less than 85 per cent scanning efficiency were rescanned. The scanning efficiency of each worker was also calculated. Those who were not doing well received closer supervision and more instruction. Also, their frames were rescanned.

The scan yielded approximately 17,000 vee event candidates with 2,212 fitting the $\bar{K}^{o}$ hypothesis.

Special treatment was given to two rolls which were to be used for cross-section calculations. These two rolls were completely scanned twice by our best scanners and also fifth frame checked for each scan. In addition, all interactions of all types were counted and recorded and a beam track count was made for every tenth frame.

2. Measuring

The measuring machines were equipped with incremental encoders in conjunction with up-down counters. The counters for each machine were on line to an IBM-1801 computer. The track coordinates could thus be entered directly into the computer's core. The computer monitored the event measurements. Before a track was accepted, the measured points were checked to see if they fell on a curve of approximately constant curvature. The measured points for each track were stored on the 1801's disc along with pertinent event identification information. This information was later punched on cards. A typical vee event consisted of about 25 cards. The measuring rate was about three events per hour for the IPD's. The measuring machines are discussed in more detail by Borak[5] and Mandzy.[4]

3. Event reconstruction and kinematic fitting

The card images of the measured events from the IBM-1801 computer were submitted as input to the Rutherford High Energy Laboratory bubble chamber analysis system HGEOM-HKINE-KINC3.[6,7] The programs were run on the CDC-6600 computer at the A.E.C. Computing Center, Courant Institute of Mathematical Science, New York University, New York, New York.

The geometrical reconstruction program, HGEOM, reads the measured track coordinates as data. The Cartesian coordinate system it uses for describing its results has the origin at the center of the liquid-glass interface of the bubble chamber window (see Figure 1). The z-axis is perpendicular to this interface and points into the liquid. As seen in Figure 1, the x and y axes are defined such that a left-handed coordinate system results, with the x-axis being approximately parallel to the beam. The programs HKINE and KINC3 also use this left-handed coordinate system. Before examining the data in order to study the dynamics, the components of three momenta were expressed in the right-handed system gotten by inverting the y-axis.

By tracing rays from the film plane through the camera lens and then through the intermediate media into the bubble chamber liquid, HGEOM is able to reconstruct the space coordinates of points on a track. The track coordinates are fit to a helix. The method of least squares is used to make this fit. Consider the projection of the momentum vector into the xy-plane. The angle this projection makes with the x-axis is called the azimuthal angle and the angle it makes with the momentum vector is called the dip angle. From the parameters of the helix, HGEOM determines the kinematic variables $1/p$, ϕ, and $\tan \lambda$ at the center of each track, where p is the track momentum, ϕ is the azimuthal angle, and λ is the dip angle. These angles are shown in Figure 1. The quantity $1/p$ is used instead of p because it is more directly related to the actual measured track quantity, the curvature, whose errors should be more normally distributed than those of the calculated quantity P.

$$p = \frac{0.3H\rho}{\cos\lambda} \times 10^{-3}\text{GeV/c}, \qquad (11\text{-}2)$$

where H is the z-component of the magnetic field in kilograms,

λ is the dip angle, and

ρ is the radius of the projection of the helix into the z = 0 plane.

The requirement of the normal distribution of errors is important because we wish to convert χ^2 figures of merit to probabilities. HGEOM supplies the helix fit of each track for the masses of a π-meson, K-meson, and a proton. HGEOM provides the kinematic variables ($1/p$, ϕ, $\tan\lambda$) and their corresponding errors as input to HKINE.

HGEOM calculates the errors in the kinematic variables using two independent methods. The results of the two calculations are compared and the larger is chosen as the appropriate error to be passed on to HKINE. One method simply computes the errors from the provided setting error and the Coulomb multiple scattering effect. The second method finds errors from the deviations of the measured points from the projection of the helix onto the film plane.

The derived variables ($1/p$, ϕ, $\tan\lambda$) and their errors are written out on paper in addition to being used as input to HKINE. Also information on events that fail geometrical reconstruction is written out. This paper output is used to check on the quality of the measurers' work and to make remeasurement lists.

HKINE, the second stage of the analysis system, is the kinematical fitting program. HKINE has available to it the measured quantities ($1/p$, ϕ, $\tan\lambda$) and their associated errors.

Most of the time we do not know what type of particles made the tracks. Consequently, for each event we must test a large number of hypotheses of particular mass assignments. A mass hypothesis consists of an assumed mass for each observed track and for neutral particles produced in the reaction, such as $\overline{K}^{o}$ and π^{o}.

For a given mass hypothesis HKINE determines those values of the kinematic variables that minimize χ^2 subject to the constraints of energy-momentum conservation.

The χ^2 for a set of measurements $[x_1^m,\ldots,x_n^m]$ of the variables is defined by

$$\chi^2 = \sum (x_i - x_i^m)\, G_{ij}^{x}\, (x_j - x_j^m), \qquad (11\text{-}3)$$

where x_i is the fitted value of the kinematic variable of interest,

x_i^m is its measured value, and

$(G_{ij}^{x})^{-1} = \delta\, x_i^m\, \delta\, x_j^m$ is the i,j^{th} element of the error matrix for the two measured variables x_i^m and x_j^m. The quantity $\delta\, x_i^m$ is the error in the ith kinematic variable.

Suppose that the frequency distribution in χ^2 is given by $f(\chi^2)$. The χ^2 probability, $P(\chi^2)$, is defined by

$$P(\chi^2) = \int_{\chi^2}^{\infty} f(\mu)\, d\mu.^{8} \qquad (11\text{-}4)$$

HKINE calculates the value of χ^2 and the χ^2 probability for each fit attempted.

This fitting program is needed for two reasons:

1. Folding in energy-momentum conservation lowers the errors in the kinematic variables. This is especially important if a π^{o} or neutron is produced in the reaction since its

three-momentum is not directly measured.

2. The χ^2 provides a figure of merit for determining if a mass hypothesis is consistent with energy-momentum conservation.

The kinematic fitting for our multi-prong-plus-vee events was a three-step process.

1. The vee was tried as a decaying Λ°, $\bar{\Lambda}^\circ$, and $\bar{K}^\circ$. The number of $\bar{\Lambda}^\circ$ fits was used as an estimate for the small number of $\bar{K}^\circ$'s we incorrectly classed as Λ°'s. This will be discussed in Chapter III, Section F.
2. All hypotheses were tried that were consistent with each passed vee fit. Using the result of the vee fit, a fit at the main interaction vertex was tried with the vee fit inserted as another measured track.
3. If step 2 was passed, a multi-vertex fit was then made using the results of both steps 1 and 2 as starting points. Multi-vertex fit results were used in studying our reactions.

The hypotheses of primary interest in this work were

$$K^-d \rightarrow P\pi^-\pi^-\bar{K}^\circ\ P_s, \qquad \text{(II-5)}$$

$$K^-d \rightarrow P\pi^-\pi^-\bar{K}^\circ\pi^\circ\ P_s, \qquad \text{(II-6)}$$

and

$$K^-d \rightarrow \pi^+\pi^-\pi^-\bar{K}^\circ n\ P_s, \qquad \text{(II-7)}$$

where P_s indicates a spectator proton.

4. Data retrieval

KINC3, the third part of the analysis system, then retrieves the measured variables and their errors plus the fitted variables and their errors for each hypothesis. It also retrieves identification and

quality control information. It then writes all of this information onto two magnetic tapes. One of these tapes is referred to as the summary tape. It contains all measured, fitted, quality control, and identification information for each track and effective masses and their errors calculated for all possible track combinations. The second tape is called the print-punch tape. This tape contains two files. As the name indicates, one file is printed on paper and the other is punched on cards. The Vanderbilt IBM-1401 computer is used for this purpose. The print file contains much of the same information as the summary tape and it is written in a format that can easily be read while checking events for ionization consistency. The punch file provides two cards for each event and also one card for each mass hypothesis that has a fit.

The summary tapes were also returned to Vanderbilt where they were packed onto long buffered tapes by the SDS Σ-7 computer.

5. Event type selection

Every event was examined on the scanning table in an effort to use bubble density to make definite mass assignments to the measured tracks. The decision of whether a particle was a proton or a meson was made on all tracks with momentum less than 1 GeV/c. When the momentum of the track was greater than 1 GeV/c, the ionization provided no information that could be used in making a decision. The decision of whether a particle was a charged pion or kaon was made on all tracks with momentum less than 0.5 GeV/c. Mass decisions based on ionization were punched by hand on cards in coded form, one card for each event. These cards, along with the long buffered tapes were provided as input to an

hypothesis picking program. The program scanned the various fits to an event and picked the best interpretation consistent with the ionization information.

The criteria used to pick the best fit were as follows:

1. In order for a fit to have even been considered it must have had a probability $\geq$ 1 per cent.
2. If the vee had both a Λ° and a $\bar{K}^{\circ}$ fit, the event was dropped as a possible $\bar{K}^{\circ}$ event. The reason for this criterion is discussed in Section F of Chapter III.
3. If an event fit hypothesis II-5, it was taken as that hypothesis, regardless of other fits it may have had because it has four constraints.
4. If an event fit both II-6 and II-7 and the ionization could not determine the correct fit, then the fit having the larger χ^2 probability was taken.

A study was made of the ambiguity of fits II-6 and II-7. Without the aid of ionization information, 25 per cent of the events were ambiguous. Considering the ionization reduced this to about 15 per cent for reaction II-6 and about 10 per cent for reaction II-7.

C. Beam Momentum

The beam momentum was determined by measuring beam tracks on precision film-plane measuring machines located at Oak Ridge National Laboratory. Especially long interacting tracks were chosen so that the momentum could be determined as accurately as possible from the curvature. Demanding interacting tracks eliminated muon contamination in the beam tracks measured.

From a sample of 137 beam tracks processed through the geometry reconstruction program HGEOM, the best value for the beam momentum was determined to be (4.910 ± .007) GeV/c.[9]

An independent check on the input beam momentum was made. We calculated the difference in the incoming energy and the outgoing measured energy, ΔE, for the fits to reaction II-5.

$$\Delta E = E_{K^-} + E_d - \sum_i E_i, \qquad \text{(II-8)}$$

where E_{K^-} is the energy of the incident K^-,

E_d is the energy of the deuteron, and

E_i is the energy of each outgoing particle.

Since the four constraint events are considered reliable, the outgoing particle masses are well determined. The incoming energy is dependent only upon the assigned beam momentum.

Figure 3 shows that this quantity is consistent with zero within the assigned beam error. This substantiates the assigned value for the beam momentum.

The energy rather than the momentum was used because the error introduced in ΔE by the unknown kinetic energy of the unseen spectators is very small. The approximate kinetic energy of a typical unseen spectator (T_{P_s}) is given by the relation

$$T_{P_s} \simeq \frac{P^2}{2m} \simeq \frac{(.05)^2}{2} \text{GeV}. \qquad \text{(II-9)}$$

$$= .0012 \text{ GeV}$$

where P is the momentum of the spectator taken to be .05 GeV/c (see Section B of Chapter III) and

Figure 3.--Distribution of missing energy for events fitting reaction II-5.

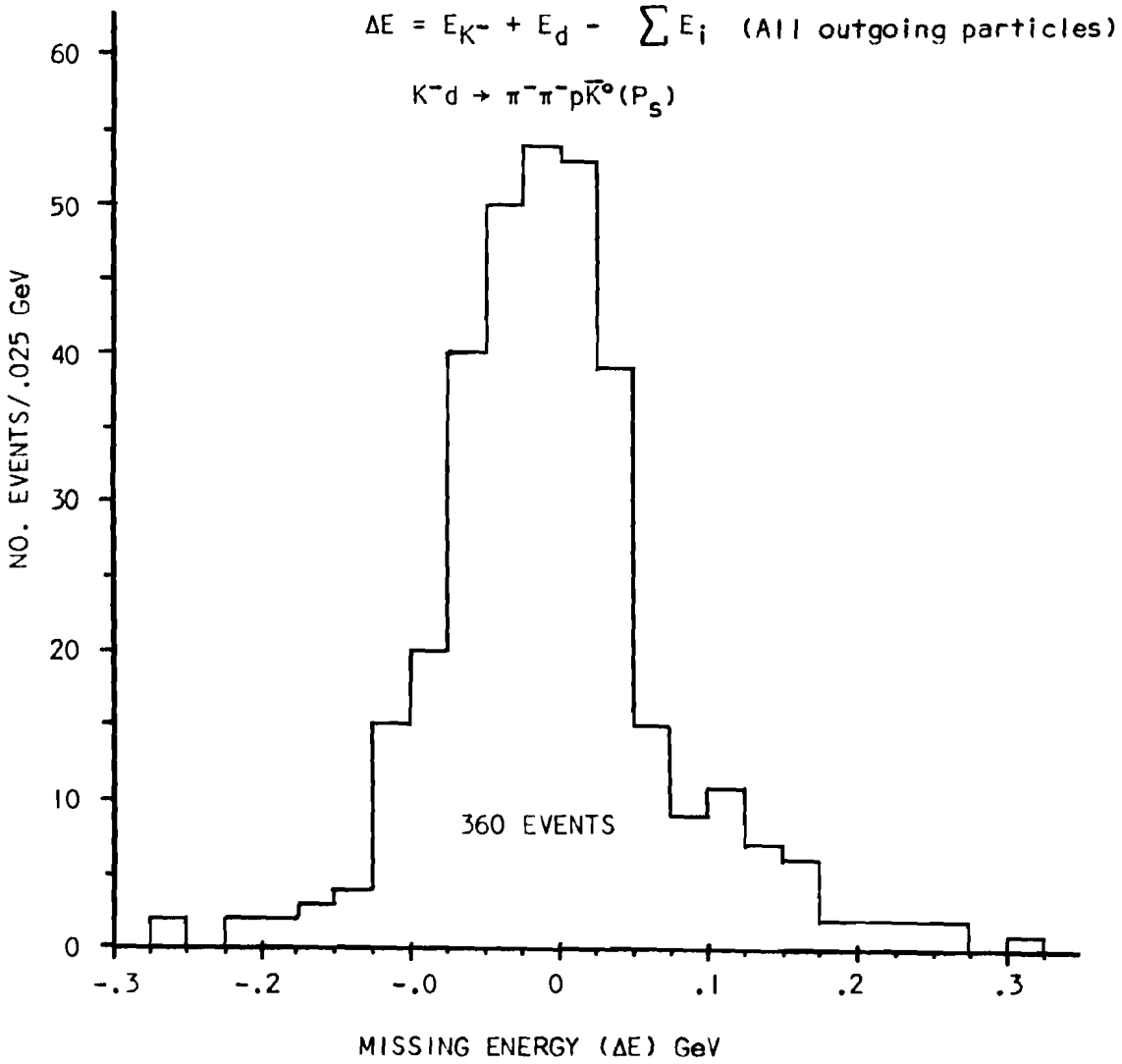
$\Delta E = E_{K^-} + E_d - \sum E_i$ (All outgoing particles)
$K^-d \rightarrow \pi^-\pi^-p\bar{K}^0(P_s)$
NO. EVENTS/.025 GeV
60
50
40
30
20
10
0
360 EVENTS
-.3
-.2
-.0
0
.1
.2
.3
MISSING ENERGY (ΔE) GeV

m is the proton mass.

The value of T_{P_s} is much smaller than the other errors in the calculation of ΔE and can have only a negligible effect on the results.

D. Cross-Section Per Event

We determined the cross-sections for reactions II-5, II-6, and II-7 and the cross-sections for producing various resonances by means of these reactions. The results are given in Table 4 of Chapter VII. We chose a method that minimized the amount of critical bookkeeping and also minimized the amount of double scanning performed by our best workers. This method did not increase the errors of our results and contained an important check. We first determined the sensitivity, i.e. number of events per μbarn, for two rolls of about 1,200 frames each. This was done by two independent methods that gave good agreement and the average of these was used. The first method used an interaction count and counter total cross-section measurements. The second method used a beam track count. We then used the number of $\bar{K}^o$ and Λ^o events with our main vertex topology that were in these two rolls, and the number in our total sample to determine that the reciprocal of the sensitivity for our total sample of events is (0.220 ± 0.033) μbarns/event. This number, the fact that (34.4 ± .2) per cent of the $\bar{K}^o$ mesons decay by $\pi^+\pi^-$ mode,[10] and small corrections described at the end of this section were used to determine the cross-sections.

The two rolls used for the cross-section calculations were scanned twice with particular care by our most competent scanners so that each event could be accounted for. The efficiency for the combined scans was better than 99 per cent. All but 3 per cent of these events were

reconstructed by HGEOM and were consequently classed as a $\overline{K}^{\circ}$ event, a Λ° event, or an event without a vee fit. The 3 per cent correction was made for these events lost in reconstruction by assuming that they were similar to the reconstructed ones.

In making the sensitivity determination by using the interaction count, we chose to use only those interactions with an even number of outgoing prongs. This eliminated the possibility of classifying K^- decays as interactions. It also removed the necessity of correcting for the K^-n interactions with small momentum transfer to an outgoing K^-, only one outgoing particle, and an invisible proton spectator. An event like this could be due to either an elastic or inelastic interaction and would be missed by the scanners.

The sensitivity for these two cross-section rolls is given by

$$S_{c,int} = \frac{N_{ep}}{\sigma_{ep}}, \qquad (11\text{-}10)$$

where N_{ep} = 4,575 is the total number of even-pronged events determined from a count made every fifth frame. The quantity σ_{ep} = 30.8 mbarns is the effective cross-section for producing events with an even number of visible prongs and is given by

$$\sigma_{ep} = \sigma_T(K^-P) - \Delta + \sigma_T(K^-n)fH. \qquad (11\text{-}11)$$

The quantity $\sigma_T(K^-P)$ = 24.8 mbarns is the total K^-P cross-section and $\sigma_T(K^-n)$ = 21.1 mbarns is the total K^-n cross-section. We determined the total cross-sections for K^-d and K^-P and thus also K^-n at our beam momentum by interpolation from results of counter experiments.[11] A linear interpolation was found to be adequate since the cross-sections are

slowly varying with energy. The small term Δ = 0.3 mbarns is the cross-section for those K^-P elastic scatterings with the absolute value of four-momentum transferred squared less than 0.010 GeV^2/c^4.[12,13] This takes into account the fact that protons with a range less than about 0.3 cm are missed. The quantity f = .325 is the fraction of K^-n events that have visibly spectators,[9] and H = .918 is a correction for the probability that one nucleon in the deuteron will hide behind the other.[14] We found that $S_{c,int}$ = 0.149 events/μbarn.

The sensitivity for the two cross-section rolls as determined by the beam track count is given by

$$S_{c,trk} = n_t \bar{X} N_{trk} (1 - \mu), \qquad (11\text{-}12)$$

where $\bar{X}$ = 128 cm is the length of the fiducial volume corrected for beam track interactions, $N_{trk} = 3.22 \times 10^4$ is the number of beam tracks, μ is the fraction of beam tracks that are muons and was assumed to be .05, and the quantity n_t is the number of target neutrons per unit volume. It is given by

$$n_t = \frac{\rho N_o}{A} \qquad (11\text{-}13)$$

where ρ = .139 gm/cm^3 is the liquid deuterium density,[15] $N_o = 6.024 \times 10^{23}$ atoms/gm-atom is Avogadro's number, and A = 2.02 is the atomic weight of deuterium. We found that $S_{c,trk}$ = 0.162 events/μbarn.

The fact that our two methods differ by only 8 per cent tends to substantiate both of them. We averaged the results of these two methods. This gave S_c = 0.155 events/μbarn.

The inverse sensitivity for the total sample of events is given by

$$S^{-1} = S_c^{-1} \left(\frac{n_v}{N_v}\right), \qquad (11\text{-}14)$$

where N_v = 5991 is the number of $\bar{K}^o$ and Λ^o events with our main vertex topology in the total sample of events. The quantity n_v = 204 is that quantity for the two cross-section rolls and contains the 3 per cent correction for those events lost in geometrical reconstruction. Our result is

$$S^{-1} = (0.220 \pm 0.033)\ \mu\text{barns/event}$$

where we have taken the error to be 15 per cent in order to be conservative.

The magnitudes of additional corrections are listed in Table I.

TABLE I

CROSS-SECTION CORRECTIONS

LOSSES	REACTION		
	11-5	11-6	11-7
K^o decays classed as Λ^o decays	4.8%	4.8%	4.8%
Vees lost near main vertex	6.1%	7.4%	5.9%
Vees lost out end of B.C.	2.5%	2.5%	2.5%
Main vertex probability cut	5.0%	5.0%	7.5%
Vee vertex probability cut	1.0%	1.0%	1.0%
Spectator momentum cut	5.7%	5.7%	5.7%
Nucleon hiding in deuteron	8.9%	8.9%	8.9%

These are for losses due to $\bar{K}^{o}$ decays classed as Λ^{o} decays, vees lost near the main vertex, vees lost through the end of the bubble chamber, and events lost due to the main vertex and vee vertex probability cuts imposed. Also, there is a correction for the spectator momentum cut and for nucleon hiding in the deuteron.

CHAPTER III

SEARCH FOR BIASES AND DETERMINATION OF SMALL CORRECTIONS

We have searched for biases in our data and have not found any of significant magnitude. In the course of this search we have determined small corrections.

A. Missing Mass

In kinematic fitting, the kinematic variables are required to satisfy four constraint equations. Three of these equations are for the conservation of the x-, y-, and z-components of momentum while the fourth is the energy conservation equation. When a missing neutral particle is hypothesized, the three components of its momentum are unknown and thus, there is only one constraint. Fits of this type are called one-constraint (1-C) fits. Fits without the supposition of a missing neutral particle are referred to as four-constraint (4-C) fits.

In an experiment where kinematic fits requiring only one constraint (1-C) are analyzed, it is usually necessary to show that there exist signals in the missing mass spectra corresponding to the hypothesized missing neutral particles. If the missing mass signals are observed strongly above the backgrounds, the probabilities of the 1-C mass hypotheses being correct are large.

Figure 4 shows the distribution in the square of the missing mass $(MM)^2$ where the positive track ionization is consistent with its

Figure 4.--Distribution of square of missing mass for $K^-d \rightarrow P_s\pi^-\pi^-p\overline{K}^0$(MM).

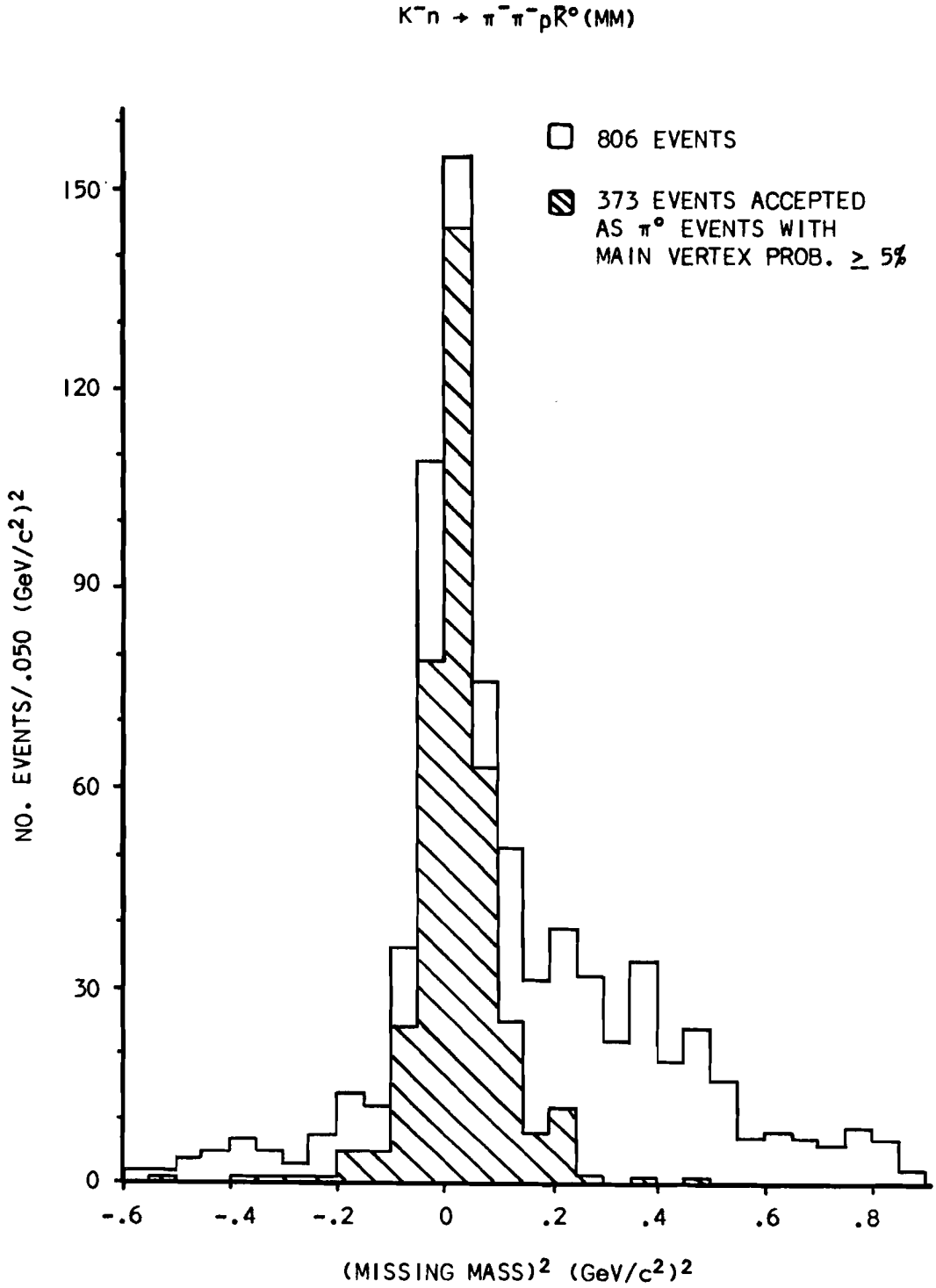
K⁻n → π⁻π⁻pR°(MM)
806 EVENTS
373 EVENTS ACCEPTED AS π° EVENTS WITH MAIN VERTEX PROB. ≥ 5%
NO. EVENTS/.050 (GeV/c²)²
150
120
90
60
30
0
-.6
-.4
-.2
0
.2
.4
.6
.8
(MISSING MASS)² (GeV/c²)²

being a proton and the event is not consistent with the 4-C interpretation.

$$(MM)^2 = (\Delta E)^2 - (\Delta P)^2, \qquad (III\text{-}1)$$

where ΔE is the missing energy and

ΔP is the missing momentum.

The distribution is characterized by a symmetric peak centered near .02 $(GeV/c^2)^2$ with a width of .150 $(GeV/c^2)^2$. This peak corresponds to a missing pion. The shaded area corresponds to those events which were accepted as π° events. They were required to have a χ^2 probability $\geq$ 5% and a spectator momentum $\leq$ .275 GeV/c. See Sections B and C for a discussion of these requirements. The high mass tail is due to events with more than one π°.

Figure 5(a) is the distribution in the square of the missing mass where the ionization of the positive track is consistent with its being a pion. The peak is near .88 $(Gev/c^2)^2$ and has a width of about .25 $(GeV/c^2)^2$. It corresponds to a missing neutron. The shaded area contains those events accepted as neutron events for the purpose of analysis. These events have a χ^2 probability $\geq$ 7.5% and have spectator proton momenta $\leq$ .275 GeV/c. These cuts on probability and momentum are discussed in Sections B and C of this chapter. In Figure 5(b) we show the same plot with those events which have an unambiguous fit to the reaction $K^-d \rightarrow P_s\ p\ \pi^-\pi^-\ K^{-\circ}\pi^\circ$. We see that the level of background for missing masses higher than the neutron mass due to this π° reaction is about four times smaller than for missing masses less than the neutron mass. Also, events with a neutron plus one or more π° mesons in the final state will contribute events to the high mass side of the peak,

Figure 5.--(a) Distribution of square of missing mass for $K^- d \rightarrow P_s \pi^- \pi^- \pi^+ \overline{K}^0$(MM). (b) Same distribution with events having unambiguous fits to reaction II-6 shaded.

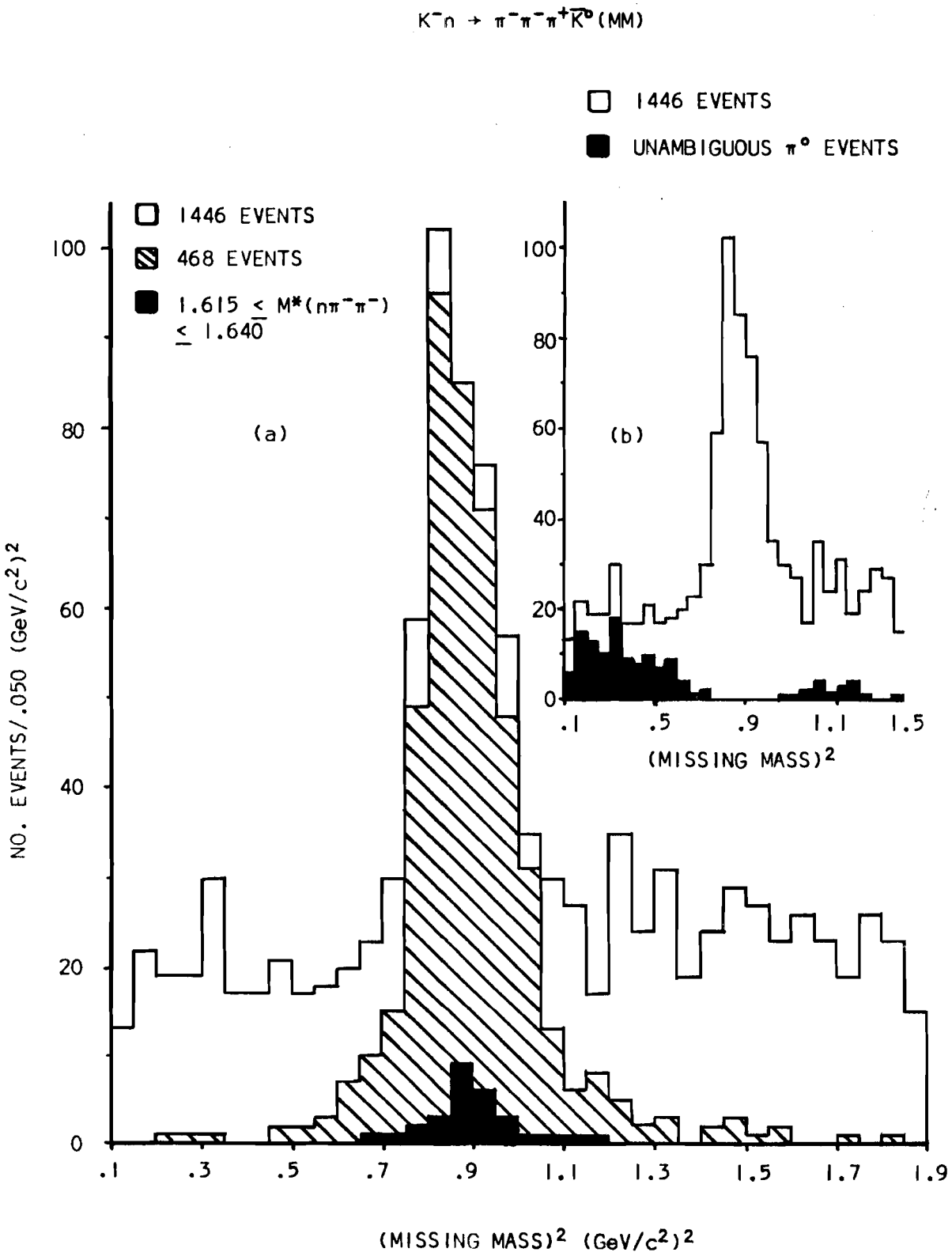
K⁻n → π⁻π⁻π⁺K̄⁰(MM)
1446 EVENTS
UNAMBIGUOUS π° EVENTS
1446 EVENTS
468 EVENTS
1.615 ≤ M*(nπ⁻π⁻) ≤ 1.640
(a)
(b)
NO. EVENTS/.050 (GeV/c²)²
(MISSING MASS)² (GeV/c²)²
(MISSING MASS)²
0
20
40
60
80
100
.1
.3
.5
.7
.9
1.1
1.3
1.5
1.7
1.9

but only a smaller number can appear, due to measuring error, on the low side of the peak. Although the level of total background is about the same on both sides of the peak, the sources of this background are different and they probably make smaller contributions under the peak than in the tails.

In order to test the quality of the separation of our events from background, we define a figure of merit F by

$$F = \frac{(MM)^2 - (M_p)^2}{\Delta(MM^2)}, \qquad \text{(III-2)}$$

where MM is the missing mass computed from the track measurement,

$\Delta(MM^2)$ is the error in this missing mass squared, and

M_p is the known mass of the neutral particle.

If there were no background, F would be normally distributed about zero with standard deviation equal to 1.[16] The presence of an appreciable background would cause the tails of the distribution to contain too many events. In Figure 6(a), F is plotted for those events chosen as missing neutron events. Figure 6(b) shows F for the π^0 hypothesis. The curve in each graph is a Gaussian normalized to the total number of events. The consistency of the histograms with the curves indicate that the correct mass assignments were made in each case with little contamination

B. Spectator Proton

We were interested in events where the incident K^- interacts with the neutron in the deuteron nucleus. The usual assumption is that since the binding energy of the deuteron nucleus is small, relative to the energy of the projectile, the proton does not enter directly into the

Figure 6.--The distribution in the quantity $F = \frac{(MM)^2 - (M_p)^2}{\Delta(MM^2)}$ for reactions (a) II-7 and (b) II-6.

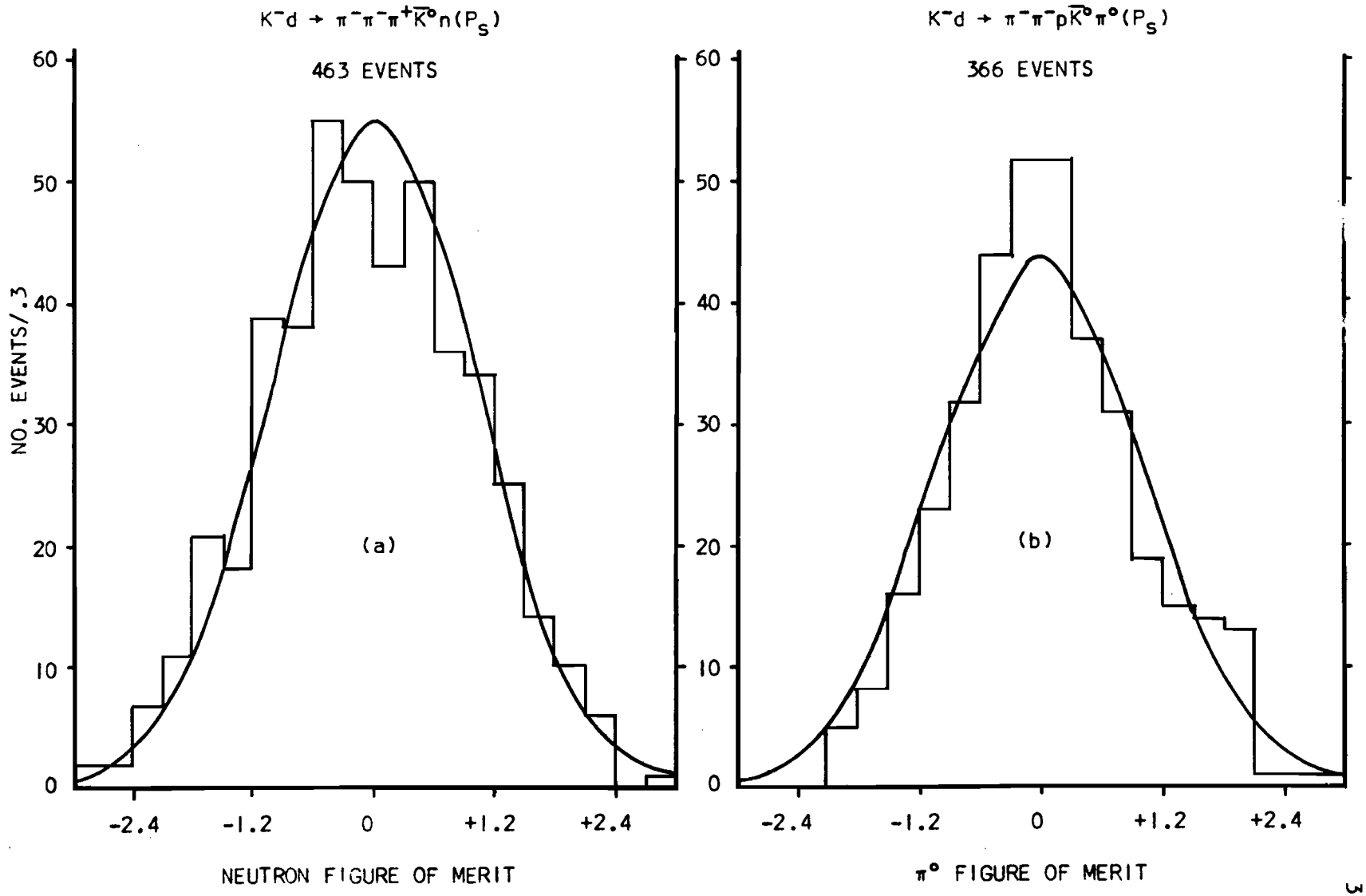
$K^-d \to \pi^-\pi^-\pi^+\overline{K}^0 n(P_s)$
463 EVENTS
(a)
NO. EVENTS/.3
NEUTRON FIGURE OF MERIT
$K^-d \to \pi^-\pi^- p\overline{K}^0\pi^0(P_s)$
366 EVENTS
(b)
π^0 FIGURE OF MERIT
0
10
20
30
40
50
60
-2.4
-1.2
0
+1.2
+2.4

interaction.[17] The proton is thus considered a "spectator" in the interaction. If this assumption is valid, the momentum distribution of the freed proton should approximate the distribution determined by the wave function of the deuteron.

To insure that we were working with reasonable K^- neutron interactions, we compared our observed "spectator" proton momentum distribution with the distribution predicted by the radial Hulthén potential[17] (Figure 7). Figure 7 contains all events which have a fitted $\bar{K}^0$ and a measured spectator. The curve in Figure 7 is the Hulthén prediction normalized to the number of events with measured spectator momenta between .120 and .160 GeV/c. The curve is seen to adequately describe the data for proton momenta above .100 GeV/c and below about .275 GeV/c. The protons with momenta below .100 GeV/c are generally too short to be seen in the bubble chamber and are consequently not measured. For these events where the spectator is too slow to be identified, the fitting program (HKINE) introduces a "dummy" track with x-, y-, and z-components of momenta equal to (0 ± 30), (0 ± 30), and (0 ± 41) MeV/c, respectively. The program then tries to fit the event just as if the track were actually measured. About 65 per cent of the final fitted events are events with dummied protons. The number of events in Figure 7 with measured spectator protons $\leq$ .275 GeV/c is 29.8 per cent of the total sample. Considering only events fitting reactions II-5, II-6, and II-7, the percentages are 28.6%, 23.2%, and 27.7% respectively. A comparison of effective mass and production cosine distributions for reactions II-5, II-6, and II-7 revealed no statistically significant difference between events where the spectator proton was measured and those where the proton was "dummied".

Figure 7.--Measured spectator proton momentum distribution.

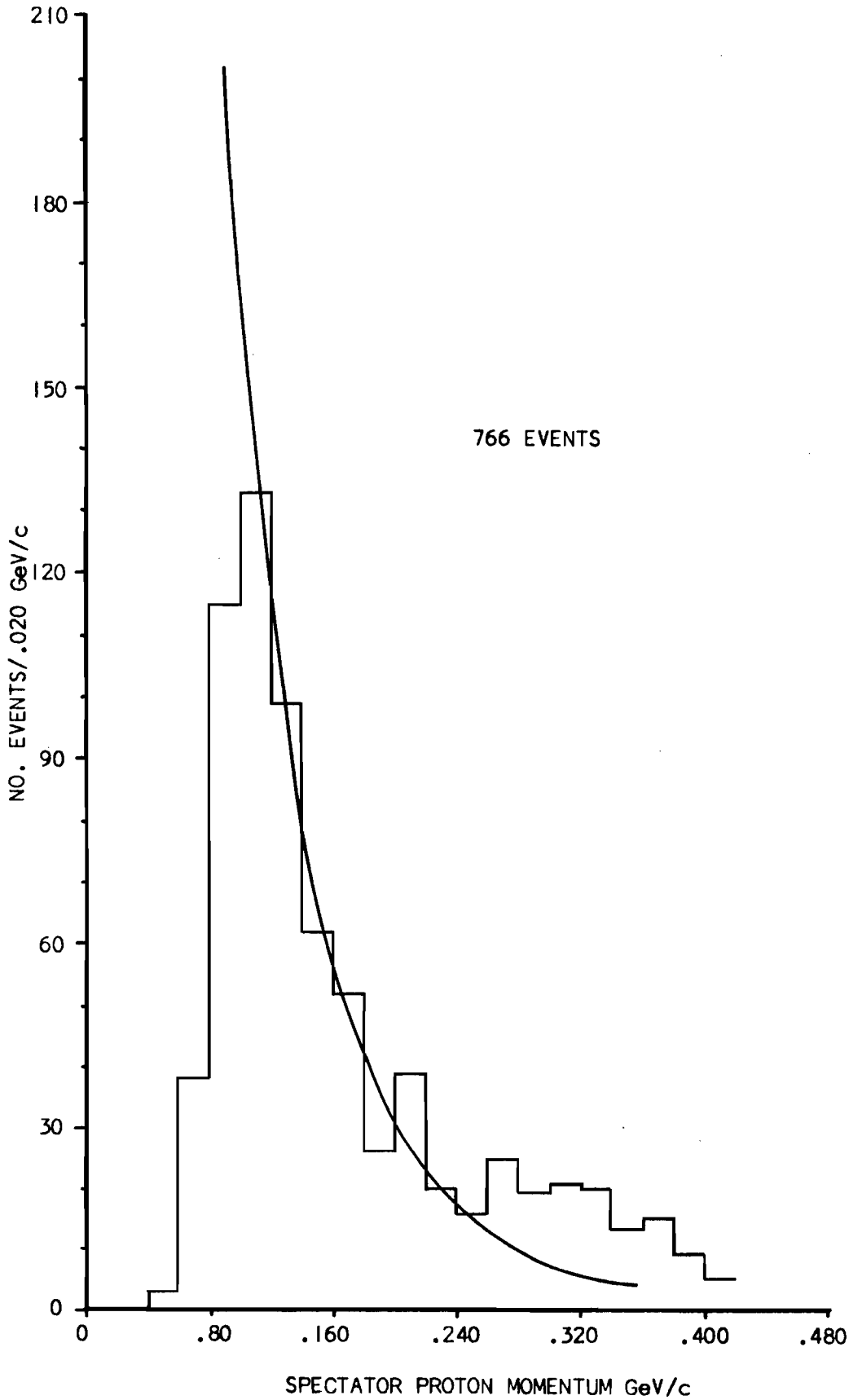
210
180
150
120
90
60
30
0
NO. EVENTS/.020 GeV/c
766 EVENTS
0
.80
.160
.240
.320
.400
.480
SPECTATOR PROTON MOMENTUM GeV/c

Figure 7 shows an excess of events above the curve for momenta > .275 GeV/c. Presumably, these excess events are those in which the proton had been involved in rescattering or was directly involved in the interaction, and thus is not a true spectator. For this reason, we have chosen to make use of only those events with spectator proton momentum $\leq$ .275 GeV/c when studying the physics of our reactions. In this cut, we have thrown away about 1.5 per cent of the true spectator events, as determined from the Hulthén curve.

Reactions II-5 and II-6 do not present a problem with respect to spectator proton identification. The problem would have been encountered if both protons in the final state had low momenta. We called the proton with the lower momentum the spectator. After the momentum cut of $\leq$ .275 GeV/c was imposed on these lower momentum protons, we examined the momentum distribution of the higher momentum protons for reactions II-5 and II-6 (see Figure 8). For reaction II-5 we found that only about 3 per cent of the recoil protons had momenta less than the maximum allowed spectator momentum of .275 GeV/c. For reaction II-6 they were only about 1 per cent of the sample. We conclude that the problem of misidentified spectators was an insignificant effect in reactions II-5 and II-6.

Reaction II-7 does not present a problem due to contamination from K^- proton interactions having a slow proton and a spectator neutron. An investigation of the neutron momentum distribution in Figure 8(c) revealed that about 3 per cent of the neutron events had neutron momenta less than .275 GeV/c. Again we conclude that this effect can be ignored in the analysis of this reaction.

Figure 8.--Momentum distributions for (a) proton produced in reaction II-5, (b) proton produced in reaction II-6, and (c) neutron from reaction II-7.

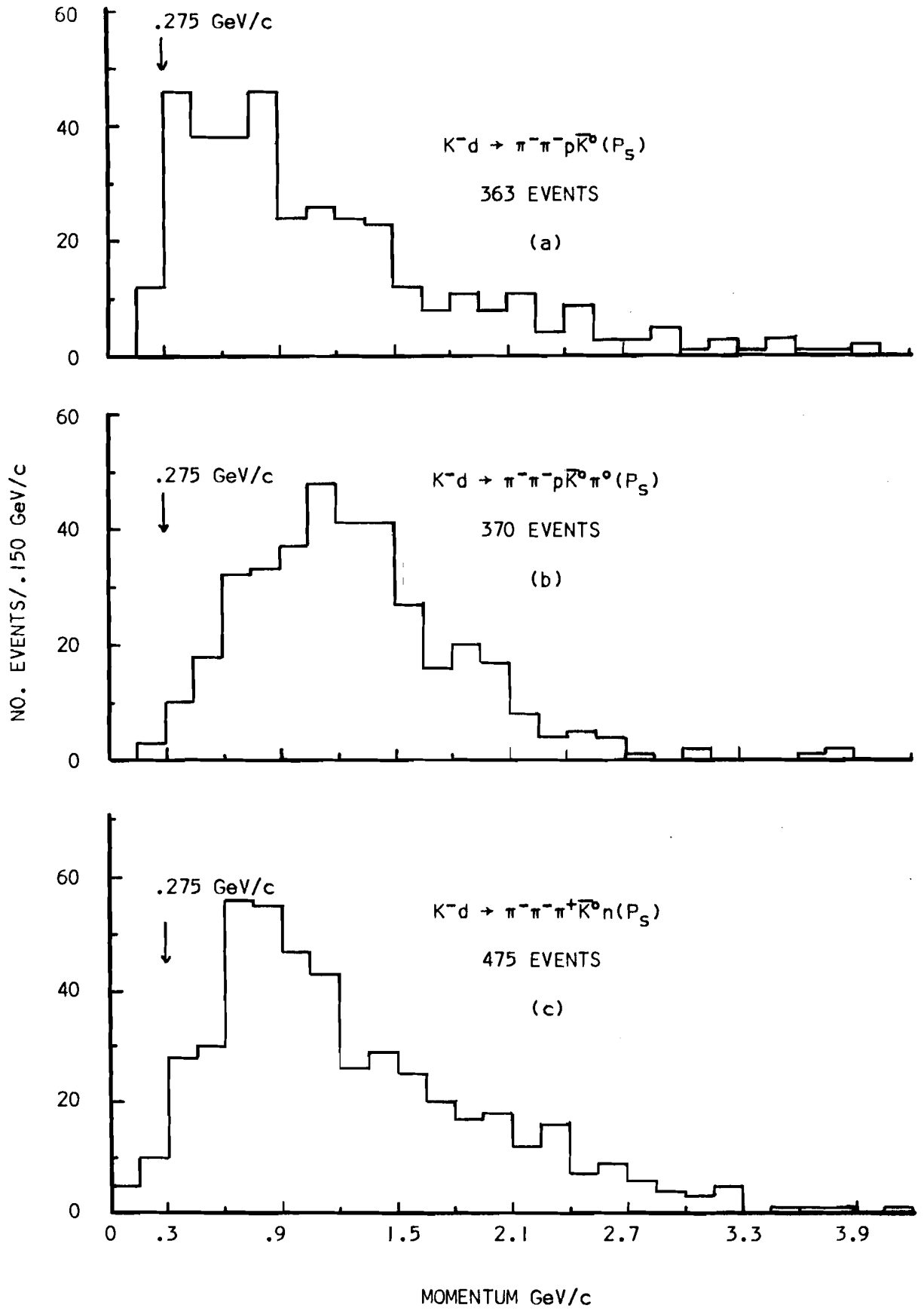
.275 GeV/c
$K^-d \to \pi^-\pi^-p\overline{K}^0(P_s)$
363 EVENTS
(a)
.275 GeV/c
$K^-d \to \pi^-\pi^-p\overline{K}^0\pi^0(P_s)$
370 EVENTS
(b)
.275 GeV/c
$K^-d \to \pi^-\pi^-\pi^+\overline{K}^0n(P_s)$
475 EVENTS
(c)
NO. EVENTS/.150 GeV/c
0
20
40
60
0
.3
.9
1.5
2.1
2.7
3.3
3.9
MOMENTUM GeV/c

C. Chi-Square Probabilities

The χ^2-probability distribution for the $\bar{K}^o$ vee fit is shown in Figure 9(a). The main vertex probability distributions for reactions II-5, II-6, and II-7 are shown in Figures 9(b), 9(c), and 9(d), respectively. The value of χ^2 for each event is calculated in HKINE, along with its associated probability. Events with $\bar{K}^o$ probability less than 1 per cent have been excluded from Figure 9. If the supposed hypothesis is the appropriate one and the assigned errors are reasonable, then the χ^2 probability distribution should be flat. This is a direct consequence of the definition of probability.

We draw the reader's attention to the spike at low probabilities in Figures 9(c) and 9(d). Perhaps there is also such a spike in Figure 9(b). This structure is presumably due to wrong mass assignments. In order to remove this contamination, we decided to discard those events with probabilities less than some minimum value and then correct the cross-sections for the good events that were thrown away. The minimum acceptable probabilities chosen were:

5% for reaction II-5,

5% for reaction II-6, and

7 1/2% for reaction II-7.

The probability distributions for the $\bar{K}^o$ vee fit and the main vertex fit for the 4-C channel show a slight skewing toward higher probabilities. The presumption is that this effect is due to input errors to HGEOM being slightly too large, and has no significant effect on the study of our reactions. The straight lines in Figures 9(a), (b), (c), and (d) represent the average bin height. The average was

Figure 9.--Chi-square probability distributions for (a) $\overline{K}^{\circ}$ vee and for the production vertices of (b) reaction II-5, (c) reaction II-6, and (d) reaction II-7.

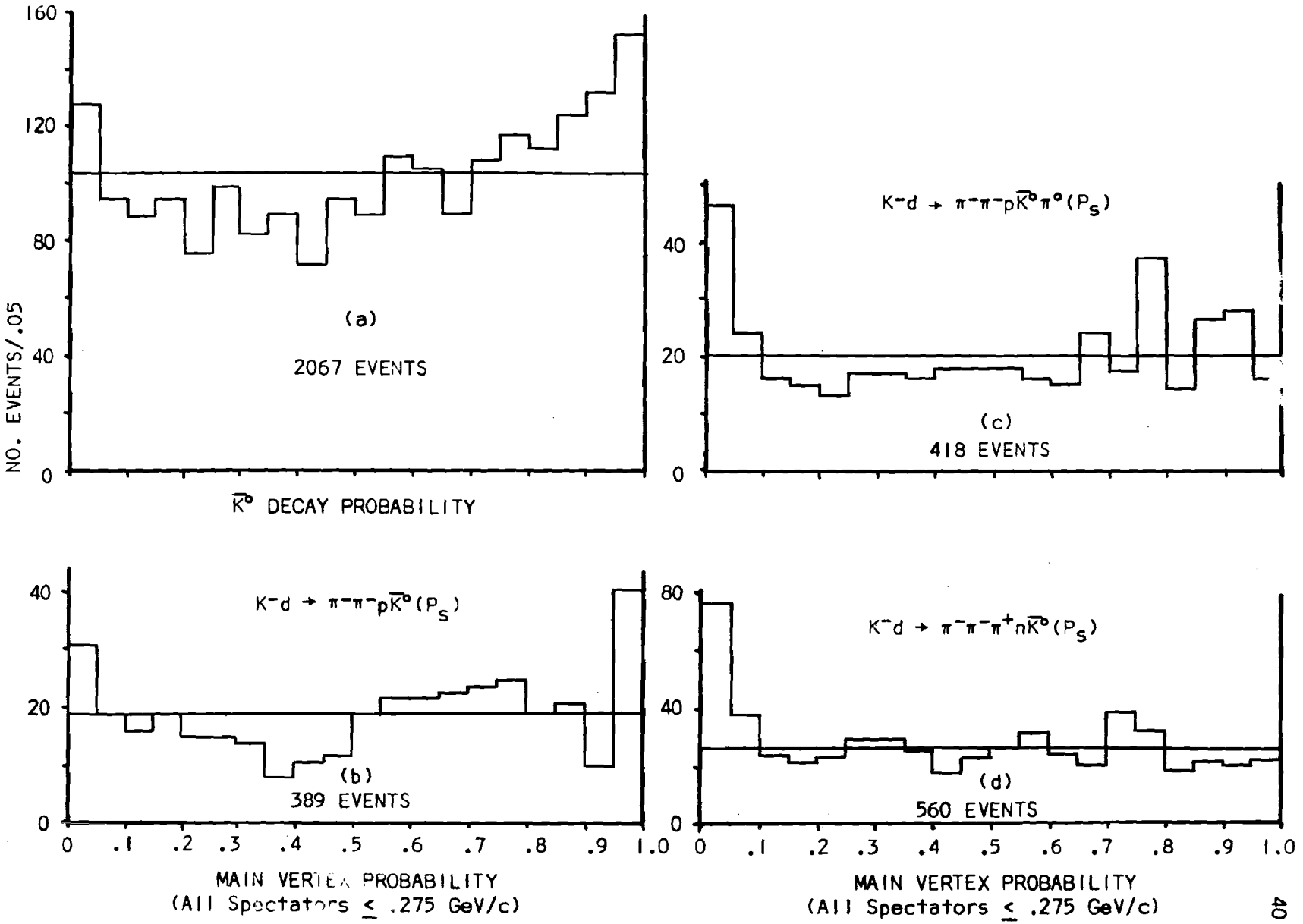
NO. EVENTS/.05
160
120
80
40
0
(a)
2067 EVENTS
$\bar{K}^0$ DECAY PROBABILITY
$K^-d \to \pi^-\pi^-p\bar{K}^0\pi^0(P_s)$
(c)
418 EVENTS
$K^-d \to \pi^-\pi^-p\bar{K}^0(P_s)$
(b)
389 EVENTS
$K^-d \to \pi^-\pi^-\pi^+n\bar{K}^0(P_s)$
(d)
560 EVENTS
0 .1 .2 .3 .4 .5 .6 .7 .8 .9 1.0
MAIN VERTEX PROBABILITY
(All Spectators ≤ .275 GeV/c)

calculated using those events in the region [.1 - 1.0].

D. Stretch Variable Distributions

The normalized stretch function[7] is defined as

$$S_\mu = \frac{\mu_f - \mu_m}{\left[(\Delta\mu_m)^2 - (\Delta\mu_f)^2\right]^{\frac{1}{2}}} , \qquad \text{(III-3)}$$

where μ_f is the value of the fitted track quantity of interest ($1/p$, ϕ, or $\tan\lambda$),

μ_m is the value of the measured track quantity of interest, and

$\Delta\mu$ is the error in the corresponding track quantity.

If there exist no systematic biases in the fitting of the events the distribution of the normalized stretch function should be normally distributed with mean value zero and standard deviation one. A skewed distribution would indicate the presence of a systematic bias. These variables are calculated in HKINE. All of the distributions were observed to be consistent with the expected distribution. Figure 10 shows the distributions for the two π^- tracks in reaction 11-5 as a representative sample. The curves in Figure 10 are Gaussians centered at 0 normalized to the total number of events.

E. Magnetic Field

As a check on the value of the magnetic field used in the geometry program, we calculated the mass of the decaying $\overline{K}^o$ from the measured momenta of the decay products. The value of the momenta are directly related to the magnetic field. Figure 11 shows the distribution in the mass of the $\overline{K}^o$ as calculated from the measured track

Figure 10.--Typical stretch variable distributions. Distributions for π^- from reaction 11-5; (a) stretch ϕ, (b) stretch tan λ, and (c) stretch $1/p$.

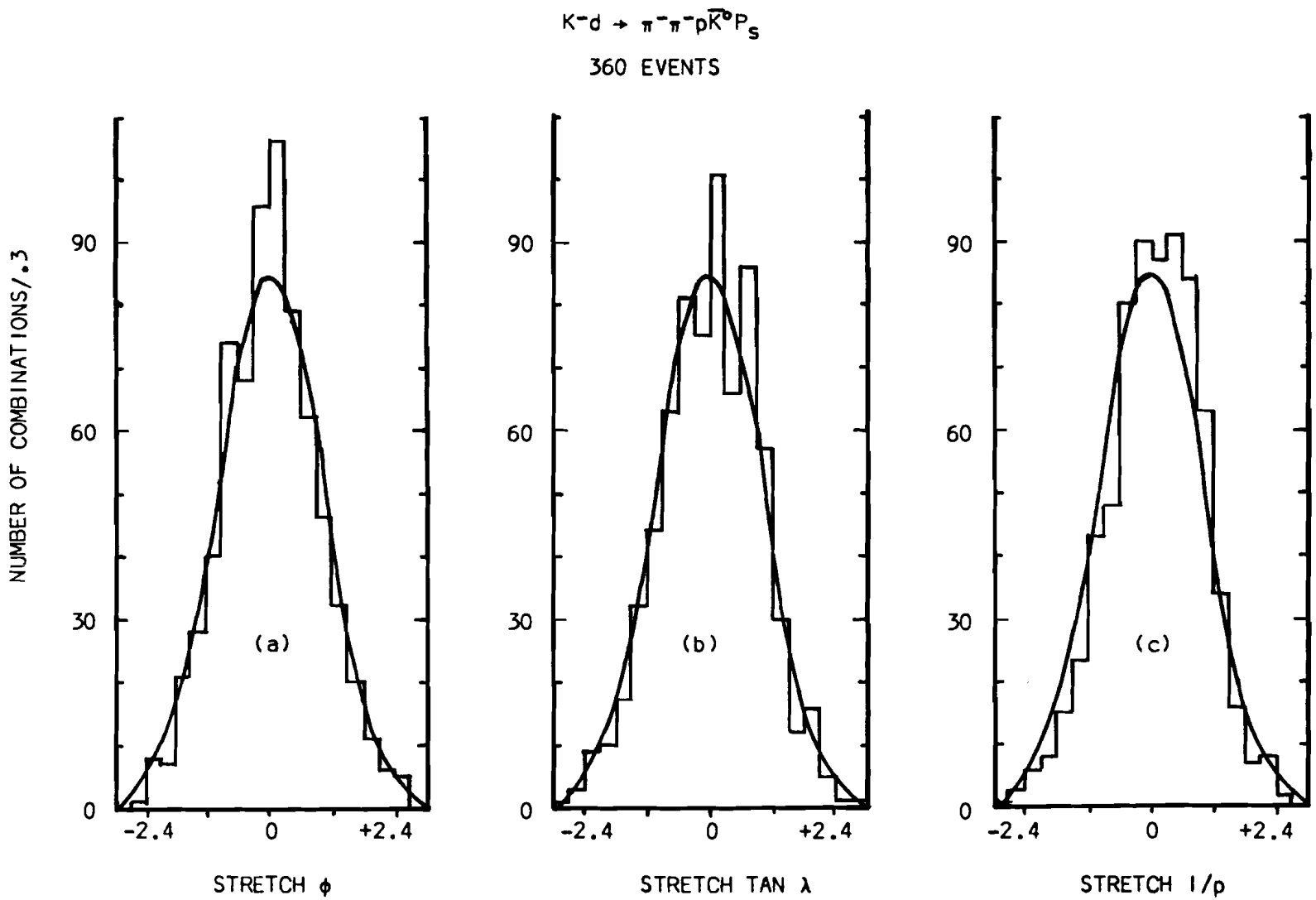
K⁻d → π⁻π⁻pK̄⁰P_s
360 EVENTS
NUMBER OF COMBINATIONS/.3
90
60
30
0
-2.4
0
+2.4
(a)
(b)
(c)
STRETCH φ
STRETCH TAN λ
STRETCH 1/p

Figure 11.--Distribution of measured $\pi^+\pi^-$ invariant mass for $\overline{K}^0 \rightarrow \pi^+\pi^-$.

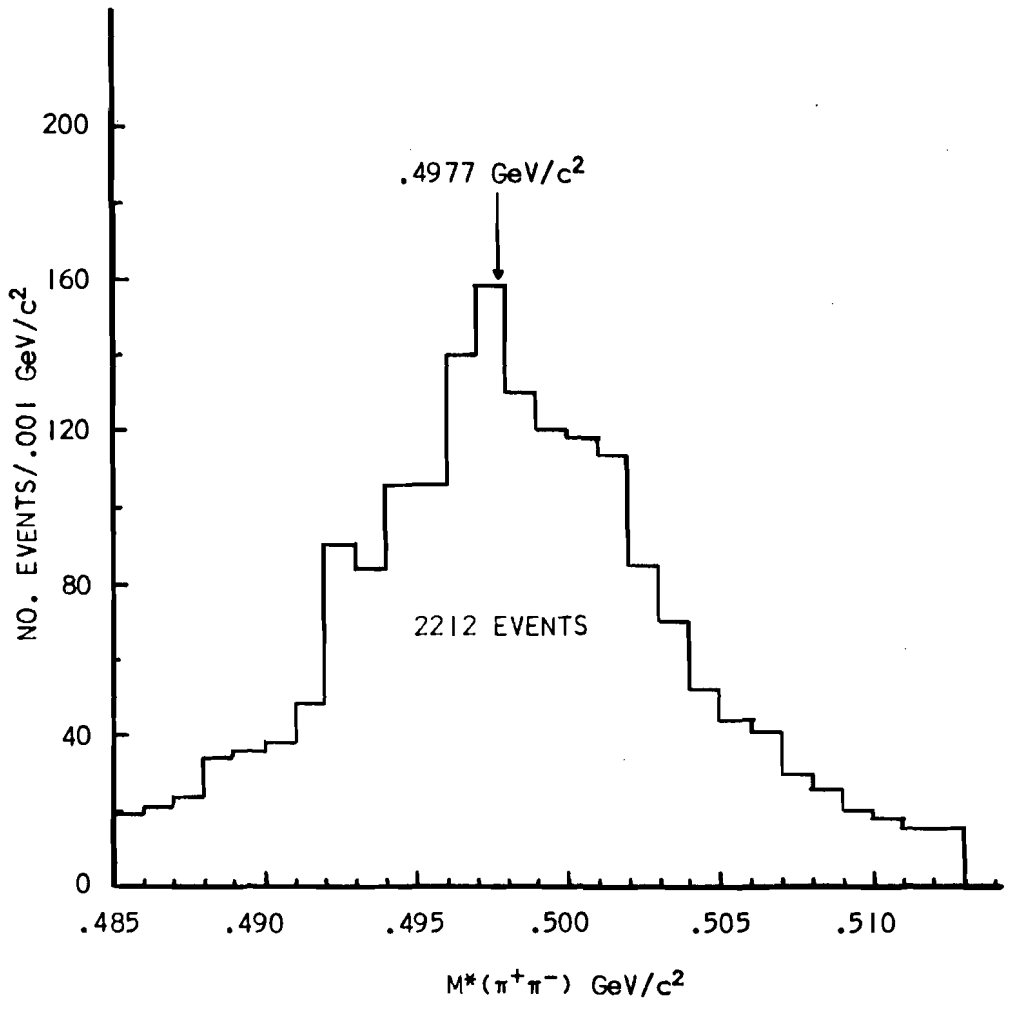
.4977 GeV/c²
2212 EVENTS
NO. EVENTS/.001 GeV/c²
200
160
120
80
40
0
.485
.490
.495
.500
.505
.510
M*(π⁺π⁻) GeV/c²

quantities. We determined the value for the mass of the $\bar{K}^{\circ}$ to be (497.7 ± .3) MeV/c^2. The accepted value is (497.76 ± 0.16 MeV/c^2). This substantiates the assigned magnetic field.

F. Corrections for Loss of Vees

The neutral decaying particle (vee) was a signature of the events of interest in this experiment. Since one of our objectives was to measure cross-sections, we studied mechanisms contributing to vee losses from our sample.

In selecting $\bar{K}^{\circ}$ fits we decided not to accept any fits that also had a fit to the Λ° decay hypothesis. This was found to be a reasonable criterion, since the region where the $\bar{K}^{\circ}$ and Λ° decays are kinematically indistinguishable is only a small fraction of the K° decay phase space.[18] As an estimator for the number of $\bar{K}^{\circ}$'s lost into the Λ° channel, we included the $\bar{\Lambda}^{\circ}$ vee hypothesis in the fitting program. Since $K^{\circ} \rightarrow \pi^{+}\pi^{-}$ is completely symmetric in the decay products, a real $\bar{K}^{\circ}$ should be fit by $\bar{\Lambda}^{\circ} \rightarrow \bar{P}\pi^{+}$ at the same frequency as it is fit by $\Lambda^{\circ} \rightarrow P\pi^{-}$. Thus by counting the number of $\bar{K}^{\circ}$'s fitting $\bar{\Lambda}^{\circ}$'s we can estimate the number of real $\bar{K}^{\circ}$'s taken as Λ° events. We can eliminate the $\bar{\Lambda}^{\circ}$ fits as valid fits since our beam momentum is too low for $\bar{\Lambda}^{\circ}$ production. Out of 2212 $\bar{K}^{\circ}$ fits 107 also fit to the $\bar{\Lambda}^{\circ}$ hypothesis. We conclude a 4.8 per cent loss of $\bar{K}^{\circ}$'s by this mechanism.

We have found that there were small scanning losses due to vees that decay close to the main interaction vertex. In these events the vee prongs were indistinguishable from the main vertex tracks. This loss can be seen in the distribution of the $\bar{K}^{\circ}$ lifetime [Figure 12(a)]. Figure 12(a) is plotted in units of t/τ, where t is the lifetime of the

Figure 12.--(a) Distribution of lifetime of $\overline{K}^{o}$ in units of t/τ. Distributions of the probability the vee would decay in the distance it traveled for reactions (b) II-7, (c) II-6, and (d) II-5.

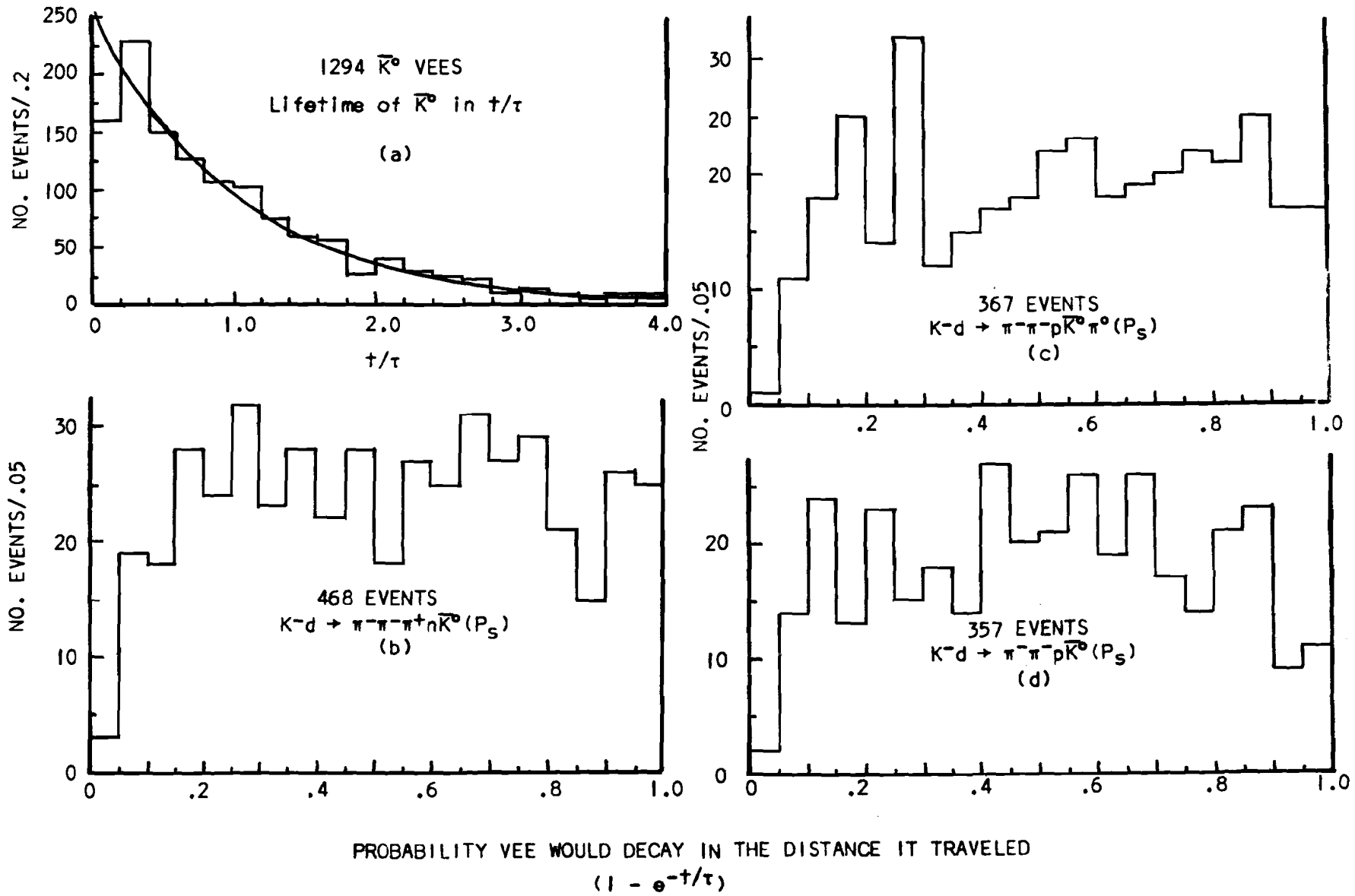
1294 $\overline{K}^0$ VEES
Lifetime of $\overline{K}^0$ in t/τ
(a)
NO. EVENTS/.2
t/τ
468 EVENTS
$K^-d \rightarrow \pi^-\pi^-\pi^+n\overline{K}^0(P_s)$
(b)
NO. EVENTS/.05
367 EVENTS
$K^-d \rightarrow \pi^-\pi^-p\overline{K}^0\pi^0(P_s)$
(c)
NO. EVENTS/.05
357 EVENTS
$K^-d \rightarrow \pi^-\pi^-p\overline{K}^0(P_s)$
(d)
PROBABILITY VEE WOULD DECAY IN THE DISTANCE IT TRAVELED
$(1 - e^{-t/\tau})$

$\bar{K}^o$ in its rest frame and τ is the $\bar{K}^o$ mean life ($\tau = .862 \times 10^{-10}$ sec.). The quantity t is easily calculated from laboratory quantities by using

$$t = \frac{LM}{P} , \qquad \text{(III-4)}$$

where L is the length of the $\bar{K}^o$ flight path, P is the $\bar{K}^o$ laboratory momentum, and M is the mass of the $\bar{K}^o$. The curve in Figure 12(a) is the decay probability density, $e^{-t/\tau}$, normalized to the 1294 $\bar{K}^o$ decays found in about the first half of this experiment.

The quantity $(1 - e^{-t/\tau})$ is the fraction of events having lifetimes less than t. A histogram of the number of events versus this quantity should therefore be flat if there is no bias. We plotted such a histogram for each hypothesis and various $\bar{K}^o$ momentum cuts. We did not find this effect to have a strong momentum dependence. Using the $(1 - e^{-t/\tau})$ histograms with no momentum cuts [Figures 12(b), (c), (d)], we determined the percentage lost for each mass hypothesis. The results were:

6.1% for reaction II-5,

7.4% for reaction II-6, and

5.9% for reaction II-7.

We examined the decay angular distribution of the $\bar{K}^o$ in order to determine if there were any scanning or fitting losses that were a function of this angle. A distribution of the cosine of the $\bar{K}^o$ decay angle should be flat if no preferential losses are present. Figures 13(a), (b), (c) are the distributions of cos θ_D for the reactions II-7, II-6, and II-5, respectively. The quantity θ_D is the angle between the direction of the π^- resulting from $\bar{K}^o$ decay as seen in the $\bar{K}^o$ rest frame and

Figure 13.--Distributions of the cosine of the $\overline{K}^{o}$ decay angle for reactions (a) II-7, (b) II-6, and (c) II-5.

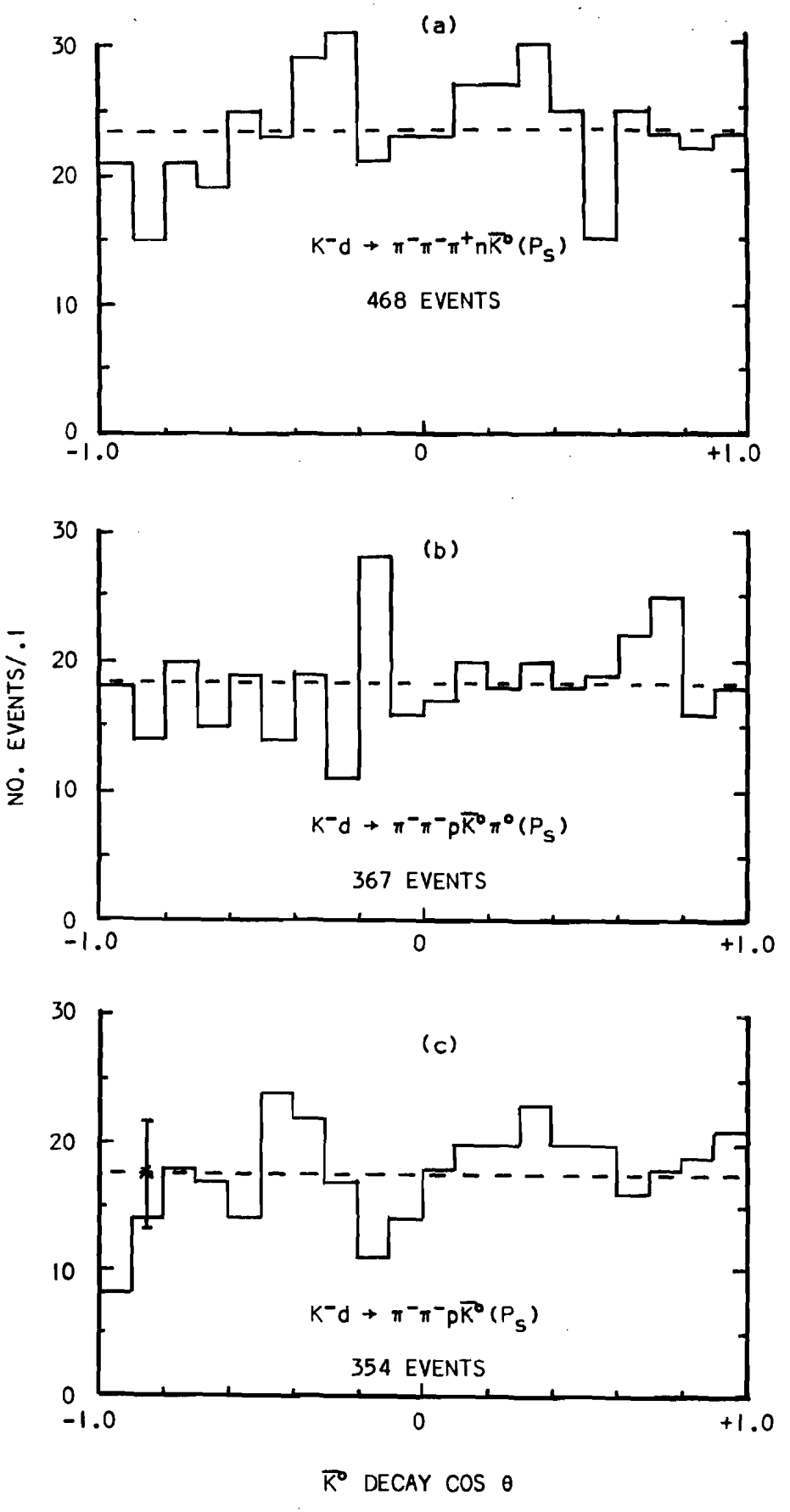
(a)
$K^-d \to \pi^-\pi^-\pi^+n\overline{K}^0(P_s)$
468 EVENTS
(b)
$K^-d \to \pi^-\pi^-p\overline{K}^0\pi^0(P_s)$
367 EVENTS
(c)
$K^-d \to \pi^-\pi^-p\overline{K}^0(P_s)$
354 EVENTS
NO. EVENTS/.1
$\overline{K}^0$ DECAY COS θ
30
20
10
0
-1.0
0
+1.0

the direction of the $\bar{K}^{\circ}$ as seen in the $K^{-}n$ center of mass frame. The distributions are all consistent with being flat, indicating no preferential losses that are a function of the decay angle. The decay angular distributions were also investigated as a function of the $\bar{K}^{\circ}$ momentum. We found no evidence for losses that were dependent upon the $\bar{K}^{\circ}$ momentum.

Vees that live long enough to leave the vee decay fiducial volume before decaying were also lost. For this correction, we calculated the average over the x-coordinates within the interaction region of the probability that the vee would decay within the fiducial volume for each event. We compensated for this loss by weighting each accepted event by the reciprocal of this average probability. This average probability P is a function of the geometry and momentum. It is given by the equation[19]

$$P = 1 - \frac{e^{-\left(\frac{L+F}{\ell \cos\theta}\right)}\left(1 - e^{-L\left(\frac{1}{G} - \frac{1}{\ell\cos\theta}\right)}\right)}{\left(1 - \frac{G}{\ell\cos\theta}\right)\left(1 - e^{-L/G}\right)}, \qquad \text{(III-5)}$$

where $\ell = \frac{P}{m}\tau$ in the K° decay mean free path. The quantity P is the $\bar{K}^{\circ}$ laboratory momentum, m is the $\bar{K}^{\circ}$ mass, and τ is the mean life ($\tau_{K^{\circ}} = 0.862 \times 10^{-10}$ sec.).

G = 532 cm., is the interaction mean free path.

The geometry of Figure 14 is assumed, and it is assumed that the beam particle moves along the x-axis. The quantity x gives the location of the main vertex and the vee flight path makes an angle θ with respect to the x-axis. The quantity L = 157 cm. is the length of the interaction fiducial volume and F = 7.48 cm. is the length of the extra vee decay fiducial volume.

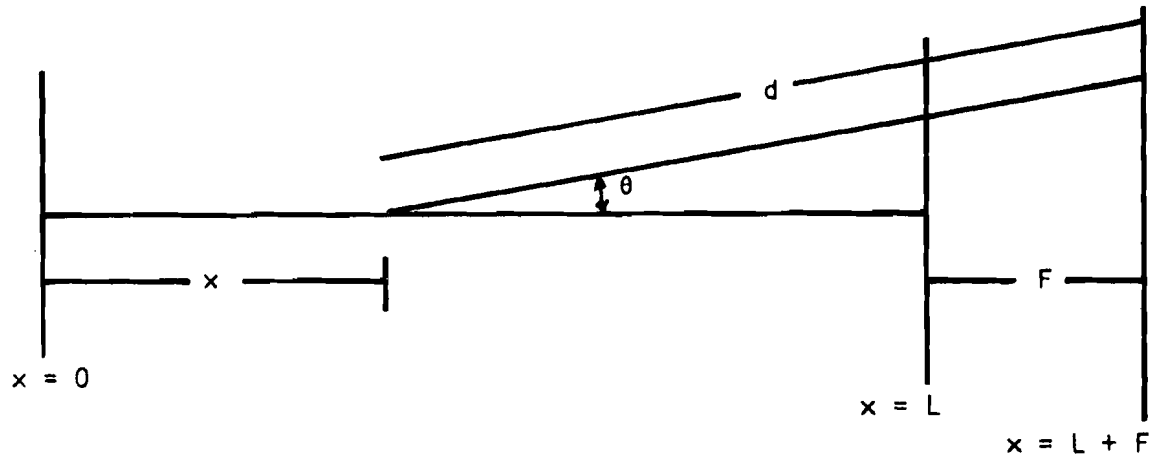

Figure 14.--Sketch of geometry used in vee-loss correction calculations.

The correction for vees lost out of the end of the bubble chamber was found to be essentially hypothesis independent. The correction was about 2.5 per cent.

CHAPTER IV

PHENOMENOLOGICAL CONSIDERATIONS

A. Multiperipheral Models

One of the most striking features of high energy interactions is the general predominance of peripheral collisions. Especially for two-body and quasi-two-body final states, the differential cross-sections have a sharp peak at very low momentum transfer. These and other experimental observations have established the one-particle-exchange peripheral model as a meaningful description of the data, for the low momentum transfer region.

The one-particle-exchange model formulates the full amplitude of a meson-baryon reaction of the type $MB \rightarrow s_1 s_2$ as proportional to the product of two vertex factors.[20] The Feynman diagram describing this process is shown in Figure 15, where the quantities M and B correspond

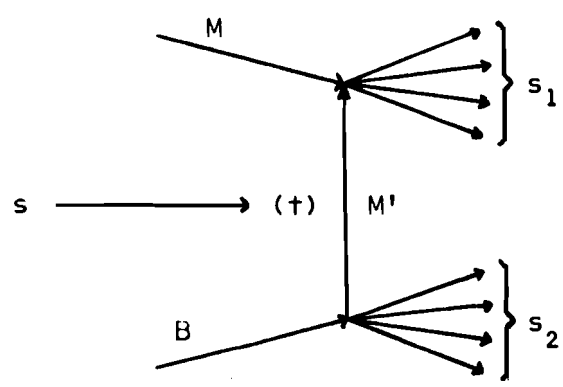

Figure 15.--Feynman diagram describing meson-baryon scattering.

to the meson and baryon lines, respectively. The quantities s_1 and s_2 refer to the subsystems of outgoing particles and also to their squared invariant masses. The quantity M' refers to the exchanged particle. The quantity s in Figure 15 is the squared invariant mass of the meson-baryon system, and t is the square of the momentum transfer between the vertices. One vertex factor describes the amplitude of $MM' \to s_1$ and the other factor describes the amplitude for $\bar{M}'B \to s_2$, where $\bar{M}'$ is the anti-particle of the exchanged particle M'. The amplitude takes the form

$$T(MB \to s_1 s_2) = V_{s_1 MM'} \frac{1}{\mu^2 - t} V_{s_2 \bar{M}'B}, \qquad \text{(IV-1)}$$

where μ is the mass of the exchanged particle, and the V's describe the scattering vertices. The quantity $(\mu^2 - t)^{-1}$ is commonly called the propagator for the exchanged particle. For s (the squared invariant mass of the M + B system) large, the subenergy s_2 can be large also. For s_2 (squared invariant mass of the $\bar{M}'$ + B system) sufficiently large, the $\bar{M}'B$ scattering may logically also be mediated by the exchange of another particle M". Consequently, the $\bar{M}'$ + B reaction can be represented by the one-particle-exchange diagram in Figure 16, where s_1' and s_2'' are

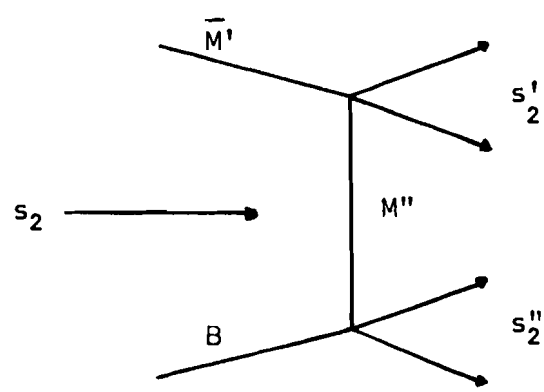

Figure 16.--Feynman diagram describing meson-baryon scattering at lower vertex.

the subsystems of system s_2 and also represent their squared invariant masses.

Noting the full amplitude (IV-1) and considering the $\bar{M}'B$ scattering in the same light as the MB scattering, the second vertex factor of the full amplitude ($V_{s_2\bar{M}'B}$ describing $\bar{M}'B \to s_2$) is now broken into two vertex factors and a propagator for M". The first of these factors is proportional to the amplitude for $M'M'' \to s_2'$, and the second factor is proportional to the $M''B \to s_2''$ amplitude.

The full amplitude can now be represented by the diagram shown in Figure 17.

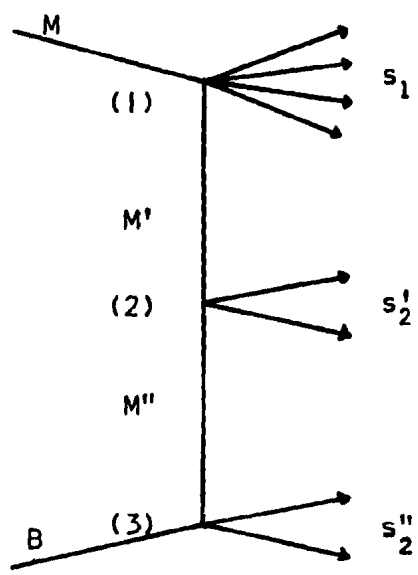

Figure 17.--Diagram representing the full amplitude of a three vertex meson-baryon interaction.

This amplitude is given by a product of three factors proportional to the scattering amplitudes of the three vertices, with the appropriate propagators sandwiched between.

This chain may be continued indefinitely with the exchanged mesons undergoing successive peripheral collisions and emitting particles. In order for the multiperipheral model to be valid, the invariant mass of adjacent sub-systems must be large.[21] Energy conservation implies that as the chain of processes grows the energy available to each pair of sub-systems will become less, and consequently the chain will terminate. At present machine energies the chain terminates rapidly.

Amati, Fubini, and Stanghellini (AFS)[22] were among the first to formulate an amplitude for an nth order multi-peripheral diagram which is factorizable.

For the nth order diagram, shown in Figure 18, the AFS transition

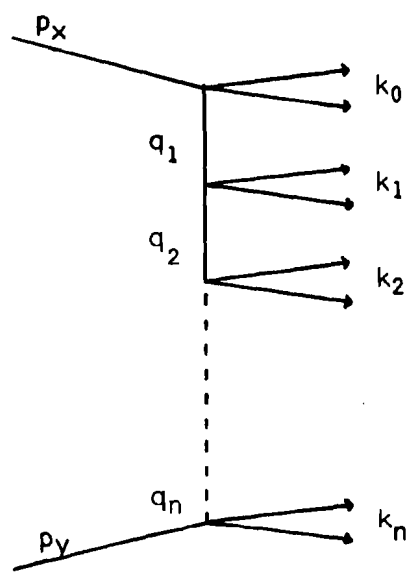

Figure 18.--Typical n^{th} order multiperipheral diagram.

amplitude $T(p_x,p_y,k_i)$ becomes

$$T_{(p_x,p_y,k_1)} = \frac{V_{p_x q_1 k_0} V_{q_1 q_2 k_1} \cdots V_{p_y q_n k_n}}{(\mu^2 - q_1)(\mu^2 - q_2)\cdots(\mu^2 - q_n)} \qquad \text{(IV-2)}$$

where q_i is the momentum transfer between the $(i - 1)^{th}$ and i^{th} vertices, and μ is the mass of the exchanged particle.

In the Reggeized formulation of the multiperipheral diagram the exchanged particles are replaced by the exchange of Regge poles.[23]

The exact form of the multiperipheral amplitude varies from model to model. In this work we have considered two such models. One was formulated by Chan, Loskiewicz, and Allison (CLA).[24] The other is a modification of this CLA model by Plahte and Roberts.[25] These models are multiperipheral in nature with an exponential approximation for the vertices. A short description of these models will follow in the next two sections, and a comparison with the data will be found in Chapter V.

I. The CLA model

The Reggeized multiperipheral model of Chan, Loskiewicz, and Allison (CLA) has been qualitatively successful in describing individual particle behavior in multi-particle final states.[26,27] They have formulated an amplitude incorporating the Reggeized multiperipheral idea. Their amplitude is factorizable. For an nth order multiperipheral diagram of the type $A + B \rightarrow 1 + 2 + 3 + \cdots + n$ (Figure 19) the amplitude A_J is given by

$$A_J = \prod_{i=1}^{n-1} A_i(s_i,t_i), \qquad \text{(IV-3)}$$

where A_i is a factor that takes the ith exchange into account and also has contributions from the i and $(i + 1)$ vertices. The variable t_i is

the momentum transfer variable defined by

$$t_i = (p_A - \sum_{r=1}^{i} p_r)^2, \qquad \text{(IV-4)}$$

where p_r is the four-momentum of particle r.

$$s_i = (p_i + p_{i+1})^2 - (m_i + m_{i+1})^2, \qquad \text{(IV-5)}$$

where m_i is the mass of the ith particle and p_i is the four-momentum of particle i.

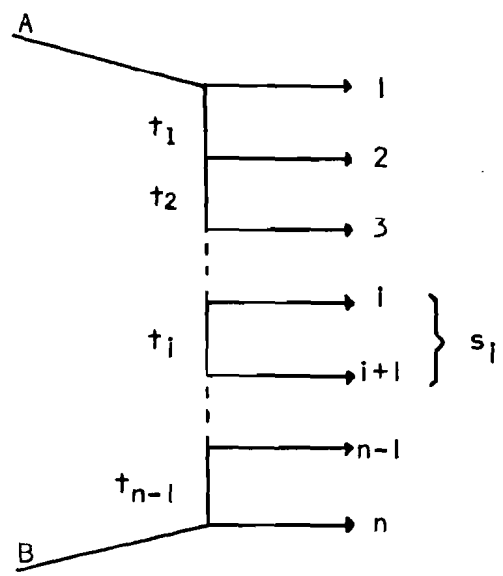

Figure 19.--Typical n^{th} order multiperipheral diagram showing the variables t_i and s_i.

The CLA variable s_i is related to the Mandelstam variable s (the energy squared of the two particle sub-system) but is defined so $s_i \to 0$ as the relative velocity of the two particles goes to zero. The convenience of this definition will become clear.

In the CLA model, the A_i are given by

$$A_i(s_i,t_i) = \left(\frac{g_i s_i + ca}{s_i + a}\right)\left(\frac{s_i + a}{a}\right)^{\alpha_i(0)}\left(\frac{s_i + b_i}{b_i}\right)^{\alpha_i' t_i} , \qquad \text{(IV-6)}$$

where α_i is the Regge trajectory of the ith exchanged particle. Here α_i has been taken to have the linear form

$$\alpha_i(t) = \alpha_i(0) + \alpha_i' t. \qquad \text{(IV-7)}$$

The quantity $\alpha_i(0)$ is the intercept of this trajectory and α_i' is the slope and is taken equal to 1.0 $(\text{GeV/c})^{-2}$. The quantity a is the energy scale factor determining the boundary between the high and low energy regions. The quantities b_i govern the exponential t-dependence of the vertices, and the quantities g_i are related to the coupling constants of the vertices.

CLA's objective in choosing this particular parameterization was to construct a multiperipheral amplitude consistent with the following considerations:

1. Since multi-Regge models have had success in describing interactions in the high energy regions of phase space, this amplitude should take the fully Reggeized form when the effective mass (energy) of the two particle systems becomes large. In the region of high energies

$$A_i \xrightarrow[s_i \to \infty]{} g_i \left(\frac{s_i}{a}\right)^{\alpha_i} e^{[\ln\frac{a}{b_i}]t_i} . \qquad \text{(IV-8)}$$

This is recognized as the form of the fully Reggeized amplitude.

2. The amplitude should be a constant and thus the process should be governed by only phase space when the two-body effective mass becomes small. This is generally found to be a reasonable description if resonance formation is disregarded. In the region of very low energy $A_i \xrightarrow[s_i \to 0]{} C$. The quantity C is a constant determining the relative strength of the amplitude at low energy.
3. The amplitude should interpolate smoothly between the high and low energy cases.

Since very little is known about the coupling of Reggeons, we followed the lead of CLA and only distinguished between meson coupling (g_M for meson exchange) and nucleon coupling (g_N for nucleon exchange).

CLA groups the b_i into three categories:

1. b_{EA} governing only the top vertex,
2. b_i for all internal vertices, and
3. b_{EB} for the bottom vertex.

Tables 2 and 3 show the values of the parameters used in our calculations.

TABLE 2

MODEL PARAMETER VALUES

	a	b_{EA}	b_i	b_{EB}	g_N/g_M	c/g_M
Original CLA Values	1.0 GeV^2	1.0 GeV^2	1.2 GeV^2	.5 GeV^2	1.3	1.4
Our Values	1.0 GeV^2	2.0 GeV^2	2.4 GeV^2	1.0 GeV^2	1.3	1.4

TABLE 3

TRAJECTORY PROPERTIES USED

Trajectory	Strangeness	Baryon Number	G-Parity	$\alpha(0)$
Nucleon	0	1	---	-.35
Strange Meson	1,-1	0	---	.30
Pomeron	0	0	+1	1.00
Non-Strange Meson	0	0	+1,-1	.50

The quantities a, g, and c were taken to be the same as the CLA values for our comparisons. The b_i were determined by comparisons with our data and will be discussed later.

A constant transition amplitude in a scattering reaction would dictate that all possible final states be produced with equal probability. All corresponding variable distributions would thus be purely statistical in nature and could be calculated by the appropriate integration over Lorentz invariant phase space. In most experiments, however, a purely statistical explanation is inadequate. Consequently, a variable amplitude must be considered. This amplitude is a function of the four-momenta describing the system. The effect of this amplitude is to preferentially populate certain areas of phase space. In order to compare the CLA model with our data, we allowed the square of the CLA amplitude to weight phase space. The resulting distributions are then compared with the data. The degree of agreement indicates how well the CLA amplitude approximates the actual physical transition amplitude describing the reaction.

Our model calculations yield distributions of arbitrary normalization. Apart from a normalization factor, the distribution of any quantity q (differential cross-section of q) is given by the integral

$$\frac{d\sigma}{dq} = \int |T(ab \rightarrow 1,2,\cdots,n)|^2 dLips(q;q_i), \qquad \text{(IV-9)}$$

where q is the variable of interest and dLips is restricted Lorentz-invariant phase space[28]. The integration is carried out over all variables except q. The q_i are the four-momenta describing the system. The quantity T is the transition amplitude describing the n-body process and is a function of the q_i. The integral of Equation (IV-9) cannot, in general, be evaluated in closed form. For this reason we have employed the Monte Carlo technique to determine the distributions predicted by the model.

The Monte Carlo technique has been discussed thoroughly in other places.[29,30] Only a short description of our particular system will be given here.

The first step was to generate a sample of fictitious events that uniformly populate Lorentz-invariant phase space.[31] If for each event in this sample the CLA amplitude is calculated and the event is plotted with a weight equal to the square of the amplitude, the resulting distributions will approximate the integral of Equation (IV-9). Deviations occur because of statistical fluctuations. The more events used the better the approximation becomes. However, these calculations are performed by a computer and the processing of large numbers of events requires much time. We therefore used a more efficient method of calculation. Our data and our parameterization of the CLA model

preferentially populated those parts of phase space that correspond to the production of K*(890) and N*(1236) and that correspond to low momentum transfers to the $\bar{K}^{o}$ and nucleon. We therefore used more Monte Carlo events that fell into those parts of phase space and gave them a correspondingly smaller weight. The procedure does not distort the phase space population. Indeed, plots of the cosine of the overall center of mass production angles and of the invariant masses for these weighted events gave the distributions predicted by pure phase space when the CLA amplitude factor was ignored. We wanted the accuracy of our results set by the number of our bubble chamber events and not our Monte Carlo procedure, and yet we wished not to waste computer time. The number of Monte Carlo events processed for each reaction was therefore chosen so the fractional error in the square of the CLA amplitude averaged over phase space was about half of the fractional error in the number of bubble chamber events.

These fake events and their corresponding weights were then written on a magnetic tape to be used in our system, just as real events were used. Our histogramming programs used both data and model events as input. The output consisted of distributions with model and real data superimposed. For ease of comparison the model events were normalized to the number of actual events.

The fake events were generated by the Monte Carlo program MONTY,[30] which was modified to run on the Vanderbilt Sigma-7 Computer. Program CHANDU, which calculated the square of the CLA amplitude for each Monte Carlo event and wrote the tape to be used for making histograms, was written at Vanderbilt.

There were many diagrams like Figure 19 that contributed to each final state. Different diagrams were formed by taking all possible permutations of outgoing particles consistent with known exchanged particles. Following CLA, the Pomeron trajectory ($J^P = 0^+$) was always used over the other meson trajectory if both were allowed. It has been experimentally verified that the contribution from I = 3/2 baryon exchange is small[32]. Thus we have chosen not to include such exchanges in our calculations.

The actual form of the square of the CLA amplitude for each Monte Carlo event is given by the incoherent sum

$$W = \sum_j |A_j|^2, \qquad \text{(IV-11)}$$

where the sum is over the diagrams contributing to this final state.

It is observed that final states with smaller numbers of outgoing particles display more peaking in their production angular distributions. In order to be more realistic we incorporated resonance production in the model, thus effectively reducing the multiplicity of the final state. We used the method prescribed by Bassompierre, et al.[33] To display this prescription, consider a diagram for the reaction $K^-n \rightarrow \bar{K}^o\pi^-\pi^-p$ (Figure 20).

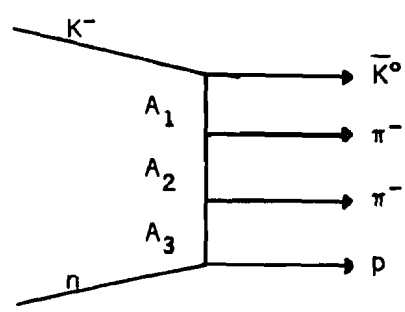

Figure 20.--One of the multiperipheral diagrams used in the CLA calculation for reaction II-5.

where

$$A_j = A_1 \; A_2 \; A_3 \qquad \text{(IV-12)}$$

and

$$W = \sum_j |A_j|^2 .$$

The quantities A_1, A_2, and A_3 are given by Equation (IV-6). For this particular reaction there are four permutations of Figure 20 which go into the sum.

To take resonance production into account we explicitly included diagrams where the resonating particles were considered to be a single outgoing line with a Breit-Wigner[34] shape. For example, we modified Figure 20 to take $K^{*-}(890)$ production into account (Figure 21) by replacing the top two particles with the $\bar{K}^{o}\pi^{-}$ system and introduced the

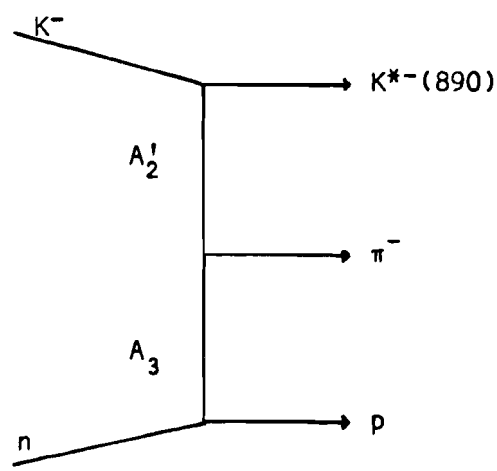

Figure 21.--A multiperipheral diagram modified to incorporate resonance production.

factor γ_{K^*} BW(K^*), where γ_{K^*} is chosen to give the experimentally determined fraction of $K^*(890)$ in this reaction and

$$BW(K^*) = \frac{\Gamma/2\pi}{(M_{K^*} - E)^2 + \frac{1}{4}\Gamma^2} \qquad \text{(IV-13)}$$

is the Breit-Wigner function for the K*(890). The quantities M_{K^*} and Γ are the mass and width of the K*(890), respectively, and E is the effective mass of the $\bar{K}^0\pi^-$ system. The amplitude squared thus becomes

$$|A_j|^2 = \gamma_{K^*}\, BW(K^*)\, |A_2'|^2\, |A_3|^2 \,, \qquad \text{(IV-14)}$$

and is included in the incoherent sum over all diagrams.

All diagrams involving resonance production were included in a similar manner.

An examination of the production angular distributions for reactions II-5, II-6, II-7, $K^-n \to \Lambda^0\pi^-\pi^-\pi^+$, $K^-n \to \Sigma^0\pi^-\pi^-\pi^+$, and $K^-n \to \Lambda^0\pi^-\pi^-\pi^+\pi^0$ revealed[9] that doubling the b_1 gives a much better fit than the original CLA values shown in Table 2. The production distributions calculated using both sets of b_1 and the data are presented in Chapter V.

2. Plahte and Roberts' modified CLA model

The CLA model as originally formulated has been modified by Plahte and Roberts.[25] As enumerated by the authors, the modifications were inspired by two shortcomings of the original CLA model.

1. The model failed to account for resonance production, even though resonance formation is known to be large.
2. The CLA model failed to take the phases of the amplitudes into account.

The modifications were suggested by the form of the Veneziano[35] amplitude for $\pi\pi \to \pi\omega$. This amplitude is

$$A(s,t) = \frac{\Gamma(\alpha_s + \alpha_t - 1)}{\Gamma(\alpha_s)} \Gamma(1 - \alpha_t)$$

$$\left[\frac{1 - \cos \pi\alpha_s}{\sin \pi\alpha_s} \sin \pi\alpha_t + 1 - \cos \pi\alpha_t\right], \qquad \text{(IV-15)}$$

where $\alpha_s = \alpha(s)$ and $\alpha_t = \alpha(t)$ are Regge trajectories. This amplitude has a definite phase, is crossing symmetric, and puts in resonance behavior directly and presumably without double counting.

Plahte and Roberts recognized that the CLA amplitude was analogous to the factor composed of three Γ-functions. They modified the CLA amplitude with a factor similar to the bracketed term in Equation (IV-15).

Plahte and Roberts thus suggest this new form for each adjacent particle pair:

$$A_i(s,t) = g\left(1 + \frac{s_i'}{a}\right)^{\alpha_t(0)} \left(1 + \frac{s_i'}{b}\right)^{\alpha_t' t}$$

$$\left[\frac{1 + \cos \pi(\alpha_s - \sigma_s)}{\sin \pi(\alpha_s - \sigma_s)} \sin \pi(\alpha_t - \sigma_t) + 1 + \cos \pi(\alpha_t - \sigma_t)\right] \qquad \text{(IV-16)}$$

where σ_t is the spin of the lowest resonance on the exchanged trajectory and σ_s is the spin of the lowest resonance on the α_s trajectory describing the adjacent pairs of particles. The quantity α_s is complex above threshold. The quantity s_i' is defined by Equation (IV-5).

The term $\frac{1 + \cos \pi(\alpha_s - \sigma_s)}{\sin \pi(\alpha_s - \sigma_s)}$ carries the resonance behavior in the s-channel. Plahte and Roberts have suggested parameterizing the imaginary part of α_s by

$$\mathrm{Im}(\pi\alpha_s) = A \ln \left(1 + \frac{s_1'}{a}\right) . \qquad \text{(IV-17)}$$

The parameter A can then be chosen so that the correct width for the lowest resonance of the trajectory is reproduced. We have found A(K*) = .372 and A(N*) = 1.30 for the K*(890) and N*(1236), respectively.

The quantities α_t are taken to be linear with unit slope and the intercepts given in Table 3. A linear approximation is also used for the real part of α_s,

$$\mathrm{Re}[\alpha(s)] = \alpha(0) + \alpha_s' s, \qquad \text{(IV-18)}$$

where $\alpha(0)$ is the intercept of the trajectory and α_s' is the slope. For the K*(890) trajectory the standard value $\alpha(0) = 0.30$ was used and $\alpha_s' = 0.88$ was used so the trajectory would pass through the square of the mass of the K*(890). For the N*(1236), $\alpha(0) = 0.13$ and $\alpha_s' = 0.89$ were used. These were chosen by drawing a straight line on a spin versus mass square plot through the points for the N*(1236) and N*(1940), its first Regge recurrence.

As with the CLA model, we wrote down all diagrams consistent with known exchanges and calculated a weight for each Monte Carlo event. This time however we included no explicit resonance diagrams in the sense of Bassompierre, et al. We formed the weight from the square of the coherent sum of the amplitudes of the contributing diagrams.

The model requires the specification of an s-channel trajectory for each outgoing particle pair. However, for example, in Figure 20 we know of no resonance trajectory with I = 2 for the $\pi^-\pi^-$ pair. For diagrams of this type we modified that part of the amplitude corresponding

to the non-resonant particles by replacing the factor

$$\frac{1 + \cos \pi(\alpha_s - \sigma_s)}{\sin \pi(\alpha_s - \sigma_s)} , \qquad \text{(IV-19)}$$

by -1. We did this because this factor goes to -1 in the limit of very broad resonances in the s-channel. We thus approximated the no resonance case by the very broad resonance case. The isospin 3/2 $\bar{K}^\circ\pi^-$ and isospin 1/2 $p\pi^-$ s-channel factors were also approximated by this method.

We took the ω°, f°, ρ, A_2, $K^*(890)$, $K^{**}(1420)$, and nucleon trajectories as relevant in the t-channels.

In the original CLA model we only classified the exchanged trajectories as Pomeron, strangeness zero meson, strangeness one meson, or nucleon. In the modified model we also specify the signature.

Since we wish to compare the amount of resonance production predicted by this model with the data, we also specified the isotopic spin of the exchanged trajectories and took the isospin Clebsch-Gordon[36] coefficients into account in an approximate manner. This method is illustrated by Figure 22 for one diagram. The amplitude was multiplied

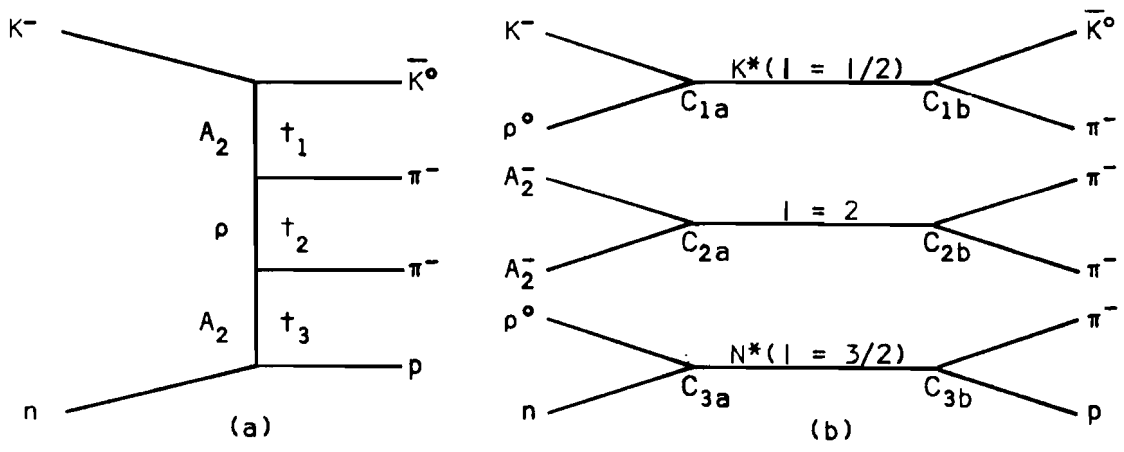

Figure 22.--(a) Multiperipheral diagram used in Plahte and Roberts model calculation. (b) Diagrams showing incorporation of isospin Clebsch-Gordon coefficients.

by $C_{1a}C_{1b}C_{2a}C_{2b}C_{3a}C_{3b}$, where each C is the isospin Clebsch-Gordon coefficient for the corresponding vertex.

The reaction $K^-n \rightarrow \pi^-\pi^-p\bar{K}^0$ was found to be specified by 60 diagrams. Also the calculation did not give good agreement with the data (see Chapter V). Each 1-C reaction (II-6 and II-7) requires as many as 500 diagrams for its specification. Because of this prohibitively large number, the model was compared only with the 4-C reaction. For other reactions[9] that are simpler in the sense that only the K*(890), K**(1420) and nucleon trajectories are exchanged, the modified model has also failed to predict the correct amount of resonance production. For example, is the reaction $K^-n \rightarrow \pi^-\pi^-\pi^+\Lambda^0$ the model predicted too much $Y^{*\pm}(1385)$ production. This lack of agreement for simpler cases also helped persuade us that further work with the model was not warranted.

B. Decay angular correlations

The decay distributions of a resonance, which has definite spin and parity, depend upon the relative populations of its magnetic substates. The populations of the magnetic substates are, in turn, determined by the production process for the resonance, i.e. the spin, parity, and alignment of the exchanged particle. Therefore, by studying the decay distributions one can gain information about the production process of the resonance, in particular, the nature of the exchanged particle.

The coordinate system used in studying the decay can be arbitrary. However, to emphasize the features of the exchanged particle, Jackson[37] recommends the following set of axes (to be specified in the rest frame of the resonance): the z-axis should be chosen parallel to the incident particle, the y-axis is taken as the normal to the

production plane, and the x-axis is defined by $\hat{x} = \hat{y} \times \hat{z}$. In this frame the z-axis is seen to be anti-parallel to the three-momentum of the exchanged particle.

For resonances decaying to two particles, the decay can be completely specified by the polar angle (θ) and the azimuthal angle (ϕ) of one of the decay products. The quantity θ is measured with respect to the z-axis and ϕ is measured in the x-y plane with respect to the x-axis.

The populations of the spin states of the resonance are described by the Hermitian density matrix elements $\rho_{mm'}$, where m and m' are magnetic quantum numbers relative to the z-axis in the Jackson frame. The quantity $\rho_{mm'}$ is therefore an element of a (2J + 1) dimensional matrix,[38] where J is the spin of the resonance.

By requiring parity conservation in the production process along with the normalization condition $Tr\rho = 1$, the density matrix for a spin 1 resonance can be written as

$$\rho = \begin{bmatrix} \frac{1 - \rho_{00}}{2} & \rho_{10} & \rho_{1,-1} \\ \rho_{10}^{*} & \rho_{00} & -\rho_{10}^{*} \\ \rho_{1,-1} & -\rho_{10} & \frac{1 - \rho_{00}}{2} \end{bmatrix} \qquad \text{(IV-20)}$$

where ρ_{00} and $\rho_{1,-1}$ are real and ρ_{10} is complex.

The decay angular distribution can be written in terms of the density matrix elements. For the parity conserving decay of a spin 1 resonance, e.g. K*(890), going to two spin zero particles

$$W(\theta\ \phi) = \frac{3}{4\pi}(\rho_{00}\cos^2\theta + \frac{1-\rho_{00}}{2}\sin^2\theta - \rho_{1,-1}\sin^2\theta\cos 2\phi$$

$$- \sqrt{2}\,\mathrm{Re}\,\rho_{10}\sin 2\theta\cos\phi) \qquad \text{(IV-21)}$$

when $W(\theta,\phi)$ is integrated over θ or ϕ separately, the distribution in the other angle results. These distributions contain the density matrix elements as parameters. When the distributions are fitted to the data, matrix elements can be determined. For the decay of the spin 1 object,

$$W(\theta) = \frac{3}{2}(\rho_{00}\cos^2\theta + \frac{1-\rho_{00}}{2}\sin^2\theta). \qquad \text{(IV-22)}$$

$$W(\phi) = \frac{1}{2\pi}(1 - 2\rho_{1,-1}\cos 2\phi), \qquad \text{(IV-23)}$$

These distributions allow the determination of ρ_{00} and $\rho_{1,-1}$ by a χ^2 minimization fit to the data. The Re ρ_{10} can be determined by the method of moments[39] or the Maximum Likelihood method.[40]

For a spin 3/2 resonance, e.g. N*(1236), decaying to a J = 1/2 and a J = 0 particle

$$W(\theta,\phi) = \frac{3}{4\pi}\left\{\frac{1}{6}(1 + 4\rho_{33}) + \frac{1}{2}(1 - 4\rho_{33})\cos^2\theta\right.$$

$$\left. - \frac{2}{\sqrt{3}}\mathrm{Re}\,\rho_{3,-1}\sin^2\theta\cos 2\phi - \frac{2}{\sqrt{3}}\mathrm{Re}\,\rho_{31}\sin 2\theta\cos\phi\right\}, \qquad \text{(IV-24)}$$

where the subscripts refer to 2m and 2m' in this case.

A comparison of these distributions with the data will be made in Chapter V.

CHAPTER V

EXPERIMENTAL RESULTS AND MODEL COMPARISONS

A. $K^-n \rightarrow \pi^-\pi^-p\bar{K}^o$

I. Data and CLA model calculation

There were 389 events satisfying the kinematic hypothesis $K^-n \rightarrow \pi^-\pi^-p\bar{K}^o$ with spectator proton momentum less than .275 GeV/c. When the requirement that the main vertex χ^2 probability be greater than or equal to five per cent was applied (see Chapter III, Section C), the sample was reduced to 360 events. When the loss correction for vees leaving the bubble chamber (see Chapter III, Section F) was made, the sample was increased to 371 events. This sample of 371 events was used in the following analysis of this reaction. The corrected cross-section for $K^-n \rightarrow \pi^-\pi^-p\bar{K}^o$ was found to be (324 ± 51) μbarns. All quoted cross-sections include a correction for those $\bar{K}^o$ that did not decay by the $\pi^+\pi^-$ mode.

In all following comparisons of the data with models, the model calculations will be represented as smooth curves. The smooth curves represent a hand smoothing of the histograms of the model's fictitious events. All quantitative comparisons of a model with the data were performed using the unsmoothed model histograms.

The model calculations used the parameters indicated in Table I as "our values". The dependence of the model results on the b_1 is discussed later in this section where we deal with the topic of single particle production angular distributions.

In many cases it was found that the interaction did not proceed directly to the final state particles, but was mediated by the formation of resonances. The most prominent of these was the formation of $K^{*-}(890) \rightarrow \overline{K}^{o}\pi^{-}$. Figure 23(a) shows the invariant mass distribution of the $\overline{K}^{o}\pi^{-}$, and it displays a very prominent $K^{*-}(890)$ signal. In all plots involving a π^{-} we include both π^{-} combinations unless otherwise noted. We did not attempt to determine a value for the mass and width of any of the well known resonances we observed since our statistics do not allow better determinations than have already been published. However, the mass and width of the $K^{*-}(890)$ appear to be in very good agreement with the currently accepted values of $M^{*} = .891$ GeV/c^2 and $\Gamma = .50$ GeV/c^2. Henceforth, K^{*} will indicate $K^{*-}(890)$ unless otherwise noted.

Curve (1) in Figure 23(a) results from using pure phase space and is normalized to the total number of events. Curve (2) is the CLA model result where the observed fraction of K^{*} in the data was part of the input to the calculation. The technique for including resonance production in the CLA model was described by Bassompierre, et al. and was discussed thoroughly in Section A of Chapter III.

The amount of K^{*} production was determined in an iterative procedure using the CLA model calculations. As a first approximation to the amount of K^{*} present in the data, a hand-calculated fit of a K^{*} Breit-Wigner times phase space plus pure phase space for the background was made to the $\overline{K}^{o}\pi^{-}$ invariant mass distribution. This result was used as input to the CLA model. The model output was examined and corrections were made in the amount of K^{*}, with the requirement that the model background fit on either side of the resonance when account was taken of the fact

Figure 23.--(a) The $\overline{K}^{o}\pi^{-}$ invariant mass plot for reaction 11-5.
(b) Corresponding production angular distribution.

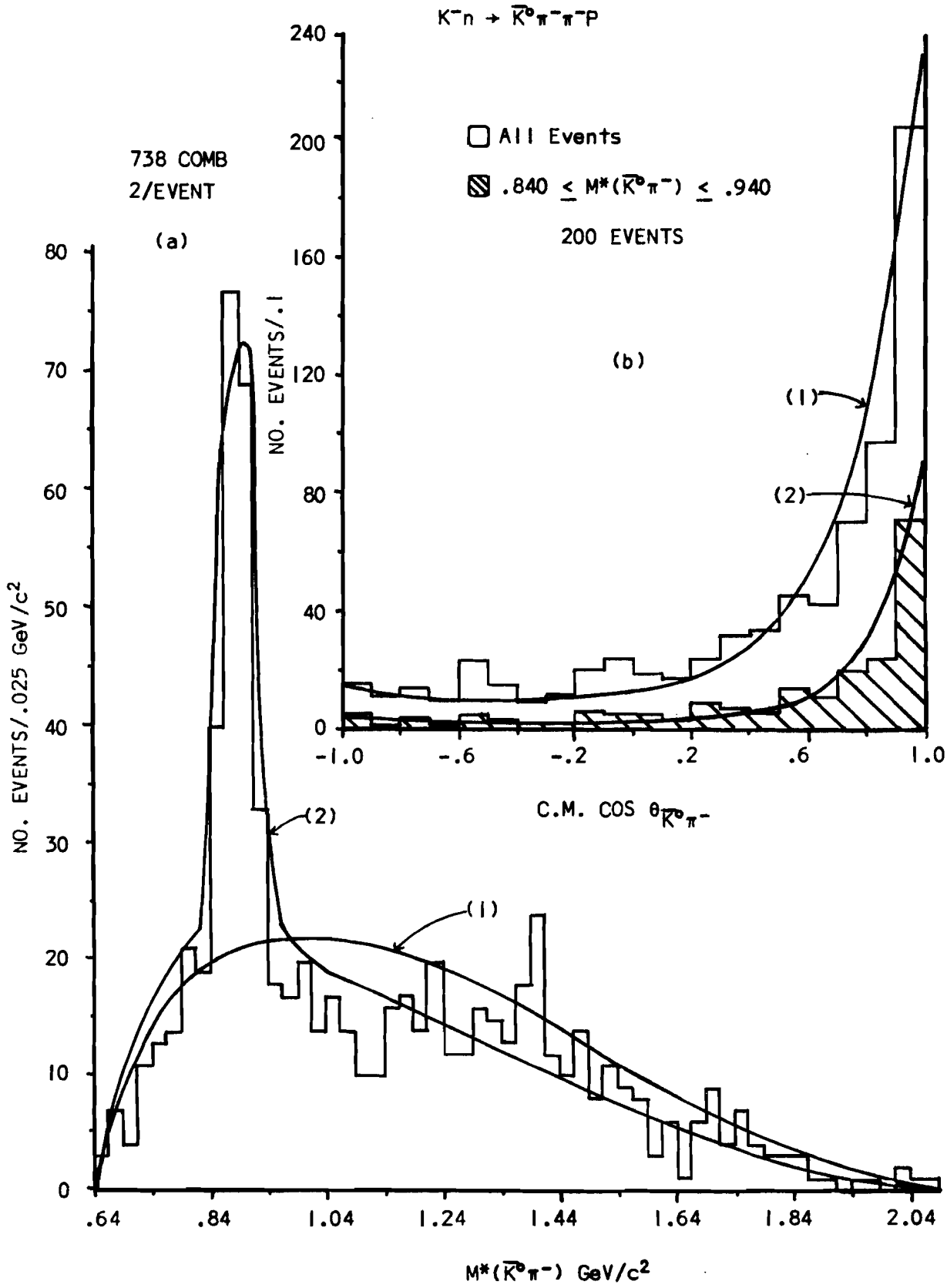
K⁻n → K̄°π⁻π⁻P
738 COMB
2/EVENT
(a)
All Events
.840 ≤ M*(K̄°π⁻) ≤ .940
200 EVENTS
(b)
NO. EVENTS/.1
NO. EVENTS/.025 GeV/c²
C.M. COS θK̄°π⁻
M*(K̄°π⁻) GeV/c²
(1)
(2)

that the data also contain K*(1420). The corrected amount of K* was then input to the model again. This procedure was continued until the agreement was such that only small corrections were needed, i.e., until the model calculation and data agreed within one standard deviation. Using this method, we determined that 192 ± 22 events belonged to the channel $K^-n \rightarrow K^{*-}(890)p\pi^-$. This corresponds to a corrected cross-section of (167 ± 32) μbarns. The corrections to this cross-section are described in Chapter II, Section D.

The open histogram in Figure 23(b) is the distribution in the cosine of the production angle of the $\bar{K}^o\pi^-$ system. The production angle is measured in the rest system of the incident K^- and the target neutron and with respect to the K^- direction. The distribution is strongly peaked in the beam direction indicating low momentum transfer between the beam and the $\bar{K}^o\pi^-$ system. Curve (1) in Figure 23(b) is the corresponding cosine distribution generated by the CLA model calculation. The model is in qualitative agreement with this observed distribution.

The shaded histogram in Figure 23(b) is the $\bar{K}^o\pi^-$ production cosine distribution for those events where the $\bar{K}^o\pi^-$ mass was between .840 and .940 GeV/c^2. This region will be referred to as the K* region throughout this work. It extends from $(M_{K^*} - \Gamma)$ to $(M_{K^*} + \Gamma)$. If both $\bar{K}^o\pi^-$ combinations happen to fall in the K* region, we have chosen to use the combination with mass closer to .890 GeV/c^2. We plotted only quantities corresponding to that one combination. Curve (2) is the CLA prediction where the model events have had the same $\bar{K}^o\pi^-$ mass cut imposed. Again, the CLA result reproduces the behavior of the data. It should be noted that the events in the shaded area are not pure K* events, but are

K*'s plus the background under the K* peak. The K* region contains about 25% background events. The CLA model has background built in, in the form of non-resonant diagrams and the "other $\bar{K}^0\pi^-$ combination" from the resonant diagrams. To the extent that the angular distributions for the K* region and the background have the same shape, the model will not be sensitive to the relative amounts of background and resonant diagrams. Within statistical errors, the production angular distribution for the K* region agrees with the corresponding distribution for the $\bar{K}^0\pi^-$ combinations of the entire sample.

As we have indicated earlier, the momentum transfer and the production angle are not independent quantities. The square of the four-momentum transfer t is defined as follows. Let P_1 be the four-momentum of one of the initial particles and P_2 be the four-momentum of some outgoing particle system. Then

$$t \equiv (P_1 - P_2)^2 \equiv -\Delta^2 \qquad \text{(V-1)}$$
$$= M_1^2 + M_2^2 - 2E_1E_2 + 2|\vec{P}_1||\vec{P}_2| \cos\theta_{12}$$

where M is the mass of the particle or particle system,

E is the corresponding energy,

$\vec{P}$ is the three-momentum, and

θ_{12} is the angle between the three-momentum vectors of the incident and outgoing systems.

Not only M_1 and M_2 but also E_1, E_2, P_1, and P_2 are independent of the production angle, θ_{12}, in the center of mass system. The quantity t assumes its maximum value at $\theta_{12} = 0$ and this value of t corresponding to this smallest θ_{12} is called t_{min}.

$$t \xrightarrow[\theta_{12} \to 0]{} t_{min}. \qquad \text{(V-2)}$$

It has been generally observed that the differential cross-section for resonance production as a function of t is approximately exponential in form for t near t_{min}. The slope of the semi-logarithmic plot λ is interpreted as a measure of the degree of peripherality of the collision. In order to make the exponential dependence easier to see, we use the quantity $|t - t_{min}|$ for our abscissa because this makes the starting point in the distribution independent of the invariant mass of the recoiling $p\pi^-$ system.

Figure 24(a) shows a semi-logarithmic plot of the number of events as a function of $|t - t_{min}|$ from the K^- beam to the outgoing $\overline{K}^o\pi^-$ systems for those events where the mass of the $K^o\pi^-$ was between .840 and .940 GeV/c^2. The data points are indicated by x's and error bars. In order to determine the nature of the background under the K*, we chose to use the behavior of two background control regions. In the $K^o\pi^-$ invariant mass histogram, we chose one control region below the K* band [.640 - .815 GeV/c^2] and the other above the K* [.965 - 1.165 GeV/c^2] so that the average value of the mass regions was approximately the K* mass.

We added the $|t - t_{min}|$ distributions for those events falling in these control regions and then compared this resulting distributions to the distribution of those events in the K* band. A χ^2 test comparing the two distributions yielded a χ^2 probability of about 75%. Since the control sample and the K* region had the same shape, no background subtraction was warranted.

Figure 24.--(a) The $|t - t_{min}|$ distribution for $K^{*-}(890)$ produced in reaction II-5. (b) The $|t - t_{min}|$ distribution for $K^{*-}(890)$ produced in reaction II-6.

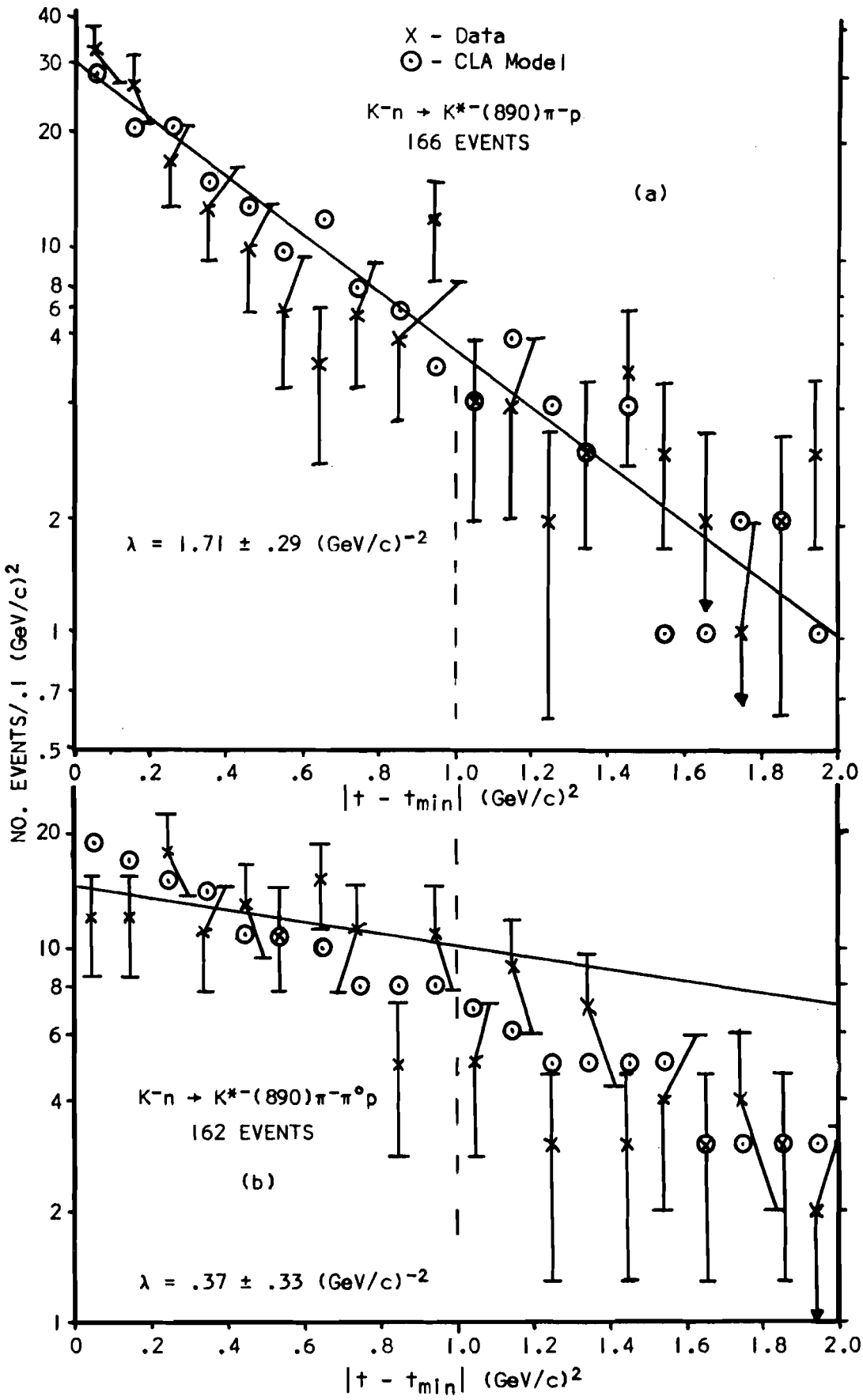
X - Data
⊙ - CLA Model
K⁻n → K*⁻(890)π⁻p
166 EVENTS
(a)
λ = 1.71 ± .29 (GeV/c)⁻²
NO. EVENTS/.1 (GeV/c)²
|t - t_min| (GeV/c)²
K⁻n → K*⁻(890)π⁻π°p
162 EVENTS
(b)
λ = .37 ± .33 (GeV/c)⁻²
|t - t_min| (GeV/c)²

The straight line in Figure 24(a) is the result of a least-squares fit to an exponential of the form

$$N = ce^{-\lambda|t - t_{min}|}, \qquad \text{(V-3)}$$

where N is the number of events per unit t interval,

$|t - t_{min}|$ is the convenient momentum transfer variable, and

c and λ are constants to be determined from the fit.

The fit was only carried out for those events with $|t - t_{min}|$ below 1.0 $(GeV/c)^2$. This cut was chosen for consistency. A previous examination of the $|t - t_{min}|$ distribution for the $K^{*-}(890)$ produced in reaction II-7 showed that events above 1.0 $(GeV/c)^2$ had only a 0.01 per cent chi-square probability of being consistent with the straight line determined from points below that value. For the sake of consistency, the K^* $|t - t_{min}|$ distributions in all three reactions (II-5, II-6, and II-7) were fit to the region below 1.0 $(GeV/c)^2$.

The least squares fit yielded the value $\lambda = 1.71 \pm .29$ $(GeV/c)^{-2}$. This fit corresponds to a χ^2 probability of about 20 per cent in a comparison to the data below 1.0 $(GeV/c)^2$. The χ^2 probability that the same exponential dependence holds for the region above 1.0 $(GeV/c)^2$ is 72 per cent.

The circles in Figure 24(a) are the results of the CLA model calculation. The size of the circles are for ease of reading only. As discussed in Chapter IV, the statistical errors of the data points are much larger than those of the model calculation. The χ^2 test comparing the model with the data yielded a χ^2 probability of about 15 per cent.

Figures 25(a), (b), and (c) show the invariant mass plots of the K^*p, $K^*\pi_B^-$, and the $p\pi_B^-$, respectively. The K^* refers to those $\bar{K}^o\pi^-$ combinations with mass in the $K^{*-}(890)$ mass interval and π_B^- refers to the other π^-. Figure 25(a) shows no evidence for the production of Y^*'s decaying via the K^*p mode. The two standard deviation bump around 2.225 GeV/c^2 lacks statistical reliability. The curve in Figure 25(a) is the CLA prediction and is in agreement with the data.

Figure 25(b) is the plot of the $K^{*-}(890)\pi_B^-$ system. The quantum numbers of this system are exotic and the existence of exotic resonances has not been established. A work by Bomse and Moses[41] gives Deck type[42] calculations of this invariant mass distribution. Their calculations were based on the diagram we show in Figure 26, where the incident K^- dissociates into a $K^{*-}(890)$ plus a π^o. The π^o then undergoes charge exchange scattering ($\pi^o n \rightarrow \pi^- p$) at the lower vertex. The low momentum transfer from the incident K^- to the outgoing K^* tends to make the final

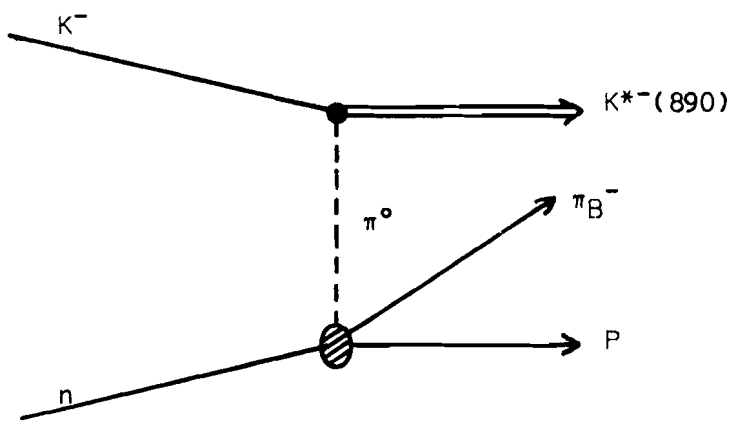

Figure 26.--Feynman diagram for $K^{*-}(890)$ production by nucleon charge-exchange scattering in reaction II-5.

Figure 25.--Distributions for the reaction $K^-n \rightarrow K^{*-}(890)\pi_2 p \rightarrow \overline{K}^0\pi_1^-\pi_2^-p$; (a) $K^{*-}(890)p$ invariant mass, (b) $K^{*-}\pi_2^-$ invariant mass, (c) $p\pi_2^-$ invariant mass, cosine of production angle for (d) π_1^-, and (e) π_2^-.

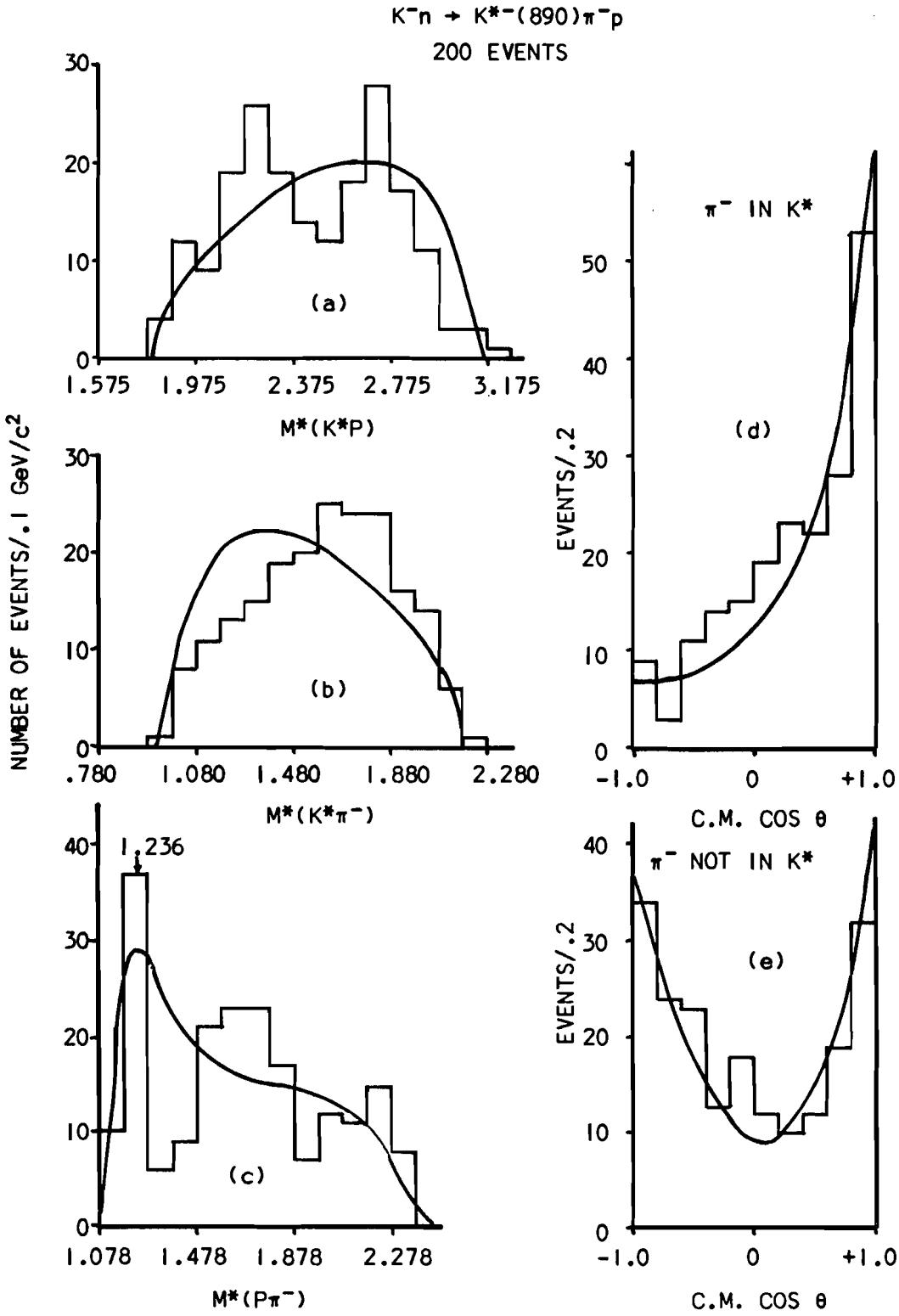
K⁻n → K*⁻(890)π⁻p
200 EVENTS
NUMBER OF EVENTS/.1 GeV/c²
(a)
1.575 1.975 2.375 2.775 3.175
M*(K*P)
(b)
.780 1.080 1.480 1.880 2.280
M*(K*π⁻)
(c)
1.236
1.078 1.478 1.878 2.278
M*(Pπ⁻)
π⁻ IN K*
(d)
EVENTS/.2
-1.0 0 +1.0
C.M. COS θ
π⁻ NOT IN K*
(e)
EVENTS/.2
-1.0 0 +1.0
C.M. COS θ

K^* go sharply in the forward direction. The forward peaking of pion-nucleon charge exchange scattering also makes the π_B^- go in the direction of the incident K^-. Consequently a low mass enhancement in the $K^{*-}(890)\pi^-$ system is predicted by these calculations. Similar Deck calculations[43] were first applied to the reactions

$$K^{\pm}p \rightarrow K^{*\circ}(890)\pi^{\pm}p \rightarrow K^{\pm}p\pi^{+}\pi^{-} \qquad \text{(V-4)}$$

to explain the low mass peak observed in the $K^{*\circ}(890)\pi^{\pm}$ spectra at about 1.3 GeV/c^2. Here, however, the elastic process ($\pi^-p \rightarrow \pi^-p$) was used to describe the lower vertex instead of the charge exchange process. Bomse and Moses contended that since the differential cross-sections of the two pion nucleon scattering processes appear quite similar in shape in the appropriate energy region, the calculations should be carried out in the same manner.

We see no evidence for a low mass enhancement in the $K^{*-}(890)\pi^-$ invariant mass spectrum. We conclude that the contribution of the diagram of Figure 26 is small.

The curve in Figure 25(b) is the prediction of the CLA model. In light of the CLA background estimate, there actually seems to be a three standard deviation depletion in the data at low effective masses. The statistical significance of this depletion is too small for it to be taken seriously.

Figure 25(c) shows the invariant mass distribution for the proton π_B^- system for the events falling in the K^* region. The most obvious feature of this spectrum is the production of $N^{*\circ}(1236)$. Although the $N^{*\circ}(1236)$ is known to have a width of .120 GeV/c^2, the enhancement

in Figure 25(c) appears to have a width considerably narrower. The narrow width may be due to some interference mechanism or possibly due to a statistical fluctuation. The scarcity of data makes the resolution of this question impossible. The four-standard deviation depletion from 1.278 to 1.478 GeV/c^2 may be related to the $N^{*o}(1236)$ question, destructive interference of the Roper resonance with background, or again may be due to a fluctuation. This question also cannot be answered in light of the available data.

We relied upon the CLA model to determine the amount of simultaneous $K^{*-}(890)$ $N^{*o}(1236)$ production. The contribution to the reaction $K^-n \rightarrow K^{*-}(890)$ $N^{*o}(1236)$ in the CLA model is given by only one diagram, which is shown in Figure 27. By varying the input fraction to the model

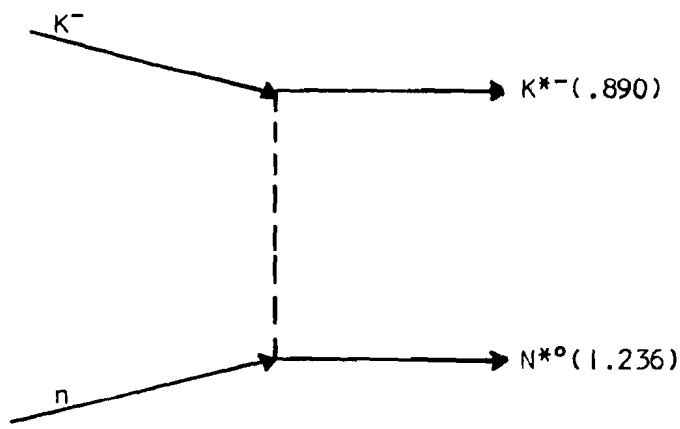

Figure 27.--Feynman diagram for simultaneous $K^{*-}N^{*o}$ production in reaction II-5.

corresponding to the amount of simultaneous $K^{*-}N^{*o}$ production, we were able to determine that (22 ± 11) events belonged to this channel. This corresponds to a corrected cross-section of (19 ± 10) μbarns. In the determination of the amount of N*, we required that the fit using the model reproduce the number of data events in a region $\pm\Gamma(\pm.120$ GeV/c^2)

around the $N^{*\circ}$ mass (1.236 GeV/c^2).

The apparent enhancement around 1.680 GeV/c^2 in the $p\pi^-$ mass distribution is discussed later in this section.

Figures 25(d) and 25(e) show the production angular distribution for the π^- from the decay of the K* and the other π^-, respectively, for those events in the K* band. Notice in particular how the CLA model is able to reproduce the marked difference in these distributions. Figure 28(a) is the distribution of the two π^-'s produced in reaction II-5. The curve in 28(a) is a result of the CLA calculation.

Figure 28(b) shows that the $\bar{K}^\circ$ from the decay of the K* is produced preferentially in the beam direction. The protons from the K* events [Figure 28(c)] are peaked strongly in the backward direction, as are the other protons. The CLA calculations for both the proton and $\bar{K}^\circ$ distributions of the events from the K* band are in qualitative agreement with the data. In addition, they appear to have about the same shape as the corresponding model calculations for the uncut sample.

The decay angular distributions of the $K^{*-}(890)$ were examined in the Jackson frame of reference as described in Chapter IV. A sketch of the axes, defined by unit vectors $\hat{x}$, $\hat{y}$, and $\hat{z}$, is shown in Figure 29. The system is defined in the K* rest frame.

The quantities P_{K^-}, $P_{\bar{K}^\circ}$, and P_{K^*} are the three-momenta of the K^-, $\bar{K}^\circ$, and K*, respectively. For convenience, the vector product defining the y-axis, was calculated in the overall center of mass system. Since this vector is orthogonal to the transformation, it is unaltered by the transformation.

Figure 28.--The single particle production angular distribution for reaction II-5, (a) π^-, (b) $\overline{K}^0$, and (c) proton.

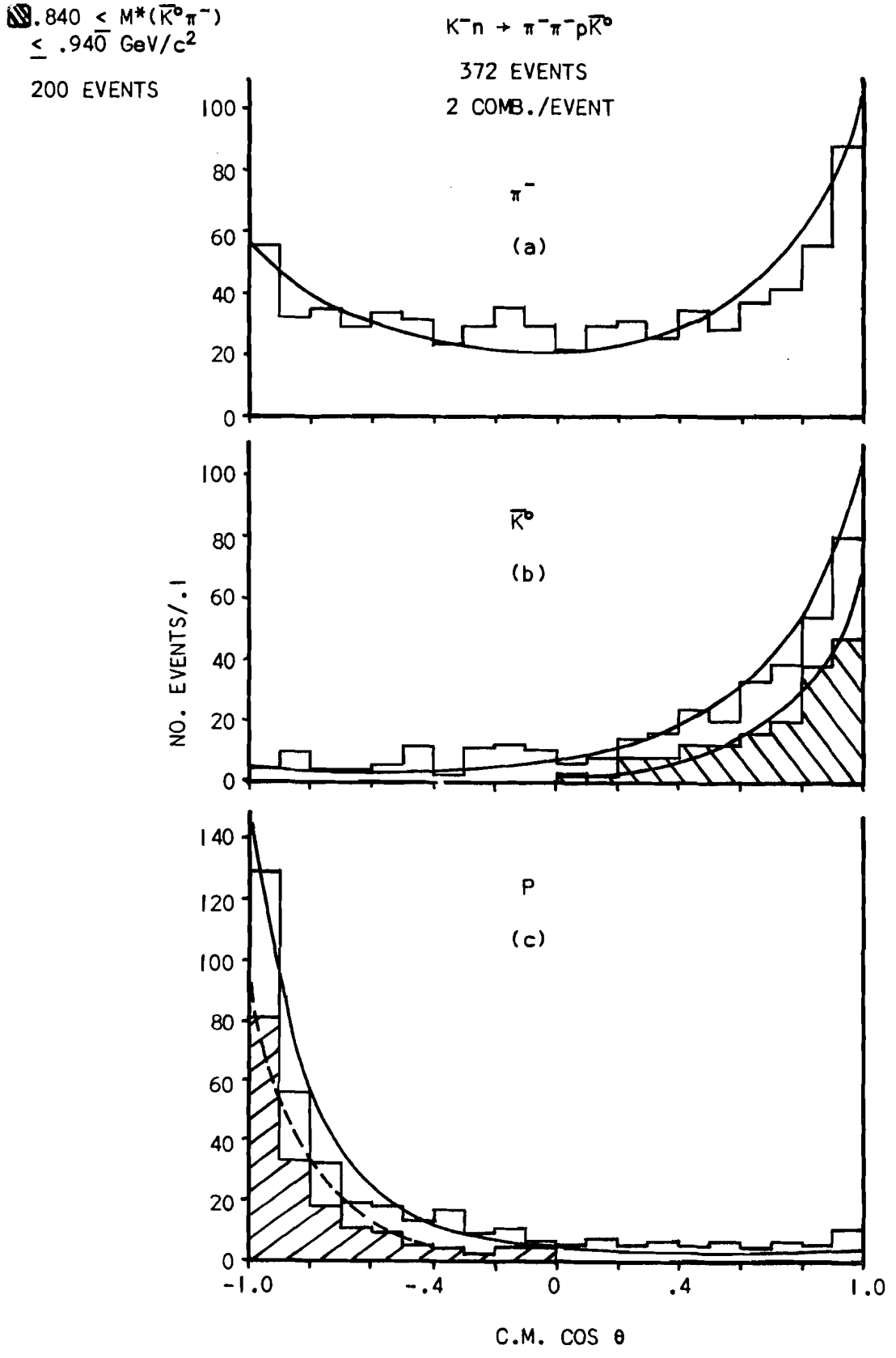
.840 ≤ M*($\bar{K}^0\pi^-$) ≤ .940 GeV/c²
200 EVENTS
$K^-n \to \pi^-\pi^-p\bar{K}^0$
372 EVENTS
2 COMB./EVENT
π^-
(a)
$\bar{K}^0$
(b)
P
(c)
NO. EVENTS/.1
C.M. COS θ
-1.0
-.4
0
.4
1.0

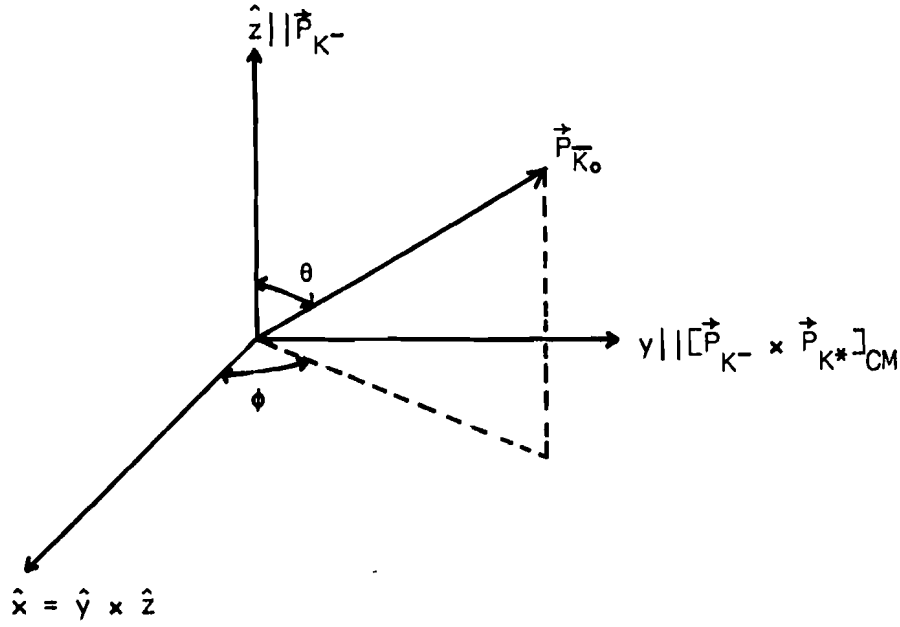

Figure 29.--Jackson frame of reference for the decay of $K^*(890) \rightarrow \overline{K}^o\pi^-$.

As stated in Chapter IV, the decay angular distribution of a resonance with $J^P = 1^-$ decaying into two spin 0 mesons via a parity conserving interaction is given by Equation IV-26. The distribution function $W(\theta,\phi)$ involves the three quantities ρ_{00}, $\rho_{1,-1}$, and Re ρ_{10}. Therefore a measurement of $W(\theta,\phi)$ will determine all of the density matrix except Im ρ_{10}.

In Figure 30(a) and (b) we have histogrammed the Jackson cos θ and ϕ distributions, respectively, for the $K^{*-}(890)$ formed in the reaction $K^-n \rightarrow K^{*-}(890)\pi^-p$. The cos θ distribution shows no strong structures and has a χ^2 probability of about 80 per cent of being flat. On the other hand, the ϕ distribution shows strong peaking at $\pi/2$ and $3\pi/2$ and has a χ^2 probability of about .05 per cent of being flat. This is similar to the behavior observed in $K^-p \rightarrow K^{*-}\pi^+n$ at 6 GeV/c by

Figure 30.--Jackson frame distributions for decay of $K^{*-}(890)$ for (a) $\cos\theta$ and (b) ϕ.

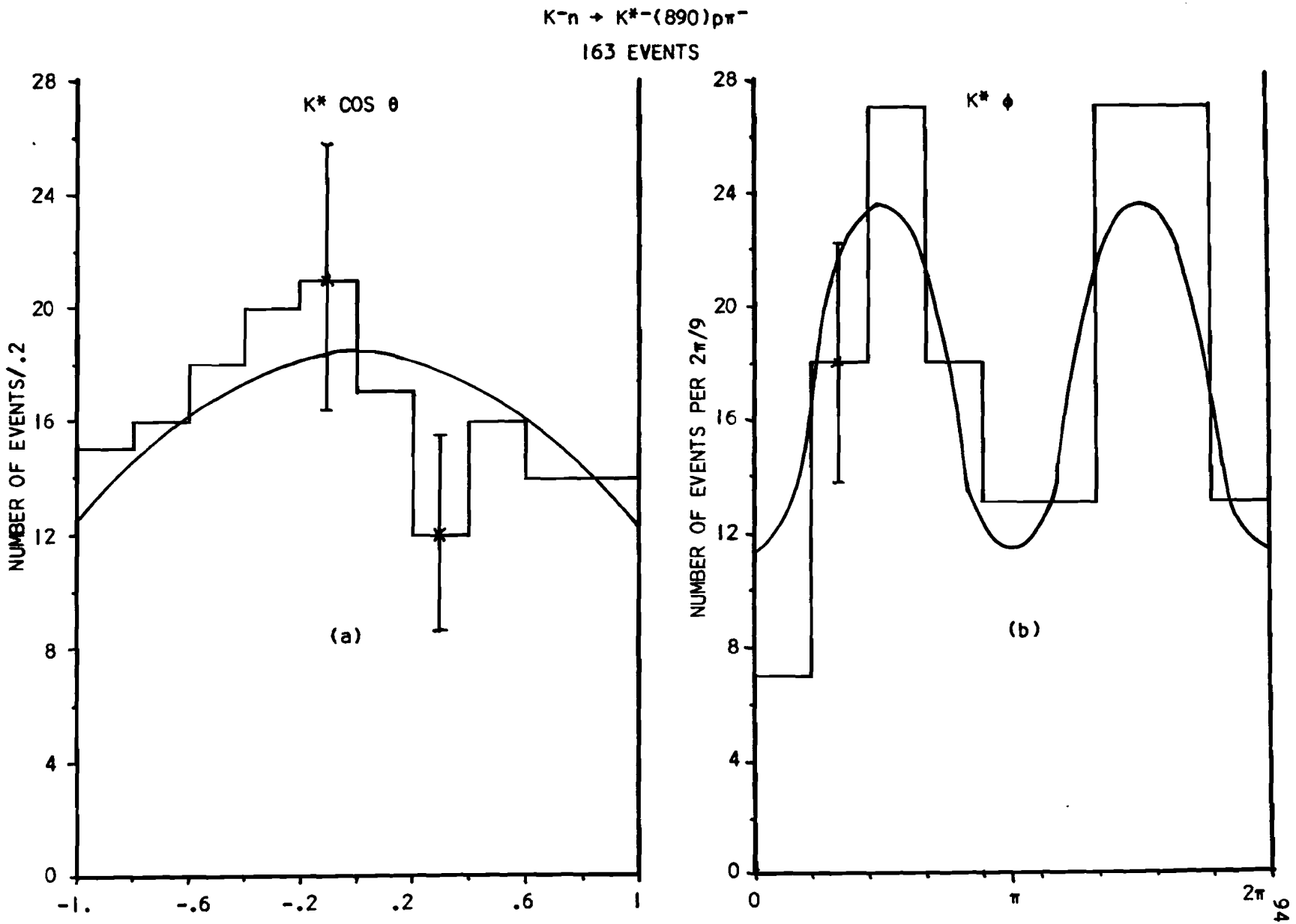
K⁻n → K*⁻(890)pπ⁻
163 EVENTS
K* COS θ
NUMBER OF EVENTS/.2
(a)
K* φ
NUMBER OF EVENTS PER 2π/9
(b)
28
24
20
16
12
8
4
0
-1.
-.6
-.2
.2
.6
1
π
2π

Colley et al.[44]

The density matrix elements ρ_{00}, $\rho_{1,-1}$, and Re ρ_{10} were determined by a maximum likelihood fit to the data.

The likelihood function $L(\alpha_j)$[45] is defined as the joint probability density of obtaining a particular experimental result, $x_1, \ldots x_N$, where the α_j's are the parameters of the distribution function describing the observations.

$$L(\alpha_j) = \prod_{i=1}^{N} f(\alpha_j; x_i), \qquad \text{(V-5)}$$

where $f(\alpha_j; x_i)$ is assumed to be the true distribution function satisfying the normalization condition

$$\int f(\alpha_j; x)dx = 1. \qquad \text{(V-6)}$$

The likelihood function is a function of the parameters α_j.

In the fit to the data we take the normalized general angular distribution $W(\theta,\phi)$ as the true distribution function. The parameters of $W(\theta,\phi)$ are ρ_{00}, $\rho_{1,-1}$, and Re ρ_{10}. A particular experimental result corresponds to a specification of θ and ϕ in the Jackson frame.

According to the maximum likelihood method, the set of parameters which maximize $L(\alpha_j)$, called the maximum likelihood solution, is the set yielding the best fit to the data. It has been proven that in the limit of large N, no other method of estimation is more accurate than this method.

Because of convenience we find the maximum in ln L instead of L. Since the maximum in L occurs at the same point as ln L, the maximum

likelihood solution will be the same.

We defined the likelihood in the following manner.[46]

$$\ln L_{K^*} = \prod_{i=1}^{N} \ln W(\theta_i,\phi_i) - \gamma_1 \prod_{j=1}^{M} \ln W(\theta_j,\phi_j) - \gamma_2 \prod_{k=1}^{R} \ln (\theta_k,\phi_k), \tag{V-7}$$

where N is the number of events with $\bar{K}^o\pi^-$ mass between .840 and .940 GeV/c^2, M is the number of events with $\bar{K}^o\pi^-$ mass between .640 and .815 GeV/c^2, and K is the number of events with $\bar{K}^o\pi^-$ mass between .965 and 1.165 GeV/c^2. The quantities γ_1 and γ_2 are the background normalization constants.

Equation (V-7) comes from the assumption that the likelihood function, governing the angular distribution of those events falling in the K* region, could be separated into contributions from two components. The first component was assumed to be the true K* events. The second was the background events falling in this region. In order to separate out the K* component, we estimated the background distribution function by using control regions. This prescription is shown symbolically in Equation (V-8).

$$L_{K^*} = \prod_{i=1}^{N-B} W(\theta_i,\phi_i) = \frac{\prod_{i=1}^{N-B} W(\theta_i,\phi_i) \quad \prod_{\ell=1}^{B} W(\theta_\ell,\phi_\ell)}{\left[\prod_{j=1}^{M} W(\theta_j,\phi_j)\right]^{\gamma_1} \left[\prod_{K=1}^{R} W(\theta_k,\phi_k)\right]^{\gamma_2}} \tag{V-8}$$

where we take $\prod_{\ell=1}^{B} W(\theta_\ell,\phi_\ell) = \left[\prod_{j=1}^{M} W(\theta_j,\phi_j)\right]^{\gamma_1}\left[\prod_{k=1}^{R} W(\theta_k,\phi_k)\right]^{\gamma_2}$.

The product through B indicates the background component which we have estimated by control regions.

We determined that there were 214 K* events produced in reaction II-5 by fitting a Breit-Wigner function times a phase space background to the data. We defined the K* region as a band $\pm\Gamma(\pm 50\ \mathrm{MeV}/c^2)$ on each side of .890 GeV/c^2. This corresponds to about 76 per cent of the total number of K*'s or 163 events as determined from the Breit-Wigner fit. Since there are 198 events in the K* region, we wish to subtract 35 background events from the histograms. This was done by using the two control regions. We plotted the distributions for the two control regions, normalized each to 35/2 events, and subtracted the sum of the two distributions from the distribution of those events falling in the K* band. Figure 30 is the result of this subtraction procedure.

The results for the density matrix elements from the maximum likelihood method are as follows:

$$\begin{aligned} \rho_{00} &= .255 \pm .055 \\ \rho_{1,-1} &= .195 \pm .050 \\ \mathrm{Re}\,\rho_{10} &= .000 \pm .025 \end{aligned} \qquad \text{(V-9)}$$

The errors in the density matrix elements were determined where the likelihood decreased to $e^{-\frac{1}{2}}$ of its maximum value when plotted as a function of the matrix element of interest.

The curves in Figure 30 are the distributions in cos θ and ϕ obtained when the maximum likelihood solution values for the parameters

were substituted into $W(\theta,\phi)$. The functional form of $W(\cos\theta)$ and $W(\phi)$ was given in Chapter IV. The χ^2 probability between the fitted curves and the data was found to be 90 per cent and 50 per cent for Figures 30(a) and 30(b), respectively.

The two distributions in Figure 30 do not involve Re ρ_{10} as a parameter. To make sure that the value we obtained for Re ρ_{10} is consistent with the data, we plotted the difference in the distributions for those events where $\cos\theta$ was between 0 and 1 and those where $\cos\theta$ was between 0 and -1. We compared this histogram (Figure 31) to the corresponding distribution obtained from

$$R(\phi) \equiv \int_0^1 W(\cos\theta,\phi)\, d\cos\theta - \int_{-1}^0 W(\cos\theta,\phi)\, d\cos\theta$$
$$= \text{Re}\,\rho_{10}\cos\phi. \qquad \text{(V-10)}$$

For Re $\rho_{10} = 0$, the distribution in ϕ given by Equation (V-10) would be flat with average value zero. We found our data to be consistent with this.

The amount of data available prevented a meaningful study of the momentum transfer (Δ^2) dependence of the matrix elements. When the Jackson angular distributions were plotted separately for the three Δ^2 regions (0 to .5), (.5 to 1.0), and ($\geq$1.0 GeV/c2), they were all found to have qualitatively similar shapes.

Jackson[47] and also Gottfried and Jackson[48] have given extensive discussions of the spin density matrix. We shall use their results to interpret our data. The result $\rho_{00} = .255 \pm .055$ is consistent with $\rho_{00} = 1/3$ which implies very little $K^{*-}(890)$ alignment along the z-axis.

Figure 31.--Histogram of the quantity R as a function of the Jackson ϕ for the decay of $K^{*-}(890)$ in reaction II-5.

$$R = \int_0^1 W(\cos\theta,\phi)\,d\cos\theta - \int_{-1}^0 W(\cos\theta,\phi)\,d\cos\theta = \frac{3}{\pi}\,\mathrm{Re}\,\rho_{10}\cos\phi$$

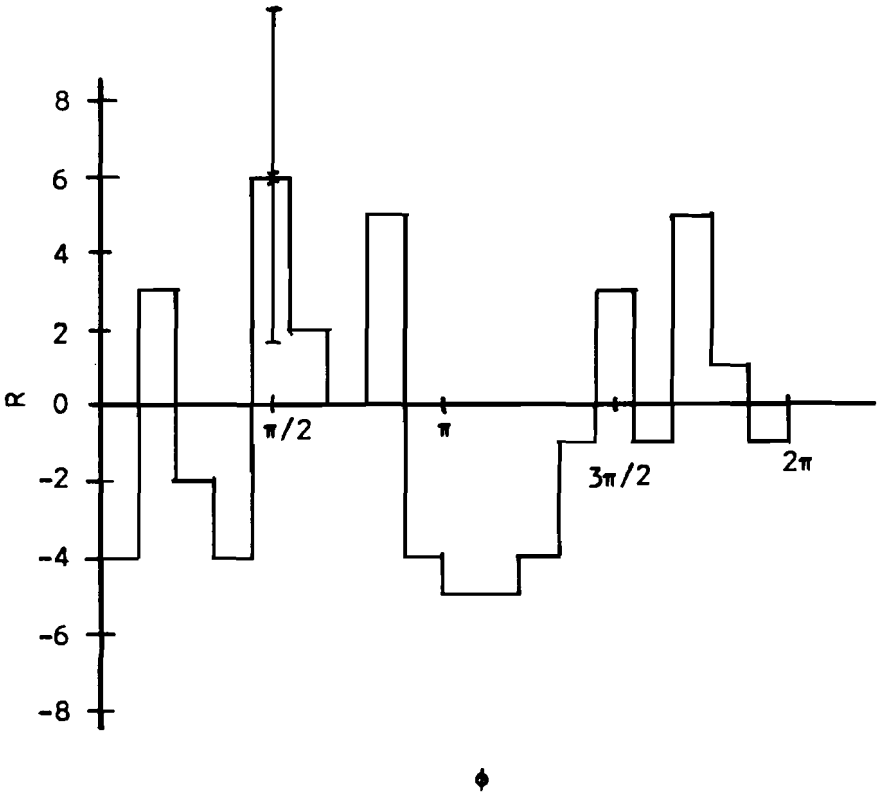

The result $\rho_{1,-1} = .195 \pm .050$ is not consistent with $\rho_{1,-1} = 0$. Our CLA model calculations imply that 69 per cent of the $K^{*-}(890)$ are produced at the top vertex. For the sake of simplicity we shall assume that all the $K^{*-}(890)$ are produced at the top vertex when interpreting our values for the spin density matrix elements. In this case the K^* is formed from the interaction of the K^- and the exchanged object. Angular momentum and parity conservation forbid $J^P = 0^+$ exchange. It is convenient to divide the exchanged objects into three classes. The first class is $J^P = 0^-$. The second class is the natural sequence $J^P = 1^-, 2^+, 3^-, \cdots$. The third class is the unnatural sequence $J^P = 1^+, 2^-, 3^+, \cdots$. Exchange of members of this unnatural sequence will in general lead to nonzero values of Re ρ_{10}, but our result is Re $\rho_{10} = .000 \pm .025$. We shall assume, for the sake of simplicity, that this allows us to rule out exchange of members of the unnatural spin-parity sequence. We thus conclude that the facts that $\rho_{00} \neq 1$ and $\rho_{1,-1} \neq 0$ each imply exchange of natural spin-parity object(s). Also, $\rho_{00} \neq 0$ implies exchange of 0^- object(s). At first thought, a prime candidate for the 0^- object is the π^- meson. The disagreement between our invariant mass plot and the calculation of Bomse and Moses implies that π^- meson exchange is not important.

We are thus at a loss for a simple physical explanation of our measured values of the spin density matrix elements. Perhaps rescattering corrections, the exchange of members of the unnatural spin-parity sequence, or interference with background must be taken into account.

Referring back to the $\bar{K}^{o}\pi^{-}$ invariant mass distribution in Figure 23(a), we observe an enhancement above the background estimate of the CLA model at the approximate mass of 1.400 GeV/c^2. We associate this with the production of the $K^{*-}(1420)$. The $K^*(1420)$ is a well established resonance often observed in the $\bar{K}^{o}\pi^{-}$ mass spectrum. The amount of $K^*(1420)$ was found by using the result of the CLA calculation as a background estimate after it had been renormalized to take the number of $K^*(1420)$ resonant events into account. Using this method we determined that there were 55 ± 13 events corresponding to the reaction $K^-n \rightarrow K^{*-}(1420)p\pi^-$. This corresponds to a corrected cross-section of (48 ± 14) μbarns.

Figure 32 is the invariant mass distribution for the $p\pi^-$ in reaction 11-5. The most prominant feature is the production of $N^{*o}(1236)$. This is a well established resonance with a known mass of 1.236 GeV/c^2 and a natural width of Γ = .120 GeV/c^2.

The iterative procedure for determining the amount of $N^{*o}(1236)$ using the CLA model yielded (22 ± 13) events of the type $K^-n \rightarrow N^{*o}(1.236)\bar{K}^{o}\pi^-$ where the $\bar{K}^{o}$ and π^- do not form a K^*.

Curve (1) in Figure 32 is pure Lorentz-invariant phase space. Curve (2) is the result of the CLA calculation. The center of the N^* enhancement appears to be shifted slightly lower than the CLA model result. The model calculation used a Breit-Wigner shape with the input parameters as the standard resonance mass (1.236 GeV/c^2) and the standard width (.120 GeV/c^2). It has been observed in other bubble chamber experiments[5] that the N^* detected in this mode tends to have a lower peak than when observed by elastic scattering experiments using counters.

Figure 32.--The invariant mass distribution for $p\pi^-$ produced in reaction II-5.

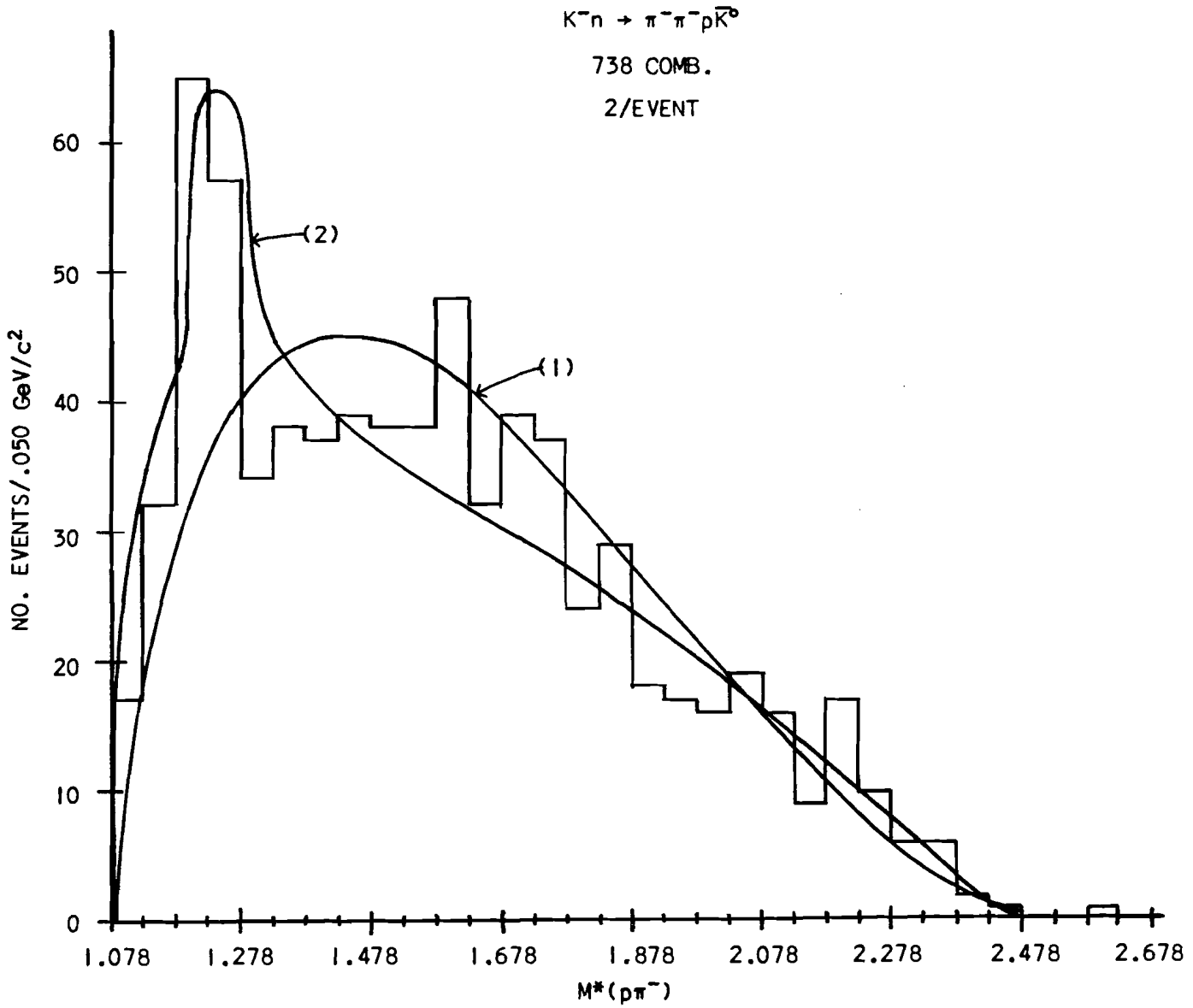
$K^-n \rightarrow \pi^-\pi^-p\overline{K}^0$
738 COMB.
2/EVENT
(2)
(1)
NO. EVENTS/.050 GeV/c^2
0
10
20
30
40
50
60
1.078
1.278
1.478
1.678
1.878
2.078
2.278
2.478
2.678
M*(pπ^-)

The reason given for this is the mass dependent width of the N*.[49] If the N* mass in Figure 32 is truly lower than 1.236 GeV/c^2, though the strength of our signal prevents an investigation of this question, we appeal to the mass dependent width as an explanation. In the CLA determination of the amount of N*, the number of model events was demanded to equal the number of data events in the region of $\pm\Gamma$ ($\pm$.120 GeV/c^2) about the mass value of 1.236 GeV/c^2.

Cuts on the data and model were made where we accepted only those events in the N* region [1.116 - 1.356 GeV/c^2]. The N* was chosen as the $p\pi^-$ combination closest to 1.236 GeV/c^2 when both $p\pi^-$ combinations fell in the region. We examined all possible invariant mass and production angle plots resulting from this kinematic cut. We found no apparent deviation from the CLA model predictions. As we discussed earlier we used a cut on the K* region to determine the amount of simultaneous K*N* production.

The production angular distribution for the $\bar{K}^o\pi^-$ is shown in Figure 23(b) as the open histogram. This is also the production angular distribution for the $p\pi^-$ system if the sign of the abscissa is reversed. As seen previously, the CLA model adequately describes this distribution. No single particle distributions for the N* region will be shown here because of the small N* signal and the large background contribution in the N* region.

We have observed a broad enhancement in the $p\pi^-$ invariant mass distribution at about 1.680 GeV/c^2 (Figure 32). This enhancement is about 200 MeV/c^2 wide. We interpret this enhancement as the production of one or all of the nucleon-pion resonances known to reside near this

energy. These are the $\Delta(1650)$, $\Delta(1670)$, $N^*(1670)$, $N^*(1688)$ and $N^*(1700)$.[10] The limited amount of data made disentanglement of this region impossible. We determined that there were (72 ± 20) events in the "$N^*(1680)$" enhancement. This number was arrived at by using the CLA calculation as a background estimate. The background was renormalized to take this resonance contribution into account.

The invariant mass and the production angular distributions for the $\pi^-\pi^-$, $\overline{K}^0p$, $\overline{K}^0p\pi^-$ and $p\pi^-\pi^-$ systems were all found to be adequately described by the CLA model.

Figure 33(b) is the invariant mass distribution for the $\overline{K}^0\pi^-\pi^-$ system. Curve (1) is the result of the CLA calculation. We see a 3.5 standard deviation enhancement above background in the region from 1.680 to 2.080 GeV/c^2. We believe at least part of this effect to be a kinematic reflection of the production of $K^{*-}(1420)$. Since the $K^{*-}(1420)$ overpopulates the high end of phase space in the $\overline{K}^0\pi^-$ spectrum, we might expect a similar phenomenon in the $\overline{K}^0\pi^-\pi^-$ spectrum.

To display the effect of $K^{*-}(1420)$ production, we first reduced the normalization of the CLA calculation [Curve (1)] by 55 events. [We believe that there are 55 $K^{*-}(1420)$ events in this channel.] We then added in pure Lorentz invariant phase space for [$K^{*-}(1420)\pi^-$] from the final state $K^{*-}(1420)\pi^-p$, normalized to 55 events. We took the mass of the $K^{*-}(1420)$ to be a unique mass at 1.420 GeV/c^2. Curve (2) is the result of this sum. The shape of the data is well represented by Curve (2) and the enhancement is reduced to about 2.5 standard deviations. This is too small to imply a $\overline{K}^0\pi^-\pi^-$ resonance.

Figure 33.--Invariant mass plots for (a) $\overline{K}^{o}\pi^{-}p$ and (b) $\overline{K}^{o}\pi^{-}\pi^{-}$.

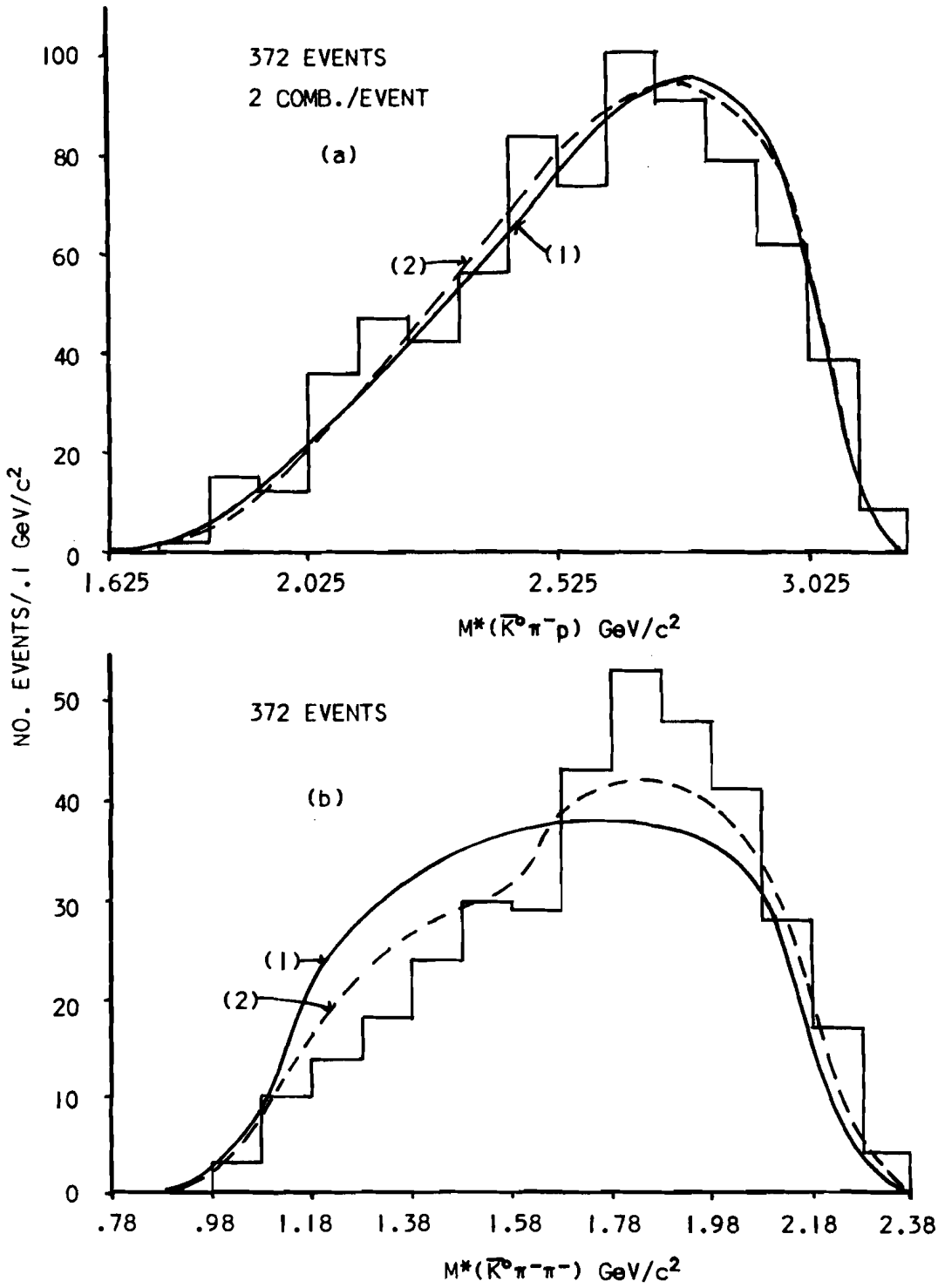
372 EVENTS
2 COMB./EVENT
(a)
(1)
(2)
100
80
60
40
20
0
1.625
2.025
2.525
3.025
M*(K̄°π⁻p) GeV/c²
NO. EVENTS/.1 GeV/c²
372 EVENTS
(b)
(1)
(2)
50
40
30
20
10
0
.78
.98
1.18
1.38
1.58
1.78
1.98
2.18
2.38
M*(K̄°π⁻π⁻) GeV/c²

We investigated what would happen to the distributions involving the $p\pi^-$ if the contribution of the 72 "N*(1680)" events were included. We found that since the "N*(1680)" occupied the middle region of the mass plot its effects were almost negligible in the three-body distributions. Figure 33(a) is the invariant mass distribution for the $\bar{K}^0\pi^-p$. Curve (1) is the CLA result. Curve (2) is the CLA model result modified to take 72 "N*(1680)" and 55 $K^{*-}(1420)$ events into account. This was done in the same manner as described for the $\bar{K}^0\pi^-\pi^-$ distribution. Curves (1) and (2) differ very little and both are reasonable descriptions of the data.

As mentioned earlier the b_i of Equation (IV-6) were found by a comparison to our data. The b_i govern the peripherality of the vertices in the region of high energies. An examination of the asymptotic form of the amplitude [Equation (IV-8) shows that small values of b_i cause the amplitude to prefer small values of momentum transfer. That is to say, smaller b_i make the model predictions more peripheral.

Figure 34 shows the dependence of the model predictions for the cosine of the single particle production angles (cos θ) on the b_i. The production angle is defined in the K^- target-neutron rest system as shown in Figure 35.

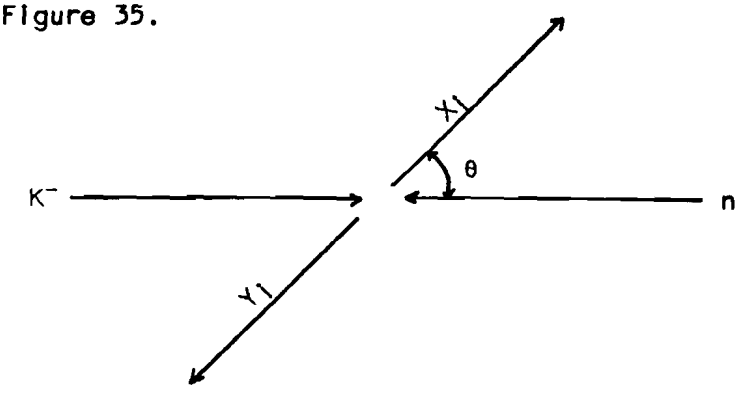

Figure 35.--A sketch defining production angle.

Figure 34.--The dependence of single particle production angle on CLA b_i for (a) π^-, (b) $\overline{K}^0$, and (c) proton.

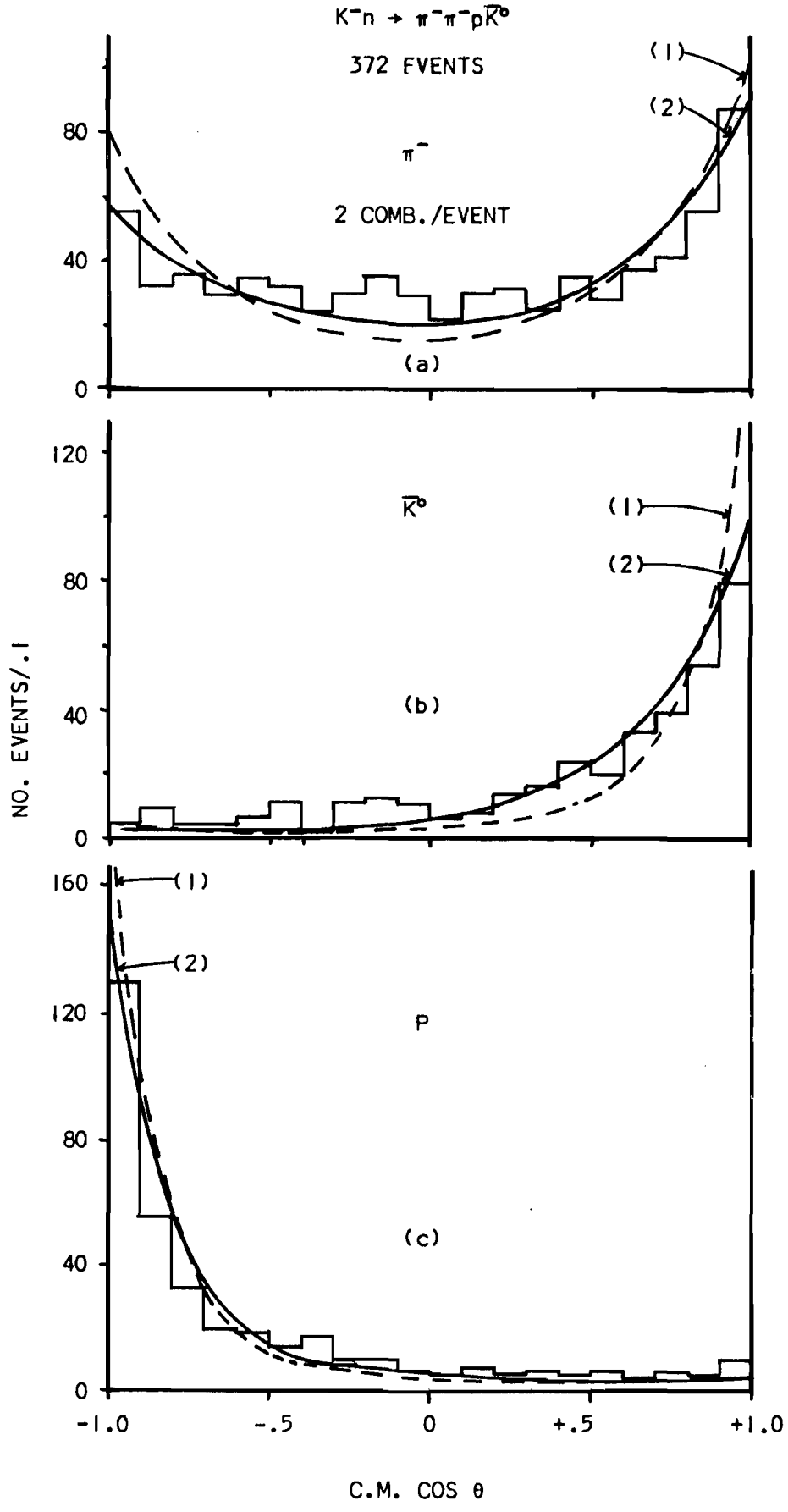
K⁻n → π⁻π⁻pK̄°
372 EVENTS
π⁻
2 COMB./EVENT
(a)
K̄°
(b)
P
(c)
(1)
(2)
NO. EVENTS/.1
C.M. COS θ
0
40
80
120
160
-1.0
-.5
0
+.5
+1.0

The angle θ is the production angle of the particle system X_i in the K^-n rest system.

Curve (1) in each case in Figure 34 is the result of the model calculations when the original CLA values for the b_i are used (1X). See Table 2. Curve (2) corresponds to the CLA calculations for the b_i set at double the CLA value (2X).

Because of the Monte Carlo approach to our model calculations, we are very dependent upon the use of a computer. Considering the computer time that would be required, we did not attempt to systematically fit all the parameters of the CLA model to our data. Instead, we attempted to find a convenient set of b_i that appeared to give a good qualitative description of all the single particle production angular distributions simultaneously. In choosing the final set of b_i that was to be used in subsequent calculations, we also examined the four- and five-body final states involving a Λ° or Σ° as well as the $\bar{K}^\circ$ four- and five-body states. Choosing one set of parameters, independent of multiplicity and final state particles, constitutes a check on the versatility of the CLA parameterization. The results of the CLA calculation for the Λ° and Σ° events is described in detail by R. Berg.[9]

As seen in Figure 34, the calculations using the b_i at one times the original values [Curve (1)] give too peripheral a prediction for the $\bar{K}^\circ$. The predictions for the b_i at 2X [Curve (2)] seem to be a more appropriate description of these data. Similar behavior was also seen in reactions II-6 and II-7. (These results will be shown later in this chapter when the two I-C reactions are discussed.)

We have chosen the 2X set as the parameters to be used in our data comparisons. This corresponds to $b_{EA} = 2.0$, $b_I = 2.4$, and $b_{EB} = 1.0$.

A χ^2 test was made comparing the data and the 2X calculations. The results were 19 per cent, 5 per cent, and 5 per cent for the $\overline{K}^o$, p, and π^-, respectively. These results along with the corresponding results for reactions II-6 and II-7 are shown in Table 6.

The π^- in Figure 34(a) is seen to be slightly peaked forward and backwards. This is not surprising since diagrams are permitted which allow the π^- to come from both the top and bottom vertices as well as the internal vertices.

The $\overline{K}^o$ in Figure 34(b) is strongly peaked in the forward direction. That is to say that the $\overline{K}^o$ continues along the direction of the initial K^-. The peaked production angular distribution corresponds to the $\overline{K}^o$ being emitted at the top vertex. For the $\overline{K}^o$ to appear at a lower vertex, a strange meson trajectory must be exchanged. Strange meson exchange is suppressed with respect to zero strangeness meson exchange because of its lower-lying trajectory (Table 3). No Pomeron exchange is allowed in this channel. Therefore the angular distributions should reflect competiton from non-strange meson, strange meson, and baryon exchange processes only. The $\overline{K}^o$ is restricted to the top two vertices in the four-vertex multiperipheral diagram because the emission from a lower vertex would require the exchange of a positively charged, negative-strangeness meson. No such particles are known to exist.

The proton, on the other hand, is strongly peaked in the backward hemisphere along the target direction. The proton is relatively

more peripheral than the $\bar{K}^{o}$. For the proton to appear at any vertex other than the bottom would require the exchange of a baryon trajectory, which is much lower-lying than the non-strange meson trajectory.

Another quantity which reflects the multiperipheral nature of the interaction is the longitudinal momentum (P_L). This quantity is defined in the K^-n rest system as the projection of the particle momentum on the K^- direction. Positive projections correspond to a component along the beam. Negative values refer to projections along the target direction (see Figure 35).

$$P_L = \vec{P} \cdot \hat{P}_{K^-} \text{ and } \hat{P}_{K^-} = - \hat{P}_n, \qquad \text{(V-11)}$$

where $\vec{P}$ is the vector momentum of the particle of interest and $\hat{P}_{K^-}$ and $\hat{P}_n$ are unit vectors in the direction of the momenta of the K^- and target neutron, respectively. Figures 36(a), (b), and (c) are the longitudinal momenta and the corresponding CLA calculations for the π^-, $\bar{K}^{o}$, and P, respectively.

Figure 36(a) shows that the π^- is generally produced with small values of longitudinal momentum and with approximate symmetry in the forward and backward directions.

Figure 36(b) shows that the $\bar{K}^{o}$ is generally produced with large longitudinal momentum in the forward direction. Figure 36(c) shows that the proton, on the other hand, is produced with an even larger longitudinal momentum in the backward direction.

We calculated the average values of P_L for the data and also the model for each single particle distribution. The result are shown in Table 7.

Figure 36.--The longitudinal momentum distributions for the single particles (a) π^-, (b) $\overline{K}^0$, and (c) proton produced in reaction II-5.

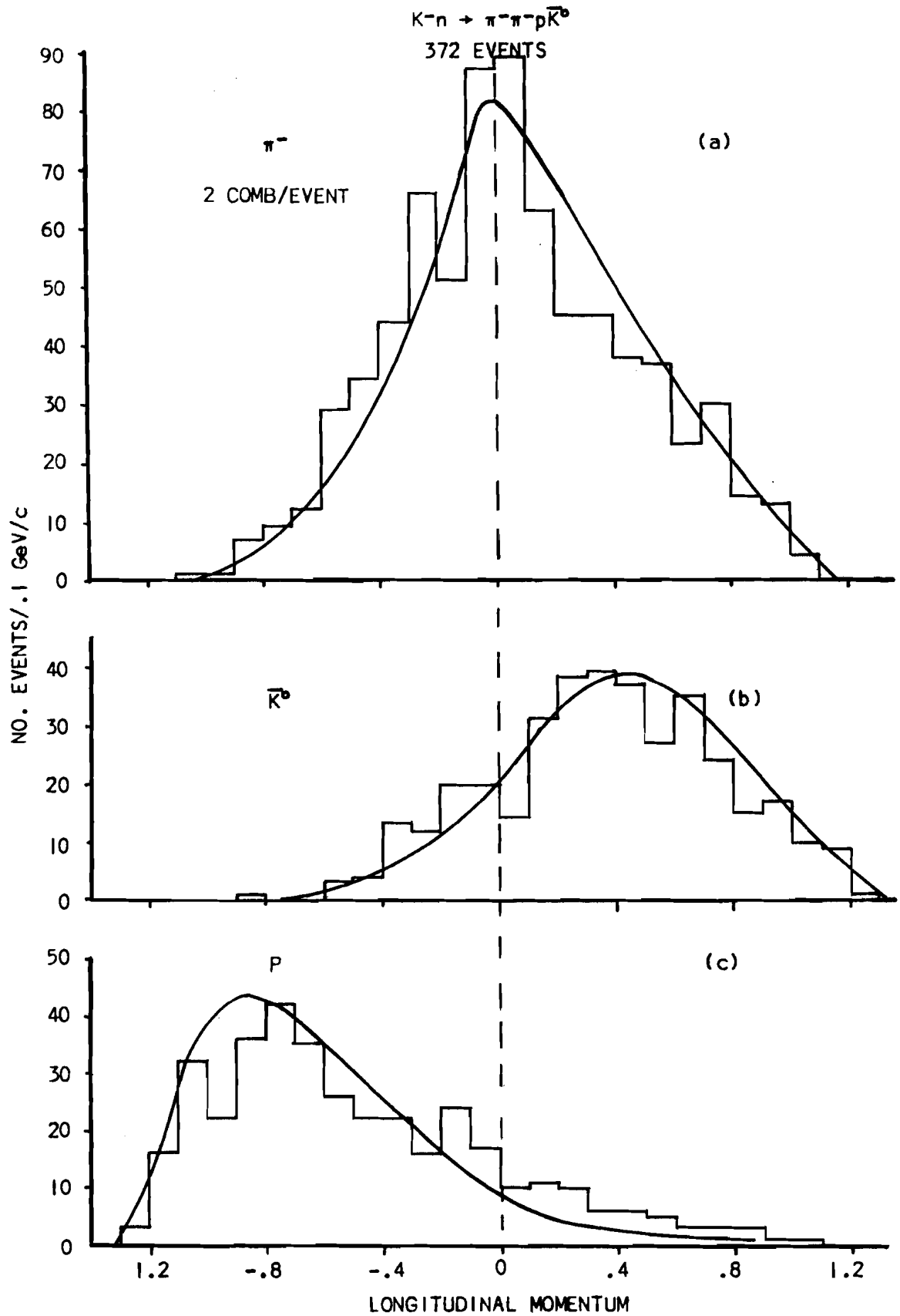
K⁻n → π⁻π⁻pK̄⁰
372 EVENTS
π⁻
2 COMB/EVENT
(a)
K̄⁰
(b)
P
(c)
NO. EVENTS/.1 GeV/c
LONGITUDINAL MOMENTUM
90
80
70
60
50
40
30
20
10
0
1.2
-.8
-.4
0
.4
.8
1.2

Figures 37(a), (b), and (c) are the distributions in the transverse momentum (P_T) for the π^-, $\bar{K}^o$, and P, respectively. This quantity is given by

$$P_T = \sqrt{|\vec{P}|^2 - P_L^2}, \qquad \text{(V-12)}$$

where $\vec{P}$ is the particle momentum and P_L is longitudinal momentum. These distributions are similar for the π^-, $\bar{K}^o$, and proton. The average measured and calculated values of P_T for each of these particles are given in Table 7.

The CLA model calculation qualitatively reproduced the observed single particle longitudinal and transverse momentum distributions.

The $|t - t_{min}|$ distributions for the π^-, $\bar{K}^o$, and proton were plotted and were found to be in qualitative agreement with the CLA model calculations. These distributions are not shown here since they are not independent of P_L and P_T. Although P_L and P_T are not independent of the production angle, they do contain additional information.

2. Comparison of the data with the model of Plahte and Roberts

The amount of resonance production is, in our opinion, the most important question to ask of this modified CLA model. Figure 38 is the invariant mass distribution of the $\bar{K}^o\pi^-$ for reaction II-5. The dashed curve is the prediction of the Plahte and Roberts model where we have included all diagrams that might contribute to the final state. The model under predicts the amount of $K^{*-}(890)$. Figure 39 is the effective mass distribution of the $p\pi^-$ system. The model in this case (dashed curve) over predicts the amount of $N^{*o}(1236)$. The effective mass distributions of the other non-resonating particle combinations ($p\bar{K}^o$, $\bar{K}^o p\pi^-$,

Figure 37.--The transverse momentum distributions for the single particles (a) π^-, (b) $\overline{K}^0$, and (c) proton produced in reaction II-5.

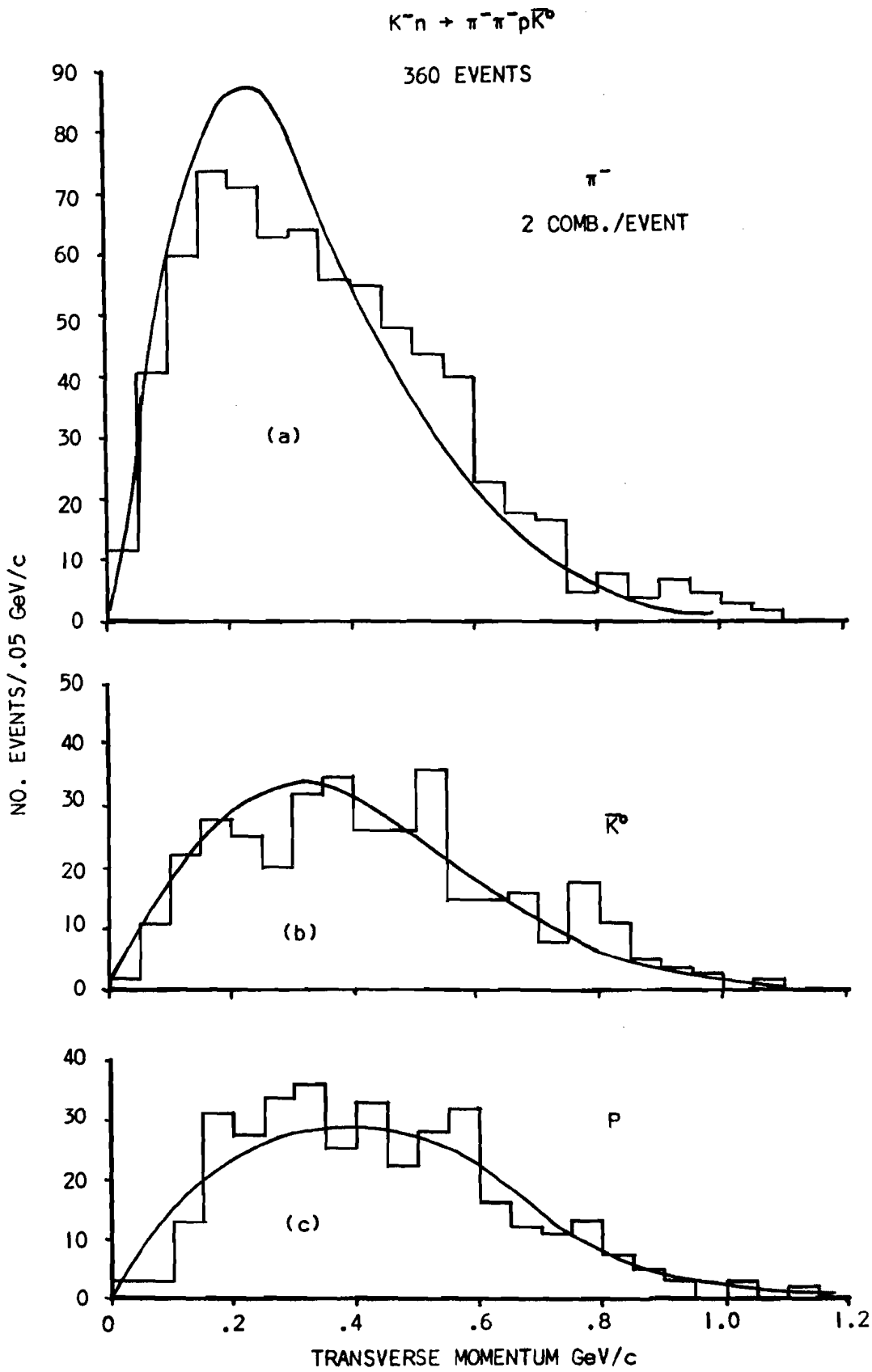
$K^-n \to \pi^-\pi^-p\bar{K}^0$
360 EVENTS
π^-
2 COMB./EVENT
(a)
(b)
$\bar{K}^0$
(c)
P
NO. EVENTS/.05 GeV/c
TRANSVERSE MOMENTUM GeV/c
0
.2
.4
.6
.8
1.0
1.2

Figure 38.--A comparison of $\overline{K}^{o}\pi^{-}$ invariant mass distribution with Plahte and Roberts model.

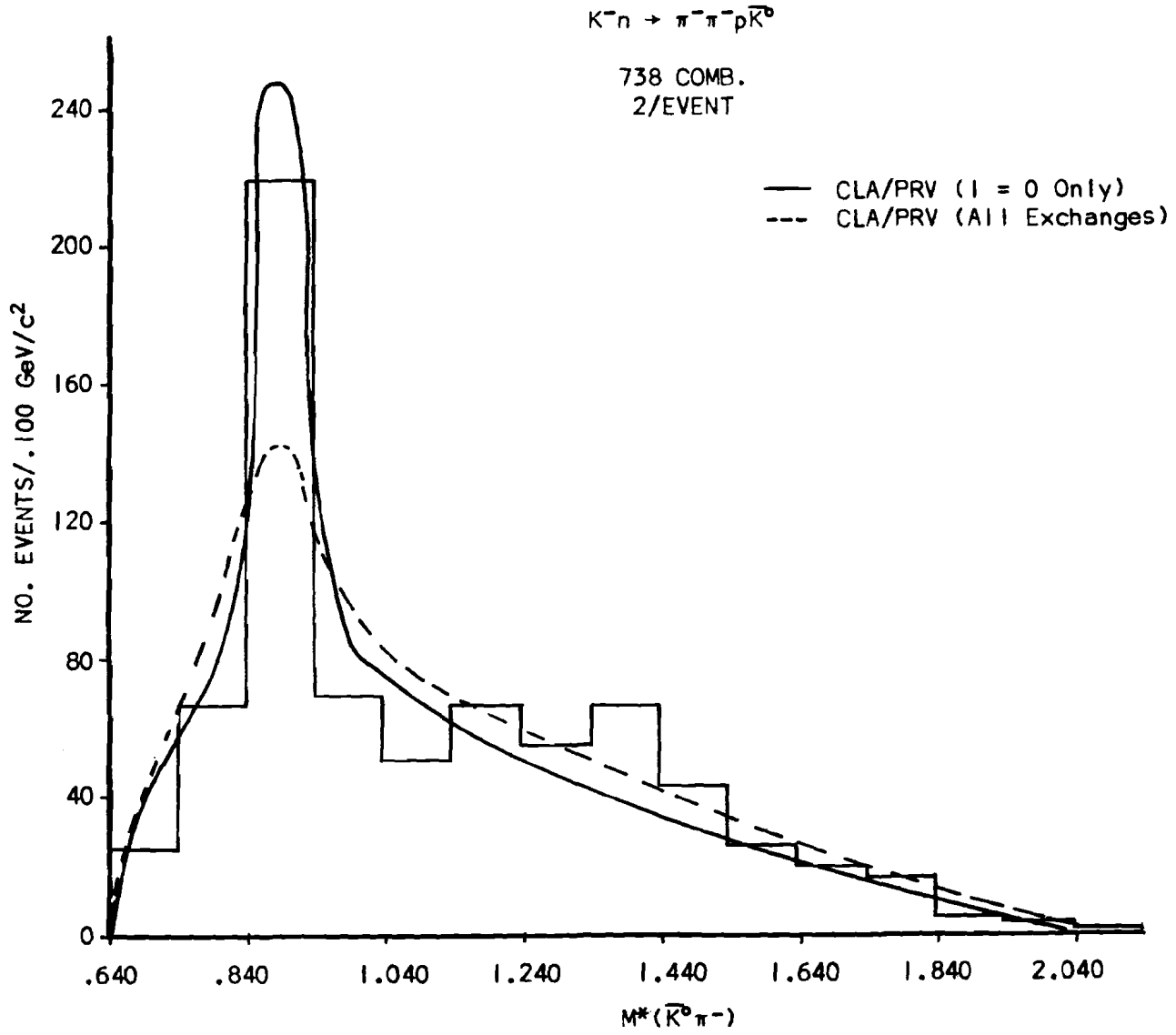
$K^-n \to \pi^-\pi^-p\overline{K}^0$
738 COMB.
2/EVENT
CLA/PRV (I = 0 Only)
CLA/PRV (All Exchanges)
NO. EVENTS/.100 GeV/c²
0
40
80
120
160
200
240
.640
.840
1.040
1.240
1.440
1.640
1.840
2.040
$M^*(\overline{K}^0\pi^-)$

Figure 39.--A comparison of $p\pi^-$ invariant mass distribution with Plahte and Roberts model.

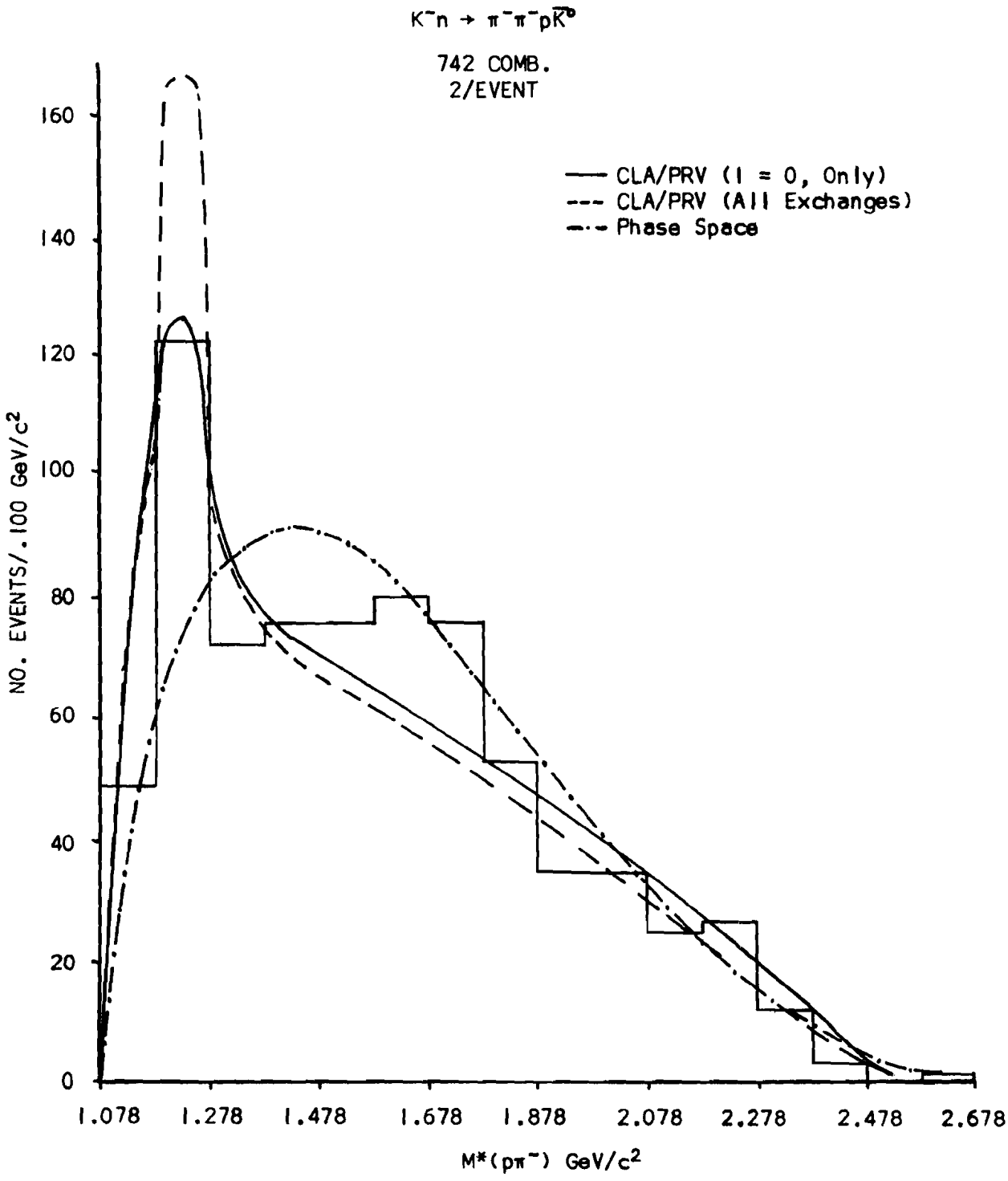
$K^-n \to \pi^-\pi^-p\bar{K}^0$
742 COMB.
2/EVENT
CLA/PRV (I = 0, Only)
CLA/PRV (All Exchanges)
Phase Space
NO. EVENTS/.100 GeV/c²
0
20
40
60
80
100
120
140
160
1.078
1.278
1.478
1.678
1.878
2.078
2.278
2.478
2.678
M*(pπ⁻) GeV/c²

$\bar{K}^{o}\pi\pi^{-}$, $p\pi^{-}\pi^{-}$) were found to be in qualitative agreement with the model. Figure 40 shows the observed and computed single particle production angular distributions. The model generally under predicts the peripherality of the proton, and correctly predicts the production angular distribution for the $\bar{K}^{o}$. The amount of π^{-} is slightly over predicted in the backward direction. Summarizing the model comparison, we find the modified model does not give realistic predictions of amounts of resonance production in our data and generally gives poorer estimates of single particle production angular distributions than the original CLA model.

In our attempt to rectify this disagreement, we found the amount of resonance formation predicted to be sensitive to the isotopic spin of the innermost exchanged trajectory. We can get an understanding of the isotopic spin dependence by considering the typical diagram for $K^{-}n \rightarrow \bar{K}^{o}\pi^{-}\pi^{-}p$ shown in Figure 41.

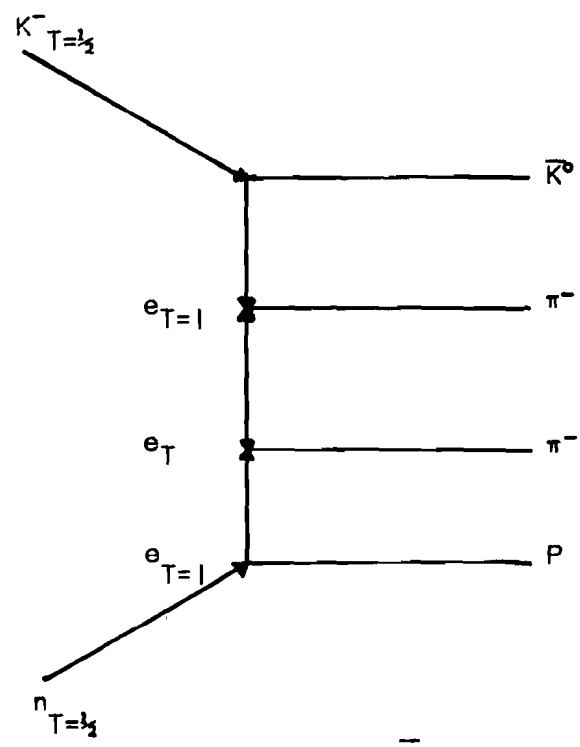

Figure 41.--A multiperipheral diagram for $K^{-}n \rightarrow \bar{K}^{o}\pi^{-}\pi^{-}p$.

Figure 40.--Dependence of single particle production angle on exchanged trajectories for Plahte and Roberts model calculation (a) π^-, (b) $\bar{K}^0$, and (c) P.

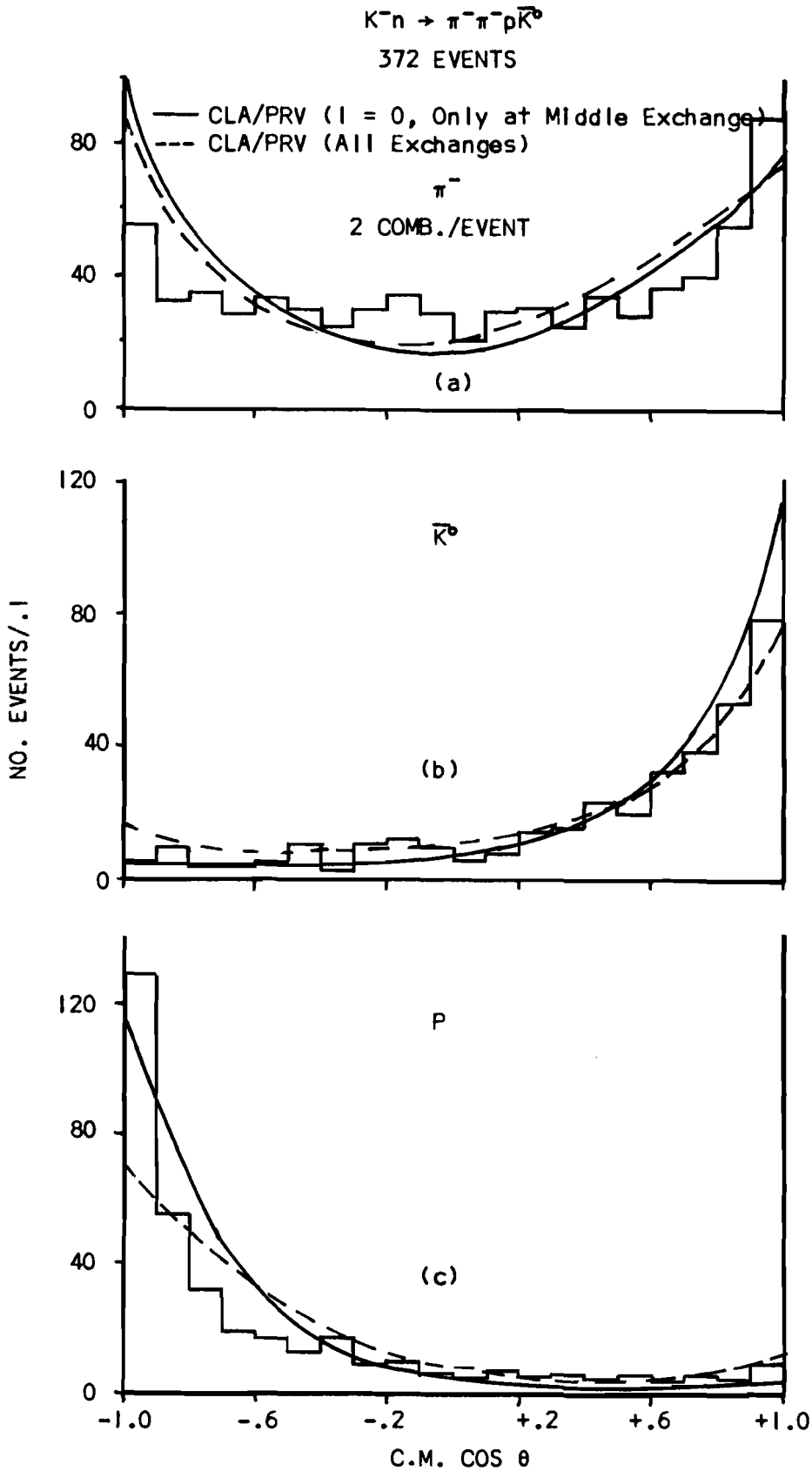
K⁻n → π⁻π⁻pK̄⁰
372 EVENTS
CLA/PRV (I = 0, Only at Middle Exchange)
CLA/PRV (All Exchanges)
π⁻
2 COMB./EVENT
(a)
K̄⁰
(b)
P
(c)
NO. EVENTS/.1
0
40
80
120
-1.0
-.6
-.2
+.2
+.6
+1.0
C.M. COS θ

In the preceeding diagram, the middle exchanged trajectory, e_T, can have isotopic spin $T_e = 0$ or $T_e = 1$. If we allow $T_e = 1$, then the $\overline{K}^0\pi^-$ system may have either $T = 1/2$ [K*(890) trajectory] or $T = 3/2$ (purely non-resonant). Likewise, $T_e = 1$ allows the $p\pi^-$ to have $T = 1/2$ (purely non-resonant) and $T = 3/2$ [N*(1236) trajectory]. However, if we allow only $T_e = 0$, the $\overline{K}^0\pi^-$ can form only K* trajectory in the diagram, and thus one expects more K*(890) production. Also, the $p\pi^-$ can not form N*; N*'s can be formed only when the proton emerges from an internal vertex. Thus one expects that allowing $T_e = 0$ only will decrease the relative amount of N*(1236) predicted.

The solid curves in Figures 38, 39, and 40 represent the model's predictions allowing only $T_e = 0$. Generally the agreement is much better in both effective mass distributions and production angular distributions. The number of events in the regions of the $K^{*-}(890)$ and $N^{*0}(1238)$ quantitatively agree with the data and the single particle angular distributions qualitatively agree with the data.

If $T_e = 0$ is demanded by the data and the proton really does come from an internal vertex, this should be reflected in the production angular distribution of the proton from the $N^{*0}(1236)$ decay.

Figure 42(a) is a plot of the proton production angular distribution for those events in the $N^{*0}(1236)$ region. The effective mass of the $p\pi^-$ system was demanded to be within $\pm\Gamma(N^*)$ of the N* mass where $\Gamma(N^*) = .120$ GeV/c^2 and the mass of the N* is 1.236 GeV/c^2. The model is seen to prefer a much less peripheral proton than the data show. We must conclude that the model's restricting the proton to an internal vertex for N*(1236) production does not seem to correspond to what is happening in

Figure 42.--(a) The $N^{*\circ}(1236)$ production angular distribution compared to Plahte and Roberts model restricted to $I = 0$ exchange. (b) Corresponding plot for control region $1.390 \leq M^*(p\pi^-) \leq 1.590$ GeV/c^2.

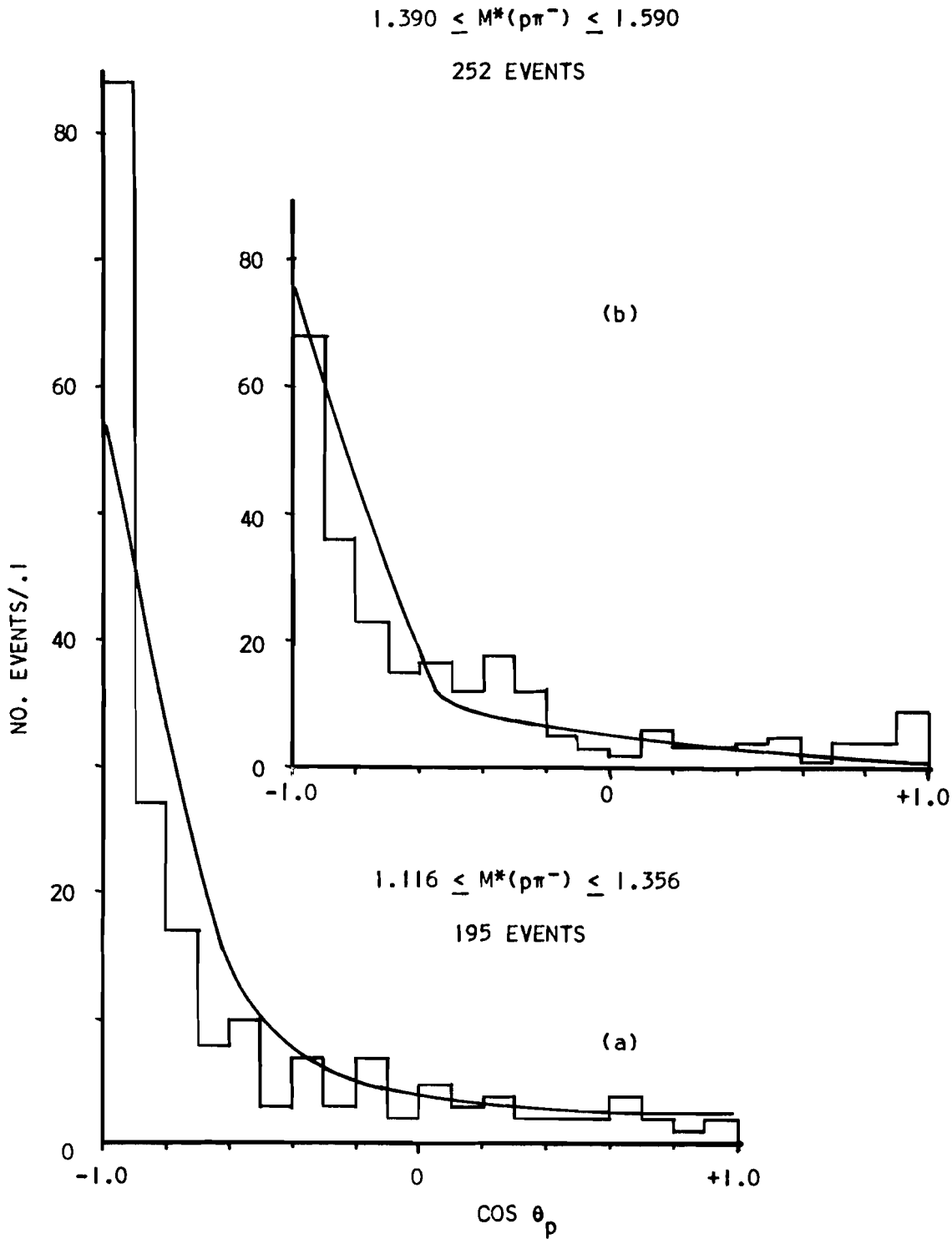
1.390 ≤ M*(pπ⁻) ≤ 1.590
252 EVENTS
(b)
1.116 ≤ M*(pπ⁻) ≤ 1.356
195 EVENTS
(a)
NO. EVENTS/.1
COS θp
0
20
40
60
80
-1.0
0
+1.0

the data and restricting $T_e = 0$ does not produce agreement with the data. Figure 42(b) is the equivalent cos θ plot where the $p\pi^-$ mass was demanded to be between 1.390 to 1.590 GeV/c^2. Here the model is able to qualitatively describe the data. This control confirms that the difficulty with the backward produced protons is associated with the N*(1236) mass region.

The production of $K^{*-}(890)$ is by far the most prominent feature of the 4-C channel. Figure 43 shows the production cos θ distribution for those events falling in the K* band. The curve is the result of the modified CLA model calculation. The calculation is in quantitative disagreement in the forward direction, but shows qualitative agreement.

The Plahte and Roberts model, as we have parameterized it, gives quantitatively wrong resonance predictions. In passing, it should be stated that it gives qualitatively poorer fits to the production angular distributions than the original CLA model. In fairness to the model we remind the reader that an approximate method was used for including isospin. If we restrict the middle exchanged trajectory to isospin zero, the model gives good qualitative agreement with the data.

B. $K^-n \rightarrow \pi^-\pi^- p\bar{K}^0\pi^0$

There were 418 events satisfying the kinematic hypothesis $K^-n \rightarrow \pi^-\pi^-p\bar{K}^0\pi^0$ with spectator proton momentum less than .275 GeV/c. The requirement that the main vertex χ^2 probability be greater than or equal 5 per cent reduced the sample to 373 events. Corrections for vees lost out the end of the bubble chamber (see Chapter III, Section F) increased the number of events to 375. This sample of 375 events was used in the following analysis of this hypothesis.

Figure 43.--The production angular distribution for $K^{*-}(890)$ compared to Plahte and Roberts model calculation requiring I = 0 exchange only.

$K^- n \rightarrow \pi^- \pi^- p \bar{K}^0$

$.840 \leq M(\bar{K}^0 \pi^-) \leq .940$ GeV/c^2

200 EVENTS

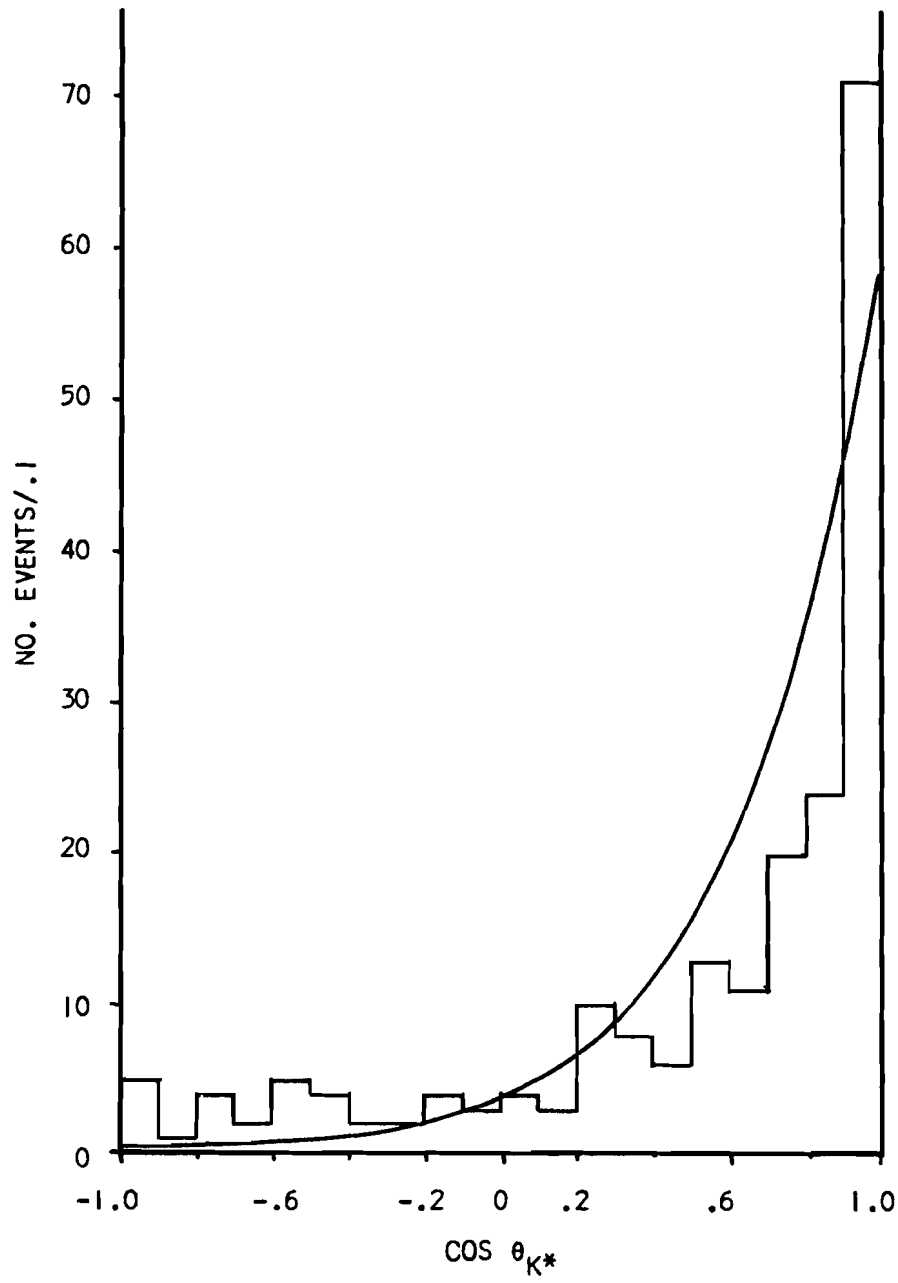

The production of $K^{*-}(890)$ is by far the most prominent feature of this channel. Figure 44(a) is the invariant mass distribution of the $\bar{K}^{o}\pi^{-}$. Each event contributed two entries to the histogram corresponding to the two possible $\bar{K}^{o}\pi^{-}$ combinations. The strong $K^{*-}(890)$ signal is apparent. Using the results of fitting the CLA model calculation to this histogram we have determined that (169 ± 20) events belong to the channel

$$K^{-}n \rightarrow K^{*-}(890)\pi^{-}\pi^{o}p.$$
$$\rightarrow \bar{K}^{o}\pi^{-}$$

The cross-section for K^{*} production in this channel after correction for unseen decay modes of the $\bar{K}^{o}$ is (149 ± 28) μbarns.

Curve (1) of Figure 44(a) is pure Lorentz invariant phase space for the $\bar{K}^{o}\pi^{-}$ from the five-bodies final state given by reaction II-6. Curve (2) in the same figure is the result of the CLA calculation. The CLA model gives an excellent fit to the data. Using the CLA model as a background estimate, we see no evidence for other resonance structure in this invariant mass distribution.

Figure 44(b) is the CM production angular distribution for the same events as shown in Figure 44(a) (the open histogram). The curve is the result of the CLA model calculation. The model calculation agrees with the data. When Figure 44(b) is compared to the corresponding $\bar{K}^{o}\pi^{-}$ distribution of the 4-C events [Figure 23(b)], the 4-C distribution is found to be much more peaked. This difference persists when the mass of the $\bar{K}^{o}\pi^{-}$ system is required to be within the K^{*} region (.840 to .940 GeV/c^{2}). The production angular distribution for those events in the K^{*} region in this channel are shown in Figure 44(b) as the shaded histogram.

Figure 44.--(a) The $\bar{K}^{o}\pi^{-}$ effective mass distribution for reaction II-6. (b) Corresponding production angular distribution.

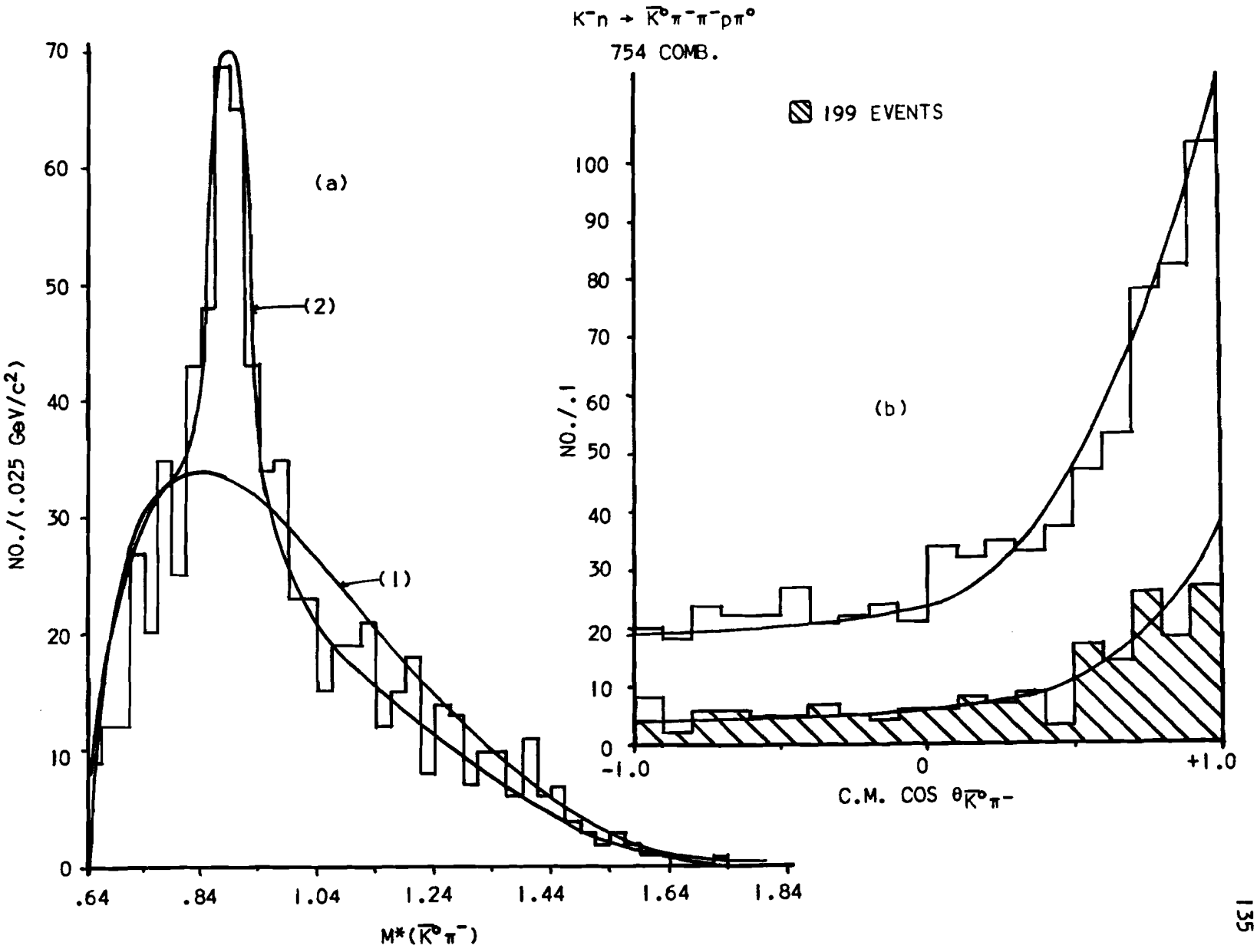
K⁻n → K̄°π⁻π⁻pπ°
754 COMB.
199 EVENTS
(a)
(b)
(1)
(2)
NO./(.025 GeV/c²)
NO./.1
M*(K̄°π⁻)
C.M. COS θK̄°π⁻
0
10
20
30
40
50
60
70
80
90
100
.64
.84
1.04
1.24
1.44
1.64
1.84
-1.0
+1.0

The curve corresponding to the shaded histogram is the CLA prediction, and is seen to be a reasonable description of the data.

The distribution in the production angle for the K* region was found to be consistent with the corresponding distribution for the total sample within statistical errors.

For a more quantitative description of the peripherality of the K*, a least squares fit to an exponential was made for the $|t - t_{min}|$ distribution for the $\overline{K}^0\pi^-$ system for those events falling in the K* band (.840 - .940 GeV/c^2). The quantities t and t_{min} are defined in Section A of this chapter and refer to the squared four-momentum transfer from the incident K^- to the outgoing $\overline{K}^0\pi^-$ system. A background estimate for the $|t - t_{min}|$ distribution was made by using the control regions above (.965 to 1.165 GeV/c^2) and below (.640 to .815 GeV/c^2) the K* region. The $|t - t_{min}|$ distribution resulting from the sum of the two control regions was compared to the $|t - t_{min}|$ distribution for the K* region. The shapes of the two distributions agreed with a χ^2 probability of about 45 per cent. This implies that the background and K* events have the same distribution. Consequently, no background subtraction was made.

Figure 24(b) is a semi-logarithmic plot of the $|t - t_{min}|$ distribution for the events in the K* region. The data are indicated by X's with the error bars determined by available statistics. The circles are the results of the CLA calculation. The straight line is the result of a least squares fit to the data. As mentioned earlier, the K* events produced in reaction II-7 could not be described by a single exponential. For consistency we chose to only fit the region below 1.0 $(GeV/c)^2$. The fit yielded an exponential slope

$$\lambda = (.37 \pm .33)(GeV/c)^{-2}.$$

This fit corresponds to a χ^2 probability of about 85 per cent for the region below 1.0 $(GeV/c)^2$. The χ^2 probability that the region above 1.0 $(GeV/c)^2$ can be described by the same exponential dependence as the region below 1.0 $(GeV/c)^2$ is 33 per cent. The CLA calculations were found to be in quantitative agreement with the data.

All invariant mass distributions were examined for those events which had a $\bar{K}^o\pi^-$ falling within the K* band. They revealed no statistically significant structure above the background. The CLA model with the same cut on the $\bar{K}^o\pi^-$ invariant was used as the background estimate.

The decay angular distributions of the K*(890) in the Jackson frame of reference are shown in Figure 45. A sketch of the coordinate axes is shown in Figure 29.

The ϕ distribution in Figure 45(a) was found to be consistent with a flat distribution. A χ^2 test comparing the data with a flat distribution yielded a χ^2 probability of about 40 per cent.

Since the Jackson cos θ distributions for the peak and control regions compared poorly (χ^2 probability of about 9%), we made a background subtraction of 87 events. The results are shown in Figure 45(b).

The cos θ distribution was found to have a χ^2 probability of about 6 per cent for being flat.

The curve in Figure 45(b) is the result of a least squares fit to the expected function of the form

$$A + B \cos^2 \theta, \qquad \text{(V-13)}$$

normalized to the total number of events. The quantities A and B are unknown parameters to be determined from the fit. When the result of

Figure 45.--Jackson frame distributions for $K^{*-}(890)$ produced in reaction II-6; (a) ϕ, and (b) $\cos\theta$.

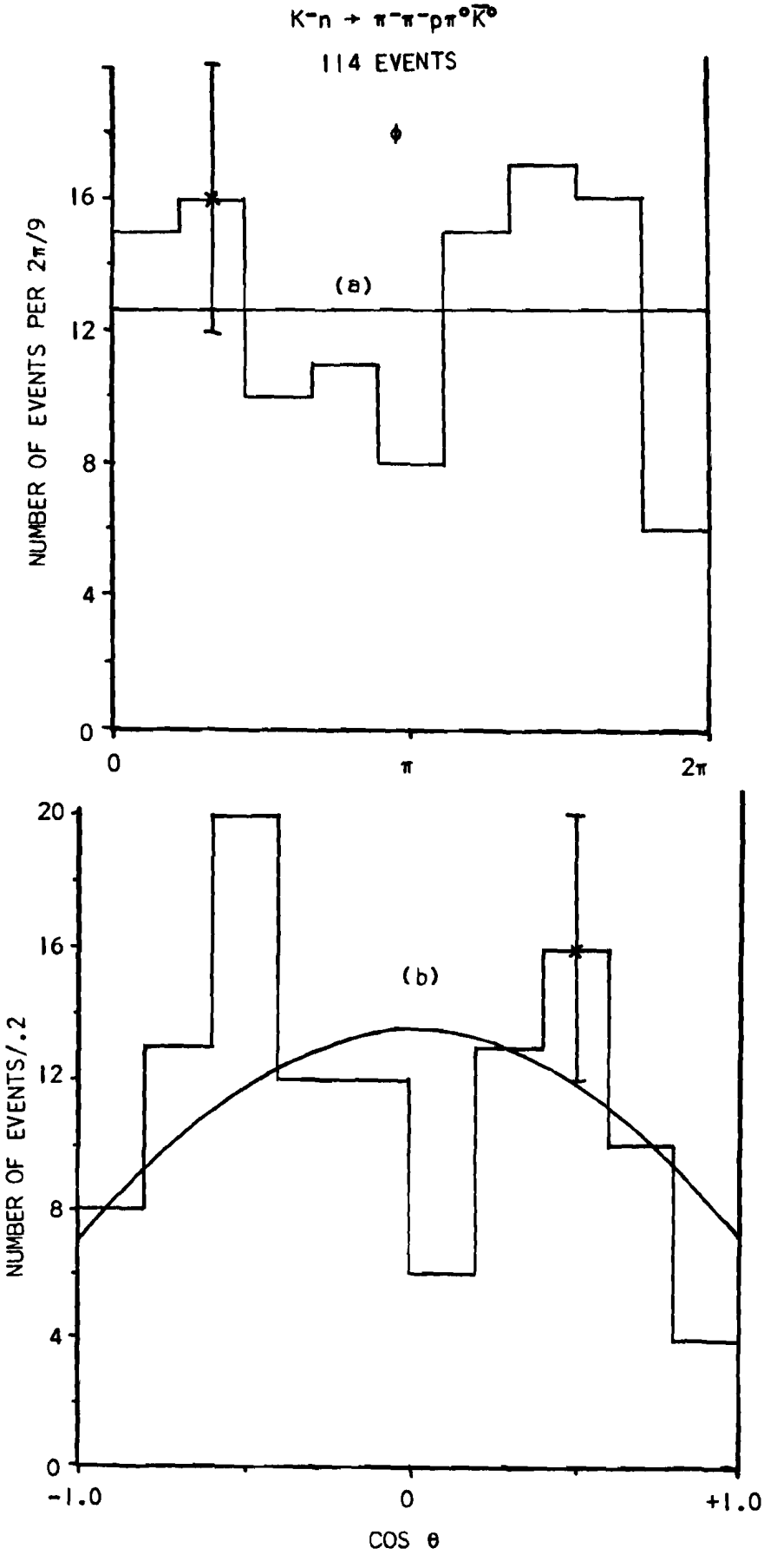
K⁻n → π⁻π⁻pπ⁰K̄⁰
114 EVENTS
φ
(a)
NUMBER OF EVENTS PER 2π/9
0
4
8
12
16
0
π
2π
(b)
NUMBER OF EVENTS/.2
0
4
8
12
16
20
-1.0
0
+1.0
COS θ

the fit was compared to the data, the χ^2 probability was found to be about 9 per cent. This is because the data apparently do not have the shape given by W(cos θ). We regard this result as no improvement over a flat interpretation, and consequently decided not to fit for all the spin density matrix elements. We remind the reader that the usual spin density matrix element formalism assumes the decay of a pure spin-parity state.[50]

There were many possible particle combinations involving some of the five particles in this final state. We examined all invariant mass histograms and all production angular distributions resulting from these particle combinations. We found that the CLA model generally gave an adequate description of the data. Because of the large number of distributions involved, we will only show those distributions where the CLA model and data do not show close agreement.

Figure 46 is the invariant mass distribution for the $\bar{K}^0\pi^-\pi^0$. Here we see a 4.4 standard deviation enhancement above the background given by the CLA model in the region from 1.580 to 1.880 GeV/c^2. This enhancement falls in the region of the controversial L-meson. The L was first reported by Bartsch et al.[51] at a mass of about 1.775 GeV/c^2 and a width of .127 GeV/c^2. They describe the L as a resonance with a branching ratio of about 20 per cent to K*(1420)π. In a much larger experiment Barbaro-Galtieri et al.[52] found a broad peak (300 - 500 MeV) and described it as a threshold enhancement of the K*(1420)π system. More recently, Aguilar-Benitez et al.[53] have reported seeing the L in $K^-p \rightarrow K^-\pi^+\pi^-p$ at 4.6 GeV/c with almost identical properties as reported by Bartsch et al.

Figure 46.--Invariant mass distribution for $\bar{K}^{o}\pi^{-}\pi^{o}$ produced in reaction 11-6.

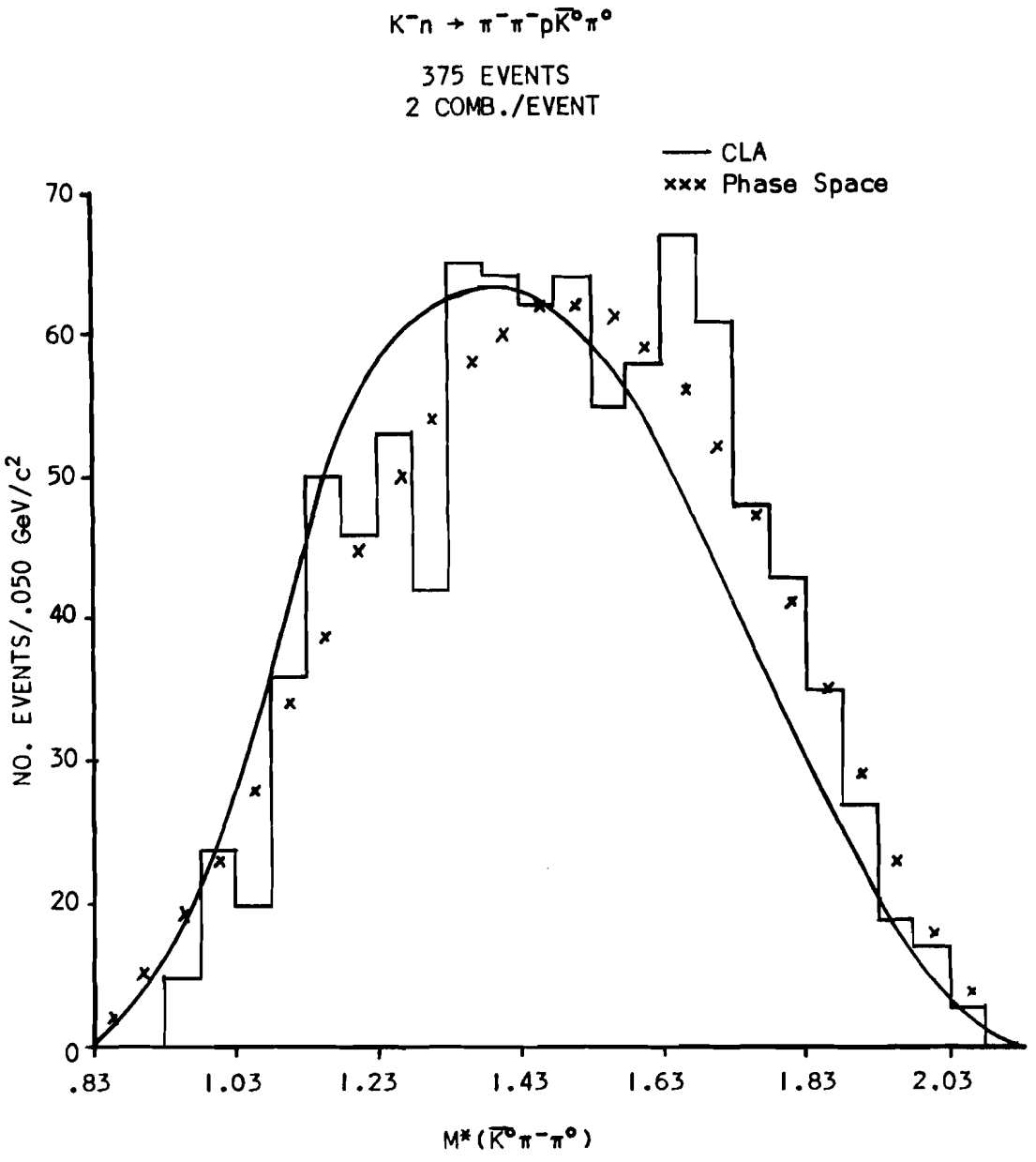
K⁻n → π⁻π⁻pK̄°π°
375 EVENTS
2 COMB./EVENT
CLA
xxx Phase Space
NO. EVENTS/.050 GeV/c²
0
20
30
40
50
60
70
.83
1.03
1.23
1.43
1.63
1.83
2.03
M*(K̄°π⁻π°)

All possible invariant mass distributions were plotted for those events with $\bar{K}^{o}\pi^{-}\pi^{o}$ mass between 1.580 and 1.880 GeV/c^2. The plots revealed no structure above background. In particular, the $\bar{K}^{o}\pi^{-}$ distribution showed no evidence of K*(1420) production. The CLA model was used as a background estimate. In a short while, we will again return to this question of the L-meson.

We have observed a 3.8 standard deviation depletion in the $\pi^{-}\pi^{o}$ invariant mass distribution from .280 to .580 GeV/c^2. This discrepancy is not significant and is mentioned here only because it will be considered as a possible contributing factor in the $\bar{K}^{o}\pi^{-}\pi^{-}\pi^{o}$ enhancement, to be discussed next.

We have observed a 5.9 standard deviation enhancement in the invariant mass distribution of $\bar{K}^{o}\pi^{-}\pi^{-}\pi^{o}$. This enhancement is in the region from 2.110 to 2.210 GeV/c^2 as seen in Figure 47. Because of the exotic quantum numbers, we do not expect resonance formation in this particle combination.

As noted previously, we have deviations from the background estimates in both the $\pi^{-}\pi^{o}$ and the $\bar{K}^{o}\pi^{-}\pi^{o}$ invariant mass distributions. Since the $\bar{K}^{o}\pi^{-}\pi^{-}\pi^{o}$ system contains these particle combinations, we made an effort to determine the effect of the $\pi^{o}\pi^{-}$ and $\bar{K}^{o}\pi^{-}\pi^{o}$ discrepancies on the $\bar{K}^{o}\pi^{-}\pi^{-}\pi^{o}$ enhancement. We used the same technique as described for the K^{*-}(1420) and "N*(1680)" corrections in Section A. We generated the pure phase space distributions for $\bar{K}^{o}\pi^{-}(\pi^{-}\pi^{o})$ and $(\bar{K}^{o}\pi^{-}\pi^{o})\pi^{-}$ combinations from the five body final state $\bar{K}^{o}\pi^{-}\pi^{-}\pi^{o}p$, where the particles in parentheses were assigned a single effective mass value. The unique mass assigned to the particle combinations was chosen as the approximate

Figure 47.--Invariant mass distribution for $\overline{K}^{o}\pi^{-}\pi^{-}\pi^{o}$ produced in reaction II-6.

$K^- n \rightarrow \pi^- \pi^- \pi^0 p \overline{K}^0$

375 EVENTS

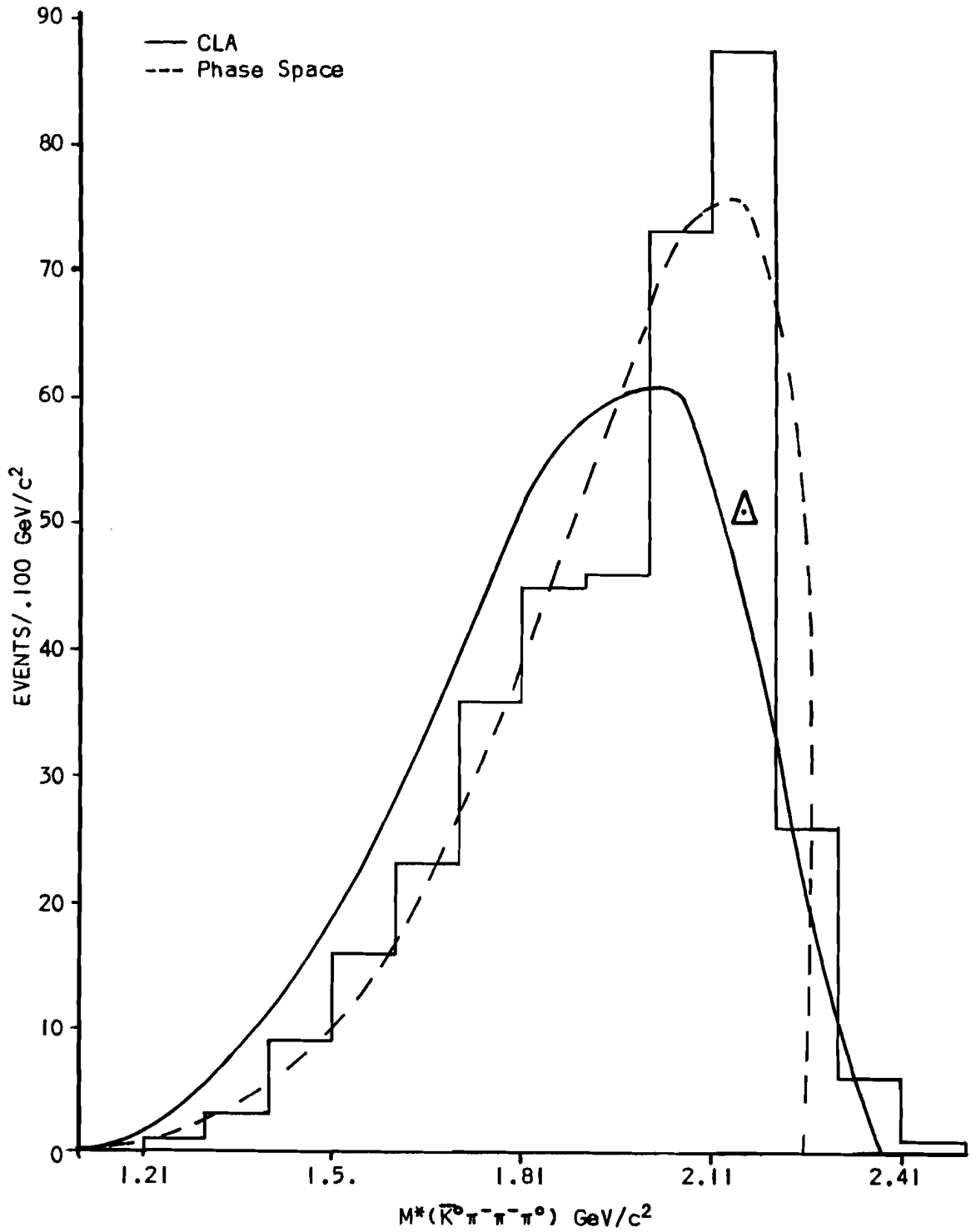

center of the enhancement in the case of the $\bar{K}^{o}\pi^{-}\pi^{o}$, and at the center of the depletion for the $\pi^{-}\pi^{o}$. When the $\bar{K}^{o}\pi^{-}\pi^{-}\pi^{o}$ distribution was corrected for those two deviations, the statistical significance of the enhancement was reduced to 4.7 standard deviations. The triangle in Figure 47 represents the resulting background prediction for the enhancement region when these corrections are applied to the CLA model calculation.

Though we were unable to completely explain the $(\bar{K}^{o}\pi^{-}\pi^{-}\pi^{o})$ enhancement as a kinematic reflection, we do not claim it to be a resonance. It lies at the extreme edge of phase space and is not narrow. The possibility exists that some unknown mechanism is causing the events to pile up at the kinematic limit. Also, the statistical evidence is not compelling.

Returning to the $\bar{K}^{o}\pi^{-}\pi^{o}$ enhancement, we found that if we corrected the distribution of the $\bar{K}^{o}\pi^{-}\pi^{o}$ invariant masses to take into account the $\pi^{o}\pi^{-}$ depletion and the $\bar{K}^{o}\pi^{-}\pi^{-}\pi^{o}$ enhancement, the statistical significance of the signal could be reduced from 4.4 standard deviations to 2.6 standard deviations. We are forced to conclude that we cannot say that we see the L-meson.

We conclude that the only resonance that we have definitely observed to be formed in Reaction II-6 is the $K^{*-}(890)$.

As discussed earlier in connection with the 4-C single particle production angular distributions, the b_i in Equation (IV-6) were chosen by an examination of the data. It was stated earlier that the b_i set at a value two times the original CLA values of Table 2 appear to give a better fit to our data and that of R. Berg.[9] Figures 48 and 49 are the

Figure 48.--The dependence of single particle production angles on CLA b_1 for (a) $\overline{K}^0$ and (b) proton produced in reaction 11-6.

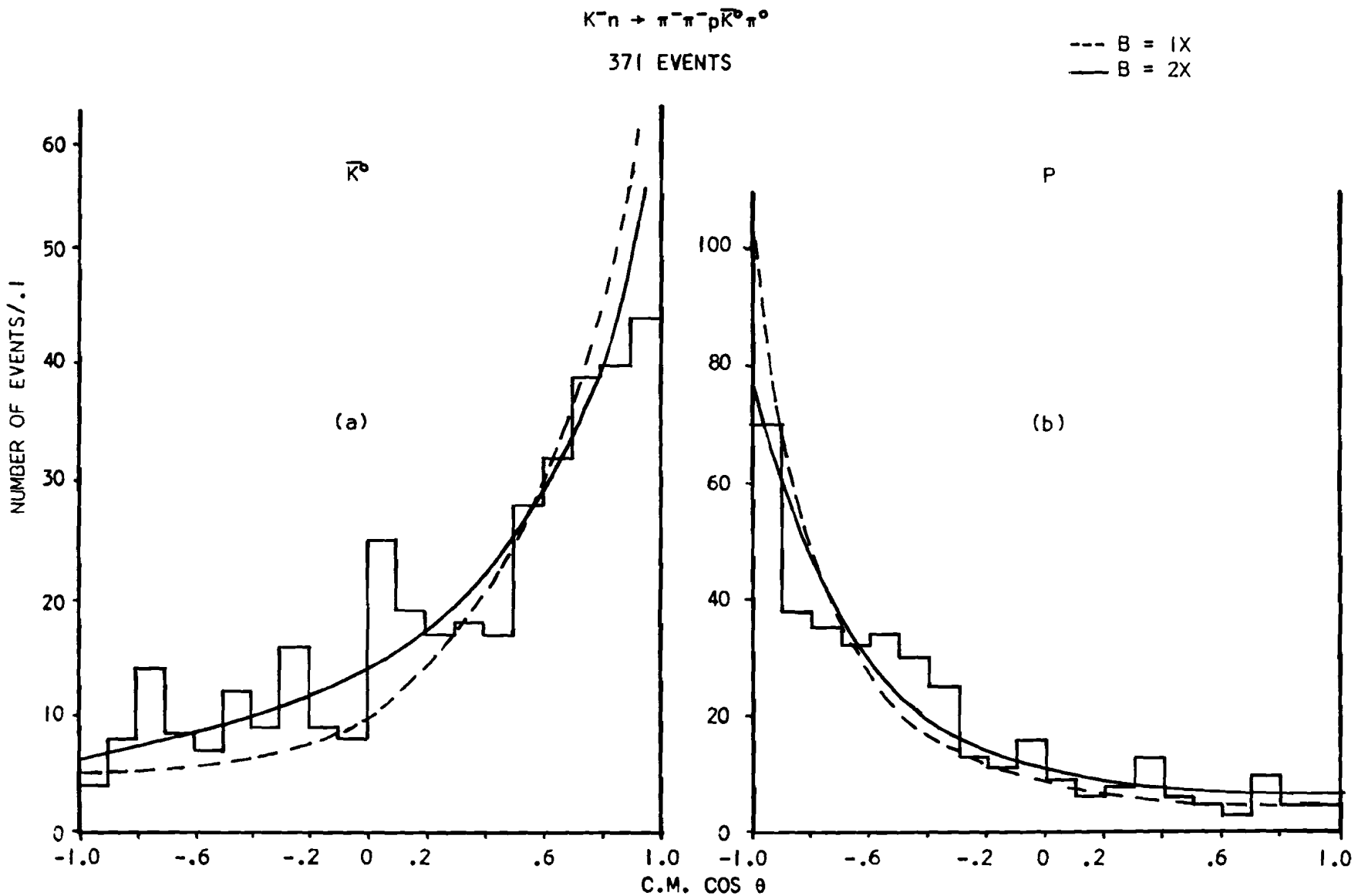
$K^-n \to \pi^-\pi^-p\overline{K}^0\pi^0$
371 EVENTS
--- B = 1X
—— B = 2X
$\overline{K}^0$
(a)
P
(b)
NUMBER OF EVENTS/.1
C.M. COS θ
0
10
20
30
40
50
60
80
100
-1.0
-.6
-.2
.2
.6
1.0

Figure 49.--The dependence of single particle production angles on CLA b_i for (a) π^0 and (b) π^-.

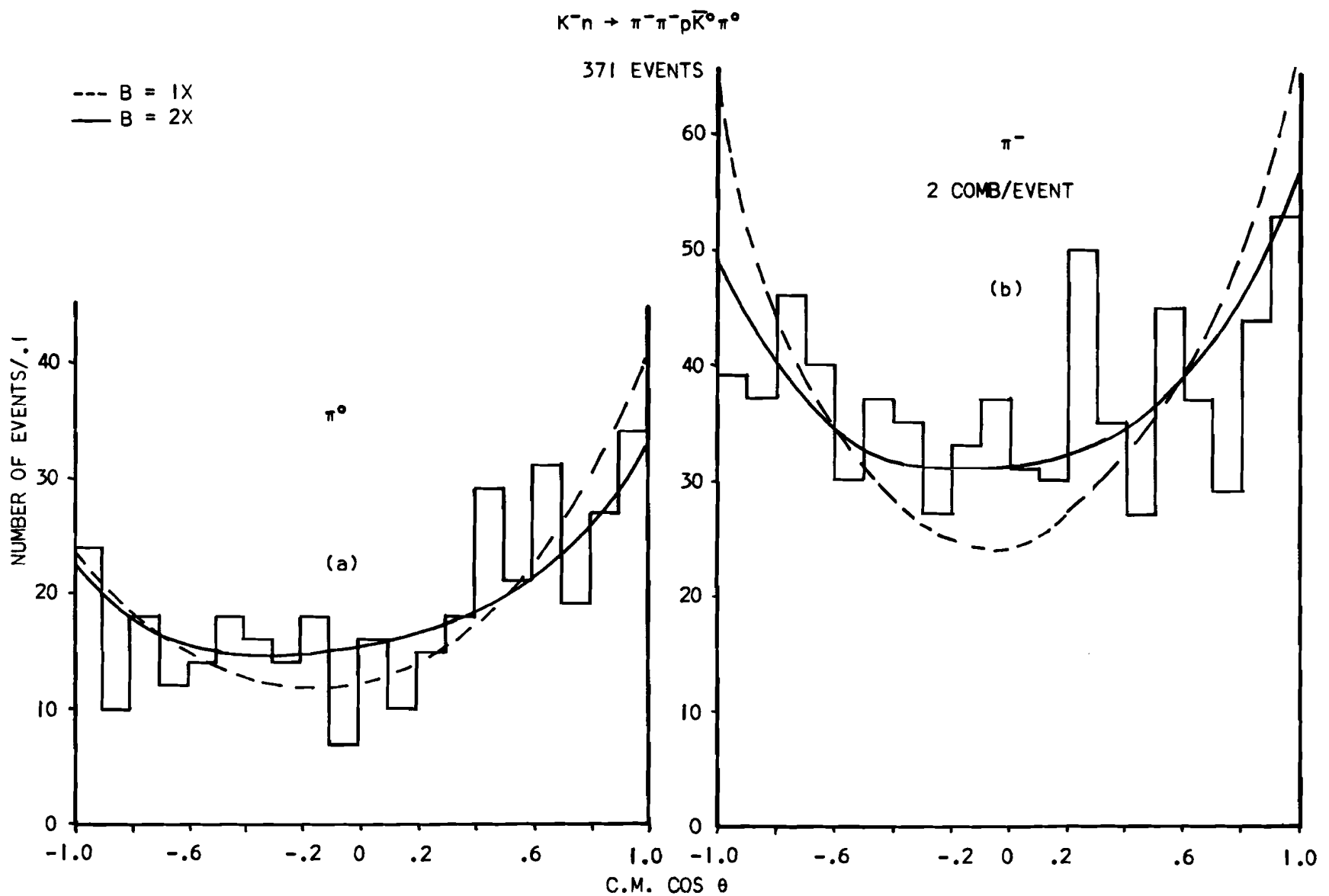
$K^-n \rightarrow \pi^-\pi^-p\bar{K}^0\pi^0$
371 EVENTS
--- B = 1X
—— B = 2X
NUMBER OF EVENTS/.1
π^0
(a)
π^-
2 COMB/EVENT
(b)
C.M. COS θ
0
10
20
30
40
50
60
-1.0
-.6
-.2
0
.2
.6
1.0

distributions in the cosine of the production angle for the single particles produced in Reaction II-6. The angles are measured with respect to the K^- beam in the rest frame of the target neutron. The dashed curves are the results of the CLA calculations where the b_i have the original CLA value (1X). The solid curves are the CLA results when the b_i are two times the original CLA values (2X). Without exception, the curves from the 2X calculations are a better description of the data. This agrees with the behavior seen in the 4-C reaction.

A χ^2 test was performed comparing the data with the results of the 2X CLA calculations for each of the single particle production angular distributions. The results are shown in Table 6.

Figures 50(a) and (b) and Figures 51(a) and (b) show the distributions in the longitudinal momentum (P_L) for the $\bar{K}^o$, proton, π^o, and π^-, respectively, for Reaction II-6. The quantity P_L is defined in the K^-n rest system by Equation (V-11).

The $\bar{K}^o$ is produced with a preference for positive momentum projections. That is, the $\bar{K}^o$ tends to go in the forward direction, i.e. along the incident K^-. This is similar to the behavior seen in the 4-C events, though not as strong an effect. The reduced strength of the effect is most probably due to the increased multiplicity of the final state.

The proton is produced primarily in the backward direction, i.e. along the direction of the target neutron. This distribution should be compared with the corresponding distribution for the proton from Reaction II-5 and the neutron produced in Reaction II-7. These comparisons are easily made by using the results found in Table 7. The proton from

Figure 50.--Single particle longitudinal momentum distribution for (a) $\overline{K}^{o}$ and (b) p produced in reaction II-6.

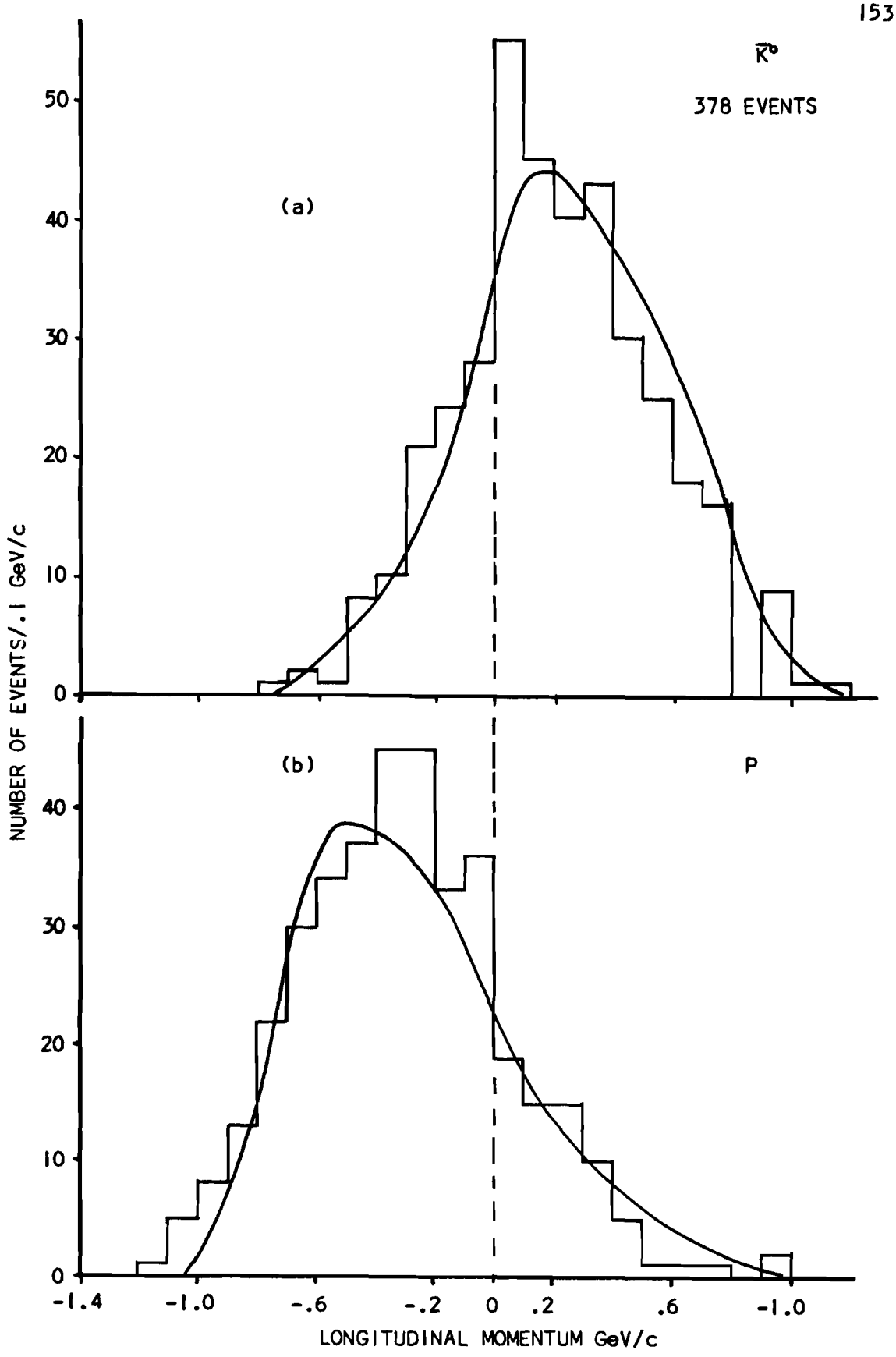
$\bar{K}^0$
378 EVENTS
(a)
(b)
P
NUMBER OF EVENTS/.1 GeV/c
LONGITUDINAL MOMENTUM GeV/c
0
10
20
30
40
50
-1.4
-1.0
-.6
-.2
0
.2
.6
-1.0

Figure 51.--Longitudinal momentum distribution for (a) π° and (b) π^{-}.

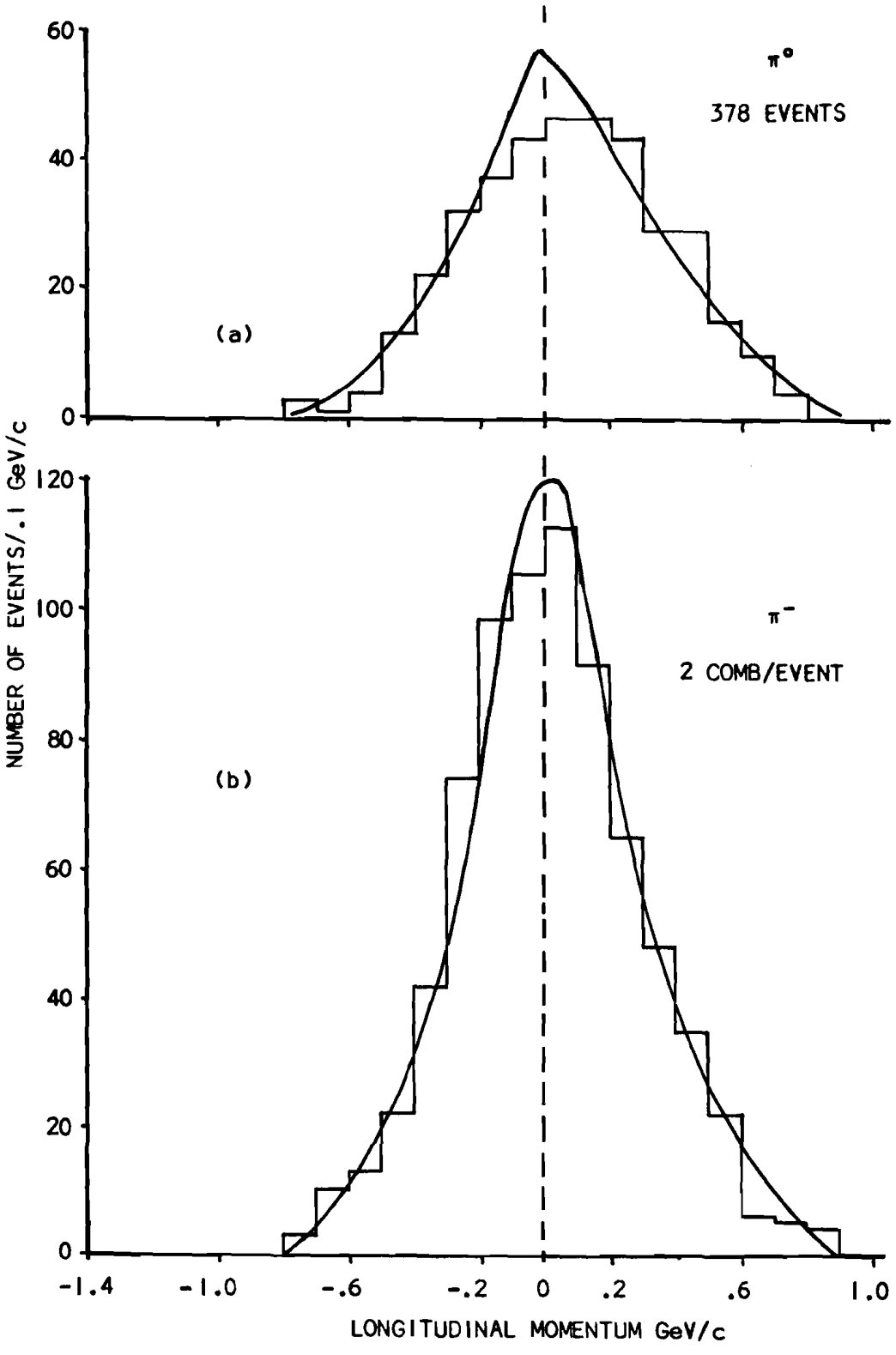
60
40
20
0
(a)
π°
378 EVENTS
120
100
80
60
40
20
0
(b)
π⁻
2 COMB/EVENT
NUMBER OF EVENTS/.1 GeV/c
-1.4
-1.0
-.6
-.2
0
.2
.6
1.0
LONGITUDINAL MOMENTUM GeV/c

Reaction II-6 and the neutron from Reaction II-7 are seen to have similar distributions. However, the proton from Reaction II-5 is produced with a larger average value of $-P_L$. This effect is most probably due to the smaller multiplicity of Reaction II-5.

The distributions for the π° and π^- are peaked near $P_L = 0$, are symmetrically distributed about their peaks, and show no other distinguishing features.

The curve in each P_L distribution is the result of the CLA calculation. The measured and calculated average of P_L for each single particle distribution are given in Table 7.

Figures 52(a) and (b) and Figures 53(a) and (b) are the distributions in the transverse momentum for the proton, $\bar{K}^\circ$, π°, and π^-, respectively, for Reaction II-6. The curves are the results of the CLA calculation. We have calculated the average value for each of the single particle distributions for both the model and the data. The results are shown in Table 7. The distributions are all seen to be similar in shape with no significant structure.

The CLA model calculation qualitatively reproduced the observed single particle longitudinal and transverse momentum distributions.

C. $K^-n \rightarrow \pi^-\pi^-\pi^+\bar{K}^\circ n$

There were 560 events satisfying the kinematic hypothesis $K^-n \rightarrow \pi^-\pi^-\pi^+\bar{K}^\circ n$ with spectator proton momentum less than .275 GeV/c. When the additional requirement that the main vertex χ^2 probability be greater than or equal to 7.5 per cent was applied, the sample was reduced to 468 events. When the correction for vees lost out of the end of the bubble chamber was made, the sample was increased to 479 events. This sample

Figure 52.--Transverse momentum distribution for (a) proton and (b) $\overline{K}^{o}$.

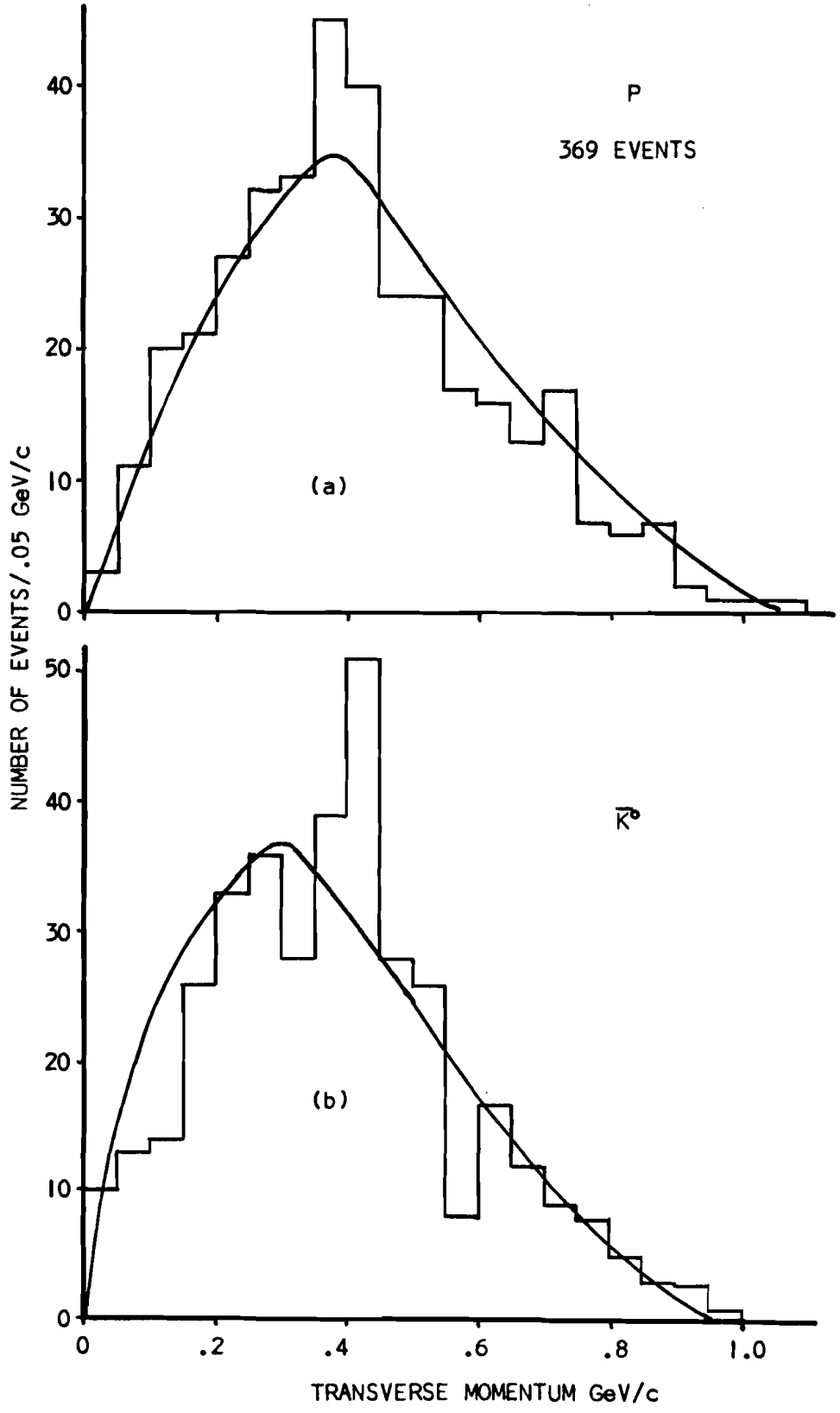
P
369 EVENTS
(a)
$\bar{K}^0$
(b)
NUMBER OF EVENTS/.05 GeV/c
TRANSVERSE MOMENTUM GeV/c
0
10
20
30
40
50
.2
.4
.6
.8
1.0

Figure 53.--Transverse momentum distribution for (a) π° and (b) π^{-}.

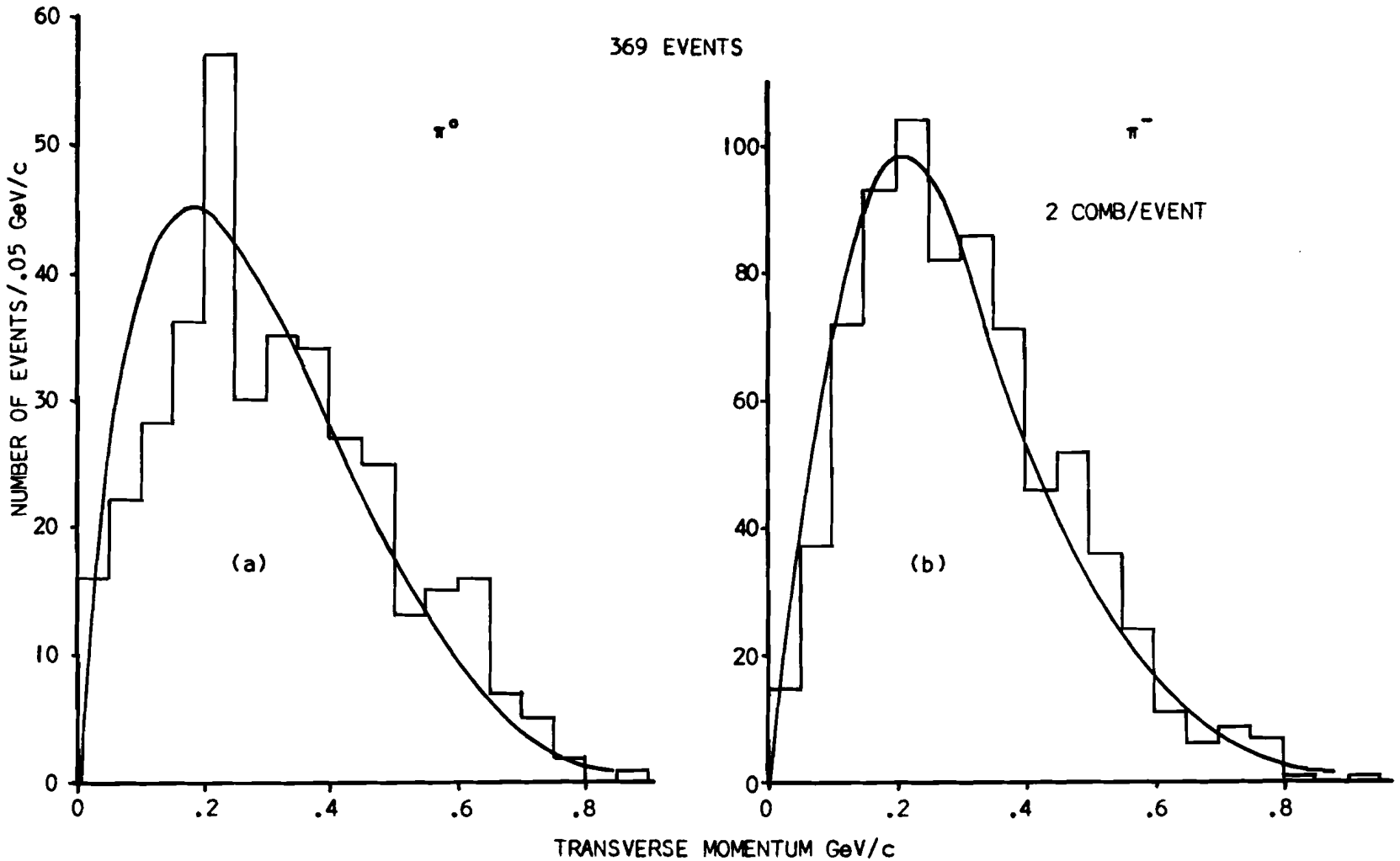
369 EVENTS
π°
π⁻
2 COMB/EVENT
(a)
(b)
NUMBER OF EVENTS/.05 GeV/c
TRANSVERSE MOMENTUM GeV/c
0
10
20
30
40
50
60
0
20
40
60
80
100
0
.2
.4
.6
.8

of 479 events was used in the following analysis.

The CLA calculations shown in this section had the b_1 set at two times the original CLA values of Table 2. The dependence of the single particle production angular distributions on the b_1 will be discussed later in this section along with other single particle distributions.

This channel is dominated by the resonance production of $K^{*-}(890)$ which subsequently decays into $\bar{K}^{o}\pi^{-}$ and $N^{*-}(1236)$ which subsequently decays into $n\pi^{-}$. We will first consider the K^{*} production and decay.

Figure 54(a) is the invariant mass distribution of the $\bar{K}^{o}\pi^{-}$. The strong $K^{*-}(890)$ signal is apparent. Curve (1) is pure Lorentz-invariant phase space for the two bodies $(\bar{K}^{o}\pi^{-})$ out of the five-body final state. Curve (2) is the result of the CLA calculation. The CLA calculation is seen to describe well this invariant mass distribution. Both $\bar{K}^{o}\pi^{-}$ combinations were included in this plot.

Using the CLA model, we were able to conclude that there were (193 ± 37) events belonging to the channel $K^{-}n \rightarrow K^{*-}(890)\pi^{-}\pi^{+}n$, which does not include the $K^{*-}(890)N^{*-}(1236)\pi^{+}$ events. This corresponds to a corrected cross-section of (172 ± 42) μbarns. The large error is the result of the uncertainty introduced by the subtraction of the double resonant $K^{*-}N^{*-}\pi^{+}$ events.

Using Curve (2) as a background estimate, we see no evidence for other resonance production in the $\bar{K}^{o}\pi^{-}$ mass distribution.

The open histogram in Figure 54(b) is the distribution in the cosine of the production angle of the $\bar{K}^{o}\pi^{-}$ system for all the events belonging to Reaction II-7. The production angle, as usual, was defined in the rest system of the K^{-} and target neutron and with respect to the

Figure 54.--(a) The invariant mass distribution for the $\overline{K}^{o}\pi^{-}$ produced in reaction II-7. (b) Corresponding production angular distribution.

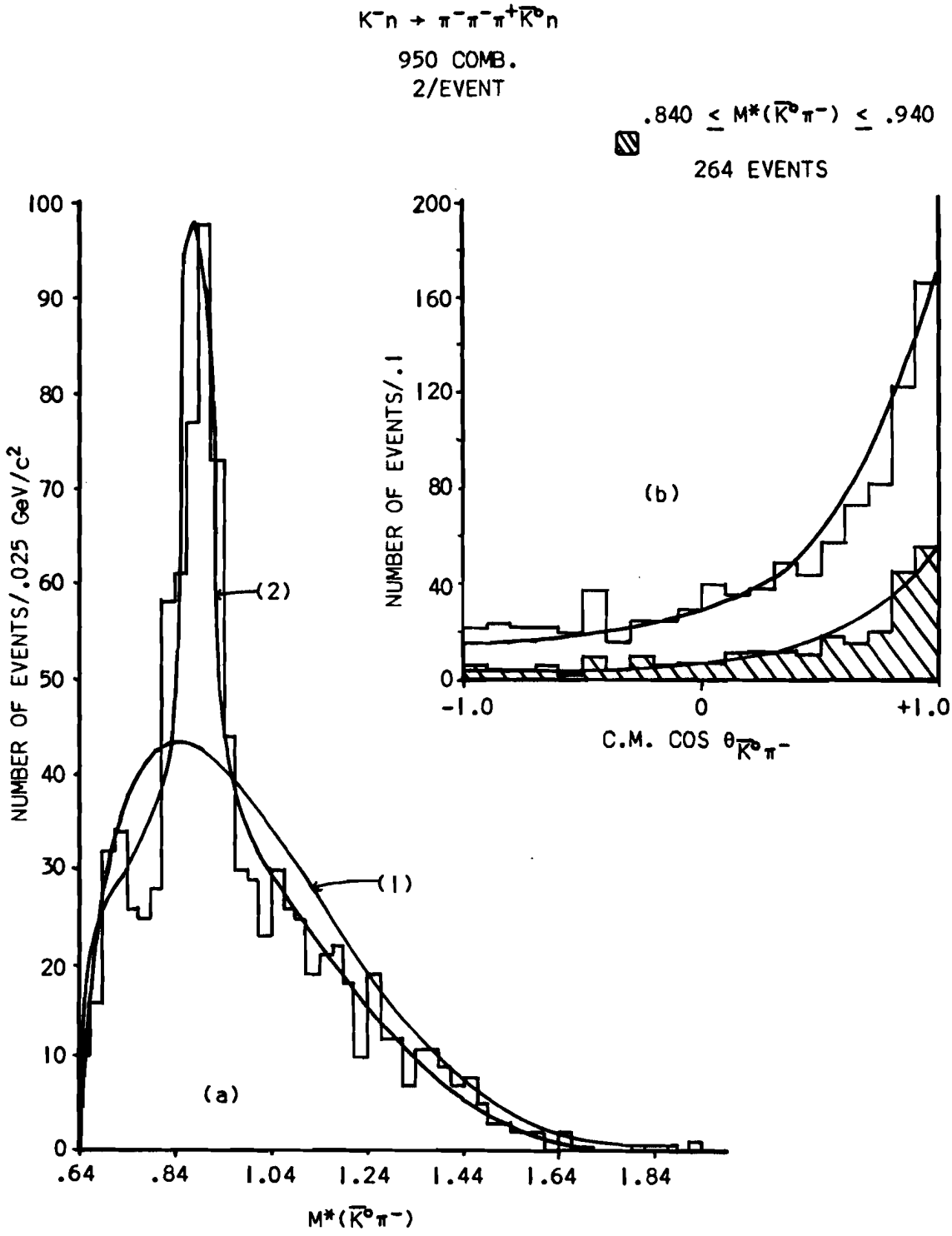
K⁻n → π⁻π⁻π⁺K̄°n
950 COMB.
2/EVENT
.840 ≤ M*(K̄°π⁻) ≤ .940
264 EVENTS
NUMBER OF EVENTS/.025 GeV/c²
M*(K̄°π⁻)
(1)
(2)
(a)
NUMBER OF EVENTS/.1
C.M. COS θK̄°π⁻
(b)

incident K^- direction. The distribution is seen to be strongly peaked in the forward direction (along the K^-). In comparing this distribution to the corresponding distribution for Reaction II-5 [Figure 23(b)] and Reaction II-6 [Figure 44(b)], we find that it is definitely less peaked than Reaction II-5 and at the 94 per cent confidence level it is more peaked than Reaction II-6. This is what one expects from the effective multiplicity of the three reactions. The lower the multiplicity the more peripheral are the reactions. We recall that the 4-C channel (Reaction II-5) is dominated by resonance production, thus reducing the effective final state multiplicity to three particles in most cases. Reaction II-7 is also found to be dominated by resonance production, reducing its multiplicity to four particles in most cases. Reaction II-6, on the other hand, has about 50 per cent of its events with no resonance formation, i.e. a five body final state. We remind the reader that the shape of an angular distribution depends not only on the effective multiplicity, but also on the diagrams that describe the reaction.

The curve associated with the open histogram is the CLA calculation. It is seen to adequately describe the data.

The shaded histogram in Figure 54(b) is the angular distribution for those events which fall in the K* region of the $\overline{K}^0\pi^-$ invariant mass plot. The K* region is taken from .840 GeV/c^2 to .940 GeV/c^2. The corresponding curve is the CLA calculation with the same restrictions imposed. The model is seen to adequately describe the data. The K* distribution has the same qualitative shape as the $\overline{K}^0\pi^-$ distribution for all events fitting Reaction II-7.

Figure 55 is the $|t - t_{min}|$ distribution for those events with at least one $\bar{K}^{o}\pi^{-}$ invariant mass in the K* region. If both $\bar{K}^{o}\pi^{-}$ combinations happen to fall in the K* region, we used the particle combination with invariant mass closer to .890 GeV/c^2. The $|t - t_{min}|$ distribution for control regions on both sides of the K* region was compared to the corresponding distribution for events in the K* region. A χ^2 test yielded a χ^2 probability of about 3 per cent that the distributions had the same shape. We take this to indicate that the background and resonance probably have different $|t - t_{min}|$ dependence. We subtracted out the background contribution from the resonance region by using the control regions. We used the distribution resulting from the sum of the two control regions, normalized to the known number of background events in the K* region (82 events), as an estimate of the background in the resonance region. Figure 55 is a semi-logarithmic plot of the $|t - t_{min}|$ distribution where the normalized background distribution has been subtracted. The X's are the data points, and the bars represent their errors, which were determined by the statistics.

The line in Figure 55 is the result of a least squares fit to an exponential [Equation (V-3)] for the $|t - t_{min}|$ region below 1.0 (GeV/c)^2. A preliminary χ^2 test revealed that the regions above and below 1.0 (GeV/c)^2 could not be fitted by a single exponential.

The result of the fit was an exponential slope λ = (1.64 ± .38) (GeV/c)$^{-2}$. The data for the region below 1.0 (GeV/c)^2 gave a χ^2 probability of 27 per cent when compared to the fit. The chi square probability that the region above 1.0 (GeV/c)^2 can be described by the same exponential as the region below 1.0 (GeV/c)^2 is 0.01 per cent. As

Figure 55.--The $|t - t_{min}|$ distribution for $K^{*-}(890)$ produced in reaction II-7, corrected for background.

$K^-n \rightarrow K^{*-}(890)\pi^-\pi^+n$

163 EVENTS

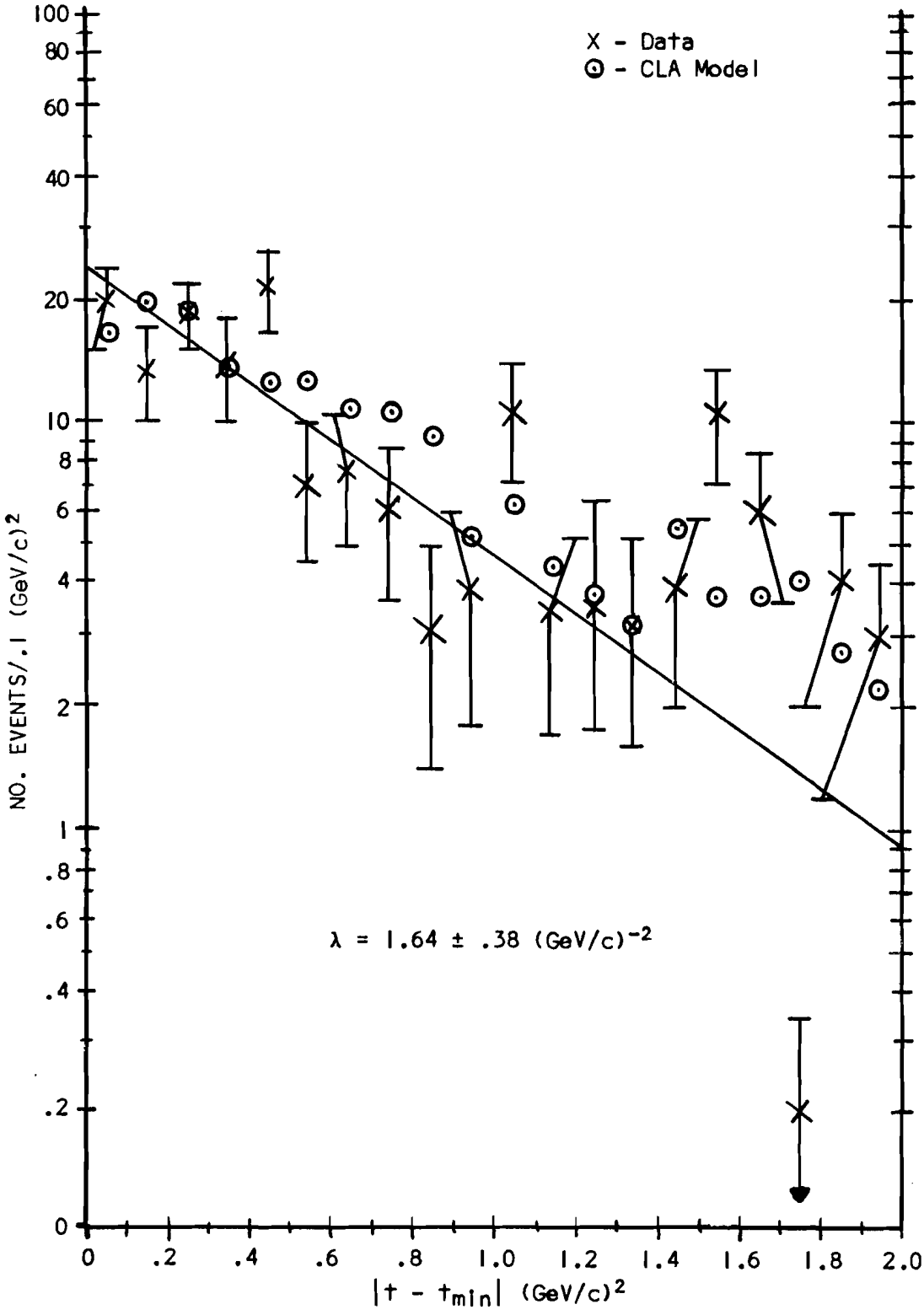

mentioned previously, the data require more than a single exponential for their description.

The circles in Figure 55 are the results of the CLA model calculation. The model distribution shown was obtained by using the same background subtraction technique as used with the data. The model and the data are in good qualitative agreement.

The decay of the K^* produced in this final state was examined in the Jackson frame of reference. The Jackson reference frame was discussed in Chapter IV, Section B. Figure 29 is a sketch of the coordinate axes used in this reference frame.

Figure 56(a) shows the distribution of the azimuthal angle (ϕ) in the Jackson frame for the $\overline{K}^0$ from the decay of the K^*. This distribution was found to be consistent in shape with regions taken above and below the K^* mass region. Consequently, we felt it unnecessary to make a background subtraction for this distribution. Figure 56(a) has a probability of about 4.5 per cent for being flat. It does not display the characteristic shape of $W(\phi)$ [see Equation (IV-23)], which assumes a pure angular momentum state. On the other hand, the data are not sufficient to establish interference of the $K^{*-}(890)$ with background.

Figure 56(b) is the distribution of the cosine of the polar angle (θ) of the $\overline{K}^0$ from the decay of the K^* in the Jackson frame. No background subtraction was made because these data have the same shape as the control regions. This distribution is consistent with being flat with a χ^2 probability of about 50 per cent.

We have detected no alignment of the $K^{*-}(890)$ in the Jackson frame.

Figure 56.--Jackson frame distributions for $K^{*-}(890)$; (a) cos θ and (b) ϕ.

$K^- n \rightarrow K^{*-} \pi^- \pi^- n$

275 EVENTS

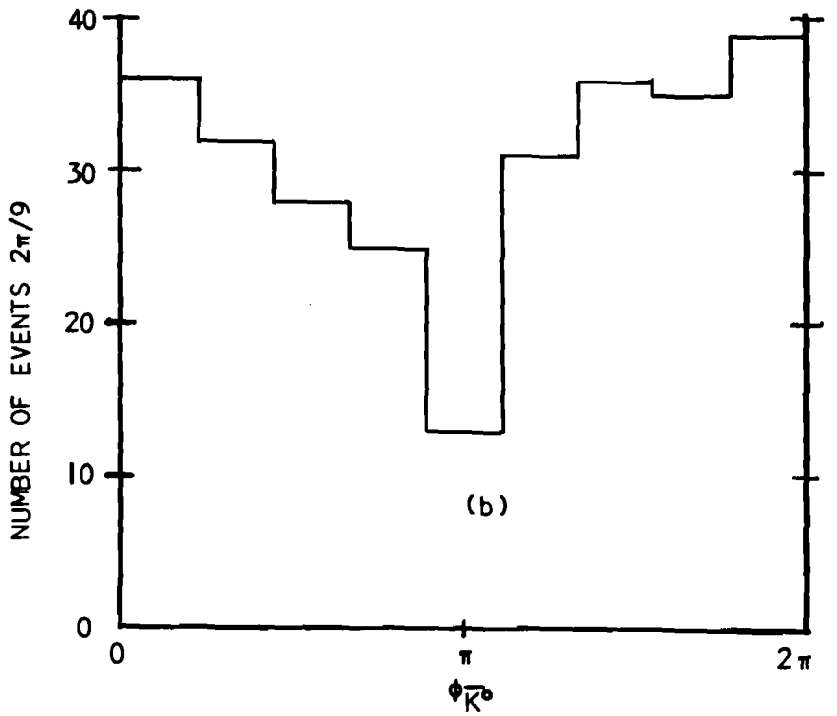

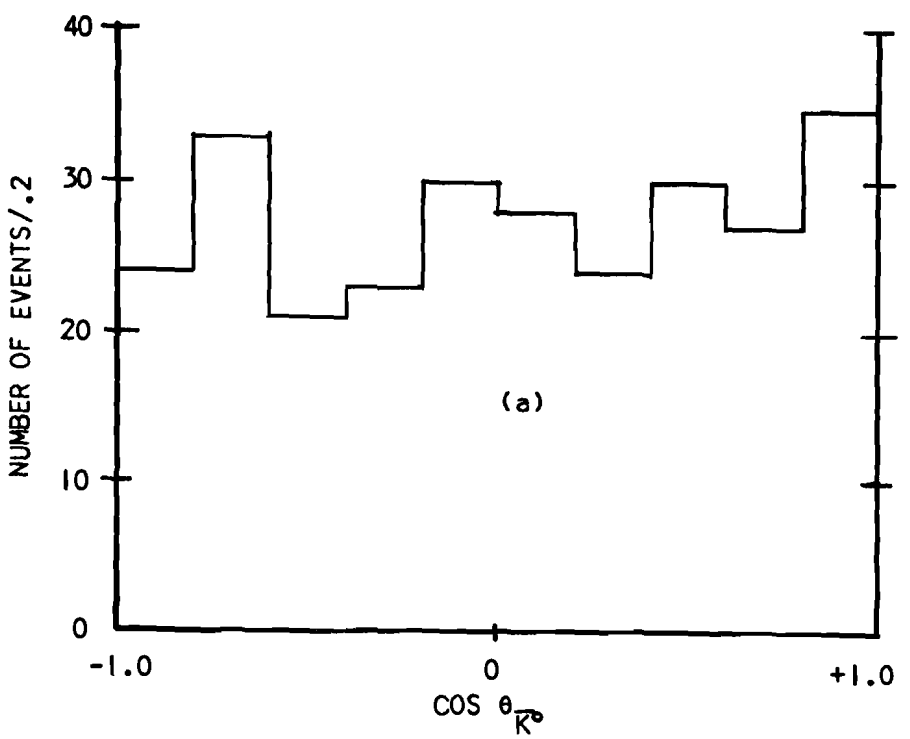

As we have already mentioned, this channel is dominated by the production of $K^{*-}(890)$ and $N^{*-}(1236)$. In order to determine the amount of simultaneous K^*N^* production, we restricted the $\bar{K}^o\pi_1^-$ to be within $\pm\Gamma(\pm.050\ GeV/c^2)$ of the K^* mass and plotted the $n\pi_2^-$ effective mass distribution. The symbols π_1^- and π_2^- refer to the two π^-'s produced in the reaction. We adjusted the number of events belonging to the channel

$$K^-n \rightarrow N^{*-}(1236)K^{*-}(890)\pi^+$$

until the CLA model gave agreement with the data in the region from 1.116 to 1.356 GeV/c^2. We found that (39 ± 27) events belonged to this channel. This corresponds to a corrected cross-section of (35 ± 24) μbarns. This contribution is small compared to single resonance production. Figure 57 is the distribution in the invariant mass of the $n\pi_2^-$. The $N^{*-}(1236)$ peak is the only structure. The curve is the result of the CLA calculation, with the same restrictions on the $\bar{K}^o\pi^-$ invariant mass. The distribution for the $n\pi_1^-$, where the π_1^- refers to the π^- associated with the K^*, showed no significant structure above the CLA background estimate. This implies that if there is any sharing of π^- between K^{*-} and N^{*-} resonances, the amount is small.

All invariant mass distributions incorporating the K^* and also those recoiling from the K^* were examined. We found no significant deviation from the CLA model predictions. Figure 58(a) is the invariant mass distribution for the $n\pi^-$. Both $n\pi^-$ mass combinations are included in the plot. The dominating feature of this histogram is the production of the $N^{*-}(1236)$ resonance. From the result of the CLA fit we were able to determine that there were (234 ± 37) events belonging to the channel

Figure 57.--The invariant mass distribution of the $n\pi_2^-$ produced in $K^-n \rightarrow K^{*-}(890)n\pi_2^-\pi^+ \rightarrow \overline{K}^0\pi_1^-n\pi_2^-\pi^+$.

$K^- n \rightarrow \bar{K}^0 \pi_1^- n \pi_2^- \pi^+$

262 EVENTS

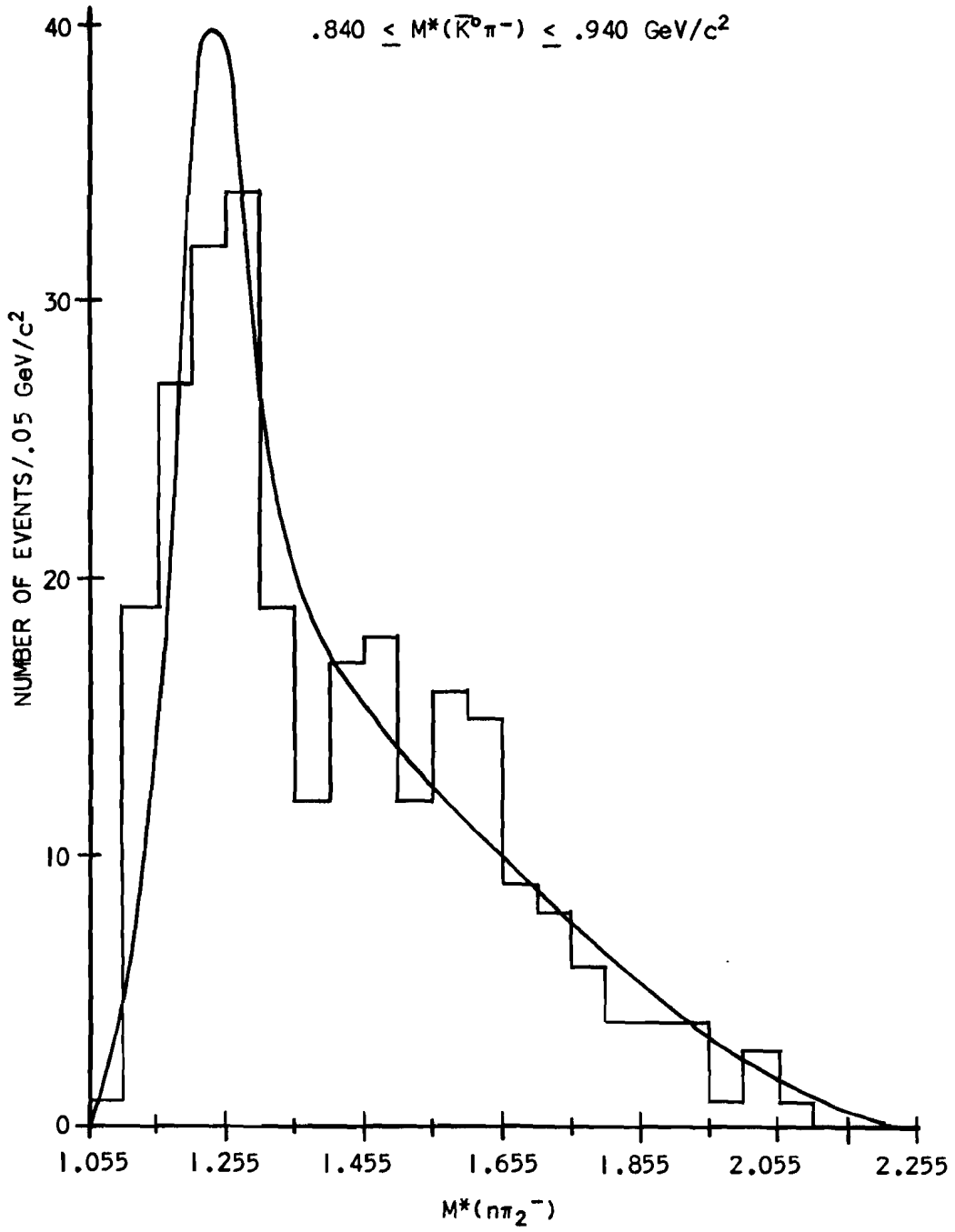

Figure 58.--(a) The invariant mass distribution for $n\pi^-$ produced in reaction II-7. (b) Corresponding production angular distribution.

$K^- n \rightarrow \pi^- \pi^- \pi^+ \bar{K}^0 n$

952 COMB.
2/EVENT

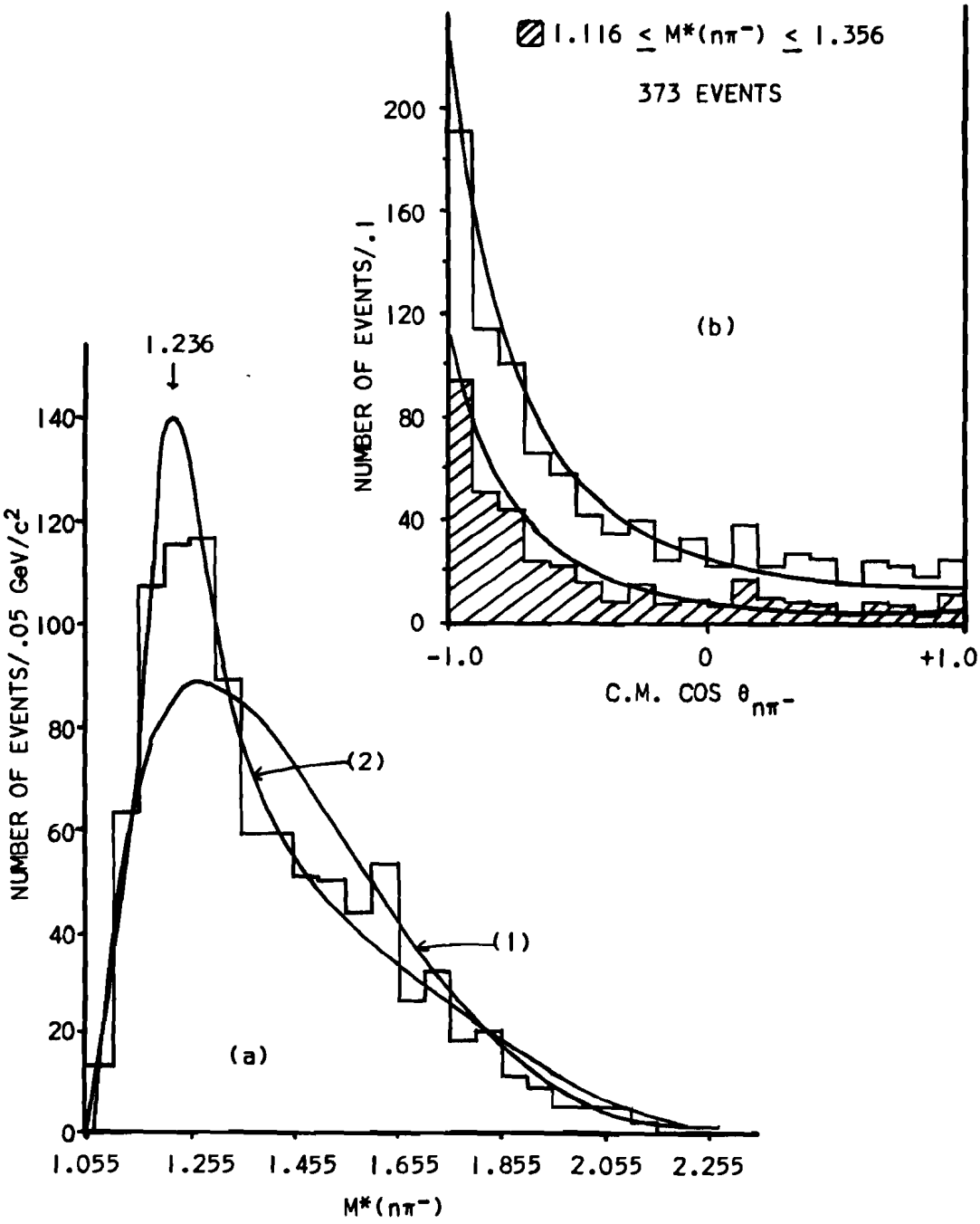

$$K^-n \rightarrow N^{*-}(1236)\pi^-\pi^+\bar{K}^\circ.$$

This corresponds to a corrected cross-section of (209 ± 46) μbarns for production of $N^{*-}(1236)$, in the single resonance channel. The N^{*-} resonance is produced in 57 per cent of the events of Reaction II-7 as compared to about 12 per cent for the production of $N^{*\circ}$ in Reaction II-5 and no detected N* production in Reaction II-6. This difference is at least partly due to the fact that the $n\pi^-$ combination is in a pure isospin - 3/2 state while the $p\pi^-$ and $p\pi^\circ$ combinations are not.

Curve (1) in Figure 58(a) is Lorentz-invariant phase space for the $n\pi^-$ system normalized to the total number of entries in the histogram. Phase space for two bodies from a five-body system is strongly peaked at low mass. This fact made the determination of the amount of N^{*-} difficult. In other words, the CLA fit to the $n\pi^-$ invariant mass distribution was relatively insensitive to small changes in the amount of N*. This is the reason for the relatively large error quoted for the number of N* events.

Curve (2) in Figure 58(a) is the result of the CLA calculation. Our criterion for selecting the appropriate model fit was to demand that the model reproduce the number of data events in the region $\pm\Gamma(\pm.120$ GeV/c^2) about the mass of 1.236 GeV/c^2, i.e. the N* region. The model prediction appears to be slightly more peaked than the data for the N* region. However, the statistical quality of the data does not let us confirm any discrepancy. We did not attempt to make a determination of the N* mass or width. We felt that the scarcity of events in our experiment precluded an accurate determination. We used the accepted mass and width for the N* (1.236 ± .120 GeV/c^2) as input to the CLA model

calculation.

The open histogram in Figure 58(b) is the distribution in the cosine of the production angle for the $n\pi^-$. Both $n\pi^-$ combinations are included in this histogram. The production angle (θ) is defined in the K^- target neutron rest system with respect to the incident K^-. The $n\pi^-$ is seen to be produced preferentially at a small angle with respect to the original direction of the target neutron, i.e. cos θ is near -1. As mentioned before, a small production angle corresponds to a small momentum transfer. That is to say that the $n\pi^-$ system is produced with relatively small momentum transfer from the incident neutron. The curve corresponding to the open histogram is the CLA model prediction. The model is in qualitative agreement with the data.

The shaded histogram in Figure 58(b) is the cosine of the production angle for those events which had at least one $n\pi^-$ invariant mass in the N* region ($\pm.120$ GeV/c^2 about 1.236 GeV/c^2). If both invariant mass combinations fell in the N* region, the combination with mass closer to 1.236 GeV/c^2 was used. The distribution for the N* region has the same shape as the distribution for the entire sample. A comparison to the equivalent distribution for the K* region [Figure 54(b)] shows that the N* and K* have the same shape. The curve corresponding to the cos θ distribution for the N* region is the CLA prediction where the same invariant mass restrictions were required. The model adequately reproduces the shape of the data.

Figure 59 is a semi-logarithmic plot of $|t - t_{min}|$ for those events in the N* region. The error bars refer to the data and are set by the available statistics. The quantity t, as defined in Equation (V-1),

Figure 59.--The $|t - t_{min}|$ distribution for N*(1236) produced in reaction II-7.

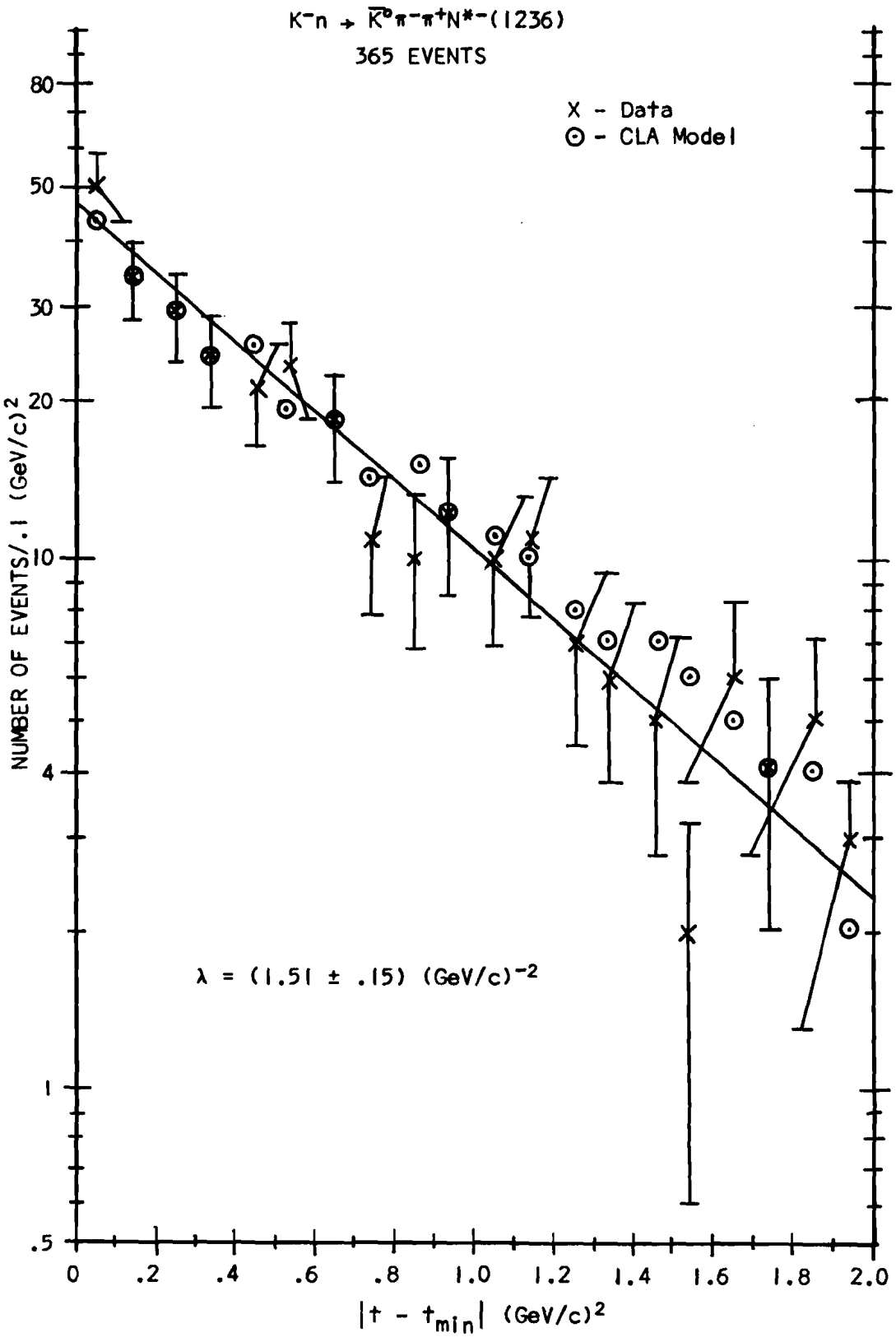
$K^-n \to \bar{K}^0\pi^-\pi^+N^{*-}(1236)$
365 EVENTS
X - Data
⊙ - CLA Model
$\lambda = (1.51 \pm .15)\ (GeV/c)^{-2}$
NUMBER OF EVENTS/.1 $(GeV/c)^2$
80
50
30
20
10
4
1
.5
0
.2
.4
.6
.8
1.0
1.2
1.4
1.6
1.8
2.0
$|t - t_{min}|\ (GeV/c)^2$

is the square of the four-momentum transfer from the target neutron to the outgoing $n\pi^-$ system. The quantity t_{min} is the value which t would have taken on if the $n\pi^-$ system had been produced with zero angle with respect to the target neutron direction. In studying the corresponding distribution for the K* band, we were able to get an estimate of the background behavior in the resonance band by examining regions above and below the resonance band. Since the N* lies very close to the $n\pi^-$ threshold, we have no lower control region and consequently cannot use the same procedure. For a background control region we took events with at least one $n\pi^-$ invariant mass falling in the region from 1.416 to 1.666 GeV/c^2. If the other $n\pi^-$ fell within the N* region, we rejected the event. If both $n\pi^-$ combinations fell in the control region, we took the combination with the lower mass as the "background N*". This criterion was chosen because the $n\pi^-$ combinations for the true N* tend to be lower than the other $n\pi^-$ combinations. The $|t - t_{min}|$ distribution for these control events was compared to the distribution from the N* region. The control region and the N* region agreed with a χ^2 probability of about 50 per cent. We concluded that the background under the N* probably had the same shape as the resonance and there was no need for a background subtraction. The events plotted in Figure 59 have no background subtraction.

The straight line in Figure 59 is the result of a least squares fit of the data to an exponential of the form of Equation (V-3). The data are well described by a single exponential. The exponential slope was found to be

$$\lambda = (1.51 \pm .15)(\mathrm{GeV}/c)^{-2}.$$

This is consistent within statistics to the slope for the K* region (see Table 5). A comparison of the N* data with the least squares fit yielded a χ^2 probability of about 90 per cent. The circles in Figure 59 are the results of the CLA calculation. The CLA calculation quantitatively describes the data; a comparison yielded a χ^2 probability of 90 per cent.

The decay of the N* was examined in the Jackson frame of reference. A sketch of the axes are shown in Figure 59. The system is defined in the N* rest frame with $\hat{x}$, $\hat{y}$, and $\hat{z}$ being unit vectors defining the axes.

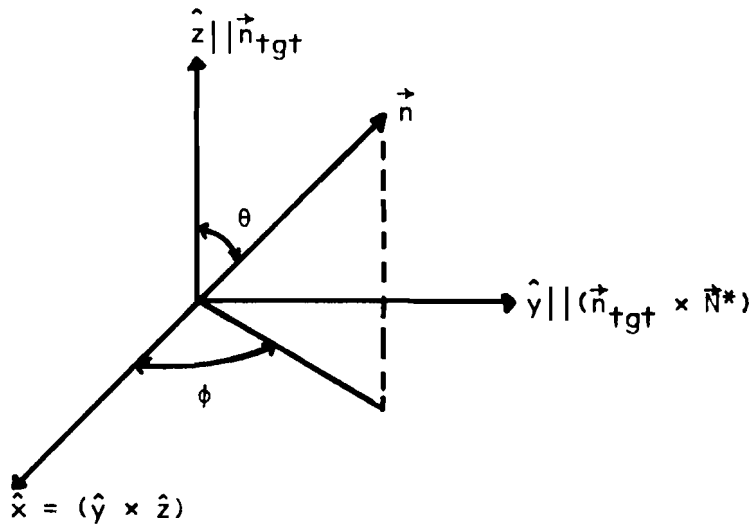

Figure 60.--A sketch of the Jackson frame of reference for the N*(1236) decay.

The quantity $\vec{n}$ is the momentum vector of the final state neutron in the N* rest system. The z-axis is taken parallel to the target neutron momentum ($\vec{n}_{tgt}$) in the N* rest frame. The y-axis is taken parallel to the normal to the production plane defined by crossing the target neutron momentum ($\vec{n}_{tgt}$) into the outgoing N* momentum ($\vec{N}^*$). The x-axis is chosen normal to the y- and z-axes so that a right-handed coordinate system

results.

The decay angular distribution in the Jackson frame, $W(\theta,\phi)$, for the spin 3/2 $N^{*-}(1236)$ decaying into spin 1/2 and spin 0 particles is given by Equation (IV-24).

Figures 61(a) and (b) are the distributions of the azimuthal angle (ϕ) and the cosine of the polar angle (θ), respectively, of the neutron from the N* decay. The specification of either decay product in a two-bodies decay completely determines the decay.

We found that about half of the events of Reaction II-7 contain a K*. We have also found that the number of double resonant (K*N*) events is small (see Chapter VII). In this light we chose to plot only those events in the N* band which were not in the K* band. This eliminated much of the background and gave a much cleaner N* sample. Figures 61(a) and (b) have these conditions imposed. The lines in Figure 61 correspond to flat distributions. The x's are the results of the CLA calculation with the same cuts as were used for the data. The CLA model result (which gives isotropy in the Jackson frame) was examined to assure ourselves that the lack of structure in the data did not result from an accidental cancellation of structure in the N* events with the remaining background. The histograms show no significant structure and are qualitatively described by the CLA calculation. We felt that a fit to $W(\theta,\phi)$ to determine the density matrix elements was unwarranted.

We have examined the invariant mass distributions of all of the possible particle combinations from the $\overline{K}^{o}\pi^{-}\pi^{-}\pi^{+}n$ final state. We have likewise calculated the CLA model for all of these distributions. In general we find that the CLA model is in qualitative agreement with the

Figure 61.--Jackson frame distributions for N*(1236); (a) ϕ and (b) cos θ.

$K^- n \rightarrow \overline{K}^0 \pi^- \pi^+ N^*$

168 EVENTS

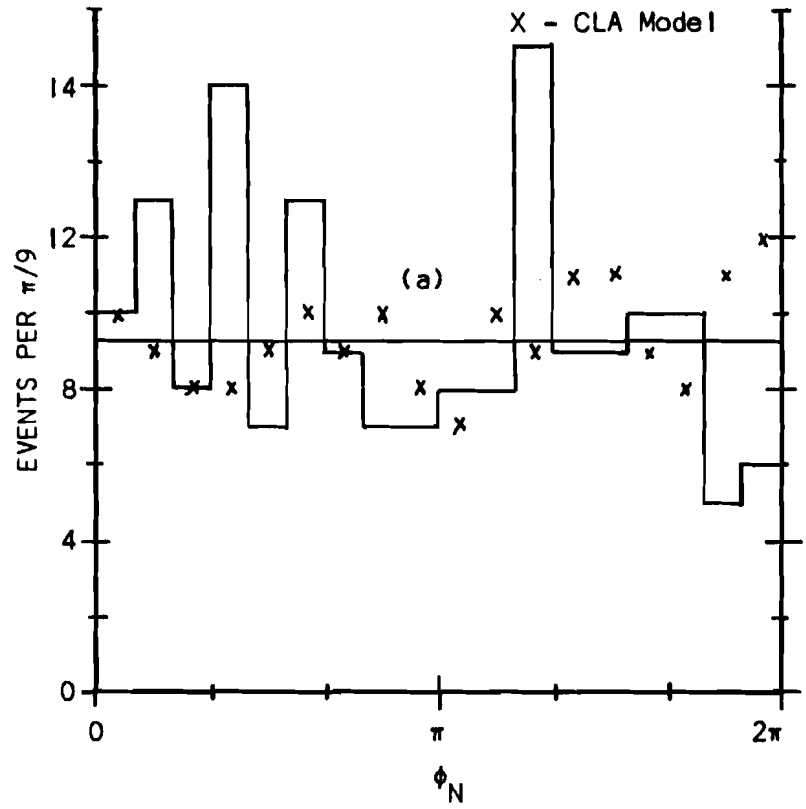

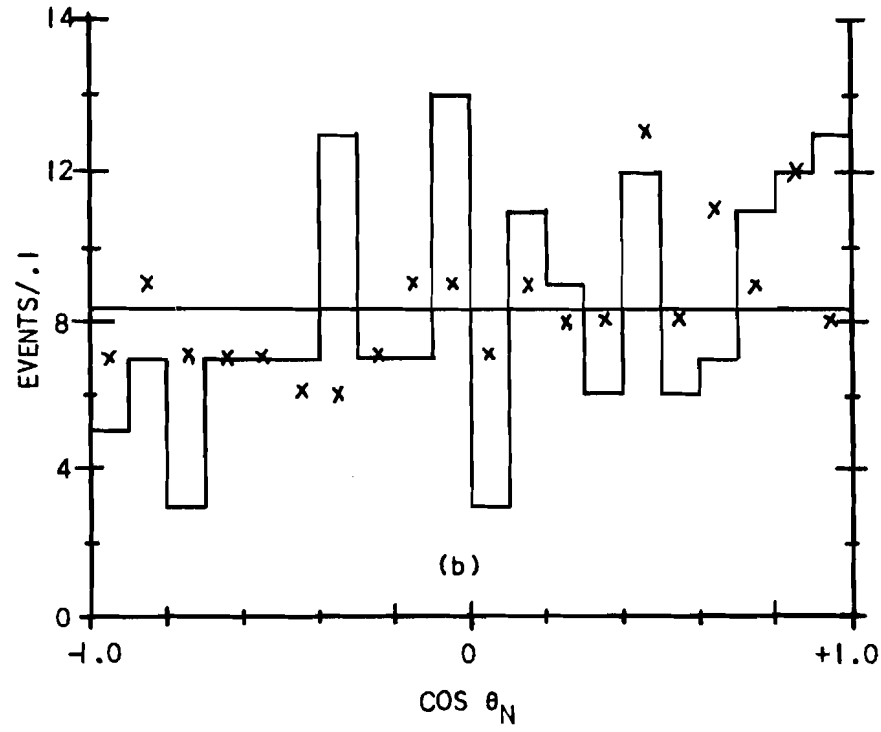

with the data. Because of the large number of distributions we will only mention those which seem to disagree with the CLA model calculations.

Figure 62 shows the invariant mass distribution of the $\pi^+\pi^-$ where both π^- combinations are plotted. We notice a depletion in the data from about .305 to .455 GeV/c^2 when compared to the CLA model prediction. This depletion is a 5.7 standard deviation effect. We did not find any resonance production decaying via the $\pi^+\pi^-$ channel, e.g. $\rho^o(765)$, which might have distorted this distribution. Momentum transfer cuts were made to see if the depletion had a strong momentum dependence and also to look for peripherally produced resonances. Figure 63 shows histograms of the data and the corresponding CLA calculation where the amount of momentum transfer above the minimum value from the incident K^- to the $\pi^+\pi^-$ system was required to be less than .2 $(GeV/c)^2$ in one case and less than 1.0 $(GeV/c)^2$ in another case. No resonance structure above the CLA model curve became apparent. Also, the depletion showed no detectable momentum transfer dependence.

It has been observed for some time that pion-pion mass distributions persistently deviate from phase space for masses near threshold. Clayton et al.[54] discussed this phenomenon in terms of a final state interaction between pion pairs and attempted to fit the two pion mass distributions obtained from several experiments. We did not make use of their model, but only made use of their data accumulation. We wanted to see if our discrepancy was consistent with that seen by other people. Figure 63(b) is a reproduction of Clayton's Figure 2. It is a visual fit to the

Figure 62.--The $\pi^+\pi^-$ invariant mass histogram with momentum transfer cuts of .2 and 1.0 $(GeV/c)^2$.

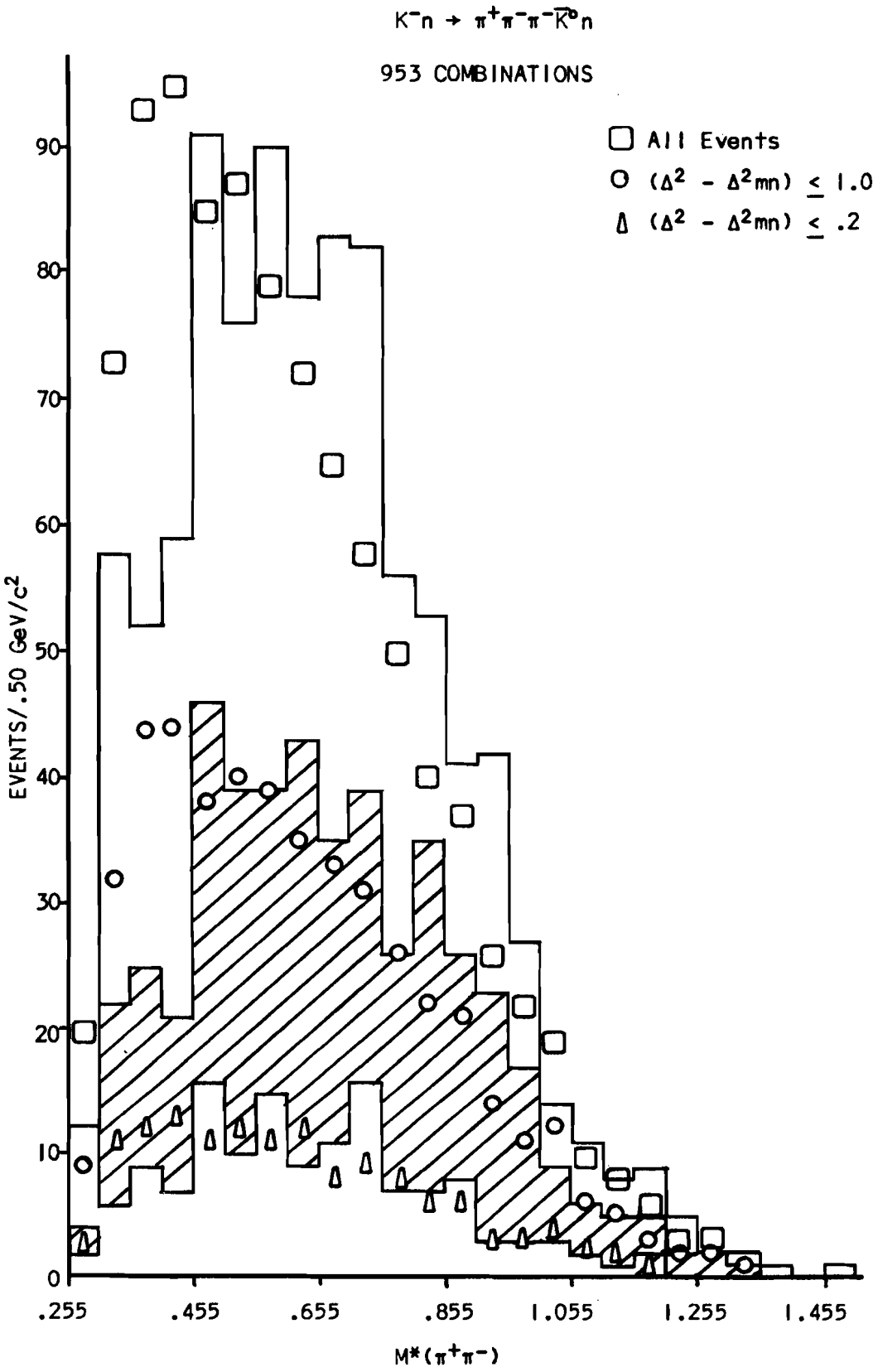
$K^-n \rightarrow \pi^+\pi^-\pi^-\bar{K}^0 n$
953 COMBINATIONS
All Events
$(\Delta^2 - \Delta^2 mn) \leq 1.0$
$(\Delta^2 - \Delta^2 mn) \leq .2$
EVENTS/.50 GeV/c^2
0
10
20
30
40
50
60
70
80
90
.255
.455
.655
.855
1.055
1.255
1.455
$M^*(\pi^+\pi^-)$

Figure 63.--(a) The $\pi^+\pi^-$ invariant mass histogram with CLA model modified by Clayton's ratio factor. (b) Curve from Claytons' paper showing deviations of $\pi\pi$ invariant mass distributions from phase space.

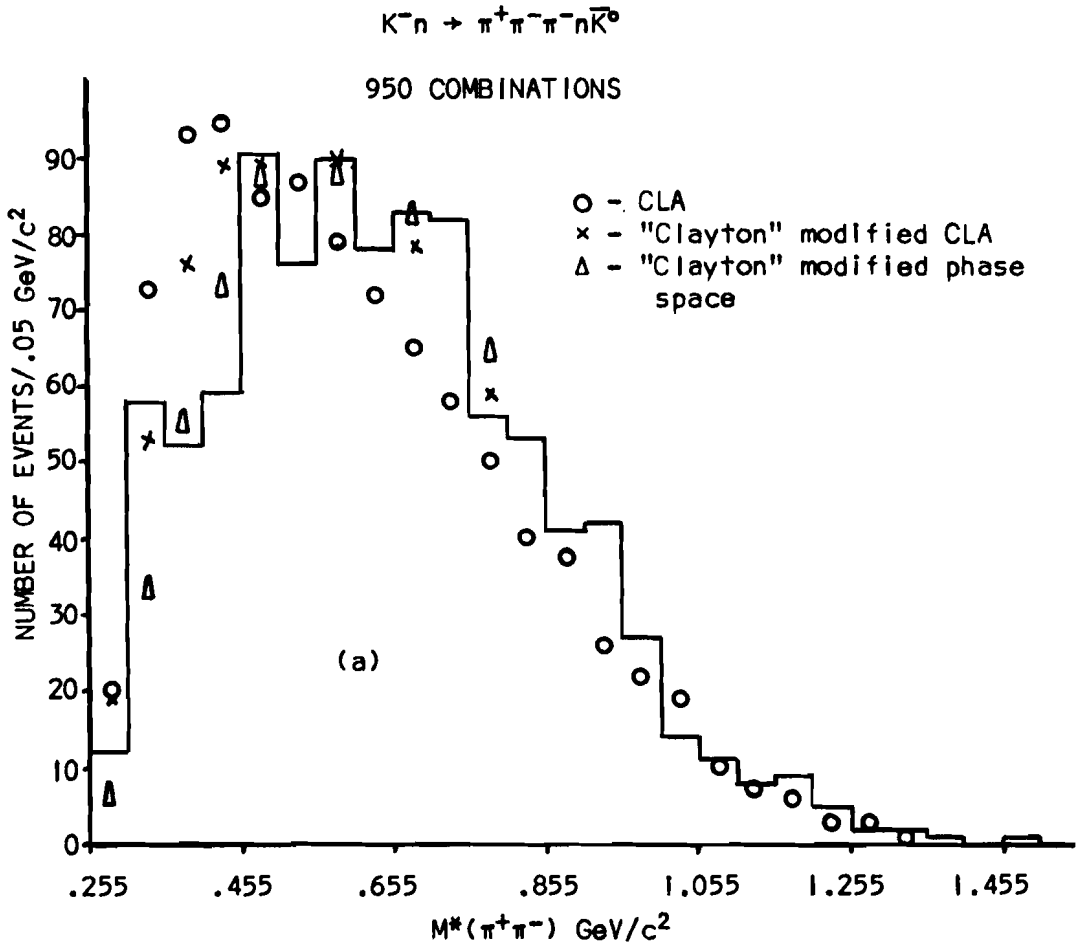
$K^-n \to \pi^+\pi^-\pi^-n\bar{K}^0$
950 COMBINATIONS
NUMBER OF EVENTS/.05 GeV/c²
0
10
20
30
40
50
60
70
80
90
.255
.455
.655
.855
1.055
1.255
1.455
M*(π⁺π⁻) GeV/c²
O - CLA
× - "Clayton" modified CLA
Δ - "Clayton" modified phase space
(a)

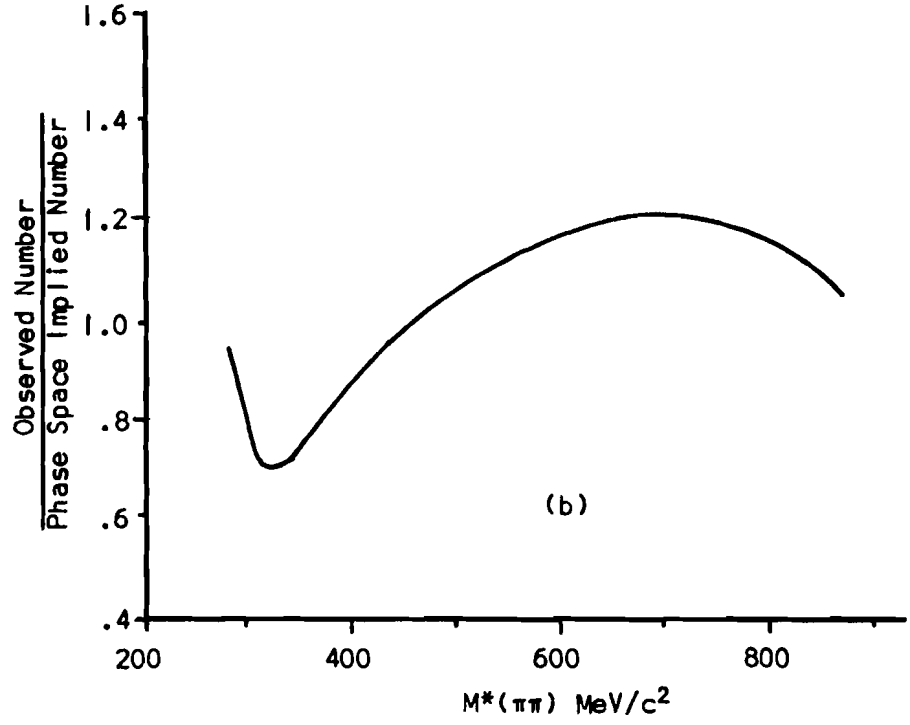
Observed Number / Phase Space Implied Number
.4
.6
.8
1.0
1.2
1.4
1.6
200
400
600
800
M*(ππ) MeV/c²
(b)

$$\text{ratio} = \frac{\text{number of } \pi^+\pi^- \text{ entries from the data}}{\text{number of } \pi^+\pi^- \text{ entries from phase space}} \qquad \text{(V-15)}$$

obtained from five independent experiments involving multi-pion production. From Figure 63(b) we see that they observe phase space to overpredict the data from threshold to about .450 GeV/c^2. This generally agrees with our observation in the $\pi^+\pi^-$ invariant mass histogram.

Figure 63(a) again shows the $\pi^+\pi^-$ invariant mass distribution for Reaction II-7. The circles are the results of the CLA calculation. the x's are the results of the CLA calculation when modified by the ratio shown in Figure 63(b). The discrepancy at low masses has been reduced to about 3.3 standard deviations by using the modified CLA prediction. The triangles are the results of pure phase space modified by the ratio. We feel that the discrepancy in the $\pi^+\pi^-$ mass distribution is similar to effects seen in other experiments.

Figure 64 is the distribution in the invariant mass of the $\overline{K}^o n\pi^+\pi^-$. We observe an enhancement in the region from 2.867 to 3.067 GeV/c^2 which is a 5.9 standard deviation effect when compared to the CLA model calculation. The solid curve in Figure 64 is the CLA calculation. The dashed curve is pure Lorentz-invariant phase space. This enhancement corresponds to a 3.9 standard deviation effect when compared to the phase space curve.

We found no evidence that the $\overline{K}^o n\pi^+\pi^-$ enhancement was preferentially associated with either $K^{*-}(890)$ or $N^{*-}(1236)$ production.

On the other extreme, we examined the $\overline{K}^o n\pi^+\pi^-$ distribution for those events with no $K^o\pi^-$ combination in the K^* region and no $n\pi^-$ combination in the N^* region. However, this cut reduced the number of events from 470 to 39. The poor statistics made it impossible to draw any

Figure 64.--The invariant mass distribution of $\overline{K}^{o}n\pi^{+}\pi^{-}$ produced in reaction II-7.

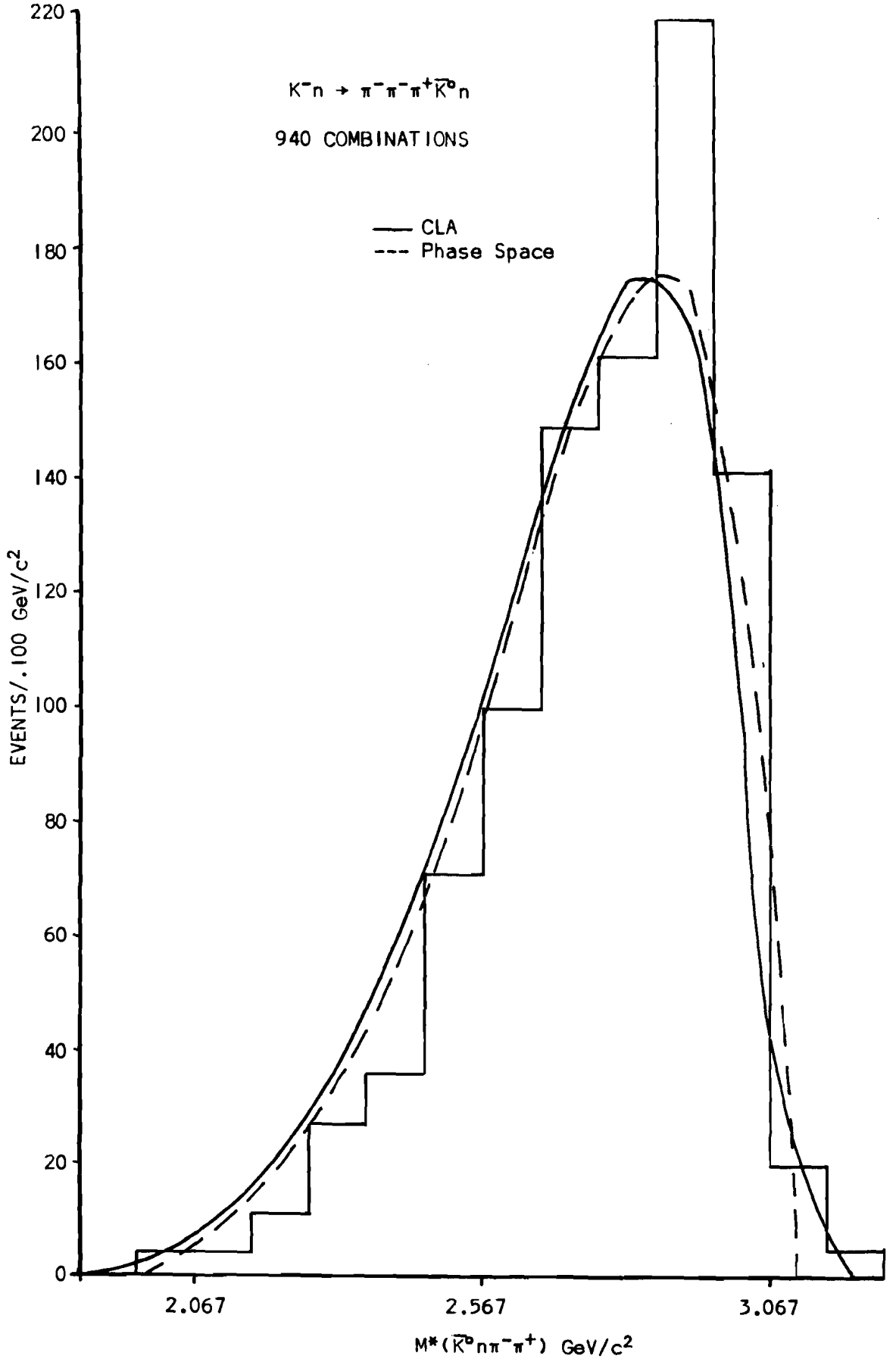
$K^-n \to \pi^-\pi^-\pi^+\bar{K}^0n$
940 COMBINATIONS
CLA
Phase Space
EVENTS/.100 GeV/c^2
220
200
180
160
140
120
100
80
60
40
20
0
2.067
2.567
3.067
$M^*(\bar{K}^0n\pi^-\pi^+)$ GeV/c^2

conclusions.

The invariant mass distributions for all possible particle combinations showed no significant deviation from background when a cut was made which accepted only those events from the $\bar{K}^{o}n\pi^{+}\pi^{-}$ enhancement between 2.867 and 3.067 GeV/c^2. The background estimate was taken as the CLA calculation with the same cut imposed.

Decay angular distributions for the enhancement were examined in two Jackson frames. Sketches of the axes are shown in Figures 65(a) and (b) where the distributions of the $\bar{K}^{o}$ and n, respectively, were examined.

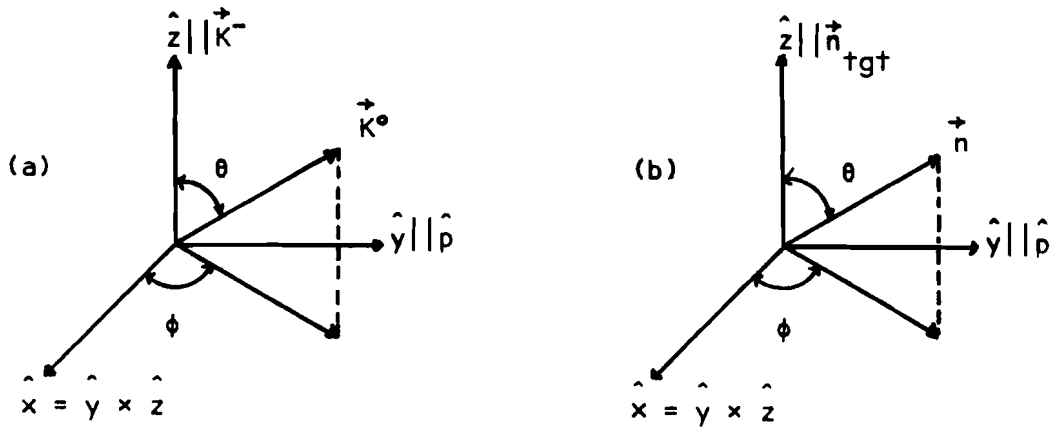

Figure 65.--(a) Sketch of Jackson frame of reference in $\bar{K}^{o}n\pi^{+}\pi^{-}$ rest frame for $\bar{K}^{o}$ distribution. (b) Jackson frame of reference for observing distribution of neutron.

The quantities $\vec{K}^-$, $\vec{K}^o$, $\vec{n}_{tgt}$, and $\vec{n}$ refer to the vector momenta of the K^-, $\bar{K}^o$, target neutron, and final state neutron, respectively. The quantities $\hat{x}$, $\hat{y}$, and $\hat{z}$ are unit vectors. The quantity $\hat{p}$ refers to the normal to the production plane of the $\bar{K}^{o}n\pi^{+}\pi^{-}$.

Looking forward to Figures 66(a) and (b) we see that the $\bar{K}^o$ and neutron are produced strongly along the incident K^- and target neutron

Figure 66.--Production angular distributions for (a) $\overline{K}^0$ and (b) neutron.

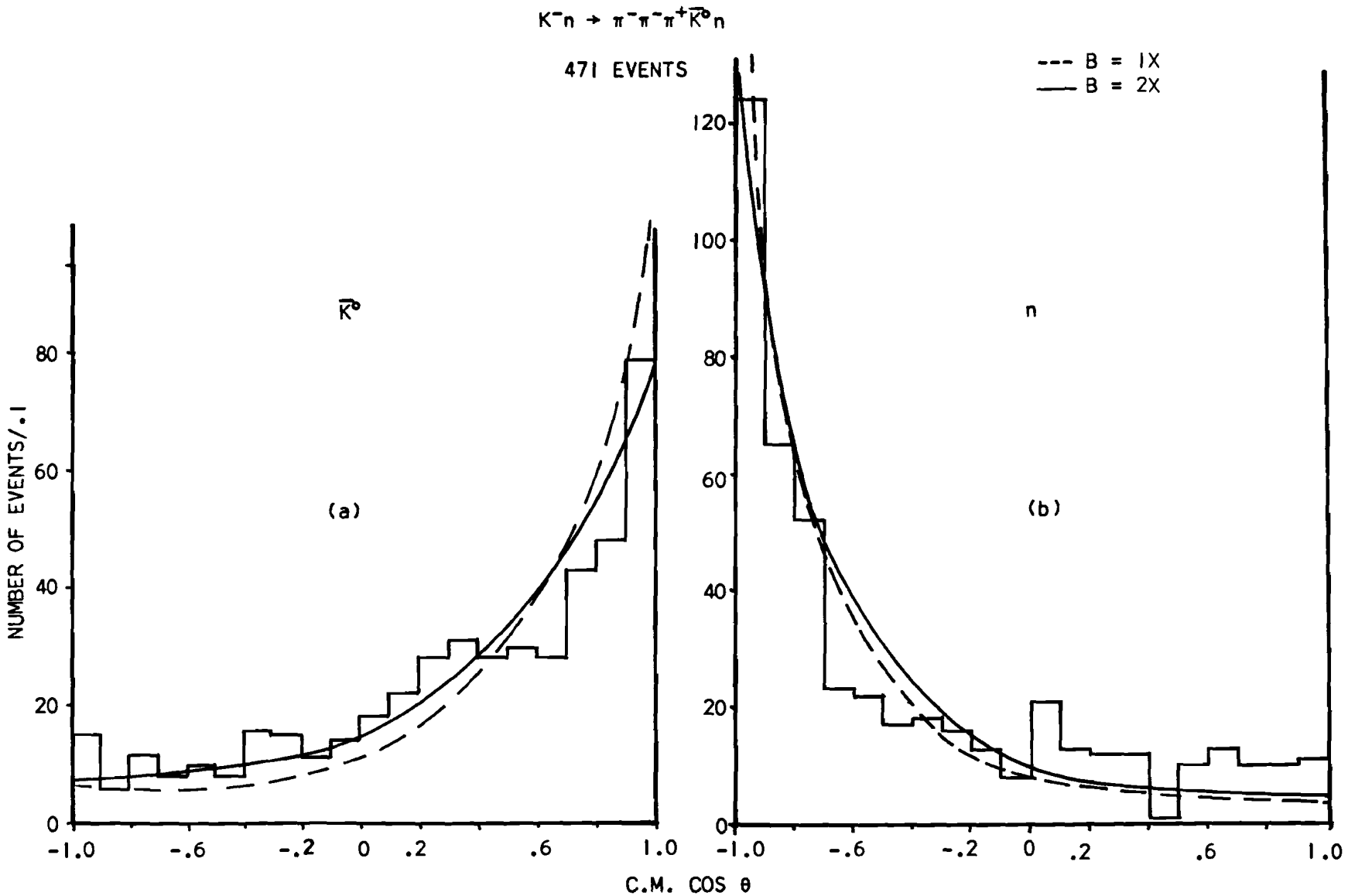
K⁻n → π⁻π⁻π⁺K̄°n
471 EVENTS
--- B = 1X
—— B = 2X
K̄°
(a)
n
(b)
NUMBER OF EVENTS/.1
C.M. COS θ
0
20
40
60
80
100
120
-1.0
-.6
-.2
0
.2
.6
1.0

directions, respectively, in the center of mass system. Since the ($\bar{K}^{o}n\pi^{+}\pi^{-}$) has a mass near the kinematic limit, its rest system is almost the same as the center of mass system. If the ($\bar{K}^{o}n\pi^{+}\pi^{-}$) enhancement were a resonant state, the $\bar{K}^{o}$ and neutron from the decay of the resonance would be expected to be produced symmetrically in the forward and backward directions (assuming no interference). We found that the Jackson cos θ distributions for those events in the enhancement region were not significantly different from the rest of the data.

We are reluctant to call the $\bar{K}^{o}n\pi^{+}\pi^{-}$ enhancement a resonance. It is not a very narrow effect (about .200 GeV/c^2 wide), thus making it a possible candidate for a kinematic interpretation. Also it occurs at the upper edge of phase space, and this increases our suspicion.

We suggest that this invariant mass region should be kept in mind, and should be examined more carefully when more events become available.

As discussed earlier with respect to both Reactions II-5 and II-6, the b_i of Equation (IV-6) were chosen by examining the data. Figures 66 and 68 are the distributions of the cosines of the production angles (cos θ) for the $\bar{K}^{o}$, n, π^{+}, and π^{-} from Reaction II-7. The dashed curve in each figure is the result of the CLA calculation where the b_i are set at the original CLA values (1X) of Table 2. The solid curves in each case are the CLA calculation results when the b_i were set at two times (2X) the original CLA values. As observed in each of the other reactions, the results of the 2X calculations were a better description of the data than the 1X calculations.

Figure 66(a) is the cos θ distribution for the $\overline{K}^0$. As usual θ is defined in the K^- target neutron rest system with respect to the K^- direction. That is, a cos θ of +1 corresponds to production along the incident K^- direction and a cos θ of -1 means production along the target-neutron direction. The $\overline{K}^0$ is seen to be produced predominantly at small angles with respect to the incident K^-. Small production angles correspond to low momentum transfers from the beam. The neutron can exchange the Pomeron. The Pomeron was parameterized with $\alpha(0) = 1.0$. Contributions from Pomeron diagrams should make the neutron more peripheral.

The effect of removing Pomeron exchange is shown in Figure 67. The curve in this figure is the result of a CLA calculation where Pomeron exchange was replaced by strangeness zero meson exchange [$\alpha(0) = .5$]. The model is seen to be less peripheral than the data require (about a 3.5 standard deviation effect in the backward direction). The curve should be compared to the solid curve in Figure 66(b) which was calculated by including Pomeron exchange and gives the correct number of backward going neutrons. The data prefer Pomeron exchange for the description of the backward going neutrons. All other comparisons of the CLA model with the data are made using Pomeron exchange where the quantum numbers allow it.

Figure 68(a) is the cos θ distribution for the π^+. The data show an almost isotropic production distribution. This corresponds to the π^+ being produced at internal vertices. The CLA model adequately describes this behavior.

The π^- cos θ distribution is almost flat, but shows a slight peaking in the forward direction. The model describes this behavior

Figure 67.--Production angular distribution for neutron. The curve is CLA calculation where all Pomeron exchange was replaced by intercept 0.5 meson exchange.

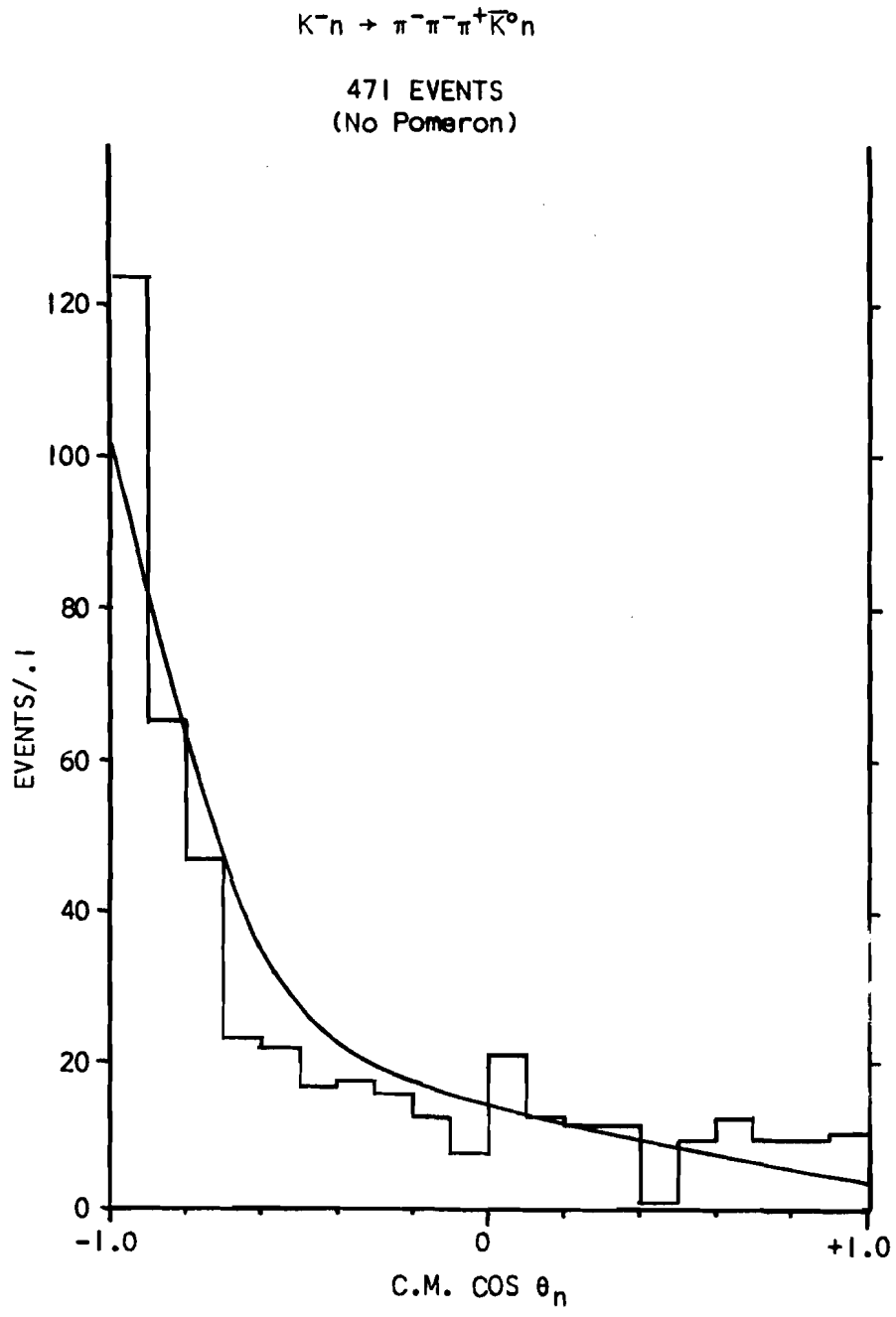
$K^-n \rightarrow \pi^-\pi^-\pi^+\overline{K}^0n$
471 EVENTS
(No Pomeron)
EVENTS/.1
120
100
80
60
40
20
0
-1.0
0
+1.0
C.M. COS θ_n

Figure 68.--Single particle production angular distributions for (a) π^+ and (b) π^-.

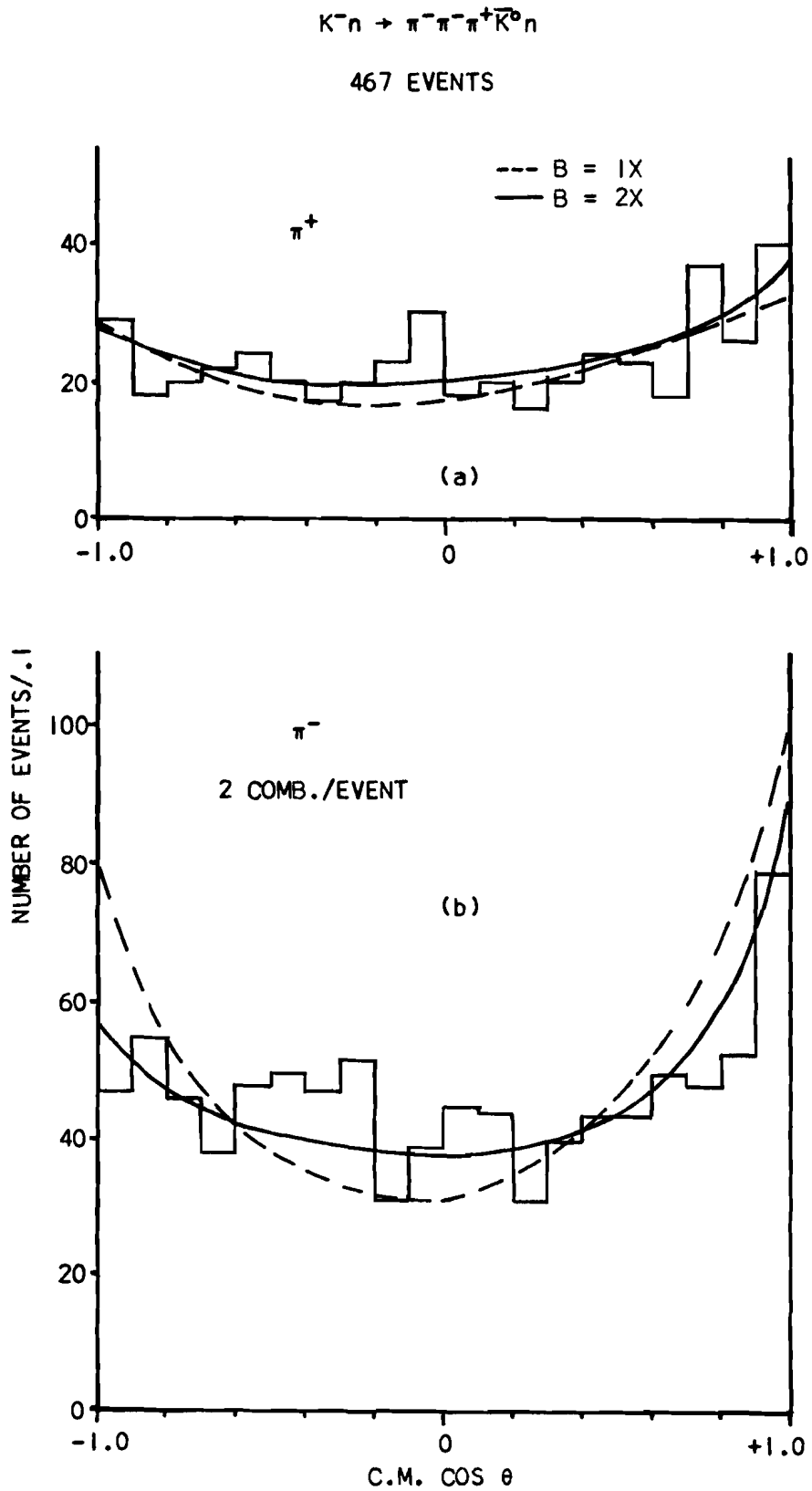
K⁻n → π⁻π⁻π⁺K̄⁰n
467 EVENTS
--- B = 1X
—— B = 2X
π⁺
(a)
π⁻
2 COMB./EVENT
(b)
NUMBER OF EVENTS/.1
C.M. COS θ
0
20
40
60
80
100
-1.0
0
+1.0

well. The π^- may be produced at the top vertex.

Table 6 is the result of a χ^2 test comparing each of the single particle distributions with the 2X CLA calculation. Although there is not quantitative agreement for the neutron, there is qualitative agreement.

Figures 69(a) and (b) are the longitudinal momentum distributions for the $\bar{K}^o$ and neutron respectively. The longitudinal momentum is defined as the projection of the particle momentum on the incident K^- direction in the rest frame of the K^- and target neutron. Positive projections correspond to particles traveling along the K^- direction, and negative ones to the neutron direction. In comparing the $\bar{K}^o$ and neutron distributions, we again see that the $\bar{K}^o$ tends to move in the forward direction and the neutron moves along the backward direction. If one looks ahead at Table 7, he will see that this effect is stronger for the neutron than the $\bar{K}^o$.

Figures 70(a) and (b) are the distributions of the longitudinal momentum for the π^+ and π^-, respectively. Both distributions are approximately peaked at and symmetric about 0. GeV/c and display no other structure.

We calculated the average value of the longitudinal momentum for each single particle distribution, and the corresponding distribution for the CLA model. These results are shown in Table 7.

Figures 71(a) and (b) are the distributions in the transverse momentum for the neutron and $\bar{K}^o$, respectively. Figures 72(a) and (b) are the distributions for the π^- and π^+, respectively. The average value of the transverse momentum for the data and the model are shown in Table 7.

Figure 69.--Lontitudinal momentum distributions for (a) $\overline{K}^0$ and (b) neutron.

$K^- n \rightarrow \pi^- \pi^- \pi^+ \overline{K}^0 n$

477 EVENTS

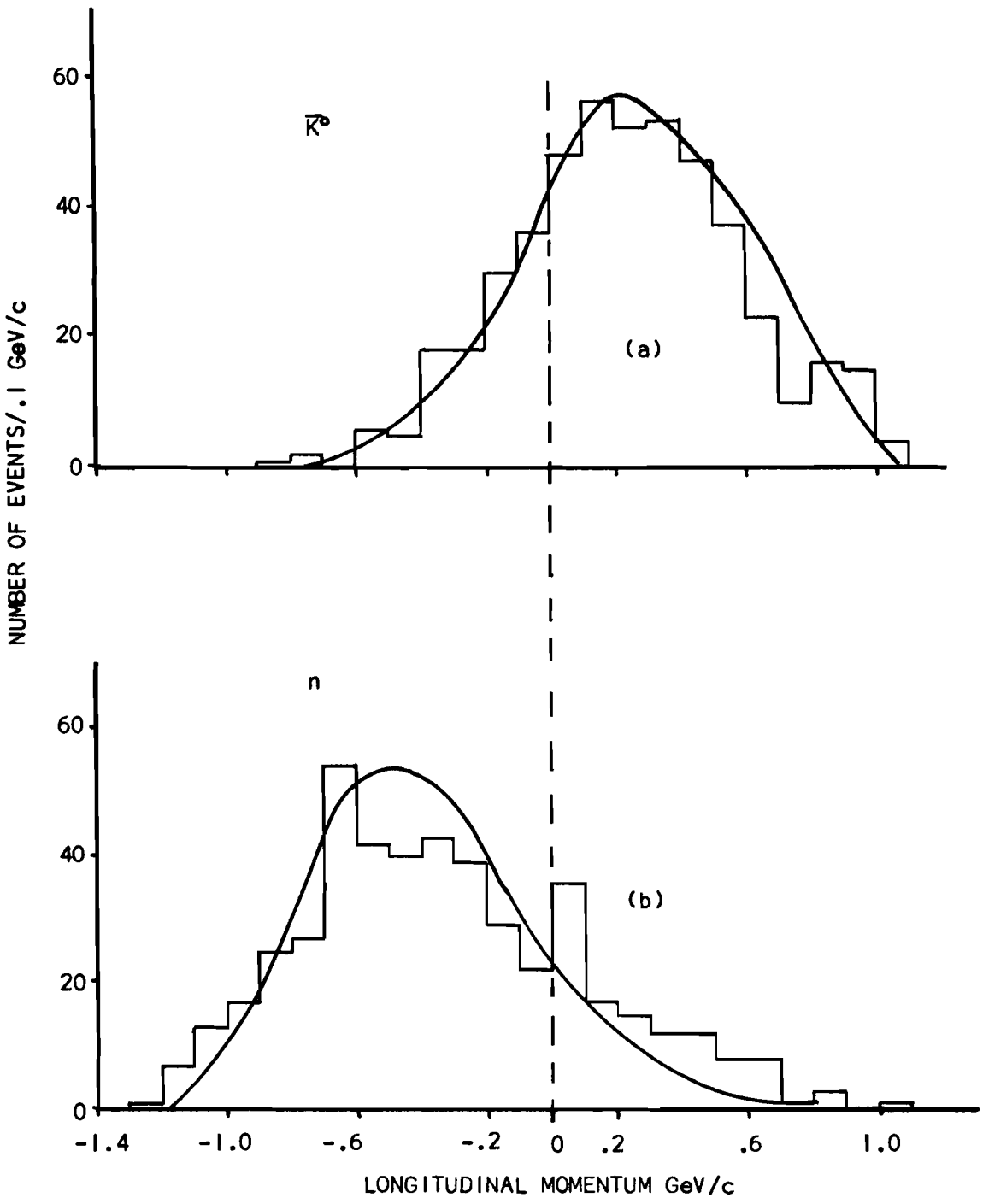

Figure 70.--Longitudinal momentum distributions for (a) π^+ and (b) π^-.

$K^- n \rightarrow \pi^- \pi^- \pi^+ \overline{K}^0 n$

477 EVENTS

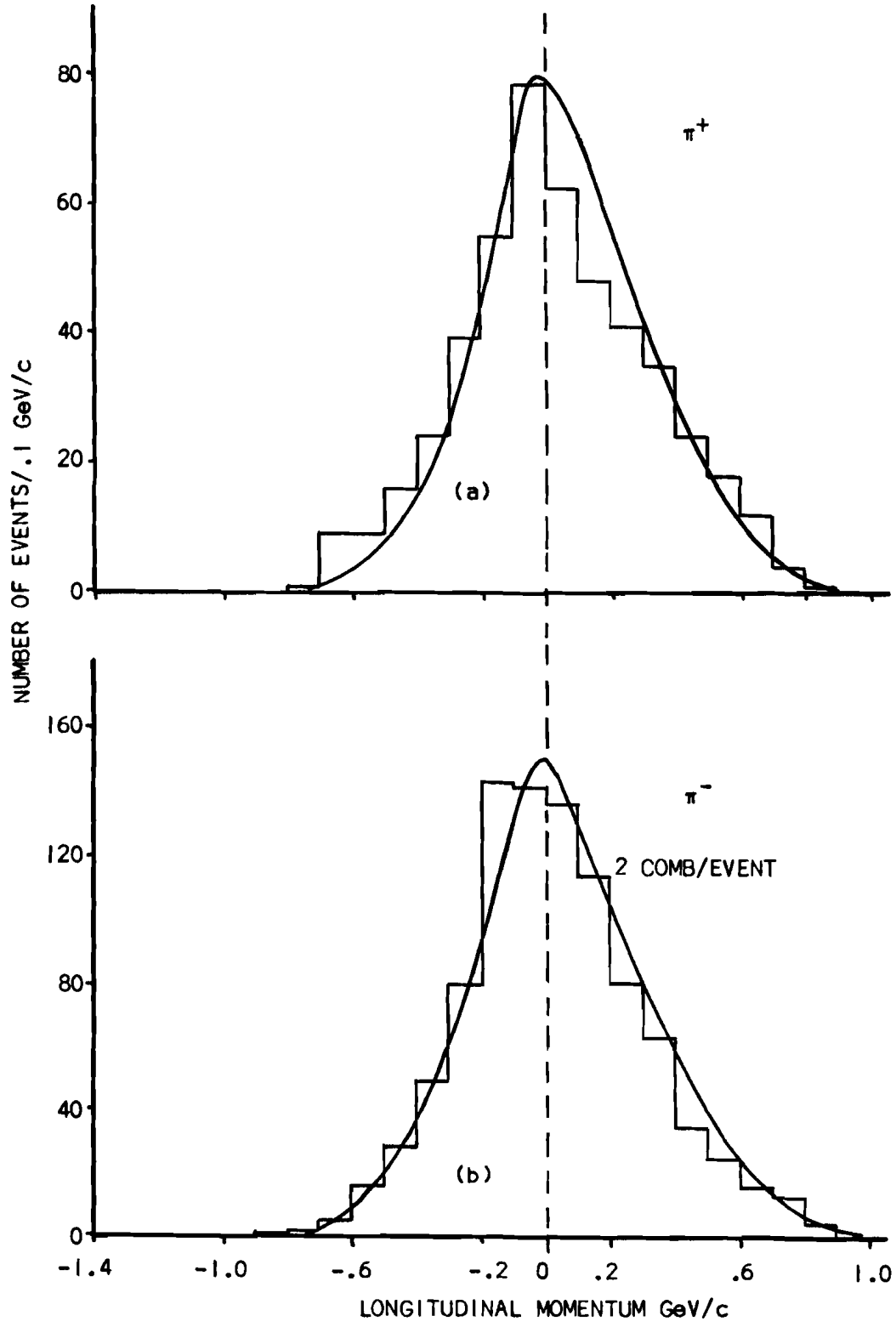

Figure 71.--Transverse momentum distributions for (a) neutron and (b) $\overline{K}^{o}$.

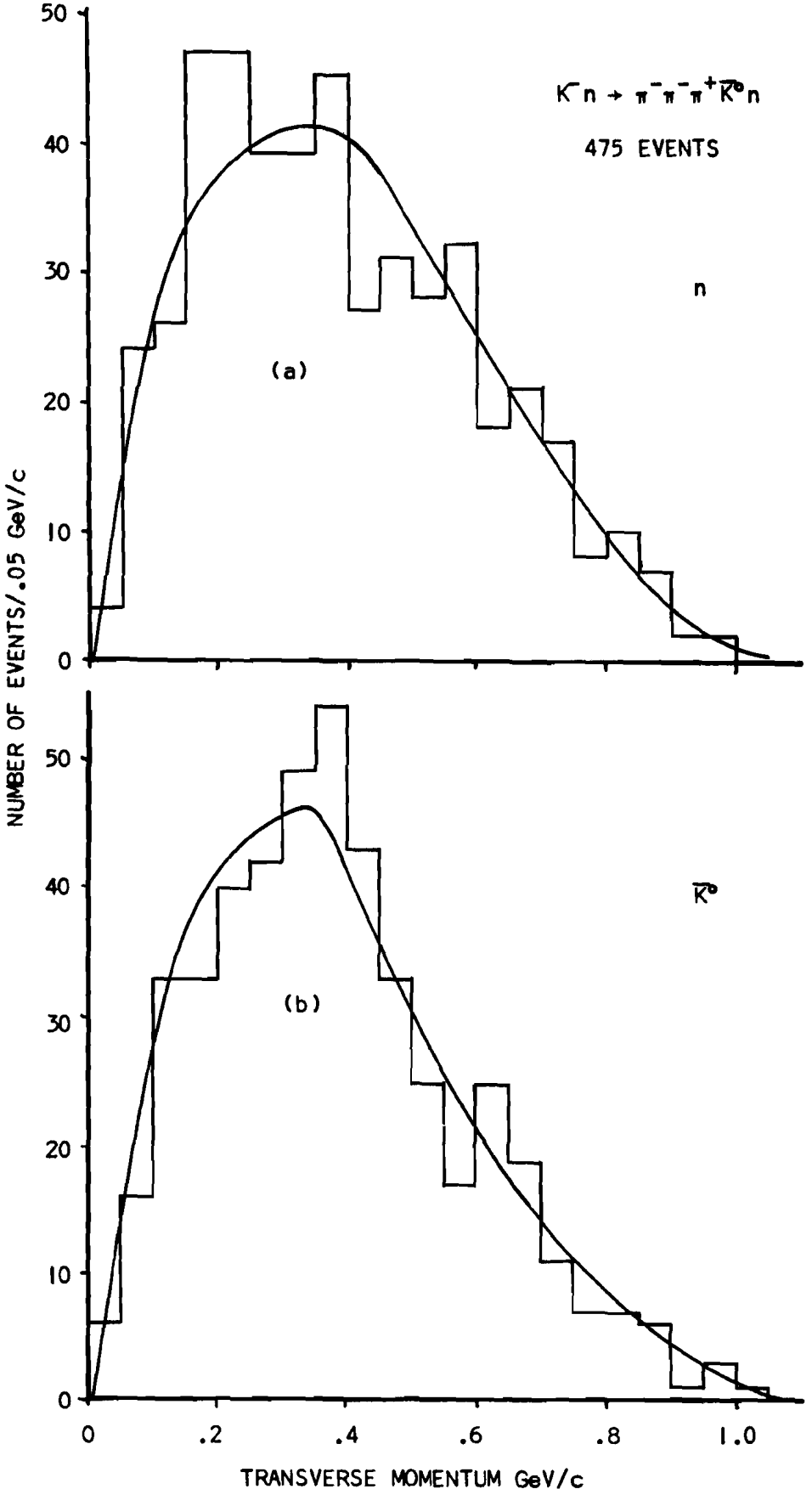
$K^- n \to \pi^- \pi^- \pi^+ \bar{K}^0 n$
475 EVENTS
n
(a)
$\bar{K}^0$
(b)
NUMBER OF EVENTS/.05 GeV/c
TRANSVERSE MOMENTUM GeV/c
0
10
20
30
40
50
.2
.4
.6
.8
1.0

Figure 72.--Transverse momentum distributions for (a) π^- and (b) π^+.

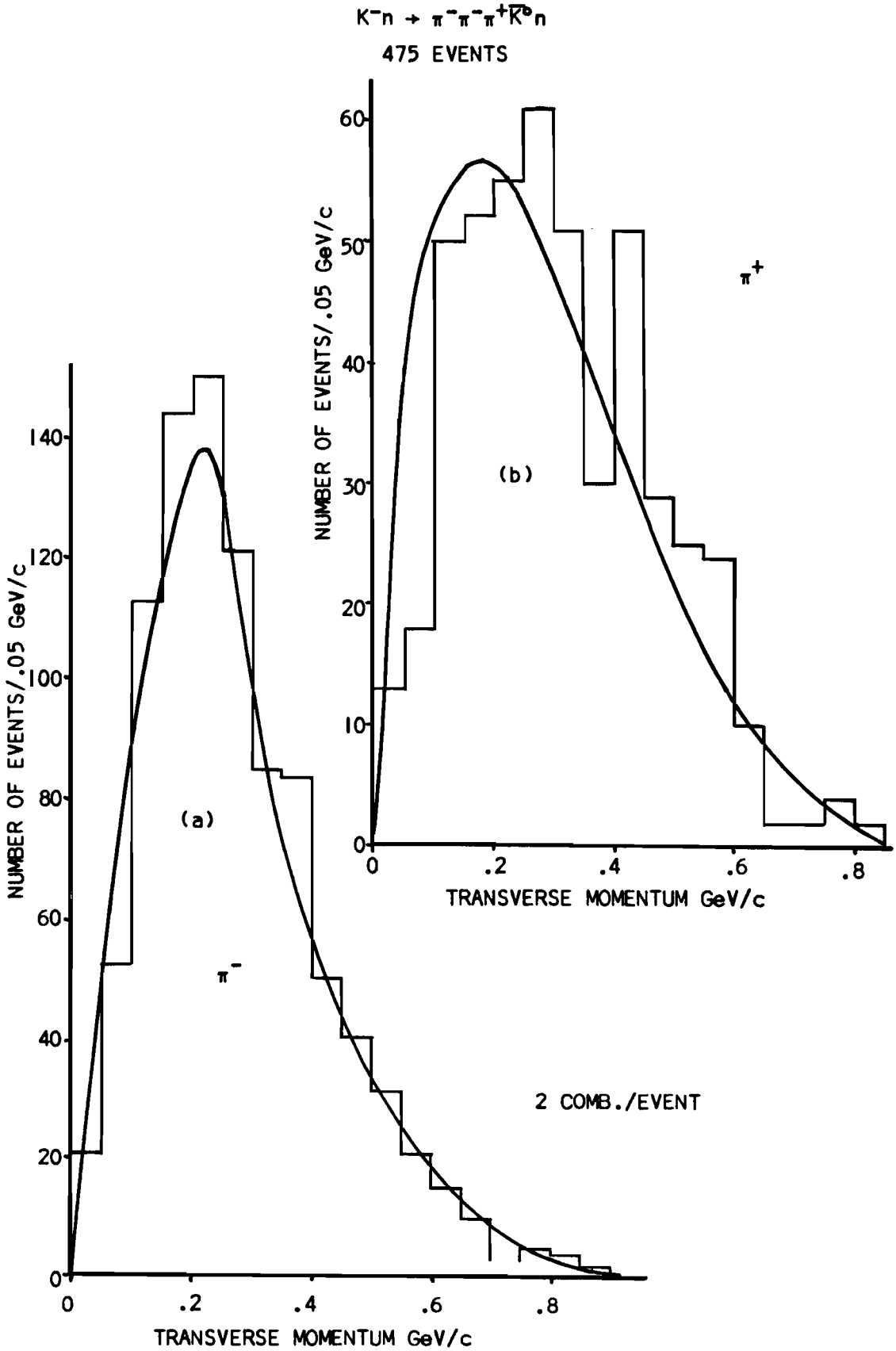
$K^-n \rightarrow \pi^-\pi^-\pi^+\bar{K}^0n$
475 EVENTS
NUMBER OF EVENTS/.05 GeV/c
(a)
π^-
2 COMB./EVENT
TRANSVERSE MOMENTUM GeV/c
(b)
π^+

Qualitatively, all of the distributions have the same shape.

The CLA model calculation qualitatively reproduced the observed single particle longitudinal and transverse momentum distributions.

CHAPTER VI

BARYON ENHANCEMENT IN THE $n\pi^-\pi^-$ INVARIANT MASS DISTRIBUTION

In the reaction $K^-n \rightarrow \pi^-\pi^-\pi^+n\overline{K}^0$, we have found[55] evidence for an enhancement in the $n\pi^-\pi^-$ invariant mass distribution at a mass of (1.627 ± .012) GeV/c^2. The production cross-section for this enhancement is (13.0 ± 3.9) μbarns, where a correction has been included for the unseen decays of the $\overline{K}^0$. If this enhancement were interpreted as a resonance, it would be a zero-strangeness baryon with an isotopic spin of 5/2. The existence of a resonance with such quantum numbers is a very important and interesting question. The most obvious problem connected with the existence of a resonance of this type is the inability to fit it into any well established SU(3) multiplet. The smallest SU(3) multiplet necessary to contain such a resonance would have 35 members, while all previously well established baryon resonances are consistent with being members of SU(3) octets or decuplets.

Figure 73(a) is a histogram of the $n\pi^-\pi^-$ invariant mass distribution for this reaction. The sample contains 468 events. These events were required to have a main-vertex probability greater than or equal to 7.5 per cent, and a spectator proton momentum less than .275 GeV/c. The reasons for these restrictions are discussed in Sections C and F of Chapter III. The events in Figure 73(a) were not corrected for vees lost out the end of the bubble chamber. When this correction is included only 11 events are added to the entire sample with 1 event falling in the

Figure 73.--(a) Invariant mass distribution for $n\pi^-\pi^-$ from reaction II-7 and (b) corresponding χ^2 probability distribution.

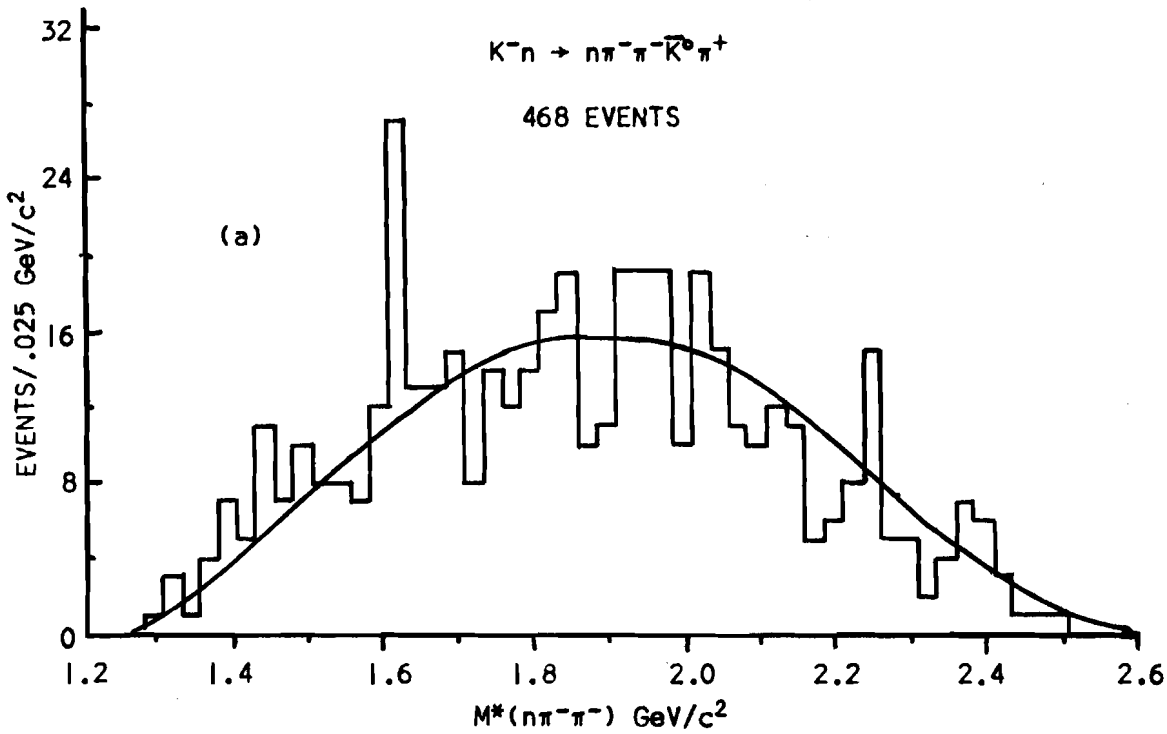
$K^-n \to n\pi^-\pi^-\bar{K}^0\pi^+$
468 EVENTS
(a)
EVENTS/.025 GeV/c^2
32
24
16
8
0
1.2
1.4
1.6
1.8
2.0
2.2
2.4
2.6
M*($n\pi^-\pi^-$) GeV/c^2

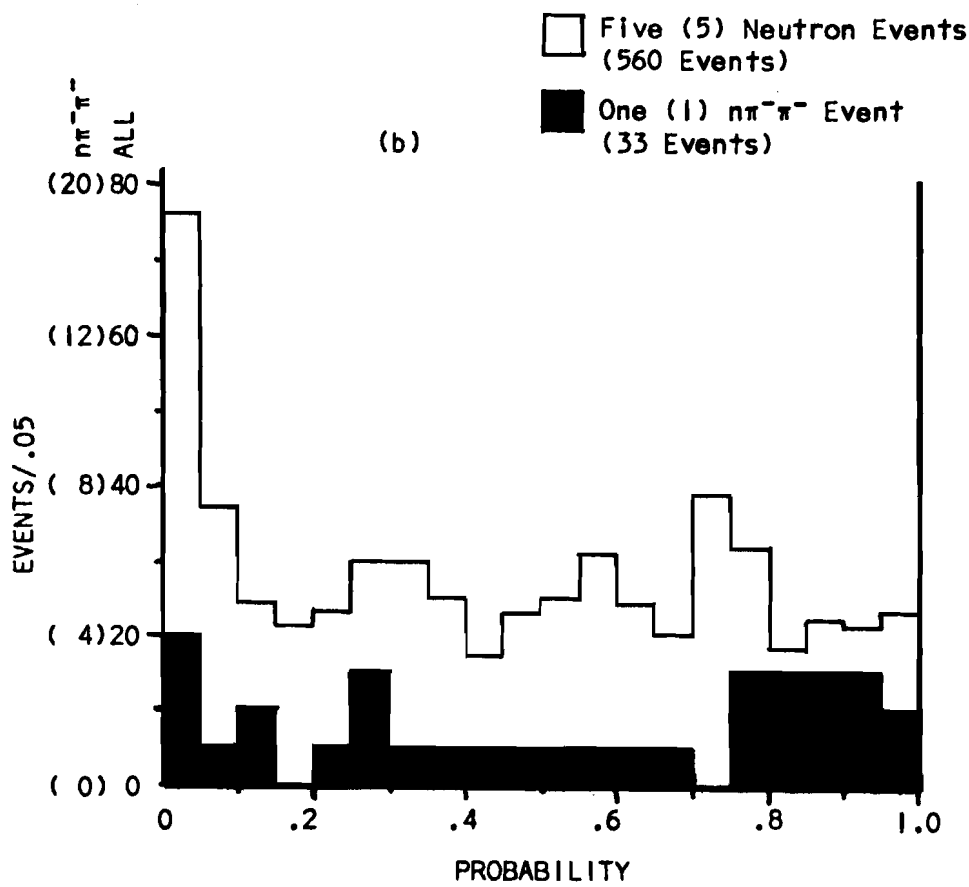
Five (5) Neutron Events
(560 Events)
One (1) $n\pi^-\pi^-$ Event
(33 Events)
(b)
$n\pi^-\pi^-$
ALL
EVENTS/.05
(20) 80
(12) 60
(8) 40
(4) 20
(0) 0
0
.2
.4
.6
.8
1.0
PROBABILITY

region from 1.615 to 1.640 GeV/c^2 (the region of the enhancement). The curve in Figure 73(a) was calculated using the CLA model (see Chapter IV). From Chapter IV we recall that this CLA calculation has the observed amounts of $N^{*-}(1236)$ and $K^{*-}(890)$ production folded in. The curve is seen to be a good representation of the background. The mass interval from 1.607 to 1.632 GeV/c^2 contains 27 events while the background curve predicts (11 ± 3.3) events. This corresponds to a 4.8 standard deviation enhancement above background. From an ideogram of the data (Figure 74), we found the mass to be (1.627 ± .012) GeV/c^2. Also from this ideogram we found that the shape of the peak was consistent with our resolution of .018 GeV/c^2. The curve in Figure 74 is the background plus a Gaussian normalized to the number of events in the enhancement region and having a width of $\sqrt{2}$ (.018 GeV/c^2). The factor of $\sqrt{2}$ is included to take into account the broadening introduced by the ideogramming. We have determined that the full width at half maximum is Γ < .030 GeV/c^2 at the 90 per cent confidence level.

In Chapter III, Figure 5(a) is the histogram of the missing mass squared for those events having ionization consistent with the reaction

$$K^- n \rightarrow \pi^- \pi^- \pi^+ \bar{K}^0 (MM). \qquad \text{(VI-1)}$$

Those events also fitting the neutron hypothesis and having the invariant mass of the $n\pi^-\pi^-$ between 1.615 and 1.640 BeV/c^2 have been blackened. It is clear that those events in the enhancement interval are consistent with the missing neutron hypothesis. The interval from 1.615 to 1.640 GeV/c^2 was chosen by making a histogram of the $n\pi^-\pi^-$ mass distribution using 5 MeV/c^2 bins and choosing the 25 MeV/c^2 interval that contained

Figure 74.--Ideogram for $n\pi^-\pi^-$ invariant mass distribution.

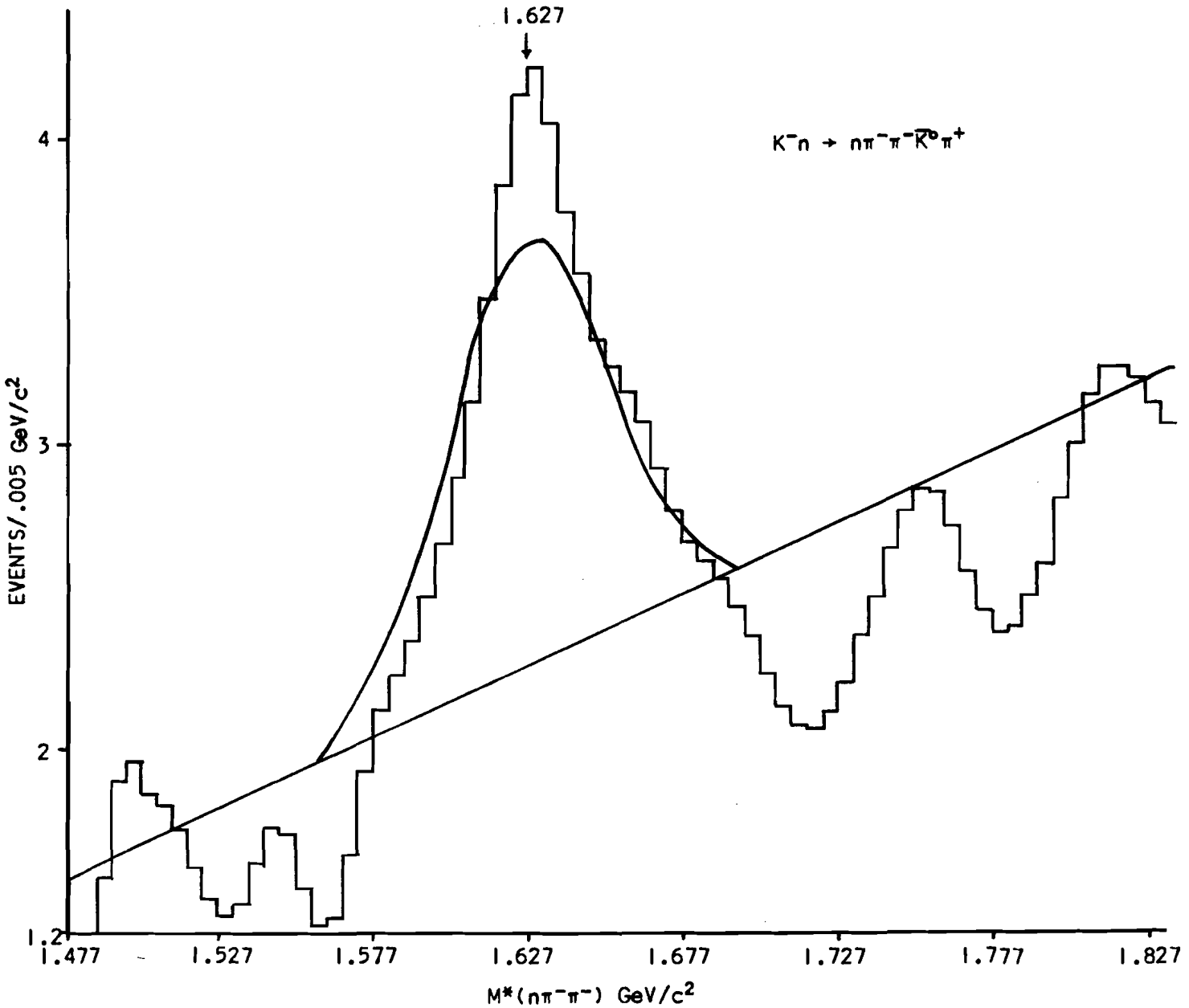
1.627
$K^-n \to n\pi^-\pi^-\bar{K}^0\pi^+$
EVENTS/.005 GeV/c²
4
3
2
1.2
1.477
1.527
1.577
1.627
1.677
1.727
1.777
1.827
M*(nπ⁻π⁻) GeV/c²

the most events. This interval will be referred to as the enhancement region and contains 29 events.

Figure 73(b) shows the main-vertex probability distribution for those events fitting the neutron reaction (11-7). Those events fitting reaction 11-7 with $n\pi^-\pi^-$ invariant mass within the enhancement region have been blackened. The scale for the enhancement region has been increased by a factor of five so that these events can be seen. No probability cut has been imposed on the events shown in Figure 73(b). The events in the enhancement region have the same general shape as the rest of the neutron events. As mentioned previously, we chose to use only those events which had main-vertex probabilities of at least 7.5 per cent. This corresponds to the 29 events mentioned earlier for the enhancement region.

Figure 75(a) shows the $n\pi^-$ invariant mass distribution for those events in the enhancement region. The $n\pi^-$ mass distribution for the entire sample of events fitting the neutron hypothesis is shown in Figure 58 of Chapter V. The smooth curve in Figure 75(a) is the prediction of pure phase space for the two particles ($n\pi^-$) out of the three ($n\pi^-\pi^-$) when these three result from the decay of an object of mass 1.627 GeV/c^2. Although a $N^{*-}(1236)$ is produced in over 50 per cent of all the events of this reaction, there is no clear evidence of $N^{*-}(1236)$ production in the enhancement region. Figure 75(b) is the Dalitz plot for the $n\pi^-\pi^-$ enhancement. Since the two π^- mesons are the same kind of particle, we have folded this plot about the symmetry axis. The $N^{*-}(1236)$ bands, as indicated in the figure, almost cover the entire Dalitz plot. Because of the limited phase space allowed to the $n\pi^-$ in the decay of the

Figure 75.--(a) Invariant mass distribution of the $n\pi^-$ from the $n\pi^-\pi^-$ enhancement region. (b) Corresponding Dalitz plot.

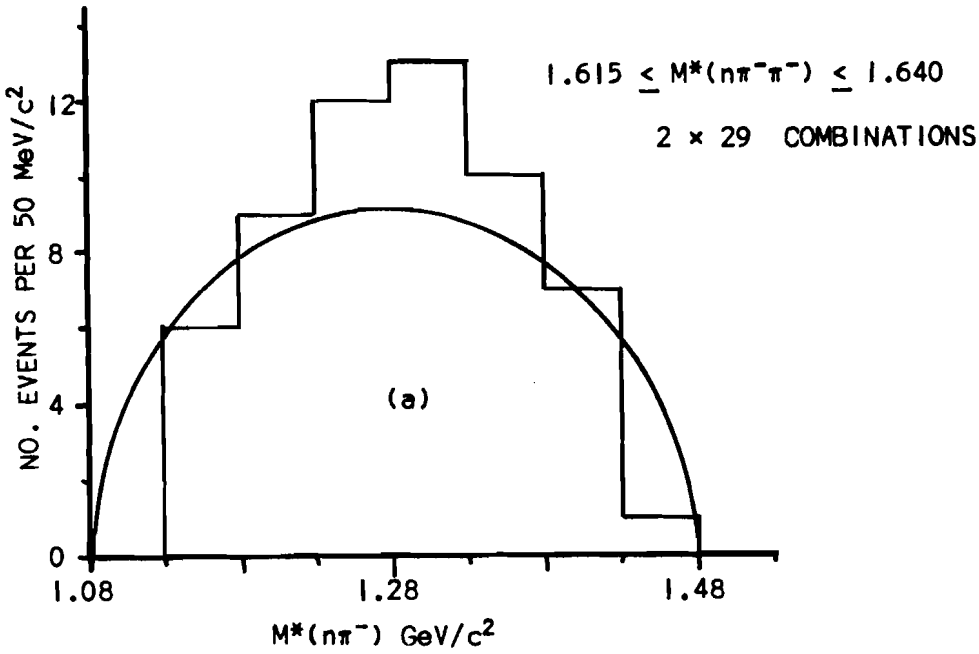
1.615 ≤ M*(nπ⁻π⁻) ≤ 1.640
2 × 29 COMBINATIONS
(a)
NO. EVENTS PER 50 MeV/c²
0
4
8
12
1.08
1.28
1.48
M*(nπ⁻) GeV/c²

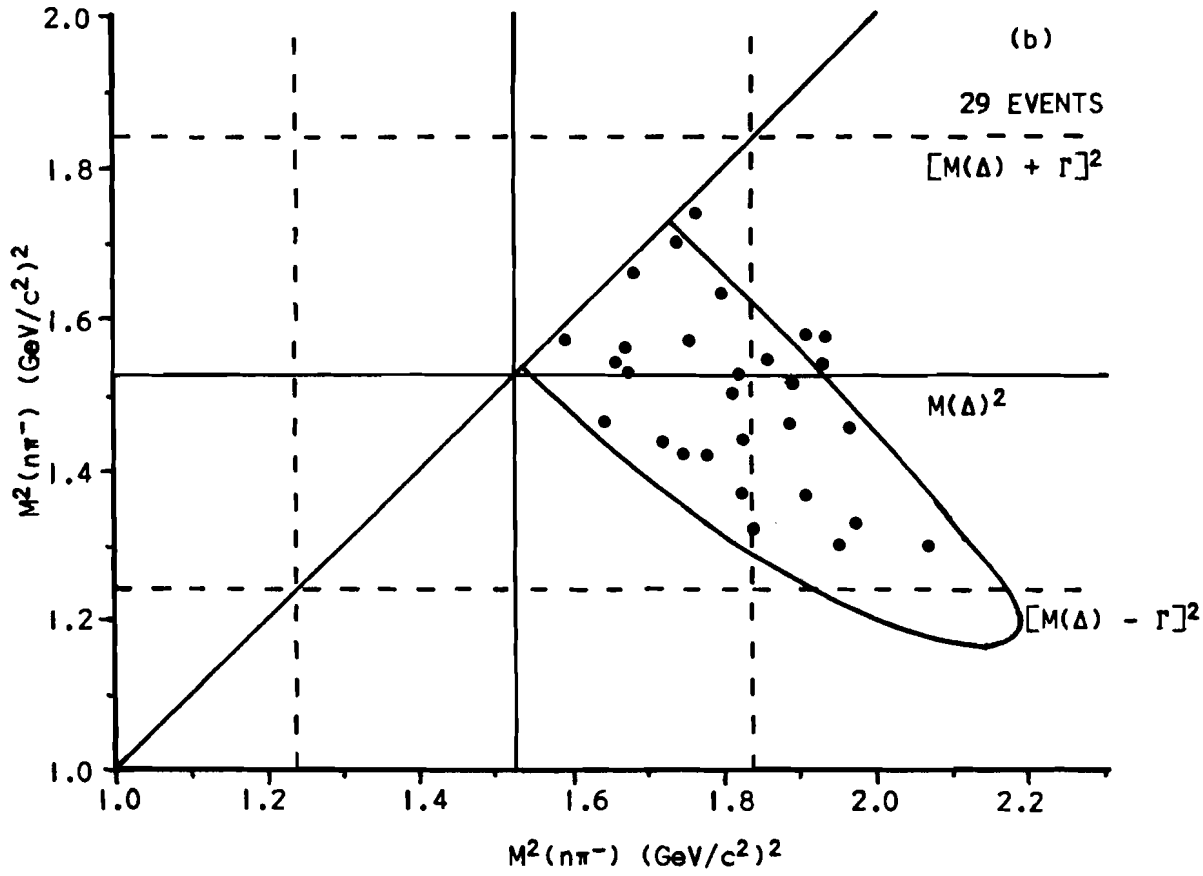
(b)
29 EVENTS
[M(Δ) + Γ]²
M(Δ)²
[M(Δ) - Γ]²
M²(nπ⁻) (GeV/c²)²
1.0
1.2
1.4
1.6
1.8
2.0
2.2
M²(nπ⁻) (GeV/c²)²

enhancement and the large width of the $N^{*-}(1236)$, we cannot rule out the possibility that the $n\pi^-\pi^-$ enhancement does have $N^{*-}\pi^-$ as a decay mode.

The $\bar{K}^o\pi^-$ invariant mass histogram for those events in the enhancement region is shown in Figure 76(a). The curve in Figure 76(a) is Lorentz-invariant phase space for the $K^o\pi^-$ from the five-particle final state. By taking control regions of the $n\pi^-\pi^-$ mass above (1.657 to 1.807 GeV/c^2) and below (1.407 to 1.582 GeV/c^2) the enhancement, we were able to conclude that the amount of $K^{*-}(890)$ in the background under the $n\pi^-\pi^-$ enhancement is consistent with the amount of $K^{*-}(890)$ in the entire sample. For the control regions, the ratio of the number of events in the K^* band (.840 to .940 GeV/c^2) to the total number of events agreed to within .5 standard deviation with the equivalent ratio calculated for the entire sample of events fitting reaction II-7. This implies that there should be (13.1 ± 3.6) $\bar{K}^o\pi^-$ combinations in the $K^{*-}(890)$ region (.840 to .940 GeV/c^2). Figure 76(a) shows that 21 combinations from the $n\pi^-\pi^-$ enhancement region fall in the K^* region. This corresponds to a 2.2 standard deviation excess. This suggests the possibility that the $n\pi^-\pi^-$ enhancement may share a π^- with the $K^{*-}(890)$. This should not be too disconcerting, since it has been previously established that two resonances may constructively interfere and thus have a particle in common.[56,57]

Let us follow an argument by Dalitz in order to display an interference term. For simplicity, assume that the total amplitude A_T, for producting events in some channel, is just the coherent sum of the two amplitudes A_1 and A_2. The production cross-section (σ) is proportional to $|A_1 + A_2|^2$.

Figure 76.--(a) Invariant mass distribution of the $\overline{K}^{o}\pi^{-}$ from the $n\pi^{-}\pi^{-}$ enhancement region. (b) Production angular distribution of $n\pi^{-}\pi^{-}$ enhancement region.

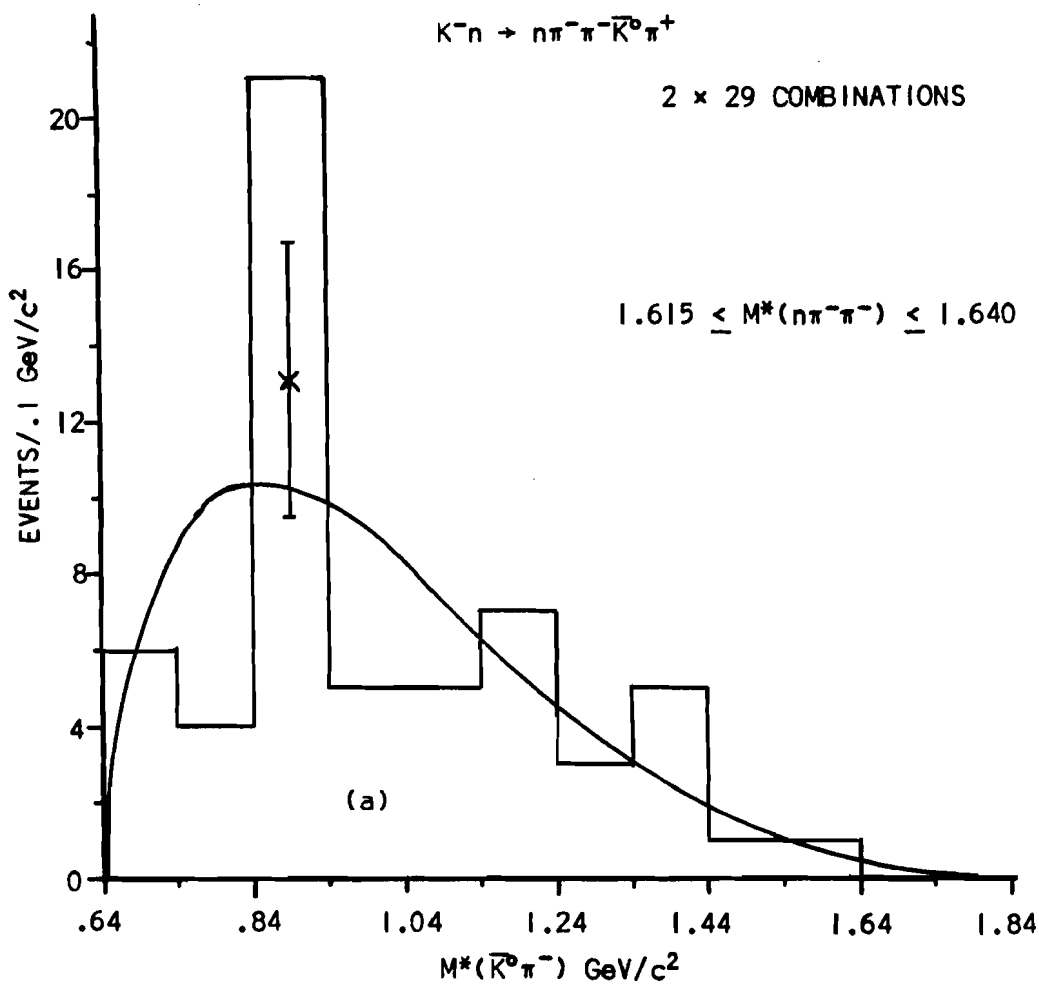
$K^-n \to n\pi^-\pi^-\bar{K}^0\pi^+$
2 × 29 COMBINATIONS
$1.615 \leq M^*(n\pi^-\pi^-) \leq 1.640$
EVENTS/.1 GeV/c²
0
4
8
12
16
20
(a)
.64
.84
1.04
1.24
1.44
1.64
1.84
$M^*(\bar{K}^0\pi^-)$ GeV/c²

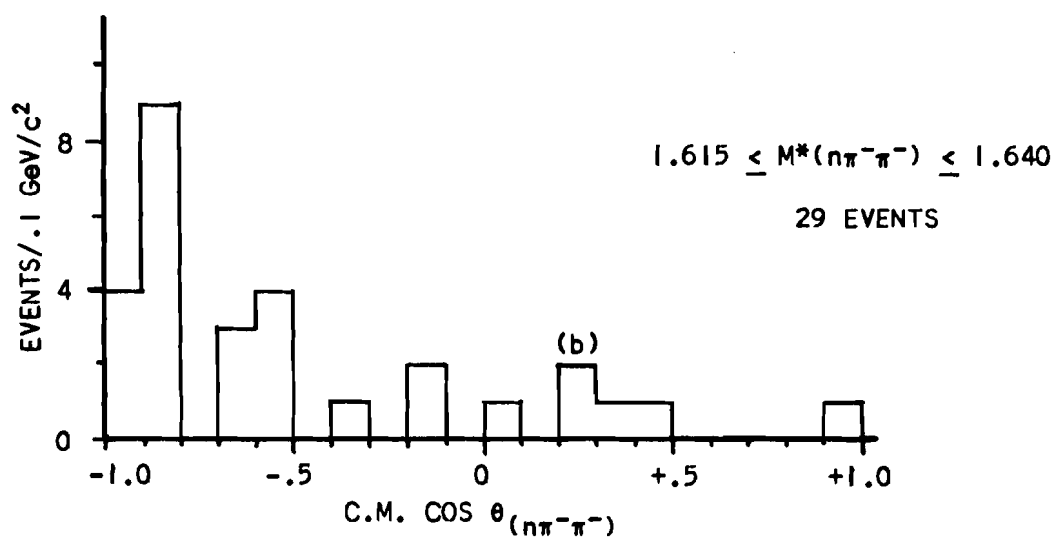
$1.615 \leq M^*(n\pi^-\pi^-) \leq 1.640$
29 EVENTS
EVENTS/.1 GeV/c²
0
4
8
(b)
-1.0
-.5
0
+.5
+1.0
C.M. COS $\theta_{(n\pi^-\pi^-)}$

$$\begin{aligned} \sigma &\sim |A_1 + A_2|^2 \\ &\sim |A_1|^2 + |A_2|^2 + A_1^* A_2 + A_1 A_2^* \\ &\sim |A_1|^2 + |A_2|^2 + 2\,\mathrm{Re}\,(A_1^* A_2) \end{aligned} \qquad \text{(VI-2)}$$

Suppose A_1 refers to the amplitude for K*(890) production and A_2 refers to the amplitude for production of the $n\pi^-\pi^-$ enhancement. If the interference term is positive, it increases the size of the enhancement observed in the $n\pi^-\pi^-$ mass distribution and also results in the sharing of a π^- between this enhancement and the $K^{*-}(890)$. We, therefore, suggest the possibility that constructive interference with the strong K* amplitude may make the production cross-section of the $n\pi^-\pi^-$ large enough to be observed.

Figure 76(b) shows the distribution in the cosine of the production angle of the $n\pi^-\pi^-$ enhancement. The angle is measured in the rest system of the incident K^- and the target neutron. In this system, the $n\pi^-\pi^-$ is seen to be produced mainly in the backward hemisphere.

We have searched for resonances that are associated with this baryon enhancement by plotting all the invariant mass histograms for the events of the enhancement. We have found none in addition to the $K^{*-}(890)$, which was discussed above. Here we present the mass plots for those two body combinations that do not have exotic quantum numbers.

In Figure 77(a) and (b) are shown the invariant mass distributions of the $n\pi^+$ for all the events in the neutron channel and just those events in the $n\pi^-\pi^-$ enhancement, respectively. Although we see no evidence for $N^{*+}(1.236)$ production in the total sample [77(a)], we looked for the preferential production of N^{*+} in the $n\pi^-\pi^-$ enhancement. Figure 77(b) shows no evidence for the production of N^{*+} in the $n\pi^-\pi^-$

Figure 77.--(a) The $n\pi^+$ invariant mass distribution from reaction II-7 and (b) invariant mass distribution of the $n\pi^+$ from $n\pi^-\pi^-$ enhancement region.

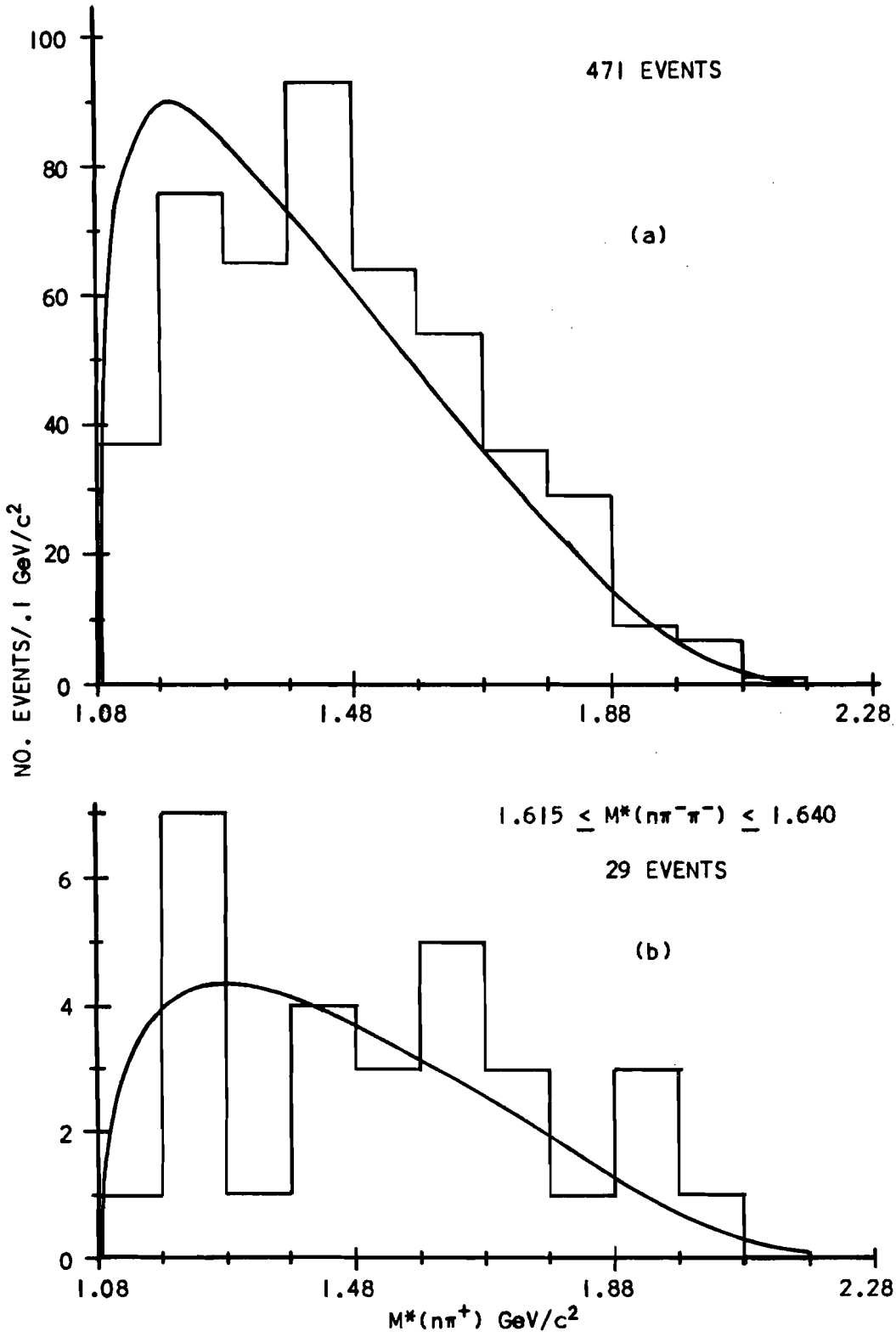
471 EVENTS
(a)
NO. EVENTS/.1 GeV/c²
100
80
60
40
20
0
1.08
1.48
1.88
2.28
1.615 ≤ M*(nπ⁻π⁻) ≤ 1.640
29 EVENTS
(b)
6
4
2
0
1.08
1.48
1.88
2.28
M*(nπ⁺) GeV/c²

enhancement. The solid curve in Figures 77(a) and (b) are the predictions of the CLA model.

Figures 78(a) and (b) show the invariant mass distributions of the $\bar{K}^{\circ}n$ for all events accepted as reaction II-7 and just the enhancement region, respectively. Again, no resonance production is observed in either histogram. The curve in each plot is the prediction of the CLA model.

Figures 79(a) and (b) display the invariant mass distributions of the $\pi^+\pi^-$ for those events fitting reaction II-7 and those in the $n\pi^-\pi^-$ enhancement, respectively. Here one should look for the production of the $\rho^{\circ}(765)$, entertaining the possibility that it may be produced in association with the $n\pi^-\pi^-$ enhancement. First of all we note that the CLA model predicts too few events above .580 GeV/c^2. This problem was discussed further in Chapter V. We take the ρ° region to be from .680 to .880 GeV/c^2. In order to get a reasonable prediction for the background in this ρ° region, we renormalized the CLA predictions for masses greater than .580 GeV/c^2. This was done by taking bands above and below the ρ° region and normalizing the CLA predictions to the observed number of events in those bands. This revised background [shown as a dashed curve in Figures 79(a) and (b)] was found to be a reasonable background estimate and indicated no evidence for ρ° production. The two normalization regions were from .580 to .680 GeV/c^2 and from .880 to 1.380 GeV/c^2. Using the same normalization factor obtained for Figure 79(a), a background for the $\pi^+\pi^-$ mass distribution for those events in the $n\pi^-\pi^-$ enhancement was drawn [Figure 79(b)]. The solid curve in Figure 79(b) is the original CLA prediction and the dashed curve is the renormalized

Figure 78.--(a) The $\overline{K}^{o}n$ invariant mass distribution from reaction II-7 and (b) invariant mass distribution of the $\overline{K}^{o}n$ from $n\pi^{-}\pi^{-}$ enhancement region.

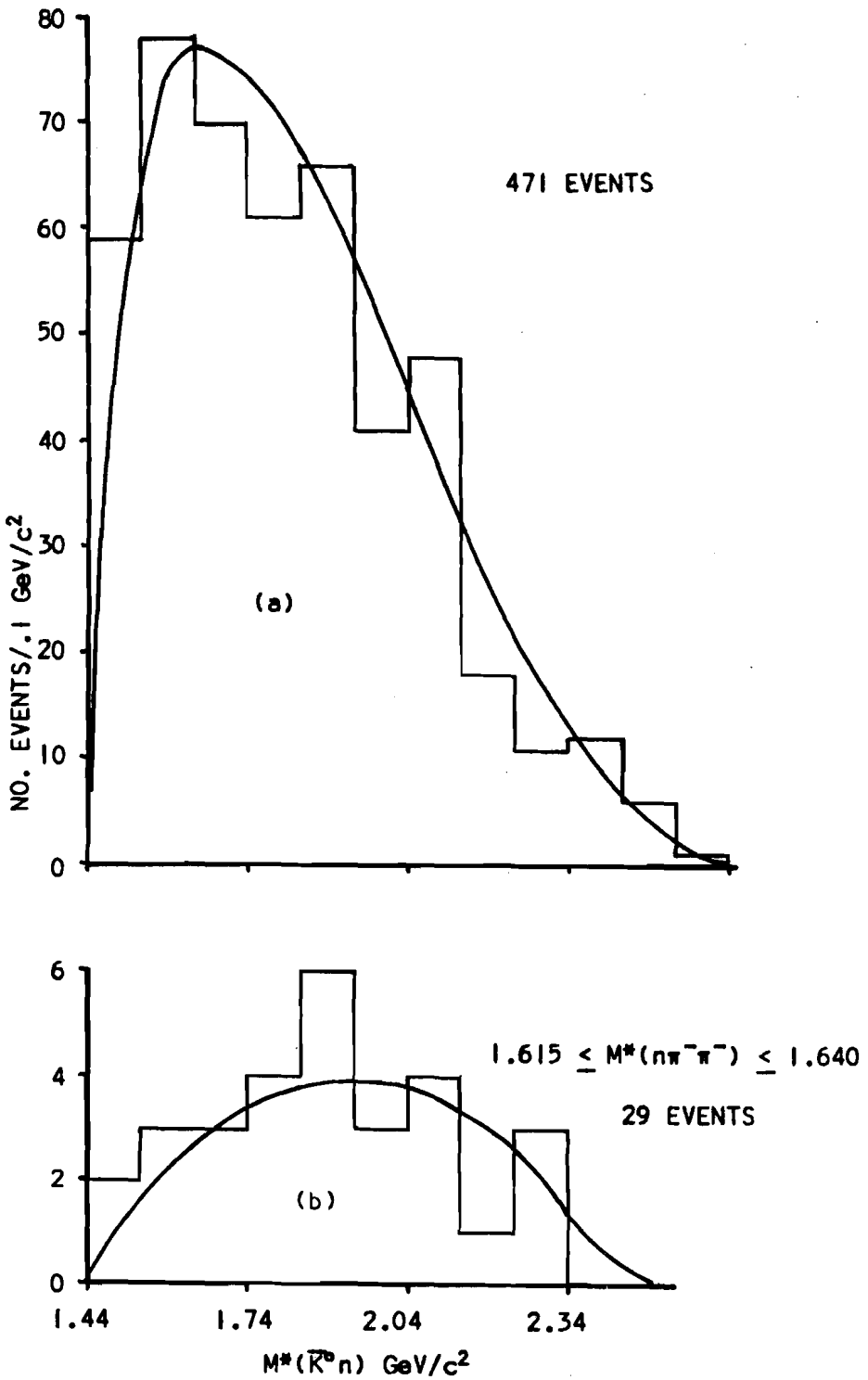
80
70
60
50
40
30
20
10
0
NO. EVENTS/.1 GeV/c²
471 EVENTS
(a)
6
4
2
0
1.615 ≤ M*(nπ⁻π⁻) ≤ 1.640
29 EVENTS
(b)
1.44
1.74
2.04
2.34
M*(K̄⁰n) GeV/c²

Figure 79.--(a) The $\pi^+\pi^-$ invariant mass distribution from reaction II-7 and (b) invariant mass distribution of the $\pi^+\pi^-$ from $n\pi^-\pi^-$ enhancement region.

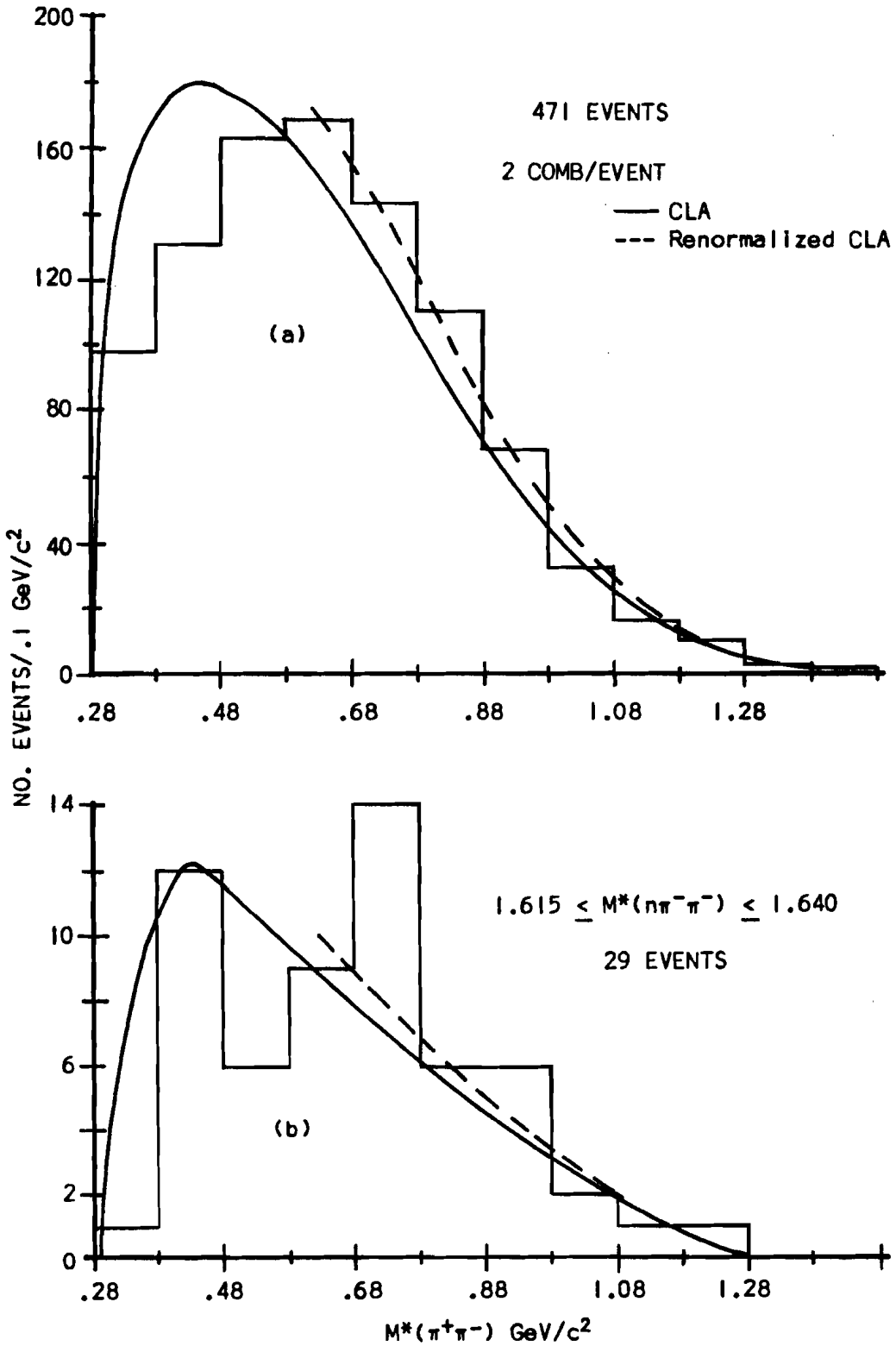
200
160
120
80
40
0
471 EVENTS
2 COMB/EVENT
CLA
Renormalized CLA
(a)
.28
.48
.68
.88
1.08
1.28
NO. EVENTS/.1 GeV/c²
14
10
6
2
0
1.615 ≤ M*(nπ⁻π⁻) ≤ 1.640
29 EVENTS
(b)
.28
.48
.68
.88
1.08
1.28
M*(π⁺π⁻) GeV/c²

prediction. In the ρ° region (.680 to .880 GeV/c^2), we find an excess of 6 events above a background of 14. This is only a 1.6 standard deviation effect and does not imply preferential production of $\rho^{\circ}(765)$ in the $n\pi^-\pi^-$ enhancement.

The narrow width of the enhancement precludes the possibility of its being a kinematic reflection of the $N^{*-}(1236)$. Since the width of the N^* is .120 GeV/c^2, any kinematic reflection containing it will not have a smaller width. If this narrow enhancement were a reflection that did not involve the $N^{*-}(1236)$, it would have the property of involving three particles without any two of them being decay products of the same parent resonance. We were unable to find any kinematic mechanism that could produce such a narrow (< .030 GeV/c^2) effect. We conclude that the $n\pi^-\pi^-$ enhancement is not a kinematic reflection and its sharing a π^- with the $K^{*-}(890)$ cannot be a kinematic reflection mechanism because the baryon enhancement is too narrow.

We will present here a short review of other findings concerning similar enhancements.

In a study of reaction ii-7 with a K^- beam momentum of 3.9 GeV/c, Kwan Wu Lai[58] and collaborators do not find a similar $n\pi^-\pi^-$ enhancement. Their sensitivity is 16 events per μbarn and ours is 4.5 events per μbarn. This is not necessarily inconsistent with our result, since the beam momenta of the two experiments are different, and it must be remembered that we have no experience with momentum dependence of the production of isospin 5/2 baryon enhancements.

In a missing mass spectrometer experiment with a π^+ beam of 1.9 GeV/c, Banner et al.[59] have investigated the reaction

$$\pi^+ p \rightarrow \pi^- (MM)^{+++}.$$

Here $(MM)^{+++}$ stands for the undetected particles, which have a total isotopic spin of 5/2. They state that they see no evidence for structure in the $p\pi^+\pi^+$ mass distribution for masses below 1.75 GeV/c^2. However, an examination of their Figure 3 reveals a 3 standard deviation enhancement in their missing-mass spectrum at a mass of about 1.660 GeV/c^2. They quote a upper limit of 40 μbarns in the production cross-section of the I = 5/2 isobar while our cross-section is (13.0 ± 3.9) μbarns.

Benvenuti, Marquit, and Oppenheimer[60] later reported confirmation of the I = 5/2 isobar of Banner et al. in a study of the reaction $\pi^- d \rightarrow (P_s) n\pi^-\pi^-\pi^+$ at 2.26 GeV/c. The symbol (P_s) indicates a spectator proton. They report an enhancement in the $n\pi^-\pi^-$ invariant mass distribution at a mass of 1.640 GeV/c^2 and with a width $\Gamma \leq .060$ GeV/c^2.

Danburg et al.[61] in response to Benvenuti et al. examined the charge symmetric state $p\pi^+\pi^+$ in the charge symmetric reaction $\pi^+ d \rightarrow (n_s) p\pi^+\pi^+\pi^-$ (n_s refers to a spectator neutron) at eight incident momenta between 1.1 and 2.37 GeV/c and found no evidence for an enhancement in the mass range 1.500 to 2.000 GeV/c^2. In addition, when just those events from the beam momenta nearest the beam momentum of Benvenuti et al. (1.86, 2.15, and 2.37 GeV/c) were examined separately the lack of an enhancement still persisted.

Fleury et al.[62] examined the reaction $\pi^- d \rightarrow (P_s) p\pi^-\pi^-\pi^\circ$ at 5 GeV/c. They report an enhancement in the $p\pi^-\pi^-$ invariant mass distribution at 1.672 GeV/c^2 with a width $\Gamma \approx .055$ GeV/c^2. Although this enhancement could have an isotopic spin of either 5/2 or 3/2, its narrow width seems

to distinguish it from the previously well-established isobars.

The data presented here by no means establishes the existence of the $I = 5/2$ isobar. We suggest only that more data at our present beam momentum may help clarify the issue.

CHAPTER VII

RESULTS AND CONCLUSIONS

We have investigated the three reactions:

$$K^- n \rightarrow \bar{K}^0 \pi^- \pi^- p, \qquad \text{(VII-1)}$$

$$\rightarrow \bar{K}^0 \pi^- \pi^- p \pi^0 \qquad \text{(VII-2)}$$

and

$$\rightarrow \bar{K}^0 \pi^- \pi^- \pi^+ n. \qquad \text{(VII-3)}$$

These final states were produced with cross-sections of (324 ± 51), (331 ± 52), and (428 ± 62) μbarns for Reactions VII-1, VII-2, and VII-3, respectively. These cross-sections have been corrected for unseen decay modes of the $\bar{K}^0$. They have been measured at 3 GeV/c[63] and are (410 ± 30), (130 ± 14), and (200 ± 17) μbarns, respectively.

All three of these reactions were found to have significant amounts of two-body resonance production. Table 4 is a summary of the relative amounts of resonance production observed in the three reactions.

An investigation of the decay angular distributions of the $K^{*-}(890)$ in the Jackson frame was made for each of the three reactions. A maximum likelihood fit to the data of Reaction VII-1 yielded the spin density matrix elements ρ_{00} = .255 ± .055, ρ_{1-1} = .195 ± .050, and Re ρ_{10} = .000 ± .025. These suggest the exchange of a 0^- object and one or more members of the natural spin-parity sequence 1^-, 2^+, 3^-,•••. On the other hand, the lack of an enhancement at low invariant mass for the $K^{*-}\pi^-$ system seems to rule out π meson exchange. We have no simple explanation for our observed spin density matrix elements. We were unable

TABLE 4

CROSS-SECTIONS

Reaction	Number of Events	Fraction (Per Cent)	Cross-Section μbarns
$K^-n \to K^{*-}(890)\pi^-p$	192 ± 22	52 ± 5	167 ± 32
$\quad \bar{K}^0\pi^-$			
$\to K^{*-}(890)\ N^{*0}(1236)$	22 ± 11	6 ± 3	19 ± 10
$\quad \bar{K}^0\pi^- \quad p\pi^-$			
$\to N^{*0}(1236)\pi^-\bar{K}^0$	22 ± 13	6 ± 4	19 ± 11
$\quad p\pi^-$			
$\to K^{*-}(1420)p\pi^-$	55 ± 13	15 ± 4	48 ± 14
$\quad \bar{K}^0\pi^-$			
$\to$ "$N^{*0}(1680)$"$\pi^-\bar{K}^0$	72 ± 20	19 ± 5	63 ± 20
$\quad p\pi^-$			
$\to \bar{K}^0\pi^-\pi^-p$	8 ± 30	2 ± 8	7 ± 26
(nonresonant)			
TOTAL	371 ± 19	100	324 ± 51
$K^-n \to K^{*-}(890)\pi^-p\pi^0$	169 ± 20	45 ± 4	149 ± 28
$\quad \bar{K}^0\pi^-$			
$\to \bar{K}^0\pi^-\pi^-p\pi^0$	206 ± 17	55 ± 4	182 ± 31
(nonresonant)			
TOTAL	375 ± 19	100	331 ± 52
$K^-n \to K^{*-}(890)\pi^-\pi^+n$	193 ± 37	40 ± 8	172 ± 42
$\quad \bar{K}^0\pi^-$			
$\to N^{*-}(1236)\pi^-\pi^+\bar{K}^0$	234 ± 37	49 ± 8	209 ± 46
$\quad n\pi^-$			
$\to K^*(890)\ N^*(1236)\pi^+$	39 ± 27	8 ± 6	35 ± 24
$\quad \bar{K}^0\pi^- \quad n\pi^-$			
$\bar{K}^0\pi^-\pi^-\pi^+n$	13 ± 46	3 ± 10	12 ± 41
(nonresonant)			
TOTAL	479 ± 22	100	428 ± 62

to observe alignment by using decay distributions in the Jackson frame for the K*'s produced in Reactions VII-2 and VII-3 and the N*'s produced in Reaction VII-3. Examination of the decay distributions in the helicity frame provided no additional information.

The $|t - t_{min}|$ distributions for the $K^{*-}(890)$ produced in Reactions VII-1, VII-2, and VII-3 and for the $N^{*-}(1236)$ produced in Reaction VII-3 were fit to an exponential using the least squares method. The exponential slopes for the distributions are shown in Table 5. They are much smaller than the slope for K^-p elastic scattering at our energy, which is $(8.3 \pm .3)$ GeV/c$)^{-2}$.

The data were compared to the predictions of a multiperipheral model proposed by Chan, Losklewiez, and Allison. The observed amounts of $K^{*-}(890)$ and $N^*(1236)$ were input to the calculation. The known masses and widths of these resonances were also input. The model agreed qualitatively with the invariant mass plots obtained from the data.

Table 6 summarizes the results of a comparison of the CLA calculation with the observed single particle production angular distributions for Reactions VII-1, VII-2, and VII-3. The model agrees qualitatively with the data.

Table 7 shows the results of a comparison of the CLA model calculation with the computed average values of the transverse and longitudinal momentum distributions for each of the individual particles produced in the Reactions VII-1, VII-2, and VII-3. Both the shapes of the distributions and the average values for the data and model are in qualitative agreement.

TABLE 5

EXPONENTIAL SLOPE OF $|t - t_{min}|$ DISTRIBUTIONS

Reaction	$\lambda_{K^{*-}}$ $(GeV/c)^{-2}$	$\lambda_{N^{*-}}$ $(GeV/c)^{-2}$
$K^-n \rightarrow K^{*-}(890)\pi^-p$	1.71 ± .29	
$K^-n \rightarrow K^{*-}(890)\pi^-\pi^\circ p$	.37 ± .33	
$K^-n \rightarrow K^{*-}(890)\pi^-\pi^+n$	1.64 ± .38	
$K^-n \rightarrow N^{*-}(1236)\pi^-\pi^+\overline{K}^\circ$		1.51 ± .15

TABLE 6

PRODUCTION COS θ CHI-SQUARE PROBABILITIES

Reaction II-5	Probability	Reaction II-6	Probability	Reaction II-7	Probability
π^-	5%	π^-	40%	π^-	25%
p	5%	p	5%	π^+	40%
$\overline{K}^\circ$	19%	$\overline{K}^\circ$	20%	$\overline{K}^\circ$	4%
		π°	20%	n	.01%

TABLE 7

AVERAGE VALUE OF SINGLE PARTICLE
TRANSVERSE AND LONGITUDINAL MOMENTUM

	P_T in GeV/c		P_L in GeV/c	
	Data	Model	Data	Model
		$K^-n \rightarrow \bar{K}^0\pi^-\pi^-\pi^+n$		
π^-	.281 ± .005	.281 ± .002	.027 ± .009	.039 ± .005
π^+	.317 ± .008	.285 ± .004	.037 ± .014	.057 ± .006
$\bar{K}^0$	.389 ± .009	.381 ± .005	.239 ± .016	.260 ± .008
n	.393 ± .010	.410 ± .005	-.331 ± .020	-.395 ± .008
		$K^-n \rightarrow \bar{K}^0\pi^-\pi^-p\pi^0$		
π^-	.309 ± .006	.283 ± .002	.016 ± .010	.020 ± .004
p	.416 ± .011	.435 ± .004	-.296 ± .018	-.323 ± .007
$\bar{K}^0$	.391 ± .010	.382 ± .004	.199 ± .017	.228 ± .006
π^0	.317 ± .009	.295 ± .003	.071 ± .015	.055 ± .005
		$K^-n \rightarrow \bar{K}^0\pi^-\pi^-p$		
π^-	.361 ± .008	.323 ± .003	.063 ± .015	.100 ± .008
p	.445 ± .012	.450 ± .005	-.476 ± .025	-.612 ± .010
$\bar{K}^0$	.440 ± .012	.406 ± .005	.352 ± .020	.413 ± .010

It is very interesting that the model can account for the fact that the fraction of baryons produced in the forward hemisphere is larger in the reactions[9]

$$K^-n \rightarrow \pi^-\pi^-\pi^+\Lambda^\circ \qquad \text{(VII-4)}$$

and

$$K^-n \rightarrow \pi^-\pi^-\pi^+\Sigma^\circ \qquad \text{(VII-5)}$$

than in Reaction VII-1. Also, this fraction is larger in reaction

$$K^-n \rightarrow \pi^-\pi^-\pi^+\Lambda^\circ\pi^\circ \qquad \text{(VII-6)}$$

than in Reactions VII-2 and VII-3. These results are given in Table 8. Chan, Loskiewicz, and Allison point out that--all other things being equal--lambdas are less peripheral than nucleons because the strange meson Regge intercept is lower than the one for zero strangeness mesons and thus lambdas are produced with more baryon exchange.

Other research workers have compared the CLA model to data on $p\bar{p}$ annihilations in flight and multiparticle final states produced by $\pi^\pm p$, $K^\pm p$, and pp interactions.[64] On the whole they also find fair qualitative agreement for the single particle production distributions and the invariant mass plots when resonance production is taken into account.

The data from Reaction VII-1 were also compared to the CLA model as modified by Plahte and Roberts. This modified model makes use of a factor from the Veneziano amplitude in an effort to account for resonance production. We found that restricting the middle exchange to isospin zero Regge trajectories resulted in qualitative agreement between the data and model for the mass plots and production angular distributions. In particular, the proton production angular distribution showed

TABLE 8

FRACTIONS OF BARYONS PRODUCED
IN THE FORWARD HEMISPHERE

Reaction	Fraction	
	Data	Model
$K^-n \to \pi^-\pi^-p\overline{K}^o$	.16 ± .02	.09
$\to \pi^-\pi^-p\pi^o\overline{K}^o$	.18 ± .02	.20
$\to \pi^-\pi^-\pi^+n\overline{k}^o$	.24 ± .02	.13
$\to \pi^-\pi^-\pi^+\Lambda^o$	.43 ± .02	.30
$\to \pi^-\pi^-\pi^+\Sigma^o$	.37 ± .03	.33
$\to \pi^-\pi^-\pi^+\pi^o\Lambda^o$	.43 ± .01	.37

quantitative disagreement.

The invariant mass plot of $n\pi^-\pi^-$ from Reaction VII-3 showed a 4.8 standard deviation enhancement (1.627 ± 0.012 GeV/c^2) above background. The full width at half maximum was less than .030 GeV/c^2 at the 90 per cent confidence level. If this enhancement should turn out to be a resonance, it would be a baryon with zero strangeness and isospin 5/2. A resonance with these quantum numbers could not be a member of an SU(3) octet or decuplet. This state, if it exists, is a member of an SU(3) multiplet of at least 35 members. The possible existence of such a resonance is an important question and should be investigated further when more data become available.

LIST OF REFERENCES

1. J. G. Androulakis et al., Nucl. Inst. and Methods 20, 100 (1963).

2. E. L. Hart, Optical Constants, Data-Box Format and Film Format of the BNL 80" Hydrogen Bubble Chamber," BNL Bubble Chamber Group Report BC-04-3-B (9 March 1965).

3. B. B. Culwick, "80" Bubble Chamber Provisional Magnetic Field Fit," BNL Bubble Chamber Group Report BC-05-2-G (22 June 1964).

4. J. Mandzy, Ph.D. Dissertation, Vanderbilt University, 1971 (unpublished).

5. T. B. Borak, Ph.D. Dissertation, Vanderbilt University, 1969 (unpublished).

6. J. W. Burren and J. Sparrow, National Institute for Research in Nuclear Science, Report NIRL/R/14 (1963), And A. G. William, NIRL/M/el (1963); "Geometry Program Manual, "Science Research Council, R.H.E.L., Chilton, Didcot, Berkshire, England (1968); "Geometry Testing Program Optical Constants," Science Research Council, R.H.E.L., Chilton, Didcot, Berkshire, England (1968).

7. "Kinematics Program Manual," Science Research Council, R.H.E.L., Chilton, Didcot, Berkshire, England (1968).

8. Philip R. Bennington, "Data Reduction and Error Analysis for the Physical Sciences," McGraw-Hill Book Company, New York, (1969) 189-190.

9. R. E. Berg, Ph.D. Dissertation, Vanderbilt University, 1971 (unpublished).

10. Matts Roos et al., "Review of Particle Properties," UCRL-8030 (August 1970).

11. V. Cook et al., Physical Review 123, 320 (1961).

12. J. Gordon, Physics Letters 21, 117 (1966).

13. K. J. Foley et al., Physical Review Letters 11 503 (1963).

14. R. Glauber, Phys. Rev. 100, 242 (1955).

15. W. E. Ellis, Internal Report, Vanderbilt University, (1967).

16. J. Orear, "Notes on Statistics for Physicists," UCRL-8416, 18 (13 August 1959).

17. T. Cochran, Ph.D. Dissertation, Vanderbilt University, 1967 (unpublished).

18. Riccardo Levi Setti, "Elementary Particle," The University of Chicago Press, Chicago, 83-85 (1966).

19. A. Weinberg, Vanderbilt University, Nashville, Tennessee (private communication).

20. N. Schmitz, H. Pilkuhn, A. M. Wetherell, Proceedings of the 1965 Easter School for Physicists, CERN 65-24, 1 (1965).

21. Geoffrey F. Chew, "Multiperipheral Dynamics," UCRL-19437 (1969).

22. D. Amati, A. Stanghellini and S. Fubini, Nuovo Cimento 26, 896 (1963).

23. B. E. Y. Svensson, Proceedings of the 1967 CERN School for Physics, CERN 67-24, 2 (1967).

24. Chan Hong-Mo, J. Loskiewicz and W. Allison, Nuovo Cimento 57A, 93 (1960).

25. E. Plahte and R. G. Roberts, Nuovo Cimento Letters 1, 187 (1969).

26. Fong-Ching Chen, Nuovo Cimento 62A, 113 (1969).

27. G. Ranft, Nuovo Cimento 58A, 425 (1968).

28. H. Pilkuhn, "The Interactions of Hadrons," John Wiley and Sons, Inc., New York, 26-32 (1967).

29. F. Cerulus and R. Hagedorn, Suppl. Nuovo Cimento 9, 646, 659 (1958).

30. J. P. Chandler and C. A. Tilger, Nucl. Instrum. Methods, 51, 117 (1967).

31. R. Hagedorn, "Relativistic Kinematics," W. A. Benjamin, Inc., 80-97 (1963).

32. J. Orear et al., Physical Review Letters 21, 389 (1968).

33. G. Bassompierre et al., Physics Letters B9, 295 (1969).

34. H. Pilkuhn, "The Interactions of Hadrons," John Wiley and Sons, Inc., New York, 36 (1967).

35. G. Veneziano, Nuovo Cimento 57A, 190 (1968).

36. Albert Messiah, "Quantum Mechanics," John Wiley and Sons, Inc., New York, 1054-1060 (1966).

37. J. D. Jackson, Reviews of Modern Physics 37, 484 (1965).

38. Stephen Gasiorowicz, "Elementary Particle Physics," John Wiley and Sons, Inc., New York, 214-215 (1967).

39. N. Schmitz, H. Pilkuhn, A. M. Wetherell, Proceedings of the 1965 Easter School for Physicists, CERN 65-24, 1, 26-27 (1965).

40. N. Schmitz, H. Pilkuhn, A. M. Wetherell, Proceedings of the 1965 Easter School for Physicists, CERN 65-24, 1, 27 (1965); Philip R. Benington, "Data Reduction and Error Analysis for the Physical Sciences," McGraw-Hill Book Company, New York, 67-68 (1969).

41. F. Bomse and E. J. Moses, Physical Review 176, 2163 (1968).

42. Robert T. Deck, Physics Review Letters 13, 169 (1964).

43. J. C. Park et al., Physical Review Letters 20, 171 (1968).

44. D. C. Colley et al., Nuovo Cimento 59A, 519 (1969).

45. Jay Orear, "Notes on Statistics for Physicists," UCRL-8417, 6 (13 August 1959).

46. F. Schweingruber et al., Physical Review 166, 1317 (1968).

47. J. D. Jackson, Nuovo Cimento 34, 1644 (1964).

48. K. Gottfried and J. D. Jackson, Nuovo Cimento 33, 309 (1964); Physics Letters 8, 144 (1964).

49. J. D. Jackson, Nuovo Cimento 34, 1650 (1964).

50. Stephen Gasiorowicz, "Elementary Particle Physics," John Wiley and Sons, Inc., New York, 289-312 (1967).

51. J. Bartsch et al., Nuclear Physics B8, 9 (1968).

52. Angela Barbara-Gaitieri et al., Physical Review Letters 22, 1207 (1969).

53. M. Aguilar-Benitez et al., Physical Review Letters 25, 54 (1970).

54. J. Clayton et al., "Pion-Pion Corrections at Low Energies," University of Liverpool Preprint.

55. R. R. Price et al., Physics Letters 33B, 533 (1970).

56. R. H. Dalitz, Ann. Rev. Nucl. Sci. 13, 339 (1963).

57. R. W. Bland et al., Phys. Rev. Letters 17, 939 (1966).

58. Kwan Wu Lai, private communication.

59. M. Banner et al. , Nucl. Physics B15, 205 (1970).

60. A. Benvenuti, E. Marquit and F. Oppenheimer, Phys. Rev. Letters 22, 970 (1969).

61 J. S. Danburg et al., Phys. Rev. Letters 23, 41 (1969).

62. P. Fleury et al., Phys. Letters 26B, 686 (1968).

63. D. Merrill et al., Nuclear Physics B18, 403 (1970).

64. G. W. Brandenburg et al., Nuclear Physics B22, 157 (1970);
C. Caso et al., Nuovo Cimento 66A, 11 (1970);
W. DeBaere et al., Nuclear Physics B22, 131 (1970);
R. Honecker et al., Nuclear Physics B13, 571 (1969);
I. R. Kenyon, Nuclear Physics B13, 255 (1969);
G. Ranft and R. Turnbull, Nuovo Cimento 61B, 317 (1969).